Alma Mater Studiorum – Università di Bologna

DOTTORATO DI RICERCA IN

CHIMICA

Ciclo XXXII

Settore Concorsuale: 03/A2

Settore Scientifico Disciplinare: CHIM/02

ROTATIONAL AND RO-VIBRATIONAL SPECTROSCOPY OF SMALL NITROGEN-CONTAINING SPECIES AND THEIR ASTROPHYSICAL APPLICATIONS

Presentata da: Mattia Melosso

Coordinatore Dottorato

Prof.ssa Domenica Tonelli

Supervisore

Prof. Luca Dore

Co-supervisore

Dott. Filippo Tamassia

Esame finale anno 2020

Contents

1 Scope

This thesis presents the study of small nitrogen-bearing molecules by means of rotational and ro-vibrational spectroscopy. Besides their theoretical relevance, which spans from anharmonic force field analyses to energetic and structural properties, I have chosen this family of species because of their astrochemical importance. Molecular spectroscopy is one of the most powerful tool that chemists, and scientist in general, have to study astronomical sources. Such distant objects cannot be investigated directly and, thus, require the use of something which can easily travel for long distances: light.

Rotational spectroscopy has demonstrated to be a precious tool to detect molecules in the Interstellar Medium (ISM). The number of species observed thanks to radio-telescopes increase constantly and more laboratory studies are demanded to understand the chemistry in Space. Indeed, only the comparison of astronomical observations with laboratory measurements allows to infer physical properties (e.g., temperature, density) of stars and interstellar clouds and their chemical composition.

In the three years I spend as PhD student, I focused my research activity on the laboratory characterization of stable and unstable species with different spectrometers. However, my education includes not only the physical chemistry behind the spectroscopy, but also a bit of astronomy, programming, electronics, quantum chemistry, and organic chemistry. The interdisciplinary aspect of spectroscopy is what fascinating me most.

The structure of this thesis is as follow:

Chapter 2 introduces some basic knowledge of molecular spectroscopy and astrochemistry. The notions of rigid rotor and harmonic oscillator are briefly given, as well as radiative transfer processes which occur in astronomy. The synergy between laboratory measurements and astronomical radio-observations is also explained.

In **Chapter 3** the instrumentation used during the course of my PhD school is described. It includes the Bologna millimeter/submillimeter-wave spectrometer and Fourier-transform infrared spectrometer, the Supersonic Jet Spectrometer for Terahertz Applications (SuJeSTA) in Kassel, and the AILES beamline at SOLEIL Synchrotron. Most of my researches have been performed with the submillimeter spectrometer located at the Department of Chemistry "Giacomo Ciamician" (University of Bologna). This instrument is described more in detail than the other ones.

Chapter 4 presents the most relevant studies I conducted during the last three years. This Chapter is the core of the thesis. Generally speaking, a number of molecules of astrophysical relevance have been characterized spectroscopically. These molecules, either stable or unstable, have been studied by means of rotational and ro-vibrational spectroscopy. The sample of studied species is constituted by small radicals (imidogen, amidogen, and titanium nitride),

cyanopolyynes (cyanoacetylene) and pre-biotic molecules (aminoacetonitrile).
Other studied species, including imines (C-cyanomethanimine, ethanimine), oxygen-bearing species (ethylene glycol), and halocarbons (trifluoroethene, mono-deuterated chloroform), are not extensively presented but they are shortly reported in the **Appendix**.

Some results related to the spectroscopic studies are reported in **Chapter 5**. Here, the first astronomical detection of the singly- and doubly-deuterated amidogen radicals (NHD and ND_2) is presented. These two species have been observed towards the pre-stellar core IRAS 16293-2422 and the deuterium fractionation of NH_2 is discussed. I also report the detection of vibrationally excited aminoacetonitrile NH_2CH_2CN in Sagittarius B2, as observed in the ReMoCa survey. This is the second detection of aminoacetonitrile in the interstellar medium and the first astronomical observation of vibrationally hot lines. A comparison between previous and new observations is discussed.

Finally, few general remarks are discussed in **Chapter 6**. The importance of future laboratory studies is pointed out, along with possible perspectives.

2 Introduction

The aim of this chapter is to offer some insight into molecular spectroscopy and the relationship between laboratory data and astrochemical observations. Since I have decided not to burden this work with much theory found in numerous books, this chapter is not intended to be fully exhaustive for a non-expert reader. However, more details about Hamiltonians and theoretical notions will be offered in the following chapters as far as they are needed.

2.1 Rotational and ro-vibrational spectroscopy

Spectroscopy is one of the most helpful tool we have to investigate atoms and molecules. Matter can interact with electromagnetic radiations at different wavelengths, giving rise to different phenomena. In any case, useful information about atomic and molecular properties, structures and behaviors can be derived. This thesis focuses on rotational and ro-vibrational spectroscopy, i.e., the study of molecules by means of a radiation whose wavelength is comprised between 1 cm and 1 μm. These wavelengths have the right energy to excite the rotational and the vibrational energy levels of small molecules [1]. Each study has been conducted in the gas-phase, the only state of matter in which molecules can rotate freely. Even though vibrational spectra can be recorded in the liquid and solid phases as well, gas-phase spectra recorded at low pressure (typically few Torr of sample) show a spectral resolution that cannot be reach in liquids and solids. Moreover, if the investigated molecules are not too large and the pressure is kept low, their vibrational spectra would be rotationally resolved.

From the analysis of these spectra, plenty of information can be derived. The rotational energy level spacing depends, in the first instance, on the mass distribution within the molecule; in particular, it depends on which atoms are present in the molecule and how they are connected. Rotational spectroscopy is very sensitive to the geometry of a molecule and, thus, is a precious tool to determine structural parameters (e.g., bond lengths, angles, and so on) with unprecedented accuracy. The number of properties that can be studied by molecular spectroscopy are quite large and include: electric and nuclear dipole moments, conformational behaviors, large amplitude motions and hindering barriers, molecular force fields, hyperfine interactions, potential energy surfaces, and many others. Also, molecular spectroscopy has successfully been applied to the characterization of gaseous systems, e.g., Earth and planetary atmospheres and the interstellar medium. The chemical composition of the Earth's atmosphere is of big importance, especially because of its interactions with living organisms. Besides the changes of its composition due to natural processes, the chemical equilibrium in the Earth's atmosphere has also been influenced by human activity. Some of the problems which have been recognized and monitored by atmospheric chemistry are ozone depletion, photochemical smog, greenhouse effect and, among all, global warming. These problems are mainly caused by enormous human emissions of CO_2 and other gases such as CH_4, NO_x, and chlorofluorocarbons (CFCs), whose

[1] Here, the term "small" intends a species with few heavy atoms, where any element but hydrogen is considered "heavy".

presence in the Earth's atmosphere can unequivocally be confirmed by their infrared signatures. Spectroscopy aims to understand the origin of such problems, allowing possible solutions to be evaluated.

On the other hand, the interstellar medium does not affect our lives directly but its study is interesting from many points of view. The term ISM refers to the matter (gas and dust) and radiation (cosmic rays) located in the space between stellar systems. Mainly, the interstellar medium is composed by gas particles (atoms, molecules, and radicals) either in their neutral or ionic forms. Dust grains (silicates and carbonates) are also present in the ISM, but they represent only ∼1% of the total mass. Most of our knowledge of the interstellar medium comes from spectroscopic observations. All atoms and molecules possess characteristic "fingerprints", i.e., each species has its particular spectrum: these spectral lines can be detected through (radio-) telescopes and carry important details about the composition and physical properties of the sources from which they arise. For example, the temperature of the object and its dynamical state can be easily derived from the intensity and shape of molecular signals. To date, more than 200 molecules have been found in the ISM and circumstellar shells. They include species that range in size from two to seventy atoms and have been detected in the majority of the case (*ca.* 80%) using radio astronomy facilities at centimeter (cm), millimeter (mm), and submillimeter (submm) wavelengths. This means that in most cases molecules have been detected thanks to their rotational features, either in emission or absorption. The energetics of the environments in which most molecules are found is comparable to that required to populate these rotational energy levels, thus making possible to observe rotational transitions in the ISM. Obviously, matching signals at specific wavelengths with a specific molecule requires laboratory studies. Spectroscopy is a well-known subject and it is beyond the scope of this thesis to give an exhaustive state-of-the-art overview of the spectroscopic techniques. They can be roughly divided into absorption or emission spectroscopy and in those techniques that simultaneously collect data over a wide spectral range (multiplex spectroscopy) or those which measures intensity over a narrow range of wavelengths at a time (scanning spectroscopy). In the works presented here, only absorption experiments have been conducted. Some details about the instruments used will be presented in **Chapter 3**.

However, what really matters in laboratory studies is to use models (Hamiltonian) which are able to reproduce the spectra observed experimentally. The Hamiltonian used in ro-vibrational spectroscopy relies on the physical notions of the rigid rotor and harmonic oscillator. To understand rotational spectra, we have first to consider molecules as rigid bodies rotating around their center of mass. If the coordinate system is properly chosen (principal axes of inertia), the inertia tensor **I**(3x3) is diagonal and only its principal components I_x, I_y, and I_z need to be considered. In this system, the rotational Hamiltonian can be written as [1]:

$$\mathscr{H}_{\text{rot}} = \frac{P_x^2}{2I_x} + \frac{P_y^2}{2I_y} + \frac{P_z^2}{2I_z}\,, \tag{2.1}$$

where P_x, P_y, and P_z are the components of angular momentum $\mathbf{P}$. The eigenvalues of $\mathscr{H}_{\text{rot}}$ are the quantized rotational energy levels. Usually, the axes notation x, y, and z is replaced with a, b, and c, where a, b, and c denote the axis of the principal inertia system and $I_a \leq I_b \leq I_c$. The type of rotor depends on the values of the three principal moment of inertia as follow:

- linear rotor ($I_b = I_c, I_a = 0$);
- spherical rotor ($I_a = I_b = I_c$);
- symmetric-top rotor, prolate ($I_a < I_b = I_c$) or oblate ($I_a = I_b < I_c$);
- asymmetric rotor ($I_a < I_b < I_c$).

It has to be pointed out the rotational Schrödinger equation can be solved exactly for linear, spherical, and symmetric-top rotors, while there is no exact solution for the asymmetric rotor. In the latter case, the Hamiltonian contains the angular momentum $\mathbf{P}$ and all its three components but it does not exist a set of functions which are simultaneously eigenfunctions of the four operators $\mathbf{P^2}$, P_z^2, P_x^2, and P_y^2.
On the contrary, $\mathscr{H}_{\text{rot}}$ for a symmetric-top rotor contains only the operators which have common eigenfunctions designed as $\psi_{J,K}$ and the matrix elements associated with these operators are known. In this case, $\mathscr{H}_{\text{rot}}$ contains only the operators $\mathbf{P^2}$ and P_z^2; the matrix of the Hamiltonian operator in the symmetric-top representation is diagonal [1]:

$$\langle J, K, M| \mathbf{P^2} |J, K, M\rangle = \hbar^2 J (J+1) \,, \tag{2.2}$$

$$\langle J, K, M| P_z^2 |J, K, M\rangle = \hbar^2 K^2 \,, \tag{2.3}$$

where J is the rotational quantum number quantizing the total angular momentum of a molecule and K and M quantize its projection along the z axes in the body-fixed or laboratory-fixed system, respectively. The eigenvalues of the rotational Hamiltonian for an asymmetric-top molecule can be found using the eigenfunctions of a symmetric-top as a basis to construct a matrix representation of the $\mathscr{H}_{\text{rot}}$ asymmetric-top operator. In this latter case, the matrix elements of the operators P_x^2 and P_y^2 are also required. They are both diagonal:

$$\langle J, K, M| P_x^2 |J, K, M\rangle = \frac{\hbar^2}{2}\left[J (J+1) - K^2\right] = \langle J, K, M| P_y^2 |J, K, M\rangle \tag{2.4}$$

and off-diagonal:

$$\langle J,K,M|\,P_x^2\,|J,K\pm2,M\rangle = -\frac{\hbar^2}{4}\sqrt{[J\,(J+1)-K\,(K\pm1)]} \times\sqrt{[J\,(J+1)-(K\pm1)\,(K\pm2)]} = -\langle J,K,M|\,P_y^2\,|J,K\pm2,M\rangle\ . \quad (2.5)$$

Finally, the constructed matrix is diagonalized and the eigenvalues obtained.

Albeit useful in the understanding of rotational spectra, the rigid rotor approximation is far from reality because molecules are non-rigid and vibrate during the rotation. The Hamiltonian for a semi-rigid rotor, which accounts for centrifugal distortion effects, can be written as:

$$\mathscr{H}_{\rm rot} = \frac{1}{2}\sum_{\alpha\beta}\mu_{\alpha\beta}P_\alpha P_\beta + \frac{1}{4}\sum_{\alpha\beta\gamma\delta}\tau_{\alpha\beta\gamma\delta}P_\alpha P_\beta P_\gamma P_\delta + \dots\ , \quad (2.6)$$

where the $\mu^e_{\alpha\beta}$ are elements of the inverse moment of inertia tensor, P_i ($i = \alpha,\beta,\gamma,\delta$) is the operator associated to a particular component of the angular momentum **P**, and each sum runs over the inertial axes a, b, and c. The terms on the right-hand side represent the classical rigid-rotor energy plus contributions due to the centrifugal distortion treated at increasing orders (quartic, sextic, etc.). An easy way to account these effects on rotational spectra is to treat the centrifugal distortion as a perturbation:

$$\mathscr{H}_{\rm semi-rigid} = \mathscr{H}_{\rm rot} + \mathscr{H}_{\rm dist} \quad (2.7)$$

where $\mathscr{H}_{\rm rot}$ is the Hamiltonian of Eq. (2.1) and $\mathscr{H}_{\rm dist}$ is the perturbation operator. The form of this operator varies from rotor to rotor and corresponds to exact solutions for all cases but asymmetric-top molecules. In the latter case, a "reduced" Hamiltonian is commonly employed. In addition to the distortion of a molecule caused by stretching effects of the centrifugal forces, vibrational motions have to be considered as well. The rotational and distortion constants must be averaged over the vibrational motion of atoms, and thus depend on the vibrational state in which the rotational spectrum is observed. In practice, the expectation value of a generic property X can be written as a Taylor series expansion around the equilibrium geometry:

$$\langle X\rangle = X_e + \sum_r\left(\frac{\partial X}{\partial Q_r}\right)_{Q=0}\langle Q_r\rangle + \frac{1}{2}\sum_{r,s}\left(\frac{\partial^2 X}{\partial Q_r\delta Q_s}\right)_{Q=0}\langle Q_rQ_s\rangle + \dots\ , \quad (2.8)$$

where Q_r, Q_s are normal mode coordinates. However, a complete comprehension of the models used to describe the various type of rotor, a detailed treatment of the distortable rotor, and the so-called fine and hyperfine interactions due to the presence of electronic and nuclear spins (which couple with the rotational angular momentum), will be not given here. The molecules presented in **Chapter 4** spans from linear to asymmetric rotors and they are either closed- or open-shell. The Hamiltonians used will be explained case-by-case and are based on well-known theories; these can be generally found in the book from Gordy & Cook, *"Microwave Molecular*

Spectra" [1].
Similarly, the derivation of vibrational energies starts from the notion of the harmonic oscillator. The Hamiltonian obtained from the classical vibrational energy is:

$$\mathscr{H}_{\text{vib}} = \frac{1}{2} \sum_{k}^{3N-6} \left(\dot{Q}_k^2 + \lambda_k Q_k^2 \right) , \tag{2.9}$$

where λ_k is a force constant associated to the normal coordinate Q_k (the sum runs over the $3N-6$ coordinates which identify the position of N atoms within the molecule). However, chemical bonds deviate from being harmonic oscillators and molecular systems are better described by potential energy surfaces which account for the anharmonicity of the motion.
For a poly-atomic molecule, the vibrational energy results to be a sum of many anharmonic oscillators:

$$E_{\text{vib}} = \sum_{i} \omega_i \left(v_i + \frac{d_i}{2} \right) - \sum_{i,j} \chi_{ij} \left(v_i + \frac{d_i}{2} \right) \left(v_j + \frac{d_j}{2} \right) + \dots , \tag{2.10}$$

where ω_i is the harmonic frequency of the i-th vibration, v_i the vibrational quantum number, d_i the degeneracy of the vibrational motion, and χ_{ij} the first-order anharmonicity constant from a Taylor expansion of the potential energy. Also in the case of vibrational motion, it is hard to be exhaustive without being redundant. The Hamiltonians used will be given for each studied molecules, with a particular attention for cyanoacetylene (§ 4.3.3) which is a linear rotor and exhibits effects due to l-type and Fermi resonances. As reference, the book *"Spectra of Atoms and Molecules"* by Bernath [2] was used.

2.2 Astrochemical observations

Matter emits electromagnetic radiation at any temperature above zero. The wavelength of this radiation is a function of the temperature of the emitting object. Matter at low temperature emits waves that are longer than those emitted at higher temperature.
Interstellar matter, at a temperature of few Kelvin, emits radiation in the cm to submillimeter wavelengths region (3 GHz - 3 THz). This is the reason why molecules in the interstellar medium can be observed by radio-telescopes. The general phenomenon for which matter emits at a nonzero temperature is called thermal emission and its measure depends on the nature of the matter and, of course, its temperature. Because of these dependencies, thermal radiation carries a lot of information on the matter itself, i.e., molecules in this case. The chemical composition of a nebulae and the relative abundances of each molecule can be determined from the frequency and intensity of spectral lines.
In radio observations, the intensity of a spectrum is generally depicted by a temperature scale. In practice, the studied source and an adjacent position without any interfering emission/absorption are observed alternatively and the difference between the recorded signal is taken. This difference can be written as:

$$\Delta I_\nu = [B_\nu(T) - B_\nu(T_\mathrm{b}) - B_\nu(T_\mathrm{C})]\,\{1 - e^{-\tau_\nu}\}\ , \tag{2.11}$$

where $B_\nu(T)$ is the intensity of a black-body radiation at the temperature T and wavelength ν, T_b and T_C are the cosmic background and the continuum temperatures, respectively, and τ_ν is the optical depth (a quantity related to the physical thickness of the cloud and a coefficient α_ν which reflects the absorbing properties of the cloud).
The absorption coefficient can also be expressed in terms of the properties of a molecule. Considering a simple two-level system (lower level l and upper level u), the absorption coefficient for the transition from l to u is given by:

$$\alpha_{ul} = \frac{c^2 n_u}{8\pi\nu_{ul}^2 \Delta\nu}\left\{\exp\left(\frac{h\nu_{ul}}{k_\mathrm{B}T}\right) - 1\right\} A_{ul} \tag{2.12}$$

where c is the speed of light, n_u is the population of the upper level, ν_{ul} is the frequency of the photon which corresponds to the energy difference between the levels l and u, $\Delta\nu$ is the line-width, A_{ul} is the Einstein coefficient for the spontaneous emission, and k_B is the Boltzmann constant. Here, a Boltzmann distribution for the population of the two levels at a temperature T is assumed:

$$n_i = \frac{g_i}{U(T)} n\ \exp\left(-\frac{E_i}{k_\mathrm{B}T}\right)\ . \tag{2.13}$$

In the equation above, g_i is the degeneracy of the i-th level, E_i its energy, $U(T)$ is the partition function, and n_i is the resulting population of the level i. The A_{ul} Einstein coefficient is computed

as follow:

$$A_{ul} = \frac{64\pi^4 \nu_{ul}^3 S_{ul} \mu^2}{3hc^3 g_u}\,, \tag{2.14}$$

where S_{ul} is the line strength, and μ is the dipole moment that allows the transition between the two levels. Substituting Eq. (2.14) into Eq. (2.12), and given that $\tau_{ul} = \alpha_{ul} L$ (with L being the physical thickness of the emitting source), one obtains:

$$\tau_{ul} = \frac{8\pi^3 S_{ul} \mu^2}{3h\Delta \mathrm{v} U(T)} n \left\{ \exp\left(\frac{h\nu_{ul}}{k_\mathrm{B} T}\right) - 1 \right\} \exp\left(-\frac{E_u}{k_\mathrm{B} T}\right) N\,, \tag{2.15}$$

where N is the column density ($N = nL$) of the molecule considered and the line width has been expressed as velocity width [$\Delta \mathrm{v} = \Delta\nu\,(c/\nu_{ul})$]. To derive Eq. (2.15), the level population was assumed to be represented by a Boltzmann distribution. If this assumption is true, the system is said to be in local thermodynamic equilibrium (LTE).
In LTE conditions, the excitation temperature (T_exc) is equal to the rotational temperature (T_rot). In interstellar clouds, molecules are excited and de-excited by collisions with molecular hydrogen: if collisions are frequent enough, T_rot is close to the kinetic temperature (T_kin) of the gas (H_2), and the LTE condition is satisfied. On the other hand, if collisions are less frequent in comparison with radiation probability, the radiative cooling becomes important and the population of the levels deviates from a Boltzmann distribution. In this case, the LTE does not hold and the T_exc changes from transition to transition.
Moreover, depending on the value of the optical depth τ_{ul}, we have two distinguish between two possible cases: optical thin and optical thick lines.

Optically Thin Case. When τ_{ul} of a spectral line is much lower than unity, the line can be indicated as being optically thin. Because the optical depth is proportional to N and S_{ul}, optically thin generally refers to a low column density or low line strength. In this case, its intensity can be approximated as:

$$\Delta T = \frac{h\nu_{ul}}{k_\mathrm{B}} \left\{ \frac{1}{\exp\left(h\nu_{ul}/k_\mathrm{B} T\right) - 1} - \frac{1}{\exp\left(h\nu_{ul}/k_\mathrm{B} T_\mathrm{b}\right) - 1} - \frac{1}{\exp\left(h\nu_{ul}/k_\mathrm{B} T_\mathrm{C}\right) - 1} \right\} \tau_{ul} \tag{2.16}$$

and is proportional to the column density. The value of N, as well as the excitation temperature, can be determined from:

$$\ln \frac{3k_\mathrm{B} W}{8\pi^3 \nu_{ul} S_{ul} \mu^2} = \ln \frac{N}{U(T)} - \frac{E_u}{k_\mathrm{B} T}\,, \tag{2.17}$$

where W is the integrated intensity of the line, which is generally assumed to be $W = \Delta T \Delta\nu$. If several transitions are detected for a given species, the observed values for the left-hand side can be plotted against the upper-state energy E_u and the relation should be linear if the LTE

holds. This method is called “population diagram” (or rotation diagram method).

Optically Thick Case. On the other hand, when τ_{ul} is much higher than unity (abundant species, strong lines), the line is termed as being optically thick and the observed temperature equals the excitation temperature. In the optically thick case, the photons emitted in the inner part of a cloud are completely reabsorbed within the cloud, and the intensity is determined by the surface temperature. Therefore, the column density cannot be determined from optically thick lines and rare isotopic species are used instead in determining N of the parent isotopologue.
Since τ_{ul} depends on the line strength, also the intensities of hyperfine components in open-shell molecules can deviate from LTE. This is because the strongest components might not be optically thin. The intensity ratio (R) between different components is expressed in terms of the optical depth of the strongest (s) component τ_s:

$$R = \frac{1 - e^{-\tau_\mathrm{s}}}{1 - e^{-\tau_\mathrm{s}/r}}\,, \tag{2.18}$$

where r is the LTE intensity ratio in the optically thin case and the same T_exc is assumed for both components. The optical depth τ_s can be derived more accurately by fitting all the hyperfine components simultaneously.
Generally speaking, a physical quantity more significant than the column density of a species is its fractional abundance X. Fractional abundances are typically derived relative to H_2 (X_{H_2}), for comparison with chemical models. To obtain such values, the observed column densities are simply divided by the H_2 column density in the source.

2.3 Nitrogen chemistry in the ISM

Nitrogen is the fifth most abundant element in the interstellar matter near the solar neighborhood, with a cosmic abundance relative to hydrogen of 6.76×10^{-5}. In diffuse clouds, i.e., low-density regions dominated by photodissociation and photoionization processes, nitrogen mainly exists in its neutral form N because the ionization potential of nitrogen atoms is higher than that of H atoms (14.534 *vs.* 13.598 eV). Thus, the formation of nitrogen-containing molecules starts from reaction of N atoms with other species [3].
Nitrogen first reacts with neutral species, such as CH_2, CH, or C_2 to form hydrogen cyanide (HCN) or its radical CN [3]:

$$CH_2 + N \longrightarrow HCN + H\,, \tag{2.19}$$

$$C_2 + N \longrightarrow CN + C\,, \tag{2.20}$$

$$CH + N \longrightarrow CN + H\,. \tag{2.21}$$

However, there are two pathways which are suggested to bring nitrogen into its ionized form N^+: a direct ionization of N atoms by cosmic ray-induced UV radiation, or in the reaction:

$$He^+ + CN \longrightarrow N^+ + C + He\,. \tag{2.22}$$

Once N^+ is produced, the following hydrogenation reactions chain can proceed in succession [4, 5]:

$$N^+ + H_2 \longrightarrow NH^+ + H\,, \tag{2.23}$$

$$NH^+ + H_2 \longrightarrow {NH_2}^+ + H\,, \tag{2.24}$$

$${NH_2}^+ + H_2 \longrightarrow {NH_3}^+ + H\,, \tag{2.25}$$

$${NH_3}^+ + H_2 \longrightarrow {NH_4}^+ + H\,. \tag{2.26}$$

In each step, the cation formed can react with an electron to give the corresponding neutral species (NH, NH_2, and NH_3) but the molecules thus produced are destroyed by photodissociation. The situation is different in a cold molecular cloud, where radiations are shielded at the center of the cloud and photodissociation processes become inefficient. In addition to the above series of reactions, ${NH_2}^+$ will be formed in cold clouds by the following reactions [6, 7]:

$$N_2 + {H_3}^+ \longrightarrow N_2H^+ + H_2\,, \tag{2.27}$$

$$N_2H^+ + e \longrightarrow NH + N\,, \tag{2.28}$$

$$NH + {H_3}^+ \longrightarrow {NH_2}^+ + H_2\,. \tag{2.29}$$

This route is effective, as long as CO (the main destroyer of N_2H^+) is heavily depleted onto dust grains. In this case, N_2H^+ has more chances to encounter an electron for reaction and both NH_3 and NH_2 can be formed in the gas phase. The chemical processes which form nitrogen hydrides from N atoms is summarized in Figure 2.1.

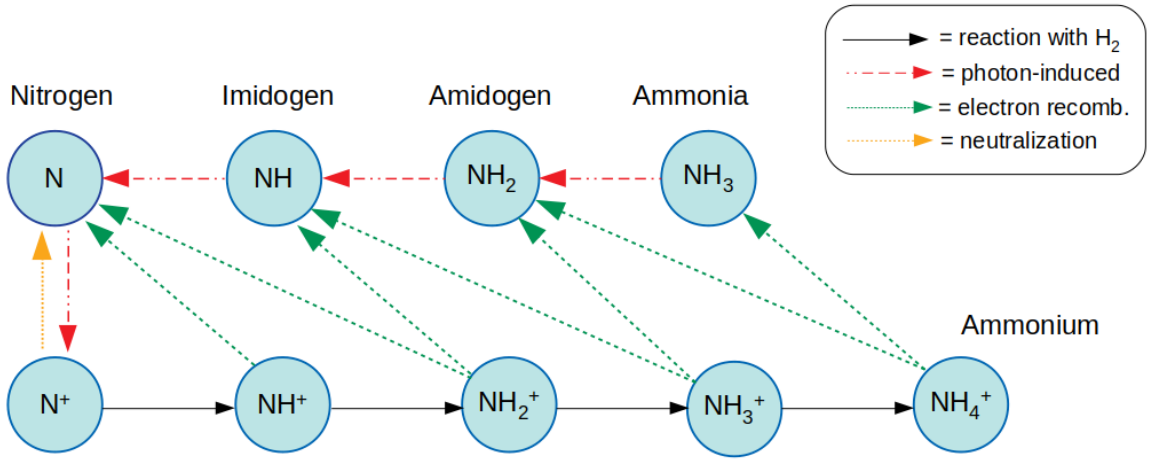

Figure 2.1: Schematic visualization of nitrogen hydrides formation [8].

Cyanopolyynes ($HC_{2n}CN$) (and their geometrical isomers) can be formed by reactions of HCN with hydrocarbon ions. For example, the ion-molecule reaction pathway forming cyanoacetylene (HC_3N) is [9]:

$$C_2H_2^+ + HCN \longrightarrow HCCCNH^+ + H\,, \tag{2.30}$$

$$HCCCNH^+ + e \longrightarrow HC_3N + H\,. \tag{2.31}$$

HC_3N can also be formed via the neutral-neutral reaction [10]:

$$C_2H_2 + CN \longrightarrow HC_3N + H \tag{2.32}$$

In addition to gas-phase reactions, dust grains may play an important role in the production of molecules. Atoms and molecules in the ISM can be absorbed on dust-grains surface, providing further opportunities for chemical reactions to take place and enhance the chemical complexity. Without going too much into details, dust-grains surfaces have the general effects of reducing the barrier height of reactions between two absorbed partners. Because H atoms and H_2 molecules have high surface mobility, hydrogenation reactions are the most important processes in grain-surface chemistry.
Complex organic molecules are thought to be mainly produced in this way and then released into the gas-phase through warm-up of dust-grain mantles or via shocked chemistry [3].

3 Experimental details

Different instruments were used to record the rotational and ro-vibrational spectra of the studied molecules. Two of them are located in Bologna and have been used daily in my PhD activity, while during the six months at Kassel Universität I have worked with the SuJeSTA spectrometer of the Laborastrophysik group. In addition, the CASAC spectrometer at the Max Planck Institute für Extraterrestrische Physik and the infrared spectrometer of the AILES beamline at SOLEIL are also mentioned because they were used for some of the studies reported here. In this section, a description of each spectrometer is given.

3.1 Bologna Submillimeter-Wave Spectrometer

Rotational spectra were recorded in Bologna using a frequency-modulation millimeter-/submillimeter-wave spectrometer (Fig. 3.1).

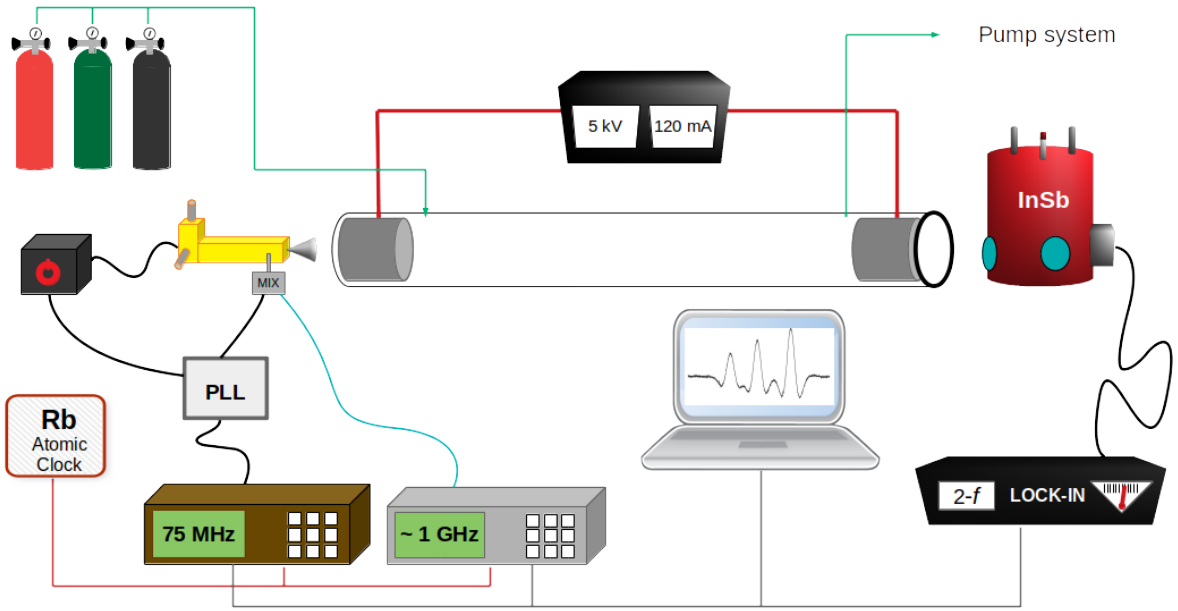

Figure 3.1: Schematic representation of the millimeter-/submillimeter-wave spectrometer [11]. The instrument is depicted in the following set-up: single-pass configuration, Gunn diode at its fundamental frequency and connected to the PLL, absorption cell equipped with a DC discharge system, some cylinder gases to inject the sample, and InSb bolometer as detector.

The main sources of monochromatic polarized radiation are several Gunn diodes (Radiometer Physics GmbH, J.E. Carlstrom Co, Farran Technology Limited) which emit in the frequency range 75–134 GHz with an output power between 30 and 48 mW. Higher frequencies, up to 1.244 THz, are obtained by coupling the Gunn diodes with passive frequency multipliers in cascade (Radiometer Physics GmbH, Virginia Diodes Co). Each frequency multiplication decreases the output power of the radiation to about 10% of the input power. The output frequency is stabilized through a Phase-Lock-Loop (PLL) system. The microwave radiation generated by

the Gunn diode is mixed with a harmonic of a centimeter-wave oscillator (HP8672A, 2–18 GHz) in a harmonic mixer, whose output is the difference-frequency or Intermediate Frequency (IF). In the synchronization cycle, the IF is matched with an external reference of 75 MHz generated by a second synthesizer (HP8642A). The frequency-modulation technique was used to improve the signal to noise ratio (S/N) of the recorded spectra. The frequency modulation of the radiation was obtained by sine-wave modulating at a frequency (f) between 0.5 and 48 kHz the reference signal of the HP8642A synthesizer. The amplitude of the modulation (FM) depends on the line-width and the required resolution. Both synthesizers are referenced to a 5 MHz rubidium atomic-clock, whose frequency stability is 3×10^{-12} Hz.

The electromagnetic radiation is focused in and out of the cell by two parabolic mirrors (Edmund optics). The absorption cell is a Pyrex glass tube with a length of 3.25 m and a diameter of 5 cm. The cell is closed at the ends by two high-density polyethylene (HDPE) windows, transparent to microwave radiations. When a double-pass configuration is used, one window is replaced with a roof-top mirror and a wire grid polarizer is placed with a 45°angle between the HDPE window and the incoming radiation. It is equipped with two cylindrical hollow electrodes for a DC plasma discharge (up to 5 kV and 120 mA), and it is jacketed by a plastic pipe for liquid nitrogen cooling. The cell is placed inside a solenoid that can generate a magnetic field longitudinal to the absorption path. The spectrometer is equipped with a second cell, slightly shorter (3 m) and thicker (d=8 cm), which is connected to a pyrolysis system. A quartz tube can be heated by a 30 cm long furnace at temperatures up to 1200°C. The quartz tube is connected at one end with a pressure gauche and two sample inlets, and to the absorption cell at the other end. This system allows the study of semi-stable molecules which can be formed during a Flash Vacuum Pyrolysis (FVP) process. The cells are connected to a pumping system, a diffusion pump and a rotary pump in cascade, that ensure high vacuum conditions ($\sim$ 0.1 bar). The pressure inside the cell is monitored with pressure gauges (MKS Baratron, resolution = 0.1 bar), while the temperature is tracked by few thermocouples (type T).

Two detector systems, operating in different frequency ranges and at different temperatures, were used to record the spectra. Room-temperature Schottky barrier detectors (Millitech, Virginia Diodes Co) were used at frequencies below 520 GHz, while a hot-electron indium antimonide (InSb) bolometer (QMC Instr. Ltd. type QFI/2), cooled to liquid helium temperature, was used at higher frequencies. The pre-amplified detector signal is demodulated by a Lock-in amplifier at twice the modulation frequency ($2f$), to record the absorption signal in second derivative. This process modifies the line shape as shown in Figure 3.2.

An additional S/N improvement is achieved by filtering the signal into an ohmic RC circuit. Finally, the Lock-in signal is analog-to-digital converted and sent to a computer. A home-written program, based on the Visual Basic 6.0 language, drives the instrument, acquires and processes the signal.

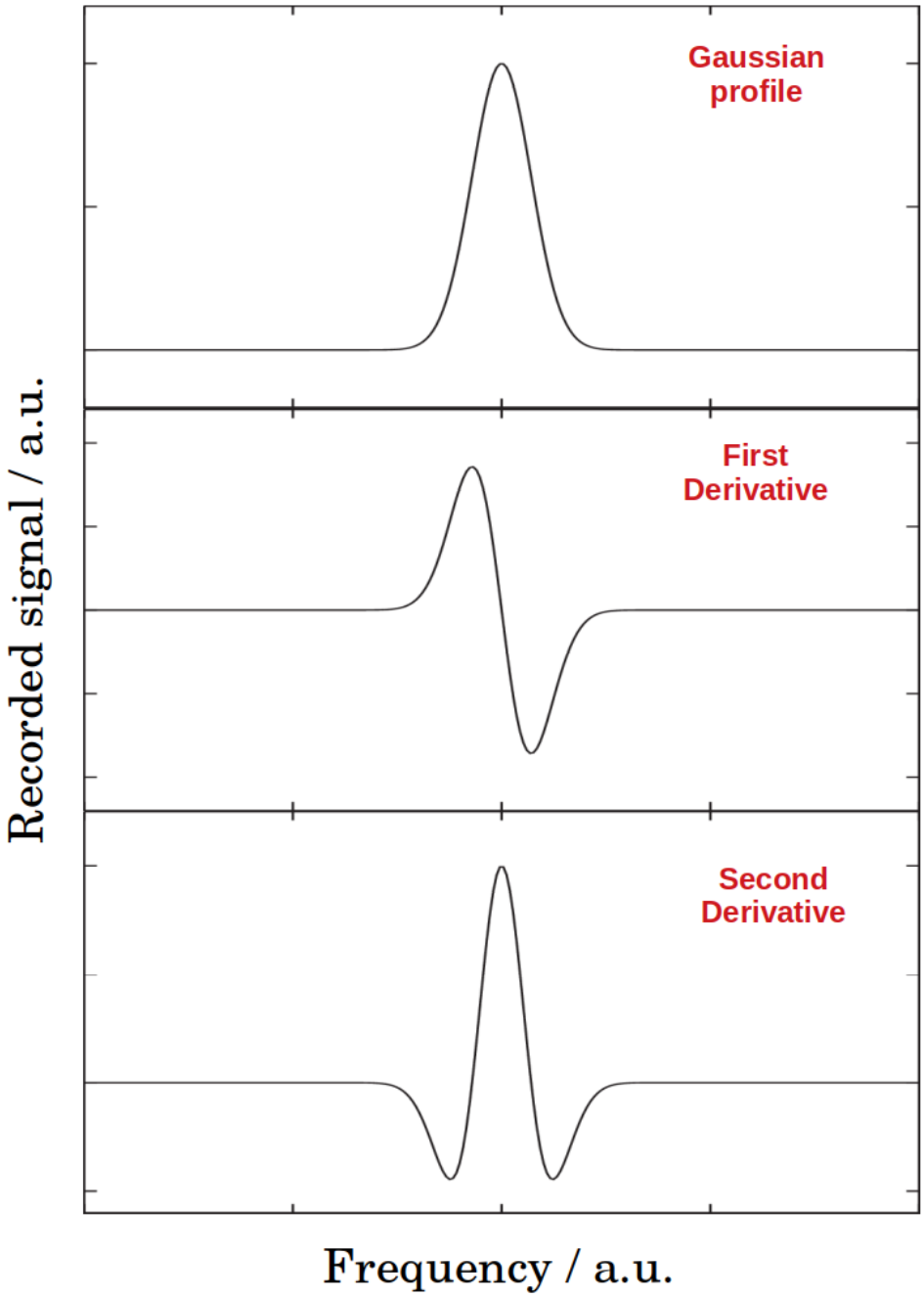

Figure 3.2: Simulation of Gaussian line profile (*top panel*) and its first (*middle panel*) and second derivative (*bottom panel*).

3.2 Center for Astrochemical Studies Absorption Cell Spectrometer

Part of the spectra observed in the millimeter and submillimeter domain were recorded with the CASAC (Center for Astrochemical Studies Absorption Cell) spectrometer at the Max-Planck-Institut für Extraterrestrische Physik (MPE). The experimental apparatus is similar to the submillimeter spectrometer described in Sec. 3.1. Briefly, the instrument employs an active multiplier chain (Virginia Diodes) as a source of millimeter radiation in the 82–125 GHz interval. By the use of two additional frequency tripler stages in cascade, this setup provides operation in the THz regime with an available power of a few W. A cryogenic-free, closed-cycle cooled InSb hot electron bolometer (QMC Instr. Ltd.) is used as a detector. The absorption cell is a Pyrex tube (3 m long and 5 cm in diameter) containing two stainless steel, cylindrical hollow electrodes separated by 2 m. The plasma region is cooled by liquid nitrogen circulation. The spectrometer employs the frequency modulation technique to enhance the signal-to-noise ratio of the recorded signals. The carrier frequency is sine-wave modulated at a rate of 33.3 kHz, then phase sensitive detection at $2f$ is performed using a digital lock-in amplifier.

3.3 SuJeSTA. A Supersonic Jet Spectrometer for Terahertz Applications

Rotational spectra were recorded in Kassel using the Supersonic Jet Spectrometer for Terahertz Applications (SuJeSTA, Fig. 3.3) [12].

The source of radiation is the Active Multiplication Chain (AMC, Virginia Diodes) WR9.0AMC-I which emits in the 82–125 GHz frequency range with a typical output power of 14 dBm. It is driven by a 8–20 GHz Frequency Synthesizer, referenced to a 10 MHz GPS signal which ensures the frequency stability. Higher frequencies were obtained using passive frequency-multipliers in a cascade. All mirrors are made of aluminum for high reflectivity, while the other optical accessories, e.g., lenses and windows, are made of either Teflon or HDPE, offering high transmittance for submillimeter waves.

A laser ablation system followed by a supersonic expansion is used for the production of unstable species. Briefly, a 1064 nm Q-switched Nd:YAG laser beam at a maximum 30 Hz repetition rate is focused onto a rotating metal rod and the ablated material is seeded in a pulsed gas flow of a noble gas (possibly mixed with a co-reagent) at pressures between 1 and 10 bar. The timing of the nozzle pulses is often crucial and needed to be adjusted case-by-case.

The sensitivity of the spectrometer is greatly enhanced by a 16-path Herriott-type cell, perpendicular to the jet, inside the vacuum chamber. All the species formed during the laser ablation process cool down when they enter the cell and expand adiabatically. The low rotational temperature of molecules allows the spectroscopic investigation of their lowest energy levels only. In this experiment, rotational temperatures can be typically assumed as low as 20 K. A helium-

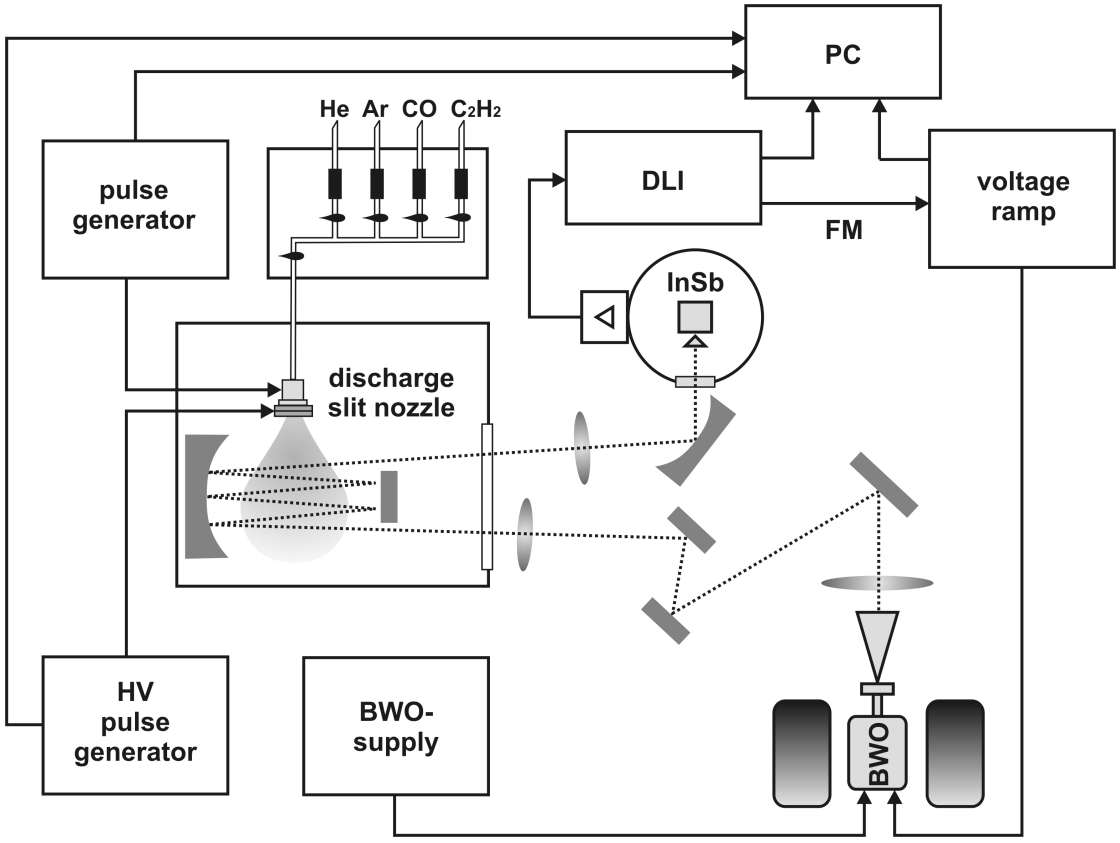

Figure 3.3: Schematic representation of SuJeSTA in one of its possible configuration. Currently, the BWO oscillators are replaced by an active multiplication chain and a laser ablation system is used instead of the discharge nozzle.

cooled InSb Hot Electron Bolometer was used to record the spectra. The signal is recorded during a few tens to few hundreds s time window and subsequently processed in a pre-amplifier before data acquisition. The S/N is improved by averaging the signal at each frequency position over several laser-shots.

3.4 Fourier-Transform Infrared Spectrometer

Infrared spectra were recorded in Bologna using a Bomem DA3.002 Fourier-Transform Infrared Spectrometer (FT-IR). A schematic representation is shown in Figure 3.4.

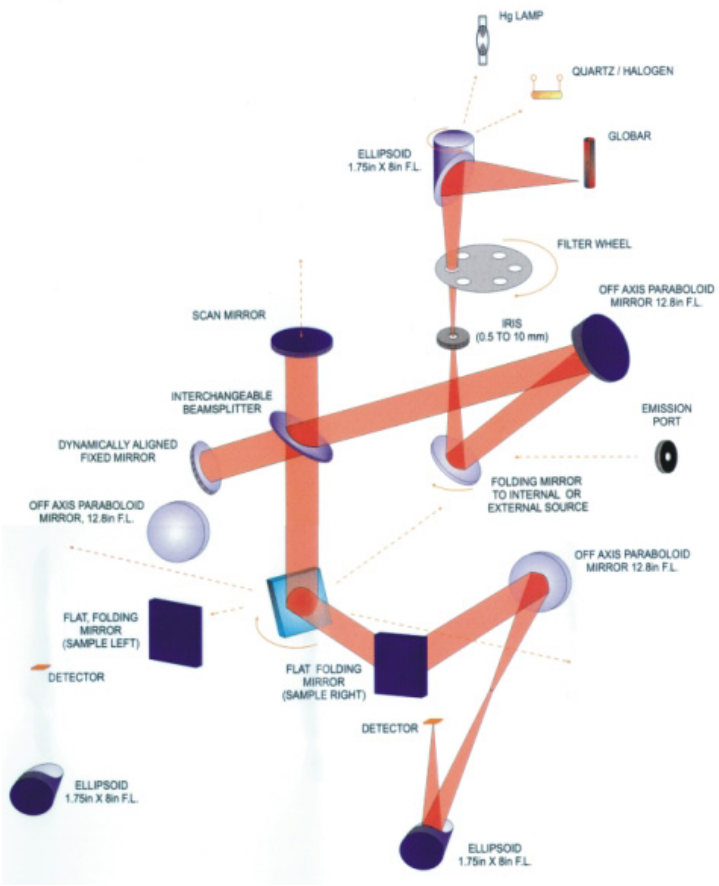

Figure 3.4: Scheme of Bomem DA3.002 FT-IR spectrometer at Dipartimento di Chimica Industriale "Toso Montanari" as taken from the user manual.

The radiation sources are several lamps which emit in different frequency ranges: a Hg lamp for the Far-Infrared region (FIR), a Globar source (silicon carbide bar) in the Mid-Infrared (MIR), and a quartz halogen lamp at Near-Infrared (NIR) frequencies. Firstly, the output radiation is focused to an iris (0.5 to 10 mm) and then, through a series of mirrors, it hits a beamsplitter, which is either made of CaF_2, KBr, or Mylar film for best performance in the NIR, MIR, and FIR, respectively. By this, the radiation is split in two beams. The core of the FT-IR is a Michelson interferometer. Each beam has a light path of different length (one mirror is fixed, the other one is movable) and is reflected back toward the beamsplitter where they are recombined. The interferogram is generated by measuring the signal at different positions of the movable mirror. The resulting interference pattern is directed to the absorption cell. A White-type multipass cell, with path-lengths up to 10 m, was commonly used to contain the sample. The radiation coming out from the absorption cell is focused onto the detector. Several

systems, thermal (bolometers) and photodetectors, are used to collect the output radiation. The best sensitivity was obtained by choosing the detector case-by-case, depending on the working frequency. The various setup configurations are summarized in Figure 3.5.

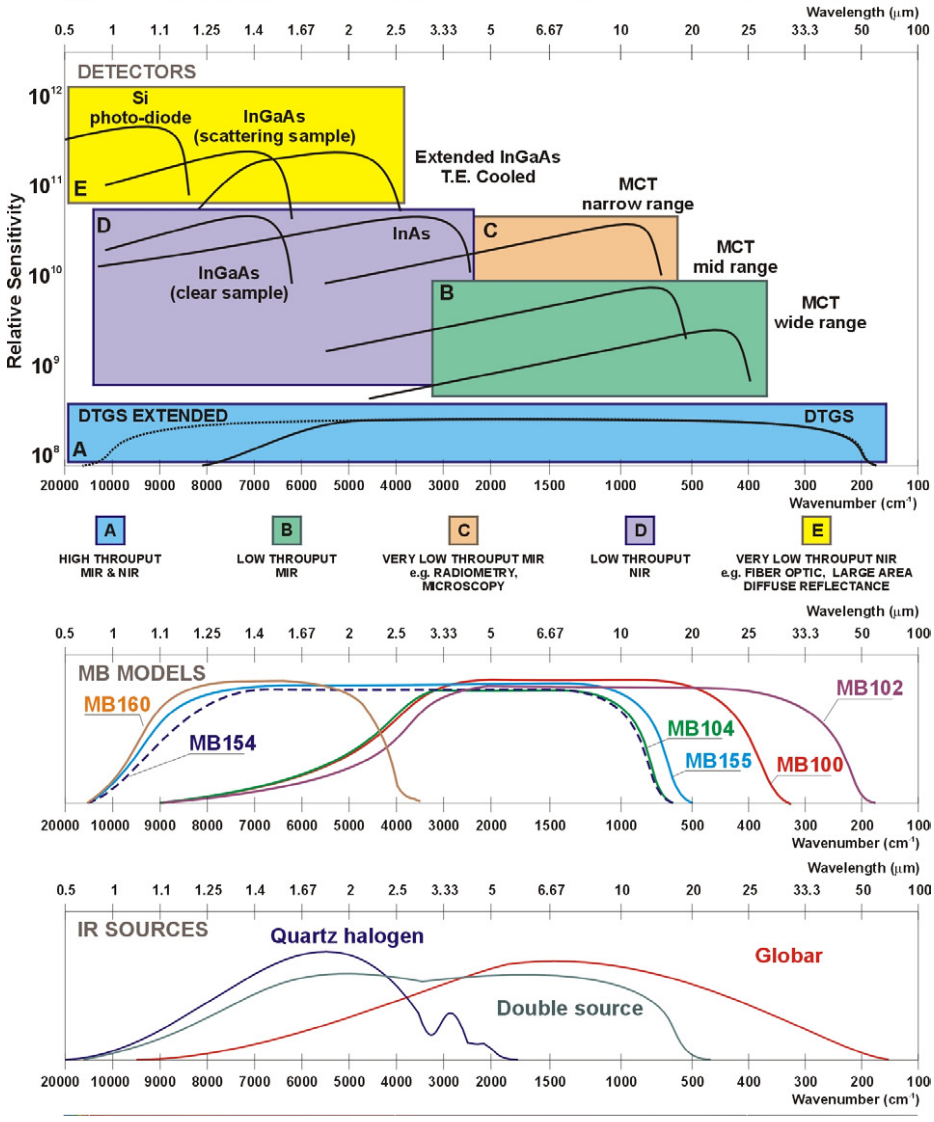

Figure 3.5: Possible configurations (sources, beamsplitters, and detectors) of the FT-IR spectrometer as illustrated within the user manual.

3.5 AILES beamline at SOLEIL Synchrotron

Infrared spectra were recorded at the AILES Beamline at SOLEIL Synchrotron. The spectral range goes from the MIR to the FIR domains, with the best performances below 1000 cm^{-1} and a maximum resolution of 0.00102 cm^{-1}.

The AILES Beamline uses a Bruker IFS125HR FT spectrometer which works analogue to the Bomem spectrometer described in Sec. 3.4. The collected Synchrotron Radiation, brighter than any other source at FIR frequencies, is extracted by a movable mirror toward the entrance slit of the interferometer. A wide range of beam splitters and detectors is available to cover the above-mentioned frequency range. Among them, a silicon fast bolometer ($\sim$ 1 kHz band-pass) has been implemented in the beamline. A White-type multipass absorption cell (4–150 m) is used for gaseous samples and can be equipped with a post-discharge set-up for plasma generation. In the latter configuration, a radio-frequency discharge cell is connected perpendicularly to, and at the center of, the absorption cell.

The spectrometer is vacuum pumped to a pressure of 10^{-4} mbar by means of a turbomolecular pump, and the flow in the post-discharge experiment is kept constant by a booster pump.

4 Case studies

4.1 Imidogen radical

Several isotopologues of imidogen, namely ^{14}NH, ^{15}NH, ^{14}ND, and ^{15}ND, have been thoroughly studied during the course of my PhD. After explaining the importance of this small diatomic radical (§4.1.1), the studies are reported one-by-one in detail (§4.1.3–4.1.6). Subsequently, a multi-isotopologues global analysis is presented (§4.1.7) along with the most relevant results (§4.1.8).
Part of these studies are reported in two publications:

- L. Bizzocchi, M. Melosso, L. Dore, C. Degli Esposti, F. Tamassia, D. Prudenzano, V. Lattanzi, J. Laas, S. Spezzano, B. Giuliano, C. Endres, and P. Caselli, "Accurate laboratory measurement of the complete fine structure of the $N = 1 - 0$ transition of ^{15}NH," *Astrophys. J.*, vol. 863, no. 1, p. 3, 2018 [13].

- M. Melosso, L. Bizzocchi, F. Tamassia, C. Degli Esposti, E. Canè, L. Dore, "The rotational spectrum of ^{15}ND. Isotopic-independent Dunham-type analysis of the imidogen radical," *Phys. Chem. Chem. Phys.*, vol. 21, no. 7, p. 3564–3573, 2019 [14].

The unpublished results will be collected with data from future experiments and eventually presented in a paper for *The Journal of Molecular Spectroscopy*.
Sections §4.1.1, §4.1.2, §4.1.6, §4.1.7, §4.1.8 are a reproduction of Ref. [14], while Section §4.1.3 is reproduced from Ref. [13].
My contribution to this work can be summarized as follow:

- recording of all the spectra, with the exception of the FIR spectrum of ^{14}ND;

- data analysis, including the fitting procedures of each isotopologue and the Dunham fit;

- testing and debugging the pipeline code, which has been written by Dr. L. Bizzocchi;

- derivation of the molecular properties presented in §4.1.8, with the aid of Prof. L.Dore for the Propagation of uncertainties;

- manuscripts writing and editing, including all tables and figures.

4.1.1 Introduction

The imidogen radical NH has been the subject of several spectroscopic, computational and astrophysical studies. This simple diatomic radical belongs to the first-row hydrides, is commonly observed in the combustion products of N-bearing compounds [15, 16], and is also an intermediate in the formation process of NH_3 in the ISM [17]. The main isotopologue of imidogen, NH,

has been detected in a large-variety of environments, from the Earth atmosphere to astronomical objects, e.g., comets [18], many types of stars [19, 20] including the Sun [21, 22], diffuse clouds [23], massive star-forming regions [24] and, recently, in prestellar cores [25]. Also its deuterated form ND has been identified in the ISM, towards the young solar-mass protostar IRAS16293 [26] and in the prestellar core 16293E [25].

A lot of studies have been devoted to the origin of interstellar NH and different formation models have been proposed to explain its observed abundances. Two main formation routes have been devised for the NH radical: from the electronic recombination of NH^+ and $NH_2{}^+$, intermediates in the synthesis of interstellar ammonia starting with N^+ or, alternatively, via dissociative recombination of N_2H^+ (see §2.3). However, the mechanism of NH production in the ISM is still debated [24], and grain-surface processes might also play a significant role [27]. Imidogen, together with other light hydrides, often appears in the first steps of chemical networks leading to more complex nitrogen-bearing molecules. Its observation thus provides crucial constraints for the chemical modeling of astrophysical sources [28]. Also the rare isotopologues of this radical yield important astrochemical insights. Being proxies for N and D isotopic fractionation processes, they may help to trace the evolution of gas and dust during the star formation, thus shedding light on the link between Solar System materials and the parent ISM [29]. This is particularly relevant for nitrogen, whose molecular isotopic compositions exhibits large and still unexplained variations [30, 31]. Measuring the isotopic ratios in imidogen provides useful complementary information on the already measured D/H and $^{14}N/^{15}N$ ratios in ammonia (including the $^{15}NH_2D$ species [32]).

As far as the laboratory work is concerned, there is a substantial amount of spectroscopic data for the most abundant species and less extensive measurements for ^{15}NH and ND. A detailed description of the spectroscopic studies of imidogen can be found in the latest experimental works on NH [33], ^{15}NH [13], and ND [34]. It has to be noticed that no experimental data or theoretical computations were available in literature for the doubly substituted species ^{15}ND before this work.

In this thesis, I report:

- the observation of the complete $N = 1 \leftarrow 0$ transition of ^{15}NH in both the ground and $v = 1$ states around 0.9 THz;
- new transition frequencies for the isotopologues NH and ND in their $v = 1$ excited state;
- new high-N transition of ND in its ground vibrational state recorded with a synchrotron-based FTIR spectrometer;
- the first study of the pure rotational spectrum of ^{15}ND in its ground electronic state $X\,^3\Sigma^-$ recorded up to 1.068 THz;

These new sets of data, together with the literature data for NH, ^{15}NH and ND, have been analysed in a global multi-isotopologue fit to give a comprehensive set of isotopically inde-

pendent spectroscopic parameters. Thanks to the high precision of the measurements, several Born–Oppenheimer Breakdown (BOB) constants (Δ_{lm}) could be determined from a Dunham-type analysis [35]. The alternative Dunham approach proposed by [36] has been also employed. In this case, the results are expressed in terms of the parent species coefficients Y_{lm} plus some isotopically dependent BOB constants (δ_{lm}).

Finally, very accurate equilibrium bond distances r_e (including the Born–Oppenheimer bond distance r_e^{BO}) and Zero-Point Energies (ZPE) for each isotopologue have been computed from the determined spectroscopic parameters. This set of constants can be also used to compile line catalogs for astronomical searches of imidogen.

4.1.2 Theory

Imidogen is a diatomic free radical with a $X^3\Sigma^-$ ground electronic state. It exhibits a fine structure due to the dipole–dipole interaction of the two unpaired electron spins and to the magnetic coupling of the molecular rotation with the total electron spin.

The coupling schemes of the various angular momenta in NH are well described by Hund's case (b) [37]:

$$\mathbf{J} = \mathbf{N} + \mathbf{S}\,, \tag{4.1}$$

where $\mathbf{J}$ is the total angular momentum excluding nuclear spins, $\mathbf{N}$ represents the end-over-end rotational angular momentum and $\mathbf{S}$ is the electronic spin angular momentum. Each fine-structure level is labeled by the quantum numbers J and N, with $J = N+1, N, N-1$. For $N = 0$, only the $J = 1$ component exists. Inclusion of nitrogen and hydrogen hyperfine interactions leads to further couplings:

$$\mathbf{F}_1 = \mathbf{J} + \mathbf{I}_{\mathrm{N}}\,, \qquad \mathbf{F} = \mathbf{F}_1 + \mathbf{I}_{\mathrm{H}}\,. \tag{4.2}$$

For a given ro-vibrational state, the effective Hamiltonian can be written as:

$$\mathscr{H} = \mathscr{H}_{\mathrm{rv}} + \mathscr{H}_{\mathrm{fs}} + \mathscr{H}_{\mathrm{hfs}} \tag{4.3}$$

where $\mathscr{H}_{\mathrm{rv}}$, $\mathscr{H}_{\mathrm{fs}}$ and $\mathscr{H}_{\mathrm{hfs}}$ are the ro-vibrational, fine- and hyperfine-structure Hamiltonians, respectively:

$$\mathscr{H}_{\mathrm{rv}} = G_v + B_v\mathbf{N}^2 - D_v\mathbf{N}^4 + H_v\mathbf{N}^6 + \ldots \tag{4.4}$$

$$\mathscr{H}_{\mathrm{fs}} = \frac{2}{3}\left(\lambda_v + \lambda_{Nv}\mathbf{N}^2 + \ldots\right)\left(3S_z^2 - \mathbf{S}^2\right) + \left(\gamma_v + \gamma_{Nv}\mathbf{N}^2 + \ldots\right)\mathbf{N}\cdot\mathbf{S} \tag{4.5}$$

$$\begin{aligned}\mathscr{H}_{\rm hfs} = &\sum_i b_{F,v}(i)\,\mathbf{I}_i\cdot\mathbf{S} + \sum_i c_v(i)\left(I_{iz}S_z - \frac{1}{3}\mathbf{I}_i\cdot\mathbf{S}\right)\\ &+ \sum_i eQq_v(i)\,\frac{(3I_{iz}^2 - \mathbf{I}_i^2)}{4I_i(2I_i-1)} + \sum_i C_{I,v}(i)\,\mathbf{I}_i\cdot\mathbf{N}\end{aligned} \tag{4.6}$$

Here, G_v is the energy of a vibrational state v, B_v the rotational constant, D_v and H_v, the centrifugal distortion parameters up to the third power in the $\mathbf{N}^2$ expansion, λ_v and λ_{Nv} are the electron spin–spin interaction parameter and its centrifugal distortion coefficient; γ_v, and γ_{Nv} are the electron spin–rotation constant and its centrifugal distortion coefficient, respectively. $\mathbf{S}$ is the electron spin operator and S_z one of its component, whereas $\mathbf{I}_i$ is the nuclear spin operator for the i-th nucleus and I_{iz} its z component. The constants $b_{F,v}$ and c_v are the isotropic (Fermi contact interaction) and anisotropic parts of the electron spin–nuclear spin coupling, eQq_v represents the electric quadrupole interaction and $C_{I,v}$ is the nuclear spin–rotation parameter. In Eq. (4.6) the index i runs over the different nuclei present in a given isotopologue. The four nuclear spins are: $I = 1/2$ for H and ^{15}N and $I = 1$ for D and ^{14}N.

For diatomic species only, ro-vibrational data of all isotopologues can be treated together in a global analysis. In such a sense, it is advantageous to use a Dunham-type expansion [35]. The ro-vibrational energy levels are given by the equation:

$$E_{\rm rv}(v,N) = \sum_{l,m} Y_{lm}\left(v+\tfrac{1}{2}\right)^l \left[N(N+1)\right]^m . \tag{4.7}$$

The fine- and hyperfine-structure parameters [i.e., λ_v, λ_{Nv}, γ_v, γ_{Nv}, $b_{F,v}$, c_v, eQq_v, and $C_{I,v}$ in Eqs. (4.5)–(4.6)], are given by similar expansions:

$$y(v,N) = \sum_{l,m} \mathcal{Y}_{lm}\left(v+\tfrac{1}{2}\right)^l \left[N(N+1)\right]^m , \tag{4.8}$$

where $y(v,N)$ represents the effective value of the parameter y in the ro-vibrational level (v,N), and $\mathcal{Y}_{lm}$ are the coefficients of its Dunham-type expansion. The spectroscopic constants introduced earlier [Eqs. (4.4)–(4.6)] can be expressed in terms of the Dunham coefficients Y_{lm} and $\mathcal{Y}_{lm}$. For instance, the constants G_v and B_v of the ro-vibrational Hamiltonian are given by:

$$G_v = \sum_{l=0} Y_{l0}\left(v+\tfrac{1}{2}\right)^l , \tag{4.9a}$$

$$B_v = \sum_{l=0} Y_{l1}\left(v+\tfrac{1}{2}\right)^l . \tag{4.9b}$$

Each fine and hyperfine constant is also expressed by appropriate expansions; e.g., the electron spin-rotation constant and its centrifugal dependence can be expressed as:

$$\gamma_v = \sum_{l=0} \gamma_{l0} \left(v + \tfrac{1}{2}\right)^l , \tag{4.10a}$$

$$\gamma_{Nv} = \sum_{l=0} \gamma_{l1} \left(v + \tfrac{1}{2}\right)^l , \tag{4.10b}$$

where γ_{l0} and γ_{l1} are the $\mathcal{Y}_{lm}$ constants of Eq. 4.8 relative to the spin-rotation interaction. For a given isotopologue α, a specific set of Dunham constants $Y_{lm}^{(\alpha)}$ and $\mathcal{Y}_{lm}^{(\alpha)}$ is defined. Every constant can be described in terms of isotopically invariant parameters, using the reduced-mass dependences given by Refs. [38, 39]:

$$Y_{lm}^{(\alpha)} = U_{lm}\mu_\alpha^{-(l/2+m)} \left[1 + m_e \left(\frac{\Delta_{lm}^{\mathrm{N}}}{M_{\mathrm{N}}^{(\alpha)}} + \frac{\Delta_{lm}^{\mathrm{H}}}{M_{\mathrm{H}}^{(\alpha)}}\right)\right] , \tag{4.11a}$$

$$\mathcal{Y}_{lm}^{(\alpha)} = U_{lm}^{y}\mu_\alpha^{-(l/2+m+p)} \left[1 + m_e \left(\frac{\Delta_{lm}^{y,\mathrm{N}}}{M_{\mathrm{N}}^{(\alpha)}} + \frac{\Delta_{lm}^{y,\mathrm{H}}}{M_{\mathrm{H}}^{(\alpha)}}\right)\right] , \tag{4.11b}$$

where $M_{\mathrm{X}}^{(\alpha)}$ (with X = N, H) are the atomic masses, μ_α is the reduced mass of the α isotopologue, and m_e is the electron mass. U_{lm} and U_{lm}^{y} are isotopically invariant Dunham constants, while Δ_{lm}^{X} and $\Delta_{lm}^{y,\mathrm{X}}$ are unitless coefficients which account for the Born–Oppenheimer Breakdown [40, 39]. In Eq. (4.11b), $p = 0$ for $y = \lambda, b_F, c, eQq$, while $p = 1$ for $y = \gamma, C_I$. Note that this extra μ^{-1} factor in the mass scaling is needed to account for the intrinsic $\mathbf{N}^2$ dependence of the spin–rotation constants [41]. Here, the unknowns are the U_{lm}, U_{lm}^{y} coefficients and the corresponding Δ_{lm}^{X} and $\Delta_{lm}^{y,\mathrm{X}}$ BOB corrections. An alternative approach has been proposed by LeRoy [36], where one isotopologue (usually the most abundant one) is chosen as reference species ($\alpha = 1$), and the Dunham parameters $Y_{lm}^{(\alpha)}$ and $\mathcal{Y}_{lm}^{(\alpha)}$ of any other species are obtained by the following mass scaling

$$Y_{lm}^{(\alpha)} = \left[Y_{lm}^{(1)} + \frac{\Delta M_{\mathrm{N}}}{M_{\mathrm{N}}^{(\alpha)}}\delta_{lm}^{\mathrm{N}} + \frac{\Delta M_{\mathrm{H}}}{M_{\mathrm{H}}^{(\alpha)}}\delta_{lm}^{\mathrm{H}}\right]\left(\frac{\mu_1}{\mu_\alpha}\right)^{(l/2+m)} , \tag{4.12a}$$

$$\mathcal{Y}_{lm}^{(\alpha)} = \left[\mathcal{Y}_{lm}^{(1)} + \frac{\Delta M_{\mathrm{N}}}{M_{\mathrm{N}}^{(\alpha)}}\delta_{lm}^{y,\mathrm{N}} + \frac{\Delta M_{\mathrm{H}}}{M_{\mathrm{H}}^{(\alpha)}}\delta_{lm}^{y,\mathrm{H}}\right]\left(\frac{\mu_1}{\mu_\alpha}\right)^{(l/2+m+p)} . \tag{4.12b}$$

Here, $\Delta M_{\mathrm{X}} = M_{\mathrm{X}}^{(\alpha)} - M_{\mathrm{X}}^{(1)}$ are the mass differences produced by the isotopic substitution, with respect to the reference species, and the BOB corrections are described by the new δ_{lm}^{X} and $\delta_{lm}^{\mathrm{y,X}}$ coefficients. These are related to the dimensionless Δ_{lm}^{X} of Eqs. 4.11 through the simple relation

$$\Delta_{lm}^{\mathrm{X}} = \delta_{lm}^{\mathrm{X}} \frac{M_X^{(1)}}{m_e} \left(Y_{lm}^{(1)} + \delta_{lm}^{\mathrm{N}} + \delta_{lm}^{\mathrm{H}}\right)^{-1} . \tag{4.13}$$

Although formally equivalent, this latter parametrisation was introduced to overcome a number of deficiencies of the traditional treatment which were pointed out by Watson [39] and Tiemann [42], and its features are discussed in great detail in the original paper [36]. An obvious advantage of the alternative mass scaling of Eqs. (4.12) is that the fitted coefficients are all expressed in frequency units and are directly linked to the familiar spectroscopic parameters of the reference isotopologue (e.g., $Y^{(1)}_{10} \approx \omega_e$, $Y^{(1)}_{20} \approx -\omega_e x_e$, $Y^{(1)}_{01} \approx B_e$, $Y^{(1)}_{11} \approx -\alpha_e$, etc.). Furthermore, the BOB contributions are accounted for using purely addictive terms thus reducing the correlations among the parameters.

4.1.3 ^{15}NH

The rotational spectrum of ^{15}NH was observed in absorption using the CASAC spectrometer described in §3.2. The ^{15}NH radical was produced in the positive column of a DC glow discharge by flowing a mixture of 3 mTorr (0.4 Pa) of $^{15}N_2$, 3 mTorr of H_2 and 25 mTorr (3.3 Pa) of Ar. The cell was cooled at 90–100 K by liquid nitrogen circulation. The optimal conditions, expressing a balance between the signal strength and the discharge-generated noise, were obtained by setting a current of 70 mA and an applied voltage of 1.1 kV.

Prior to this thesis, Bailleux *et al.* [43] recorded the FIR spectrum of ^{15}NH at the SOLEIL synchrotron in the 65–225 cm^{-1} range, measuring a sequence of fine-structure triplets up to the rotational $N = 7 \leftarrow 6$ transition. That study was complemented with the recording of the lower fine-structure component of the fundamental $N = 1 \leftarrow 0$ line at 942 GHz using a submillimeter spectrometer. The same authors provided predicted rest frequencies for the two fine-structure components (including the strongest $J = 2 \leftarrow 1$) which could not be observed because they fall outside the spectral coverage of their spectrometer. It should be noted that THz measurements performed with harmonic multiplication of a synthesized radiation sources are at least a factor of 100 more precise than those obtained with a Fourier-transform infrared spectrometer. Hence, a direct measurement of all the J components of the $N = 1 \leftarrow 0$ line was desirable if one aims to use these data to guide sensitive astronomical observations.
To this respect, we studied the complete $N = 1 \leftarrow 0$ rotational transition of ^{15}NH. An overview of its fine and hyperfine pattern is shown in Figure 4.1: each group of $F_1', F' \leftarrow F_1, F$ hyperfine components is spread over ~150 MHz, and the strongest lines are those with $\Delta F = \Delta F_1 = \Delta J$. The full width at half maximum (FWHM) of the observed lines is about 2.5 MHz, because of the sizable Doppler broadening in this spectral range (~1.8 MHz at 100 K). Thus, care had to be adopted in retrieving accurate values of the corresponding central frequencies. We have modeled the recorded absorption profiles using the `proFFiT` line analysis code [44] adopting a FM Voigt profile function, and taking into account the full complex representation of the Fourier-transformed dipole correlation function. The imaginary dispersion term accounts for the line asymmetry produced by the spectral background and helps in obtaining a cleaner determination of the central frequency. In total, 26 line positions have been accurately determined with

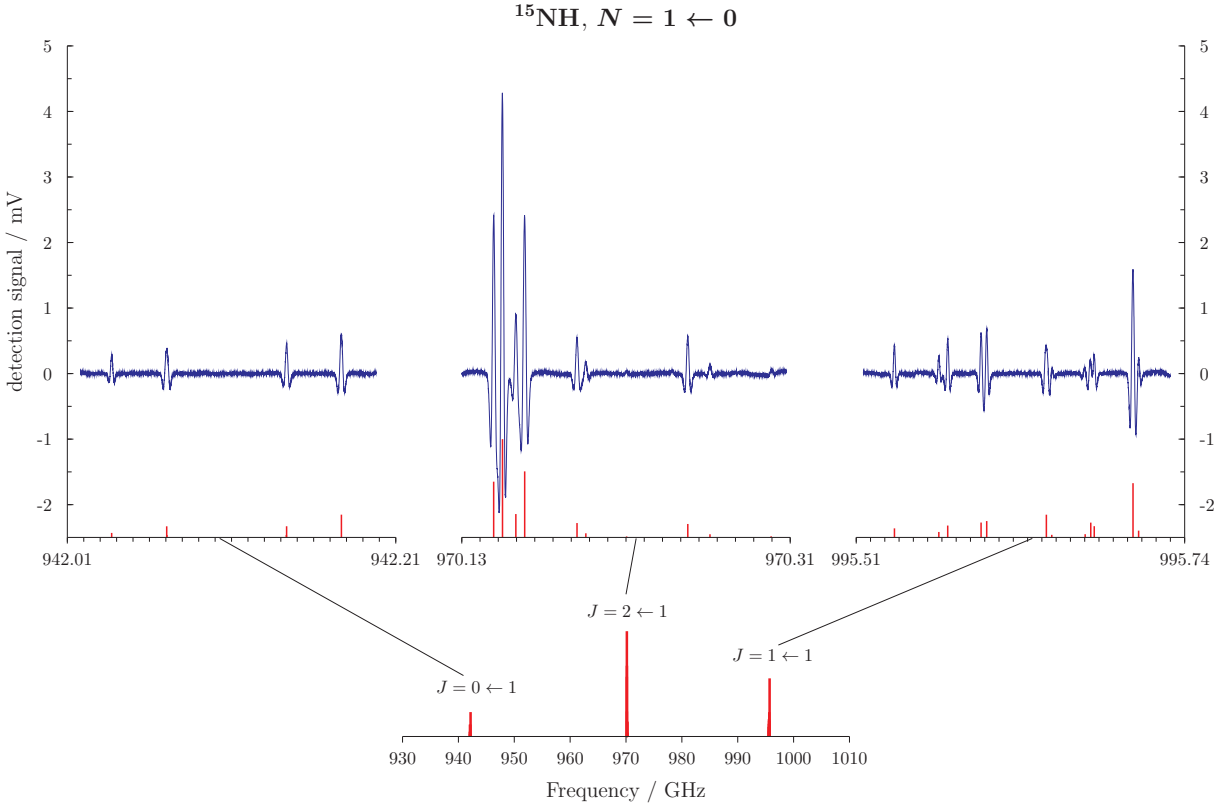

Figure 4.1: Fine and hyperfine structure of the $N = 1 \leftarrow 0$ rotational transition of ^{15}NH in its ground vibrational state. *Lower plot*: Schematic representation of the fine-structure splitting. *Upper plot*: recordings of the $J = 0 \leftarrow 1$, $J = 2 \leftarrow 1$, and $J = 1 \leftarrow 1$ fine-structure components. The blue traces are the experimental spectra recorded with time constant RC = 3 ms and accumulation times of ca. 350 s. In both plots, the red bars indicate the line positions and the relative intensities computed from the best-fit parameters of Table 4.2.

this method: they include 22 newly measured frequencies and the re-measurement of four data previously reported in Ref. [43]. An example of the results obtained using `proFFiT` is presented in Figure 4.2, which shows the four strongest transitions of the $J = 2 \leftarrow 1$ fine-structure component.

The content of the improved data set for ^{15}NH is illustrated in Table 4.1. In the third column the present measurements are listed, whereas the last column reports the Table 2 of Ref. [43] for comparison. For the $J = 0 \leftarrow 1$ lines, the discrepancies between the present and the older measurements are well within the estimated experimental uncertainties, with a maximum deviation of 64 kHz. Larger discrepancies were observed for the $J = 2 \leftarrow 1$ and $J = 1 \leftarrow 1$ fine structure groups, whose components deviate from the predicted positions by ~0.4 MHz and ~2.5 MHz, respectively.

In the present experiment we were also able to record 16 lines belonging to the $N = 1 \leftarrow 0$ transition on ^{15}NH in its $v = 1$ state. This vibrationally excited level is located at an energy of *ca.* 3200 cm^{-1} above the ground state (~4600 K) but it is appreciably populated even at 100 K because the plasma employed to produce the species is vibrationally hot [34]. The observation

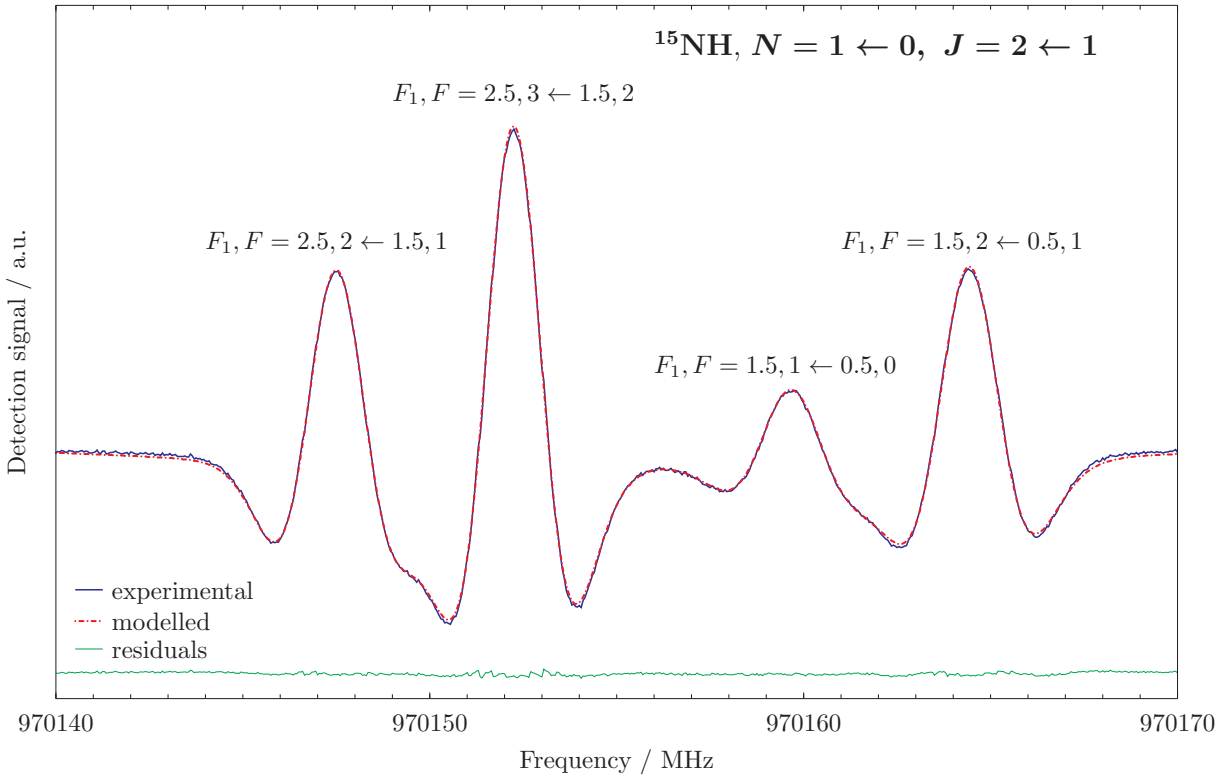

Figure 4.2: Recording (blue trace) of a portion of the $J = 2 \leftarrow 1$ fine-structure transition of ^{15}NH showing the four strongest components $F_1, F = 5/2, 2 \leftarrow 3/2, 1$, $5/2, 3 \leftarrow 3/2, 3$, $3/2, 1 \leftarrow 1/2, 0$, and $3/2, 2 \leftarrow 1/2, 1$. Integration time: 54 s; $RC = 3$ ms; scanning rate: 0.3 MHz/s; modulation depth: 1 MHz. The red dotted trace plots the modeled spectrum computed with `proFFit` using a modulated Voigt profile (see text). The green trace plots the difference between the observed and calculated spectrum.

of spectral features belonging to the $v = 1$ state implies that collisions in the low-pressure plasma employed in the present experiment to produce ^{15}NH are efficient enough to populate the bottom part of its vibrational ladder. The vibrational temperature of the plasma can be roughly estimated by comparing the intensity of the strongest $J, F_1, F = 2, 5/2, 3 \leftarrow 1, 3/2, 2$ hyperfine component recorded for both the ground and $v = 1$ states under the same experimental conditions. The intensity ratio was found to be $\sim 1/40$. Using the harmonic wavenumber of the N–H stretch reported by [45] for ^{14}NH ($\omega = 3282.7\,\mathrm{cm}^{-1}$) and assuming Boltzmann populations one can estimate a vibrational temperature of $T_{\mathrm{vib}} \sim 1270$ K.

The spectral analysis was performed considering the complete rotational data set available for ^{15}NH which comprises our new measurements and the data reported in [43]. The different precision was taken into account by assigning to each i-th entry a weight (w_i) inversely proportional to the square of its estimated measurement uncertainty (σ_i), $w_i = 1/\sigma_i^2$. For the present spectra, 35 kHz was adopted as the average measurement error. This was estimated by repeated profile analyses with `proFFiT` using different set of fitting parameters and background subtraction techniques. For the literature FIR data taken at SOLEIL we retained the original value of

Table 4.1: Measured transition frequencies[a] (MHz), least-squares residuals, and previously reported line positions for the $N = 1 \leftarrow 0$ transitions of ^{15}NH in the ground vibrational state.

$J' \leftarrow J$	$F_1', F' \leftarrow F_1, F$	This work	Fit o.−c.	Ref. [43]
$0 \leftarrow 1$	$1/2, 1 \leftarrow 1/2, 0$	942037.007(35)	−0.001	942036.954(100)
	$1/2, 1 \leftarrow 3/2, 1$	942070.538(35)[b]	0.017[c]	942070.537(100)[b]
	$1/2, 0 \leftarrow 3/2, 1$	942070.538(35)[b]	0.017[c]	942070.537(100)[b]
	$1/2, 1 \leftarrow 1/2, 1$	942143.526(35)[b]	0.008[c]	942143.471(100)[b]
	$1/2, 0 \leftarrow 1/2, 1$	942143.526(35)[b]	0.008[c]	942143.471(100)[b]
	$1/2, 1 \leftarrow 3/2, 2$	942176.869(35)	−0.024	942176.923(100)
$2 \leftarrow 1$	$5/2, 2 \leftarrow 3/2, 1$	970147.498(35)	0.030	970147.73(50)[d]
	$5/2, 3 \leftarrow 3/2, 2$	970152.248(35)	−0.052	970152.62(50)[d]
	$3/2, 1 \leftarrow 1/2, 0$	970159.678(35)	0.023	970159.93(50)[d]
	$3/2, 2 \leftarrow 1/2, 1$	970164.444(35)	−0.042	970164.82(50)[d]
	$3/2, 1 \leftarrow 3/2, 1$	970193.161(35)	0.019	970193.48(50)[d]
	$3/2, 2 \leftarrow 3/2, 2$	970197.939(35)	−0.036	970198.36(50)[d]
	$5/2, 2 \leftarrow 1/2, 1$	970220.406(35)	0.030	
	$5/2, 2 \leftarrow 3/2, 2$	970253.877(35)	0.012	970254.16(50)[d]
	$3/2, 1 \leftarrow 1/2, 1$	970266.067(35)	0.016	970266.36(50)[d]
$1 \leftarrow 1$	$1/2, 1 \leftarrow 1/2, 0$	995536.733(35)	−0.010	995534.36(90)[d]
	$3/2, 1 \leftarrow 1/2, 0$	995567.838(35)	−0.002	995565.57(90)[d]
	$1/2, 1 \leftarrow 3/2, 1$	995570.177(35)	−0.054	
	$1/2, 0 \leftarrow 3/2, 1$	995574.075(35)	0.054	995571.81(90)[d]
	$3/2, 2 \leftarrow 3/2, 1$	995597.456(35)	0.039	995595.05(90)[d]
	$3/2, 1 \leftarrow 3/2, 1$	995601.361(35)	0.016	995599.11(90)[d]
	$1/2, 1 \leftarrow 1/2, 1$	995643.101(35)	−0.038	995640.79(90)[d]
	$1/2, 0 \leftarrow 1/2, 1$	995646.957(35)	0.027	995644.70(90)[d]
	$3/2, 2 \leftarrow 1/2, 1$	995670.300(35)	−0.025	995667.94(90)[d]
	$3/2, 1 \leftarrow 1/2, 1$	995674.240(35)	−0.014	995671.99(90)[d]
	$1/2, 1 \leftarrow 3/2, 2$	995676.663(35)	0.034	995674.33(90)[d]
	$3/2, 2 \leftarrow 3/2, 2$	995703.824(35)	0.010	995701.48(90)[d]
	$1/2, 1 \leftarrow 3/2, 2$	995707.720(35)	−0.023	995705.54(90)[d]

[a] Numbers in parentheses are the estimated experimental accuracy in units of the last quoted digit. **[b]** Blended transitions. **[c]** Deviation computed from the weighted-average frequency of the blend. **[d]** Predicted frequency and 1σ estimated error.

$1 \times 10^{-4}\,\mathrm{cm}^{-1}$ (3 MHz). The transition frequencies were fitted to the Hamiltonian parameters described by Eqs. (4.3)–(4.6) using the SPFIT analysis program [46]. Eleven spectroscopic

parameters were determined for the ground vibrational state and they include: the rotational and centrifugal distortion constants, B, D, H; the spin–spin interaction coefficient λ; the spin–rotation constant γ together with its $\mathbf{N}^2$ centrifugal correction γ_N; the full set of electron spin–nuclear spin interaction constants for ^{15}N and H (b_F, c); and the nuclear rotation–nuclear spin coupling coefficient for nitrogen (C_I). Not all these Hamiltonian coefficients could be adjusted for the $v = 1$ state because the set of detected hyperfine components is smaller. Suitable constraints had to be adopted for the indeterminable spectroscopic parameters. They were obtained from the corresponding ground state values corrected for the $v = 0 \leftrightarrow 1$ vibrational dependence, as estimated from ^{14}NH literature data [47]. The two sets of constants for the $v = 0$ and $v = 1$ states are reported in Table 4.2, where previous results [43] are also shown for comparison.

Table 4.2: Spectroscopic parameters derived for ^{15}NH

			This work		Ref. [43]
Constant	Atom	Units	$v = 0$	$v = 1$	$v = 0$
B		MHz	487799.053(11)	468536.3401(51)	487798.75(15)
D		MHz	50.5977(52)	49.9514[a]	50.591(6)
H		kHz	3.657(77)	3.488[a]	3.61(6)
L		Hz	−0.4035[b]	−0.4020[a]	−0.4035[b]
λ		MHz	27577.650(10)	27564.616(18)	27576.15(63)
γ		MHz	−1637.235(22)	−1551.167(10)	−1636.53(36)
γ_J		MHz	0.443(11)	0.402[a]	0.4389[c]
b_F	(H)	MHz	−66.074(10)	−69.876(15)	−66.085(29)
c	(H)	MHz	90.546(44)	87.065(53)	90.285[c]
b_F	(^{15}N)	MHz	−26.416(13)	−25.554(19)	−26.462(35)
c	(^{15}N)	MHz	95.283(44)	94.613(54)	95.331[c]
C	(^{15}N)	MHz	−0.211(21)	−0.129(24)	−0.223[c]
no. of lines			43	16	21
MW *rms*			0.034		
FIR *rms*			1.199		
σ_w			0.835		

Number in parenthesis are one standard deviation in units of the last quoted digit.
[a] Constrained. See text. **[b]** Fixed at the value reported for ^{14}NH [47]. **[c]** Fixed in the analysis.

The spectroscopic constants determined in the present thesis are consistent with the ones previously reported in [43], but their precision has been improved substantially. The rotational parameters B and the spin–rotation constant γ have had their standard uncertainty reduced by

one order of magnitude, and a major improvement was also achieved for the spin–spin interaction parameter λ. New determinations of the dipolar spin–spin hyperfine coefficients c for both H and ^{15}N were also obtained. In the previous work, these parameters were not adjusted: c(H) was fixed at the value of the parent ^{14}NH species, whereas $c(^{15}\mathrm{N})$ was constrained to a value obtained from the ^{14}NH datum multiplied by the $^{15}\mathrm{N}/^{14}\mathrm{N}$ nuclear gyromagnetic ratio [43]. Our results are in good agreement with these figures with discrepancies not exceeding 0.5%. We have also determined the small nuclear spin–rotation constant C_I for ^{15}N to a precision of 10%, and its experimental value compares well with the one derived from the main isotopologue using the same scaling relation described above.
From the fit of the $v = 1$ lines, we have derived B, D, λ, γ, the Fermi contact (b_F) and dipolar spin–spin (c) hyperfine constants for both nuclei. The observed difference of these coefficients with respect to the corresponding ground state ($v = 0$) values are within the range expected for a regular vibrational dependence: $\sim 5\%$ for the hyperfine constants, $> 0.1\%$ for the spin–spin constant λ, and 3–6% for the rotational constant B and for the spin–rotation constant γ.

4.1.4 ^{14}NH

Following the study of the ^{15}N-rare isotopologue of imidogen, we decided to investigate the rotational spectrum of the parent species ^{14}NH in its vibrational excited state $v = 1$. This study was motivated by different reasons:

- previous studies have demonstrated that the plasma in which imidogen is produced is vibrationally hot;
- no pure rotational transitions of NH in the $v = 1$ state were ever recorded with "microwave-accuracy";
- the knowledge of as many ro-vibrational energy levels as possible, for different isotopologues, is essential to perform a high-quality Dunham analysis

Despite the large amount of spectroscopic studies devoted to NH [48, 33, 47, 49], only a few number of rotation lines in the $v = 1$ state is known from solar observations [22]. Thanks to the Atmospheric Trace Molecule Spectroscopy (ATMOS) FT spectrometer onboard Spacelab 3, Geller *et al.* [22] recorded the infrared solar spectrum from which *ca.* 50 pure rotation lines of NH in the $v = 0, 1$ states were detected. Albeit the vibrational excited lines could be easily assigned, no laboratory study has ever been reported.
We therefore recorded and analyzed the full $N = 1 \leftarrow 0$ transition of NH in the $v = 1$ state. The rotational spectrum of ^{14}NH was observed in absorption using the CASAC spectrometer at MPE (§3.2), in the same configuration described for ^{15}NH (§4.1.3). The NH radical was produced in the positive column of a DC glow discharge by flowing a mixture of N_2, H_2, and Ar in the ratio 1:1:8. The optimal yield of NH was attained at the same temperature (∼100 K) and discharge conditions (70 mA current and 1.1 kV tension) used for ^{15}NH.

A number of 19 distinct transition frequencies, belonging to the three fine-structure components ($J' \leftarrow J = 0 \leftarrow 1, 2 \leftarrow 1, 1 \leftarrow 1$), were recorded. They are listed in Table 4.3.

Table 4.3: Measured transition frequencies[a] and least-squares residuals for the $N = 1 \leftarrow 0$ transitions of NH in the vibrational state $v = 1$.

$J' \leftarrow J$	F_1', $F' \leftarrow F_1$, F	Frequency[a]	Obs.−calc.	Rel. weight
0←1	1, 3/2 ← 2, 5/2	907550.511	0.052	
	1, 1/2 ← 1, 3/2	907582.673[b]	-0.052[c]	0.4462
	1, 3/2 ← 1, 3/2	907582.673[b]	-0.052[c]	0.5538
2←1	2, 3/2 ← 2, 3/2	935746.341	-0.027	
	2, 5/2 ← 2, 5/2	935748.854	-0.078	
	1, 3/2 ← 1, 3/2	935754.744	-0.031	
	1, 1/2 ← 1, 1/2	935759.729	0.024	
	1, 3/2 ← 0, 1/2	935772.582	0.068	
	2, 5/2 ← 1, 3/2	935781.284	0.017	
	2, 3/2 ← 1, 1/2	935784.177	-0.013	
	3, 7/2 ← 2, 5/2	935788.620[b]	0.040[c]	0.6065
	3, 5/2 ← 2, 3/2	935788.620[b]	0.040[c]	0.3935
1←1	2, 3/2 ← 2, 3/2	961013.262	-0.000	
	2, 5/2 ← 2, 5/2	961106.909	-0.038	
	1, 3/2 ← 2, 5/2	961135.859	0.013	
	2, 5/2 ← 1, 3/2	961139.385	0.103	
	2, 3/2 ← 1, 3/2	961146.149	-0.032	
	1, 3/2 ← 1, 3/2	961168.195	0.015	
	0, 1/2 ← 1, 3/2	961183.247	0.084	
	1, 3/2 ← 0, 1/2	961185.844	-0.073	
	1, 1/2 ← 0, 1/2	961188.308	-0.071	

Units are MHz. **[a]** The experimental accuracy is estimated to be 60 kHz. **[b]** Blended transitions. **[c]** Deviation computed from the weighted-average frequency of the blend.

The newly observed transitions together with the solar infrared data [22] have been fitted to the Hamiltonian of Eqs. 4.3–4.6. All these data could be analyzed within their expected uncertainty and 13 parameters have been determined experimentally, without any assumption. Among the set of data, the high N transitions detected through solar observations were helpful to constrain the value of centrifugal distortion terms (D and H), whilst our measurements give important information about the fine and hyperfine structure of the energy levels. The spectroscopic constants derived from the least-square procedures are listed in Table 4.4.

Table 4.4: Spectroscopic constants determined for NH in the $v = 1$ vibrational state.

Constant	Atom	$v = 1$
B		470566.45(11)
D		−50.092(57)
$H \times 10^3$		2.889(71)
λ		110259.32(10)
γ		−1557.79(36)
γ_N		0.40(18)
b_F	(N)	18.235(18)
c	(N)	−67.433(71)
C_I	(N)	0.154(29)
eQq	(N)	−3.72(22)
b_F	(H)	−69.837(65)
c	(H)	87.33(15)
C_I	(H)	−0.121(42)
σ		0.95
MW *rms*		0.052
FIR *rms* / cm^{-1}		0.005
no. of lines		25

All units are MHz except the dimensionless fit standard deviation σ. Number in parenthesis are one standard deviation in units of the last quoted digit.

4.1.5 ^{14}ND

Albeit ND is not the most abundant isotopologue, it was perhaps the most studied in laboratory. The replacement of an hydrogen atom with deuterium, indeed, has the effect of nearly halve the rotational constant B of a diatomic species. In the particular case of imidogen, B_0 passes from 489959.056(5) MHz in NH to 263265.494(5) MHz in ND. This made possible the laboratory study of the deuterated form ND much earlier than its parent species NH. As a matter of fact, the lowest rotational transition of NH falls between 946 and 1000 GHz, a frequency region which was hardly accessible before the 80's. Contrarily, the $N = 1 \leftarrow 0$ transition of ND is located around 522 GHz. For these reasons, the amount of data available for ND is as large as that for the parent NH.

The rotational spectrum of the ND radical has been recorded for the first time by Saito &

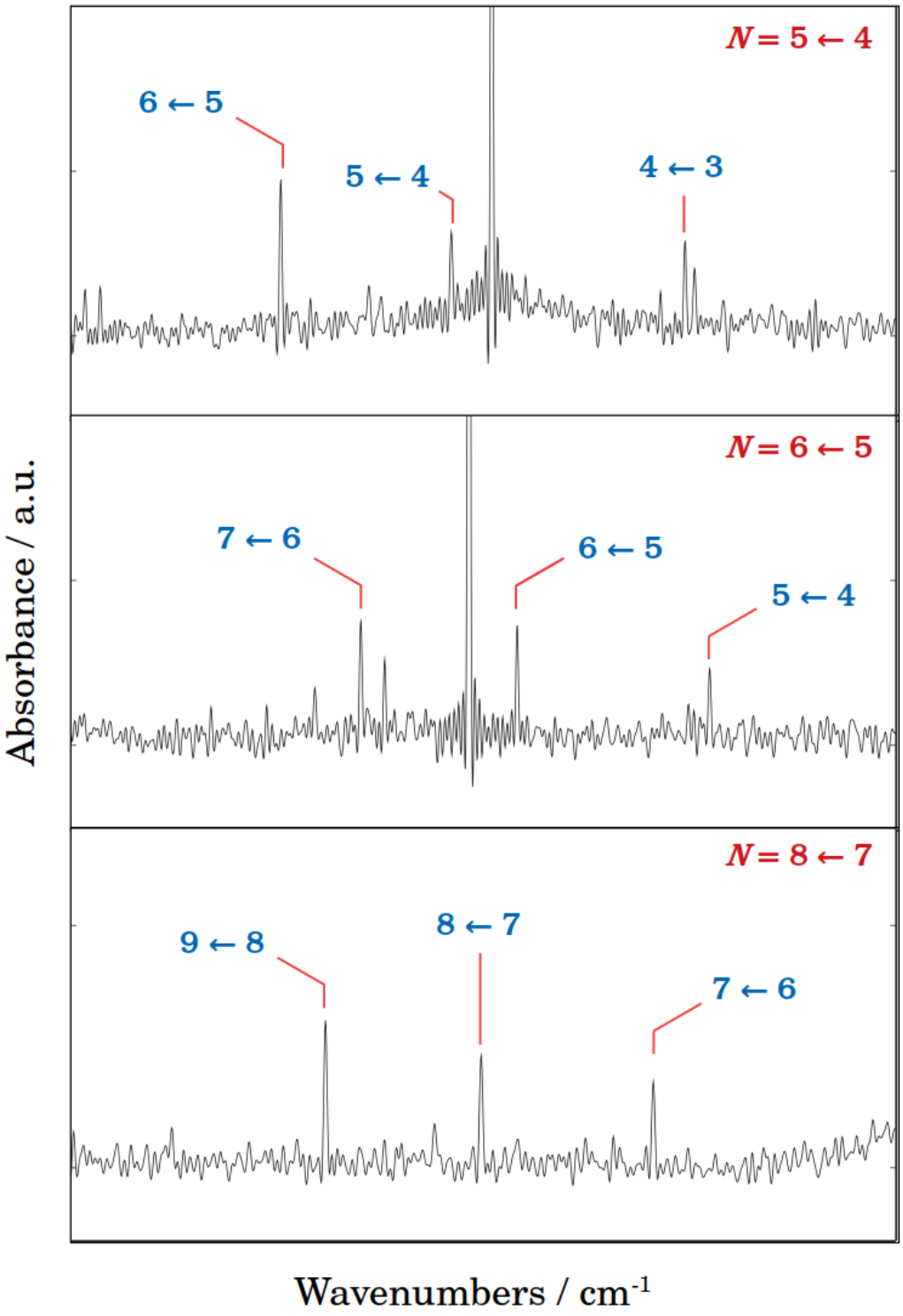

Figure 4.3: Some rotational transitions of ND as observed in the FIR spectrum. Each panel is 0.2 cm^{-1} width; the spectra are centered at 87.58 (*top*), 104.95 (*middle*), and 139.5 cm^{-1} (*bottom*).

.

Goto [50]. They observed the whole fine and hyperfine structure of the fundamental transition $N = 1 \leftarrow 0$. Later, Takano *et al.* [51] reported the next transition $N = 2 \leftarrow 1$ (above the THz) thus enabling a centrifugal analysis and prediction of the spectrum at even higher frequencies. As far as the vibrational excited levels are concerned, the first six states (from $v = 1$ to $v = 6$) have been investigated by Ram & Bernath [52] thanks to the observation of several vibration-rotation bands with a FT-IR spectrometer, but only the fine structure could be resolved for low N transitions. Lastly, Dore *et al.* [34] reported the measurements of a number of fine-structure components of the $N = 1 \leftarrow 0$ rotational transition of ND in some vibrational excited states (up to $v = 6$). In that work, most of the hyperfine structure could be resolved.
With the aim of improve the quality of the Dunham analysis discussed in § 4.1.7, a new set of data for ^{15}ND was measured. The data set was improved in two ways:

- with the extension toward FIR frequencies the study of the rotational spectrum of ND in its ground vibrational state to probe high N quantum number levels;

- by recording the $N = 2 \leftarrow 1$ transition of the first excited state $v = 1$ with "microwave-accuracy";

Since they provide additional information about high J transitions, they contributed significantly to a better determination of the higher order centrifugal distortion terms.
The FIR spectrum of ND was recorded at the French synchrotron facility SOLEIL using the Bruker FT spectrometer described in §3.5 with the bright synchrotron radiation extracted by the AILES beamline. The spectrum was obtained by the co-adding several tens of scan and recorded in the 50–250 cm^{-1} range at the maximum instrumental resolution of $R = 0.00102\,cm^{-1}$. A 6 μm Mylar beamsplitter and a 4.2 K liquid helium cooled bolometer were used. The ND radical was produced using a post-discharge set-up, already employed to produce the parent NH radicals [53] as well as its ^{15}N isotopic variants [43]. In the present case, a 2.5 m long White-type cell allowing 150 m of absorption path length was used. The ND radical was produced by a 1000 W radiofrequency discharge of ND_3 at the pressure of 30 μbar. In the investigated frequency region, it was possible to identify and measure with a discrete S/N (between 4 and 10, see Figure 4.3) the three strongest fine-components ($\Delta F = +1$) of seven rotational transitions $N' \leftarrow N$, with N from 3 to 10. They are summarized in Table 4.5.
On the other hand, the $N = 2 \leftarrow 1$ transition of ND in its first excited state $v = 1$ was observed with the Bologna submillimeter spectrometer (§3.1). The ND radical has been produced analogously to NH (§4.1.4), but using ND_3 instead of normal ammonia. In this case, only few transitions (listed in Table 4.6) could be observed with a decent S/N.
Nonetheless, the newly measured transitions have been helpful to improve the centrifugal analysis of ND in both the ground and $v = 1$ states (Table 4.7).

Table 4.5: Measured transition frequencies[a] and least-squares residuals for transitions of ND in the ground vibrational state.

$N' \leftarrow N$	$J' \leftarrow J$	Frequency	Obs.−Calc.
$4 \leftarrow 3$	$5 \leftarrow 4$	70.081026	0.000033
	$4 \leftarrow 3$	70.127714	−0.000141
	$3 \leftarrow 2$	70.206887	−0.000228
$5 \leftarrow 4$	$6 \leftarrow 5$	87.530909	0.000052
	$5 \leftarrow 4$	87.572266	0.000096
	$4 \leftarrow 3$	87.628934	−0.000111
$6 \leftarrow 5$	$7 \leftarrow 6$	104.920313	0.000020
	$6 \leftarrow 5$	104.958221	0.000019
	$5 \leftarrow 4$	105.004906	0.000060
$7 \leftarrow 6$	$8 \leftarrow 7$	122.238925	0.000104
	$6 \leftarrow 5$	122.315514	0.000014
$8 \leftarrow 7$	$9 \leftarrow 8$	139.475571	0.000067
	$8 \leftarrow 7$	139.509544	0.000051
	$7 \leftarrow 6$	139.547121	0.000025
$9 \leftarrow 8$	$10 \leftarrow 9$	156.619192	−0.000081
	$9 \leftarrow 8$	156.652067	0.000061
	$8 \leftarrow 7$	156.687324	0.000039
$10 \leftarrow 9$	$11 \leftarrow 10$	173.658874	−0.000183
	$10 \leftarrow 9$	173.690881	0.000105
$11 \leftarrow 10$	$12 \leftarrow 11$	190.583853	−0.000002

Measured frequencies and residuals are expressed in cm^{-1}. **[a]** The experimental accuracy is estimated to be 0.00008 cm^{-1}.

4.1.6 ^{15}ND

The rotational spectrum of ^{15}ND radical in its ground vibronic state $X^3\Sigma^-$ has been recorded with the frequency-modulation millimeter-/submillimeter-wave spectrometer in Bologna (Sec. 3.1). The ^{15}ND radical was optimally produced in a DC discharge of a mixture of $^{15}N_2$ (5–7 mTorr) and D_2 (1–2 mTorr) in Ar as buffer gas (15 mTorr). Typically, a voltage of 1 kV and a current of 60 mA were employed. The absorption cell was cooled down at *ca.* −190°C by liquid-nitrogen circulation. The experimental uncertainties of present measurements are between 40 and 80 kHz in most cases, up to 500 kHz for a few disturbed lines.

The spectrum of ^{15}ND had initially been predicted by exploiting the Dunham's relationships introduced in Section 4.1.2 and the available spectroscopic parameters of ^{14}NH, ^{15}NH, and ^{14}ND. The first fine-structure transitions showed a deviation from prediction of less than 1 GHz.

Table 4.6: Measured transition frequencies[a] (MHz) and least-squares residuals for the $N = 2 \leftarrow 1$ transitions of ND in the first vibrational excited state.

$J' \leftarrow J$	$F_1', F' \leftarrow F_1, F$		Obs. Frequency	Obs.−Calc.	Rel. weight
$3 \leftarrow 2$	$2,1 \leftarrow 1,$	0	1019936.310[b]	0.017[c]	0.1245
	$2,2 \leftarrow 1,$	1	1019936.310[b]	0.017[c]	0.2779
	$2,3 \leftarrow 1,$	2	1019936.310[b]	0.017[c]	0.5064
	$2,1 \leftarrow 1,$	1	1019936.310[b]	0.017[c]	0.0913
$2 \leftarrow 1$	$3,2 \leftarrow 2,$	1	1022267.470[b]	-0.017[c]	0.2167
	$3,3 \leftarrow 2,$	2	1022267.470[b]	-0.017[c]	0.3209
	$3,4 \leftarrow 2,$	3	1022267.470[b]	-0.017[c]	0.4623
	$4,4 \leftarrow 3,$	3	1022267.470[b]	0.000[c]	0.2847
	$4,5 \leftarrow 3,$	4	1022281.762[b]	0.000[c]	0.3760
	$3,2 \leftarrow 2,$	1	1022281.762[b]	0.000[c]	0.1229
	$4,3 \leftarrow 3,$	2	1022281.762[b]	0.000[c]	0.2165

[a] The experimental accuracy is estimated to be 50 kHz. **[b]** Blended transitions. **[c]** Deviation computed from the weighted-average frequency of the blend.

After the first measurements, a refined prediction was used to search for all the transitions which fall in our spectral coverage.

For the previously unobserved ^{15}ND species, we have recorded 34 lines for the ground vibrational state and 9 lines for the $v = 1$ state. They include the complete fine-structure of the $N = 1 \leftarrow 0$ transition and the strongest fine-components of the $N = 2 \leftarrow 1$ transition for the ground state (see Figure 4.4), and the $\Delta J = 0, +1$ components of the $N = 1 \leftarrow 0$ transition for the $v = 1$ state.

The corresponding transition frequencies were fitted to the Hamiltonian of Eqs. (4.3)–(4.6) using the SPFIT analysis program [46]. Because of the small number of transitions detected for the $v = 1$ state, some of the spectroscopic parameters for this state could not be directly determined in the least-squares fit and were constrained to the corresponding ground state values. The two sets of constants for $v = 0$ and $v = 1$ states are reported in Table 4.8.

4.1.7 Dunham analysis

In this thesis, I carried out a multi-isotopologue Dunham fit of the imidogen radical in its $X\,^3\Sigma$ ground electronic state using the new transition frequencies for the doubly substituted ^{15}ND variant plus all the available rotational and ro-vibrational data for the ^{14}NH, ^{15}NH and ^{14}ND species (including those newly measured). To take into account the different experimental precision, each datum was given a weight inversely proportional to the square of its estimated measurement error, $w_i = 1/\sigma_i^2$. The σ values adopted for our measurements have been discussed in

Table 4.7: Spectroscopic constants determined for ^{14}ND in the ground and $v = 1$ vibrational states.

Constant	Atom	$v = 0$	$v = 1$
B_v		263265.4927(39)	255685.2408(57)
D_v		14.63397(78)	14.4830(24)
$H_v \times 10^3$		0.5766(57)	0.5766[a]
λ_v		110180.708(24)	110168.221(33)
γ_v		−883.4663(65)	−849.630(21)
γ_{Nv}		0.1316(19)	0.121(10)
$b_{F,v}$	(D)	−10.0729(44)	−10.5245(59)
c_v	(D)	14.096(28)	13.691(36)
eQq_v	(D)	0.214(92)	0.214[a]
$b_{F,v}$	(N)	18.9296(37)	18.5208(52)
c_v	(N)	−67.806(21)	−67.637(20)
eQq_v	(N)	−4.866(57)	−4.489(51)
$C_{I,v}$	(N)	0.0986(76)	0.0704(46)
σ		1.17	
rms		0.098	
no. of lines		125	

All units are MHz except for the dimensionless standard deviation σ. Number in parenthesis are one standard deviation in units of the last quoted digit. **[a]** Parameter held fixed to ground state value.

Sections 4.1.3–4.1.6, while for literature data we retained the values provided in each original work. The content of the data set and the relevant bibliographic references are summarized in Table 4.9.

In total, the data set contains 1583 ro-vibrational transitions which correspond to 1221 distinct frequencies. These data were fitted to the multi-isotopologue model described in Sec 4.1.2, using both traditional [Eqs. (4.11)] and LeRoy [Eqs. (4.12)] mass scaling schemes to describe the Dunham-type parameters (Y_{lm} and $\mathcal{Y}_{lm}$) of each isotopic species.

The analysis was performed using a custom PYTHON code which uses the SPFIT program [46] as computational core. Briefly, the scripting routine reads the atomic masses, the spin multiplicities, and the Y_{lm} constants for the reference species. Then, the SPFIT parameter file (.PAR) is set up by defining several sets of spectroscopic constants (one for each isotopologue/vibrational state), taking into account the mass scaling factors. The SPFIT lines file (.LIN) is created by

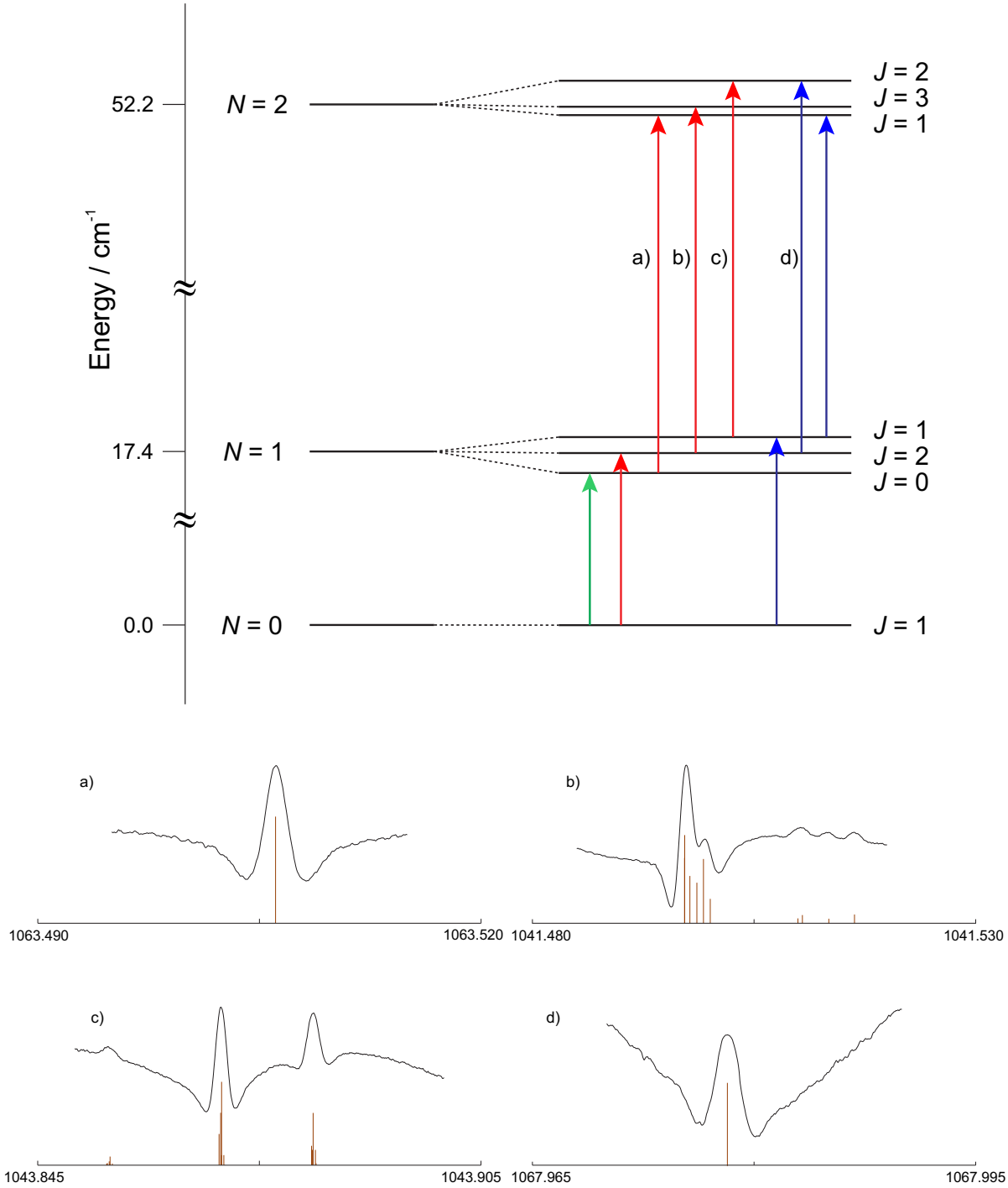

Figure 4.4: *Upper panel*: energy levels scheme of ^{15}ND in the ground vibrational state. The hyperfine-structure is not shown. The arrows mark the transitions observed in this study: $\Delta J = +1$ (red), $\Delta J = 0$ (blue), and $\Delta J = -1$ (green). *Lower panel*: spectral recordings for the transitions marked with the labels *a*, *b*, *c* and *d* showing the corresponding hyperfine structure. The brown sticks represent the positions and the intensities of the hyperfine components computed from the spectroscopic parameters of Table 4.8. The frequency range of each spectrum is reported on the *x* axes (units are GHz).

Table 4.8: Spectroscopic constants determined for ^{15}ND in the ground and $v = 1$ vibrational states.

Constant	Atom	$v = 0$	$v = 1$
B_v		261083.4809(96)	253597.797(24)
D_v		14.3906(13)	14.3906[a]
λ_v		27544.852(22)	27544.852[a]
γ_v		−876.139(15)	−841.674(46)
γ_{Nv}		0.1241(20)	0.1241[a]
$b_{F,v}$	(^{15}N)	−26.519(20)	−25.944(41)
c_v	(^{15}N)	95.154(56)	94.48(30)
$C_{I,v}$	(^{15}N)	−0.124(14)	−0.124[a]
$b_{F,v}$	(D)	−10.062(21)	−10.524(42)
c_v	(D)	14.236(78)	13.18(22)
eQq_v	(D)	0.271(93)	0.271[a]
σ		0.84	
rms		0.080	
no. of lines		34	9

All units are MHz. Number in parenthesis are one standard deviation in units of the last quoted digit. **[a]** Parameter held fixed to ground state value.

Table 4.9: Summary of the data used for the multi-isotopologue fit of imidogen

	Pure rotational			Ro-vibrational		
	Lines	Vib. states	Refs.	Lines	Bands	Refs.
NH	96	2	[49], [47], TT	451	6	[48],[22], [33]
ND	164	5	[50], [51], [34], TT	406	6	[52]
^{15}NH	61	2	[43], TT	–	–	
^{15}ND	43	2	This thesis (TT)	–	–	

collecting the experimental data. In this process, half integer quantum numbers are rounded up and a "quantum number state" is assigned to each isotopologue in a given vibrational state, in conformity with the SPFIT format. At the end of the least-squares optimization, the SPFIT output is post-processed, and the final parameters list is reformatted in the same fashion of the initial input data set. The atomic masses used were taken from the Wang *et al.* [54] compilation. The optimized parameters are reported in Tables 4.10–4.12.

Table 4.10: Ro-vibrational Dunham Y_{lm} constants and isotopically invariant U_{lm} parameters determined in the multi-isotopologue fit for imidogen radical

			Y_{lm}		U_{lm}	
	l	m	units	value	units	value
	1	0	/ cm^{-1}	3282.3630(39)	cm^{-1} $u^{1/2}$	3184.2023(35)
	2	0	/ cm^{-1}	−78.6809(47)	cm^{-1} u	−73.9830(43)
	3	0	/ cm^{-1}	0.2222(25)	cm^{-1} $u^{3/2}$	0.2026(23)
	4	0	/ cm^{-1}	−0.02949(68)	cm^{-1} u^{2}	−0.02607(60)
	5	0	/ cm^{-1}	−0.000268(88)	cm^{-1} $u^{5/2}$	−0.000229(76)
	6	0	/ cm^{-1}	−0.0001390(45)	cm^{-1} $u^{5/2}$	−0.0001155(37)
	0	1	/ MHz	499690.494(83)	cm^{-1} u	15.7043686(37)
	1	1	/ MHz	−19494.28(34)	cm^{-1} $u^{3/2}$	−0.593913(10)
	2	1	/ MHz	67.04(48)	cm^{-1} u^{2}	0.001977(14)
	3	1	/ MHz	−7.61(31)	cm^{-1} $u^{5/2}$	$-2.178(87) \times 10^{-4}$
	4	1	/ MHz	−1.600(94)	cm^{-1} u^{3}	$-4.43(26) \times 10^{-5}$
	5	1	/ MHz	0.133(14)	cm^{-1} $u^{7/2}$	$3.56(37) \times 10^{-6}$
	6	1	/ MHz	−0.01471(76)	cm^{-1} $u^{7/2}$	$-3.83(20) \times 10^{-7}$
	0	2	/ MHz	−51.44647(89)	cm^{-1} u^{2}	−0.001527418(68)
	1	2	/ MHz	0.8230(23)	cm^{-1} $u^{5/2}$	$2.3529(65) \times 10^{-5}$
	2	2	/ MHz	−0.0637(15)	cm^{-1} u^{3}	$-1.764(42) \times 10^{-6}$
	3	2	/ MHz	0.00259(37)	cm^{-1} $u^{7/2}$	$6.95(99) \times 10^{-8}$
	4	2	/ MHz	−0.001454(28)	cm^{-1} u^{4}	$-3.790(72) \times 10^{-8}$
	0	3	/ MHz	0.0037986(78)	cm^{-1} u^{3}	$1.0866(30) \times 10^{-7}$
	1	3	/ MHz	$-1.285(42) \times 10^{-4}$	cm^{-1} $u^{7/2}$	$-3.45(11) \times 10^{-9}$
	2	3	/ MHz	$-1.31(18) \times 10^{-5}$	cm^{-1} u^{4}	$-3.42(47) \times 10^{-10}$
	3	3	/ MHz	$-4.19(31) \times 10^{-6}$	cm^{-1} $u^{9/2}$	$-1.057(79) \times 10^{-10}$
	0	4	/ MHz	$-4.58(16) \times 10^{-7}$	cm^{-1} u^{4}	$-1.194(41) \times 10^{-11}$
	1	4	/ MHz	$-3.82(28) \times 10^{-8}$	cm^{-1} $u^{9/2}$	$-9.64(71) \times 10^{-13}$
	0	5	/ MHz	$4.39(86) \times 10^{-11}$	cm^{-1} $u^{9/2}$	$1.08(21) \times 10^{-15}$
X	l	m		δ^{X}_{lm}		Δ^{X}_{lm}
N	0	1	/ MHz	75.65(11)		−3.8559(57)
N	1	1	/ MHz	−3.40(13)		−4.44(17)
H	1	0	/ cm^{-1}	1.6112(14)		−0.90136(78)
H	2	0	/ cm^{-1}	−0.01101(24)		−0.2571(56)
H	0	1	/ MHz	1005.080(32)		−3.68728(12)
H	1	1	/ MHz	−0.3589(21)		−3.2016(29)
H	0	2	/ MHz	−34.038(31)		−12.728(76)
H	0	3	/ MHz	$1.215(76) \times 10^{-4}$		−56.9(36)

Notes.
The Dunham constants Y_{lm} are referred to the most abundant NH isotopologue. The BOB coefficients Δ^{X}_{lm} are dimensionless. Number in parentheses are the 1σ statistical errors in units of the last quoted digit.

Table 4.11: Fine Dunham $\mathcal{Y}_{lm}$ constants and isotopically invariant U^{y}_{lm} parameters determined in the multi-isotopologue fit for NH

Dunham type			Isotopically invariant		
Fine structure parameters					
λ_{00}	/ MHz	27573.427(23)	U^{λ}_{00}	/ MHz u	0.9174535(52)
λ_{10}	/ MHz	16.195(46)	U^{λ}_{10}	/ MHz u$^{1/2}$	$5.861(20) \times 10^{-4}$
λ_{20}	/ MHz	−14.642(22)	U^{λ}_{20}	/ MHz u	$-4.5914(68) \times 10^{-4}$
λ_{01}	/ MHz	0.0107(39)	U^{λ}_{01}	/ MHz u$^{3/2}$	$3.3(12) \times 10^{-7}$
γ_{00}	/ MHz	−1688.268(31)	U^{γ}_{00}	/ MHz u	−0.0528434(13)
γ_{10}	/ MHz	88.136(93)	U^{γ}_{10}	/ MHz u$^{3/2}$	0.0026739(27)
γ_{20}	/ MHz	−1.355(78)	U^{γ}_{20}	/ MHz u$^{3/2}$	$-3.96(23) \times 10^{-5}$
γ_{30}	/ MHz	0.361(21)	U^{γ}_{30}	/ MHz u$^{3/2}$	$1.028(61) \times 10^{-5}$
γ_{01}	/ MHz	0.4631(31)	U^{γ}_{01}	/ MHz u^{2}	$1.3656(92) \times 10^{-5}$
γ_{11}	/ MHz	−0.0290(82)	U^{γ}_{11}	/ MHz u$^{3/2}$	$-8.3(23) \times 10^{-7}$
γ_{21}	/ MHz	0.0150(45)	U^{γ}_{21}	/ MHz u^{2}	$4.2(13) \times 10^{-7}$
γ_{31}	/ MHz	−0.00328(72)	U^{γ}_{31}	/ MHz u^{2}	$-8.8(19) \times 10^{-8}$
$\delta^{\lambda,\mathrm{N}}_{00}$	/ MHz	−3.61(16)	$\Delta^{\lambda,\mathrm{N}}_{00}$		0.840(37)
$\delta^{\lambda,\mathrm{H}}_{00}$	/ MHz	−65.244(40)	$\Delta^{\lambda,\mathrm{H}}_{00}$		1.08948(67)
$\delta^{\lambda,\mathrm{H}}_{10}$	/ MHz	1.930(40)	$\Delta^{\lambda,\mathrm{H}}_{10}$		−48.9(10)
$\delta^{\gamma,\mathrm{H}}_{00}$	/ MHz	1.712(18)	$\Delta^{\gamma,\mathrm{H}}_{00}$		3.515(38)
$\delta^{\gamma,\mathrm{H}}_{10}$	/ MHz	−0.090(17)	$\Delta^{\gamma,\mathrm{H}}_{10}$		3.81(67)

Notes.
See notes of Table 4.10.

From the multi-isotopologue analysis we obtained a highly satisfactory fit. Its quality can be evaluated in several ways. First of all, we were able to reproduce the input data within their estimated uncertainties: the overall standard deviation of the weighted fit is $\sigma = 0.90$, and the root-mean-square deviations of the residuals computed separately for the rotational and ro-vibrational data are of the same order of magnitude of the corresponding measurements error, $rms_{\mathrm{rot}} = 0.107$ MHz and $rmr_{\mathrm{vibrot}} = 3.4\times 10^{-3}$ cm^{-1}, respectively. Then, the various sets of Y_{lm} for a given m constitute a series whose coefficients decrease in magnitude for increasing values of the index l, as expected for a rapidly converging Dunham-type expansion. In general, most of the determined coefficients have a relative error lower than 5%. Higher errors are observed only for those constants with high l-index and this is due to the smaller number of transitions available for highly vibrationally excited states. Finally, the Kratzer [55] and Pekeris [56] relation can also be used as a yardstick to asses the correct treatment of the Born–Oppenheimer

Table 4.12: Hyperfine Dunham $\mathcal{Y}_{lm}$ constants and isotopically invariant U^y_{lm} parameters determined in the multi-isotopologue fit for NH

Dunham type				Isotopically invariant			
Hyperfine structure parameters							
$b_{F,00}$	(H)	MHz	−64.194(13)	$U^{b_F}_{00}$	(H)	cm^{-1}	−0.00214129(45)
$b_{F,10}$	(H)	MHz	−3.785(15)	$U^{b_F}_{10}$	(H)	cm^{-1}	$-1.2243(48) \times 10^{-4}$
c_{00}	(H)	MHz	92.216(61)	U^{c}_{00}	(H)	cm^{-1}	0.0030760(20)
c_{10}	(H)	MHz	−3.391(58)	U^{c}_{10}	(H)	cm^{-1}	$-1.097(19) \times 10^{-4}$
C_{00}	(H)	MHz	−0.068(11)	U^{C}_{00}	(H)	cm^{-1}	$-2.14(33) \times 10^{-6}$
$b_{F,00}$	(D)	MHz	−9.836(12)	$U^{b_F}_{00}$	(D)	cm^{-1}	$-3.2810(41) \times 10^{-4}$
$b_{F,10}$	(D)	MHz	−0.632(10)	$U^{b_F}_{10}$	(D)	$cm^{-1}\,u^{1/2}$	$-2.044(34) \times 10^{-5}$
c_{00}	(D)	MHz	14.233(74)	U^{c}_{00}	(D)	cm^{-1}	$4.746(25) \times 10^{-4}$
c_{10}	(D)	MHz	−0.372(99)	U^{c}_{10}	(D)	$cm^{-1}\,u^{1/2}$	$-1.19(32) \times 10^{-5}$
c_{20}	(D)	MHz	−0.117(32)	U^{c}_{20}	(D)	$cm^{-1}\,u^{1/2}$	$-3.66(100) \times 10^{-6}$
eQe_{00}	(D)	MHz	0.080(32)	U^{eQq}_{00}	(D)	cm^{-1}	$2.7(11) \times 10^{-6}$
$b_{F,00}$	(^{14}N)	MHz	19.084(18)	$U^{b_F}_{00}$	(^{14}N)	cm^{-1}	$6.3660(59) \times 10^{-4}$
$b_{F,10}$	(^{14}N)	MHz	−0.421(31)	$U^{b_F}_{10}$	(^{14}N)	$cm^{-1}\,u^{1/2}$	$-1.365(99) \times 10^{-5}$
$b_{F,20}$	(^{14}N)	MHz	−0.088(13)	$U^{b_F}_{20}$	(^{14}N)	$cm^{-1}\,u^{1/2}$	$-2.76(41) \times 10^{-6}$
c_{00}	(^{14}N)	MHz	−68.135(31)	U^{c}_{00}	(^{14}N)	$cm^{-1}\,u^{1/2}$	−0.0022727(10)
c_{10}	(^{14}N)	MHz	0.467(26)	U^{c}_{10}	(^{14}N)	$cm^{-1}\,u^{3/2}$	$1.509(83) \times 10^{-5}$
eQq_{00}	(^{14}N)	MHz	−3.367(54)	U^{eQq}_{00}	(^{14}N)	cm^{-1}	$-1.123(18) \times 10^{-4}$
eQq_{10}	(^{14}N)	MHz	0.395(38)	U^{eQq}_{10}	(^{14}N)	$cm^{-1}\,u^{1/2}$	$1.28(12) \times 10^{-5}$
C_{00}	(^{14}N)	MHz	0.172(11)	U^{C}_{00}	(^{14}N)	$cm^{-1}\,u^{1/2}$	$5.42(36) \times 10^{-6}$
C_{10}	(^{14}N)	kHz	−0.0293(85)	U^{C}_{10}	(^{14}N)	$cm^{-1}\,u^{3/2}$	$-9.0(26) \times 10^{-7}$
$b_{F,00}$	(^{15}N)	MHz	−26.848(16)	$U^{b_F}_{00}$	(^{15}N)	cm^{-1}	$-8.9556(52) \times 10^{-4}$
$b_{F,10}$	(^{15}N)	MHz	0.860(18)	$U^{b_F}_{10}$	(^{15}N)	$cm^{-1}\,u^{1/2}$	$2.789(58) \times 10^{-5}$
c_{00}	(^{15}N)	MHz	95.428(49)	U^{c}_{00}	(^{15}N)	cm^{-1}	0.0031831(16)
c_{10}	(^{15}N)	MHz	−0.556(54)	U^{c}_{10}	(^{15}N)	cm^{-1}	$-1.80(17) \times 10^{-5}$
C_{00}	(^{15}N)	MHz	−0.259(22)	U^{C}_{00}	(^{15}N)	$cm^{-1}\,u^{1/2}$	$-8.18(71) \times 10^{-6}$
C_{10}	(^{15}N)	MHz	0.099(24)	U^{C}_{10}	(^{15}N)	$cm^{-1}\,u^{1/2}$	$3.06(74) \times 10^{-6}$

Notes.
See notes of Table 4.10.

Breakdown effects. Using the formula [1]

$$Y_{02} \simeq \frac{4Y_{01}^3}{Y_{10}^2}\,, \tag{4.14}$$

we obtained for Y_{02} a value of 51.54051 MHz which compares well with the fitted one of

51.4472(9) MHz.

4.1.8 Molecular properties

Equilibrium bond distance

The precision yielded by the high-resolution spectroscopic technique led to a very accurate determination of the equilibrium bond length r_e for the imidogen radical. The rotational measurements of a diatomic molecule in its ground vibrational state ($v = 0$) allow the determination of precise value of r_0, which includes the zero point vibrational contributions and differs from r_e. This latter is determinable from the rotational spectrum in at least one vibrationally excited state. In the present analysis, data of four isotopic species in several vibrational excited states have been combined, allowing for a very precise determination of r_e for each isotopologue α. The equilibrium bond distance is given by:

$$r_e^{(\alpha)} = \sqrt{\frac{N_a h}{8\pi^2} \frac{1}{B_e^{(\alpha)} \mu_a}} \,. \tag{4.15}$$

where $N_a h$ is the molar Planck constant. Actually, the values of $B_e^{(\alpha)}$ differ from those of $Y_{01}^{(\alpha)}$ obtained from the Dunham-type analysis. This discrepancy should be ascribed to a small contribution, expressed by [1]:

$$Y_{01} = B_e + \Delta Y_{01}^{(\mathrm{Dunh})} = B_e + \beta_{01} \left(\frac{B_e^3}{\omega_e^2} \right) , \tag{4.16}$$

with

$$\beta_{01} = Y_{10}^2 \left(\frac{Y_{21}}{4 Y_{01}^3} \right) + 16 a_1 \left(\frac{Y_{20}}{3 Y_{01}} \right) - 8 a_1 - 6 a_1^2 + 4 a_1^3 \,, \tag{4.17}$$

and

$$a_1 = \frac{Y_{11}}{3 \sqrt{-Y_{02} Y_{01}}} - 1 \,. \tag{4.18}$$

From Eq. (4.15), it is evident that the bond length r_e assumes different values for each isotopologue. On the contrary, by substituting the product $B_e^{(\alpha)} \mu_a$ with U_{01}, one obtains an isotopically independent equilibrium bond length r_e^{BO}. In the present case, r_e^{BO} takes the value of 103.606721(13) pm. In Table 4.13, this result is compared with the equilibrium bond distances calculated from the B_e of each isotopologue NH, ^{15}NH, ND, and ^{15}ND. In this case, B_e was obtained by correcting the corresponding Y_{01} constant according to Eqs.. (4.16)–(4.18). It should be noticed that the values differ at sub-picometer level but these differences, even if small, are detectable thanks to the high-precision of rotational measurements.

The experimental value derived for r_e^{BO} has been compared with a theoretically best estimate obtained following the prescriptions of Ref. [57]. A composite calculation have been carried out

considering basis-set extrapolation, core-correlation effects, and inclusion of higher-order corrections due to the use of the full coupled-cluster with single and double excitation, augmented by a perturbative treatment of triple excitation [CCSD(T)] model:

$$\text{fc-CCSD(T)/cc-pV}\infty\text{Z} + \Delta\text{core/cc-pCV5Z} + \Delta\text{T/cc-pVTZ}\,. \tag{4.19}$$

The computation have been performed using CFOUR [58]. From this theoretical procedure we obtained $r_e^{\text{theor}} = 103.5915\,\text{pm}$ (see also Table 4.13), which is in very good agreement with the experimentally derived value, the discrepancy being 15 fm.

Table 4.13: Born–Oppenheimer and equilibrium bond distances (in pm) from the individual isotopologues (see text).

Species	r_e	$r_e - r_e^{\text{BO}}$
NH	103.716377(16)	0.109656
^{15}NH	103.715864(16)	0.109143
ND	103.665420(10)	0.058699
^{15}ND	103.664908(10)	0.058187
$r_e^{\text{BO}} = 103.606721(13)$		
$r_e^{\text{theor}} = 103.5915$		

Born–Oppenheimer Breakdown

The BOB coefficients Δ_{lm}^X determined in the present analysis account for the small inaccuracies of the Born–Oppenheimer approximation in describing the ro-vibrational energies of the imidogen radical. For the rotational constant ($\approx Y_{01}$), it is possible to identify three different contributions to the corresponding BOB parameter [59]

$$\begin{aligned}\Delta_{01}^X &= \left(\Delta_{01}^X\right)^{\text{ad}} + \left(\Delta_{01}^X\right)^{\text{nad}} + \left(\Delta_{01}^X\right)^{\text{Dunh}} \\ &= \left(\Delta_{01}^X\right)^{\text{ad}} + \frac{(\mu g_J)_{X'}}{m_p} + \frac{\Delta Y_{01}^{(\text{Dunh})}\mu}{m_e B_e}\,,\end{aligned} \tag{4.20}$$

namely an adiabatic contribution (ad), a non-adiabatic term (nad), and a Dunham correction (Dunh), respectively. The last two terms on the right side of Eq. (4.20) can be computed from purely experimental quantities: $\left(\Delta_{01}^X\right)^{\text{Dunh}}$ arises from the use of a Dunham expansion and contains the term $\Delta Y_{01}^{(\text{Dunh})}$ of Eq. (4.16), whereas $\left(\Delta_{01}^X\right)^{\text{nad}}$ depends on the mixing of the electronic ground state with nearby electronic excited states, and can be estimated from the molecular electric dipole moment μ and the rotational g_J factors [40]. The adiabatic term can be simply

computed as the difference between the experimental Δ_{01}^X and the terms $\left(\Delta_{01}^X\right)^{\text{Dunh}}$ and $\left(\Delta_{01}^X\right)^{\text{nad}}$. Tiemann *et al.* [42] found that the adiabatic term $\left(\Delta_{01}^X\right)^{\text{ad}}$ basically depends on the corresponding X atom rather than on the particular molecular species. Hence, it is interesting to derive this contribution in order to compare the results obtained for different molecules and to verify the reliability of the empirical fitting procedure.

All the contributions of Eq. (4.20) are collected in Table 4.14. The non-adiabatic contribution has been computed using the literature value of the dipole moment [60] $\mu = 1.389\,\text{D}$ and the ground state g_J value estimated from a laser magnetic resonance study [61], $g_J = 0.001524$.

From the adiabatic contribution to the Born–Oppenheimer Breakdown coefficients for the rotational constants, $\left(\Delta_{01}^X\right)^{\text{ad}}$, one may derive the corresponding correction to the equilibrium bond distance, a quantity which can also be accessed by *ab initio* computations. From our Eq. (4.11a) and Eq. (6) of Ref. [62], the following equality is obtained

$$\Delta R_{\text{ad}} = -\frac{r_e}{2}\left[\frac{m_e}{M_{\text{N}}}\left(\Delta_{01}^{\text{N}}\right)^{\text{ad}} + \frac{m_e}{M_{\text{H}}}\left(\Delta_{01}^{\text{H}}\right)^{\text{ad}}\right]. \tag{4.21}$$

The adiabatic correction to the equilibrium bond distance, ΔR_{ad}, can be theoretically estimated through the computation of the adiabatic bond distance, i.e., the minimum of the potential given by the sum of the Born–Oppenheimer potential augmented by the diagonal Born–Oppenheimer corrections (DBOC) [62]. The difference between the equilibrium bond distances calculated with and without DBOC, with tight convergence limits, performed at the CCSD/cc-pCVnZ level ($n = 3, 4, 5$), yielded $\Delta R_{\text{ad}} = 0.026\,\text{pm}$. This value is in very good agreement with the purely experimental one obtained by Eq. (4.21) which results 0.020 pm, thus providing a confirmation for the validity of our data treatment.

Table 4.14: Contributions of the Born–Oppenheimer Breakdown coefficients to the U_{01} constant

Atom	Δ_{01}(exp)	adiabatic	non-adiabatic	Dunham
N	-3.8592	-0.6515	-3.1326	-0.0751
H	-3.6874	-1.0379	-2.5744	-0.0751

Zero-point Energy

The results of our analysis make possible to estimate the ZPE for each isotopologue from the Dunham's constants Y_{lm} with $m = 0$, namely:

$$G(0) = \sum_l Y_{l0}\left(\frac{1}{2}\right)^l. \tag{4.22}$$

As we determined anharmonicity constants up to the sixth order, the ZPE is derived with a negligible truncation bias [63] from the expression:

$$G(0) = Y_{00} + \frac{Y_{10}}{2} - \frac{Y_{20}}{4} + \frac{Y_{30}}{8} + \frac{Y_{40}}{16} + \frac{Y_{50}}{32} + \frac{Y_{60}}{64}\,. \tag{4.23}$$

The Y_{00} constant present in the Dunham-type expansions is not experimentally accessible. Its value can be estimated, to a good approximation, through [63]

$$Y_{00} \simeq \frac{B_e}{4} + \frac{\alpha_e\omega_e}{12B_e} + \frac{\alpha_e^2\omega_e^2}{12^2B_e^3} - \frac{\omega_e x_e}{4}\,. \tag{4.24}$$

The value for the main isotopologue NH is 1.9987(12) cm^{-1}.
The values obtained for the ZPE of the four isotopologues are collected in Table 4.15. For comparison, the values of literature are also given.

Table 4.15: Zero Point Energies (in cm^{-1}) of imidogen isotopologues.

Species	This work	Ref. [63]	Ref. [64]
NH	1623.5359(17)	1623.6(6)	1621.5 [a]
^{15}NH	1619.9485(17)		1617.9 [b]
ND	1190.0859(11)	1190.13(5)	1189.5 [c]
^{15}ND	1185.1413(11)		1183.6 [b]

Number in parentheses are the 1σ statistical errors in unit of the last quoted digit. **[a]** From Ref. [33]. **[b]** Computed. **[c]** From Ref. [34].

Our results agree well with those reported in the literature [63], but our precision is more than one order of magnitude higher. The errors on our ZPE values are *ca.* 1×10^{-3} cm^{-1} and were calculated taking into account the error propagation

$$\sigma_f^2 = g^T V g \tag{4.25}$$

where σ_f^2 is the variance in the function f [i.e., Eq. (4.23) in the present case] of the set of parameters Y_{l0}, whose variance-covariance matrix is V, with the i^{th} element in the vector g being $\dfrac{\partial f}{\partial Y_i}$.
Discrepancies of $\sim 2\,cm^{-1}$ are observed by comparing our data with those reported in Ref. [64] because their definition of the ZPE does not include the term Y_{00}, which is non-negligible for light molecules [63]. These newly determined values should be used in the calculation of the exoergicity ΔE of chemical reactions relevant in fractionation processes.

4.1.9 Outlook

After the study of the ^{15}ND isotopologue, the spectroscopic characterization of imidogen is quite complete. Rotational spectra have been recorded and analysed for each isotopologue (at least their lowest N transitions) and ro-vibrational stretching bands have been studied for NH and ND. So, what could be done in the future is to record and assign the same band for the ^{15}N-substituted species, whose analysis can improve the quality of the Dunham fit.

From an astrophysical point of view, it would be more interesting to search for ND and ^{15}NH in publicly available spectral surveys (e.g., those deposited in the Herschel archive) and with the new high-frequencies facilities. The former species has been observed only two times, in IRAS16293 and its prestellar core 16293E, but NH is almost ubiquitous in the ISM and deuteration processes are very efficient in many different objects. The latter one, ^{15}NH, has never been observed and is certainly less abundant than ND. However, its astronomical detection would be of great help, because nitrogen fractionation can be used as a tool to trace the evolution of gas and dust during the star formation. Dedicated searches with high-sensitivity facilities, such as ALMA, may be needed to achieve this goal.

4.2 Amidogen radical

In the course of my PhD school, I have studied several isotopologues of the amidogen radical NH_2. Specifically, I have put the focus on the deuterated forms of this species. Amidogen is an abundant interstellar radical and the possibility to detect its deuterated isotopologues is briefly reported in § 4.2.1. Then, the complexity of the rotational energy levels of NH_2 is explained and the Hamiltonian is given (§ 4.2.2). After that, the studies of NHD, ND_2, and $^{15}ND_2$ are presented one-by-one (§ 4.2.3–4.2.5). Finally, the prospect of investigating the ^{15}NHD radical is presented in § 4.2.6.
Part of these studies are collected in the articles:

- M. Melosso, C. Degli Esposti, and L. Dore, "Terahertz Spectroscopy and Global Analysis of the Rotational Spectrum of Doubly Deuterated Amidogen Radical ND_2" *Astrophys. J. Suppl. S.*, vol. 233, issue 1, no. 15 (5pp), 2017 [65].

- M. Melosso, L. Bizzocchi, F. Tamassia, C. Degli Esposti, E. Canè, L. Dore, "The pure rotational spectrum of $^{15}ND_2$ observed by millimetre and submillimetre-wave spectroscopy," *J. Quant. Spectrosc. Ra.*, vol. 222-223, p. 186–189, 2019 [66].

- L. Bizzocchi, M. Melosso, B. M. Giuliano, L. Dore, F. Tamassia, M. Martin-Drumel, O. Pirali, L. Margulès, and P. Caselli, "Submillimetre and far-infrared spectroscopy of monodeuterated amidogen radical (NHD): improved rest-frequencies for astrophysical observations," submitted to *Astrophys. J. Suppl. S.*.

The following subsections are reproduction of the above-mentioned articles with some additions and changes. My contribution to this work can be summarized as follow:

- conceptualization and literature search;

- measurements of all the spectra but the FIR spectrum of ^{14}NHD;

- data analyses, with the help of Dr. M. Martin-Drumel for the FIR data of ^{14}NHD;

- presentation of the most relevant results in a scientific meeting (25th HRMS conference);

- manuscripts writing (for $^{14}ND_2$) or co-writing (for $^{15}ND_2$ and ^{14}NHD);

- co-writing of the SOLEIL proposal for ^{15}NHD, for which I am the principal investigator.

4.2.1 Introduction

Recent discoveries of multiply deuterated molecules in the ISM [67, 68, 69, 70] have confirmed the interest in deuterium-bearing species, since deuterium fractionation is a powerful tool to study the evolution of the Solar System [71, 72, 73, 74]. Both gas-phase models [75, 76] and active chemistry on grain-surface [77] have been invoked to explain the formation of doubly or even triply deuterated species and their anomalous large amount. Further detections of multiply deuterated species are thus fundamental to constrain the chemical models and spectroscopic laboratory data are necessary to the goal.

The singly and doubly deuterated forms of amidogen radical, NHD and ND_2, represent a possible target, since NH_2 is involved in the formation process of ammonia [6] and all the deuterated isotopologues of ammonia have been detected in space [68, 78, 79]. The main isotopologue NH_2 was first observed in 1943 in a comet [80] by optical astronomy. More recently, it has also been detected via radio observation of the star-forming region Sagittarius B2 [81] and of many other sources [24, 82]. Moreover, in 2013/2014 the rare ^{15}N-substituted isotopologue has been observed through cometary emissions [83, 84]. However, no detection of deuterated amidogen, even in its mono deuterated form NHD, has been reported to date.

Nevertheless, the existence of deuterated forms of amidogen in the ISM seems to be plausible as predicted by the gas-phase chemical models, in which the dissociative recombination of partially deuterated intermediates results in a higher probability for the ejection of a hydrogen atom than deuterium. Roueff *et al.* [85] presented a steady state model of the gas phase chemistry aimed at understanding the deuterium fractionation of ammonia in various sources: these authors considered different physical conditions and could derive a general trend. At high density and high depletion, deuteration of N-containing species is very efficient at 10 K. Actually, the abundances of singly and multiply deuterated forms of H_3^+ can reach exceptionally high values under conditions of extreme CO-depletion, and these high degrees of deuteration can propagate to the residual nitrogen-bearing species [86], that appear to be less depleted and subsist longer in the gas phase (see [87] and [88] for the cases of NH_3 and N_2H^+, respectively). The deuterium fractionation is sensitive to the temperature, but it remains large for temperatures between 5 and 20 K. Thus, the model predicts high fractional abundances of ammonia progenitors and their deuterated isotopologues, namely NH, ND, NH_2, NHD, and ND_2, in dense cores. In general, the predicted abundance ratios of the deuterated ammonia isotopologues and their progenitors agree reasonably well with existing observations, and, noticeably, the fractional abundance of NHD is predicted to be as high as that of NH_2D, while for ND_2 is estimated to be from 2 to 9 times larger than the ND_3 abundance.

From a spectroscopic point of view, the parent species NH_2 has been widely studied over the past 40 years [89, 90, 91, 92, 93, 53]. Driven by the current observational facilities (e.g., ALMA, SOFIA), the $^{15}NH_2$ species has recently been investigated for the first time in the mm/THz/FIR domain [94]. A thorough spectroscopic study was still missing for deuterated species NHD

and ND_2, which are likely to be the most abundant variant of amidogen in the ISM after NH_2. Moreover, no spectroscopic studies were ever reported for ^{15}NHD and $^{15}ND_2$.
The rotational spectrum of NHD has been observed first-ever in the discharge products of ammonia and deuterium [95] with a Fourier-Transform Far-Infrared (FT-FIR) spectrometer. Almost simultaneously, Kobayashi *et al.* [96] published an analogous study in the millimeter-/submillimeter-wave domain using a microwave absorption spectrometer. In the former case, the spectral resolution did not allow the observation of the hyperfine-structure but the spectral coverage (103–363 cm^{-1}) led to a detailed centrifugal analysis; in the latter case, hyperfine splittings were resolved for many transitions, and several spin-spin and spin-rotation constants were determined for N, H, and D. The ND_2 radical has been long studied with various spectroscopic techniques: electronic, Laser Magnetic Resonance (LMR), Microwave Optical Double Resonance (MODR), millimeter-wave and FT-FIR spectroscopy. Briefly, the rotational constants were first derived from the electronic spectrum [97], while quartic centrifugal distortion and fine interaction parameters were obtained by means of LMR studies [98]. Later on, [99] determined the hyperfine coupling constants using MODR spectroscopy and [100] measured the pure rotational spectrum in the range 265–531 GHz using a submillimeter-wave spectrometer. Lastly, in the same study of NHD, Morino *et al.* [95] observed the far-infrared spectrum of ND_2 in the 102–265 cm^{-1} region.
In this thesis, I report:

- the extension towards THz frequencies of the rotational spectrum of NHD and a reanalysis of its FIR spectrum, recorded at higher resolution (0.001 cm^{-1}) than in Ref. [95] using synchrotron radiation on the AILES beamline at SOLEIL;
- new rotational transitions from 588 GHz to 1.13 THz for ND_2 recorded with high accuracy, i.e., better than 100 kHz;
- the ro-vibrational analysis of the ν_2 band of ND_2 recorded at SOLEIL;
- the first and accurate determination of the rotational, fine and hyperfine constants of $^{15}ND_2$, for which no spectroscopic investigation was ever performed before;
- the very first step of the incoming project of ^{15}NHD, which was also unstudied.

For both NHD and ND_2, newly observed and previous field-free data were analyzed together, so that a unique set of highly accurate spectroscopic constants has been produced for each species, which will assist future astronomical searches.

4.2.2 Theory

The NH_2 radical in its electronic ground state X^2B_1 is an asymmetric rotor of C_{2v} symmetry whose dipole moment (1.82 D) lies along the b axis [101] (Fig. 4.5).
Because of the spin of the unpaired electron ($S = \frac{1}{2}$) and the spin of the $^{14/15}N$ and H/D nuclei ($I_{^{14}N} = 1$, $I_{^{15}N} = \frac{1}{2}$, $I_H = \frac{1}{2}$, $I_D = 1$), this radical shows a complex spectrum with fine and

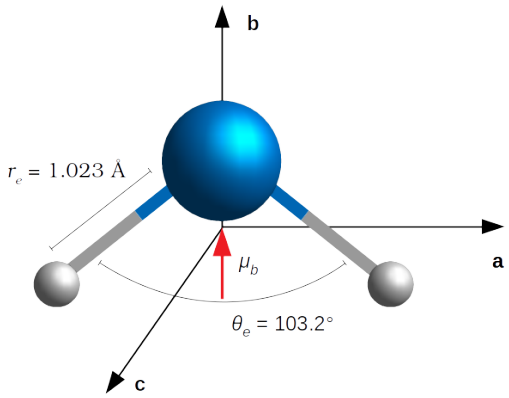

Figure 4.5: ND_2 in its principal system of inertia. Equilibrium bond-length and angle from Ref. [57].

hyperfine structures. In fact, each rotational level with quantum number $N \neq 0$ is split into two sublevels with $J = N + \frac{1}{2}$ and $J = N - \frac{1}{2}$ because of the coupling of the rotation with the electron spin. Each of these two sublevels is then split by the interaction with the nitrogen nuclear spin. A further splitting of the nitrogen hyperfine components is due to hydrogen and/or deuterium nuclear spins.

This thesis focuses onto three different isotopologues, namely ^{14}NHD, $^{14}ND_2$, and $^{15}ND_2$. In the cases of the doubly-deuterated species $^{14}ND_2$ and $^{15}ND_2$, the Bose-Einstein statistics has to be taken into account. Deuterium is a boson, therefore the total wavefunction has to be symmetric upon exchange of the two identical nuclei, that is of A symmetry. Since the X^2B_1 electronic state is antisymmetric and the vibrational ground state is symmetric, then symmetric rotational levels [$K_aK_c = (ee)$ or (oo)] combine with antisymmetric deuterium spin functions, with $I_D = I_{D_1} + I_{D_2} = 1$, while antisymmetric rotational levels [$K_aK_c = (eo)$ or (oe)] combine with spin functions with $I_D = 0, 2$, which are symmetric upon exchange of the D nuclei. Thus the symmetric rotational levels are split in three further hyperfine sublevels and the antisymmetric ones in six sublevels.

The coupling scheme used in the present work is the following:

$$\mathbf{J} = \mathbf{N} + \mathbf{S}$$
$$\mathbf{F}_1 = \mathbf{J} + \mathbf{I}_N$$
$$\mathbf{F} = \mathbf{F}_1 + \mathbf{I}_D.$$

On the other hand, ^{14}NHD has no spin statistics; all hyperfine levels are permitted and the cou-

pling scheme is:

$$\begin{aligned}\mathbf{J} &= \mathbf{N} + \mathbf{S}\\ \mathbf{F}_1 &= \mathbf{J} + \mathbf{I}_\mathrm{N}\\ \mathbf{F}_2 &= \mathbf{F}_1 + \mathbf{I}_\mathrm{H}\\ \mathbf{F} &= \mathbf{F}_2 + \mathbf{I}_\mathrm{D}.\end{aligned}$$

Moreover, NHD belongs to the C_s symmetry group, has a X^2A'' ground electronic state, and possesses two dipole moment components, μ_a=0.67 D and μ_b=1.69 D [101].

The effective Hamiltonian for the amidogen radical can be expressed as [95]:

$$\mathscr{H} = \mathscr{H}_\mathrm{rot} + \mathscr{H}_\mathrm{fs} + \mathscr{H}_\mathrm{hfs}, \tag{4.26}$$

The $\mathscr{H}_\mathrm{rot}$ term is the Watson A-reduced Hamiltonian in the I^r representation [102], which includes the rotational energy and the centrifugal distortion terms.

$$\mathscr{H}_\mathrm{rot} = \mathscr{H}^{(A)} + \mathscr{H}^{(4)}_\mathrm{cd} + \mathscr{H}^{(6)}_\mathrm{cd} + \ldots \tag{4.27}$$

where $\mathscr{H}^{(A)}$ contains the rotational constants in the A-Watson reduced form:

$$\mathscr{H}^{(A)} = \tfrac{1}{2}(B+C)\,\mathbf{N}^2 + \left[A - \tfrac{1}{2}(B+C)\right]N_a^2 + \tfrac{1}{2}(B-C)\left(N_b^2 - N_c^2\right), \tag{4.28}$$

the $\mathscr{H}^{(4)}_\mathrm{cd}$ part accounts for the centrifugal distortion terms with the 4$^\mathrm{th}$ power of the angular momentum

$$\mathscr{H}^{(4)}_\mathrm{cd} = -\Delta_N\mathbf{N}^4 - \Delta_{NK}\mathbf{N}^2N_a^2 - \Delta_K N_a^2 - \delta_N\mathbf{N}^2\left(N_b^2 - N_c^2\right) - \delta_K\left[\mathbf{N}^2\left(N_b^2 - N_c^2\right) + \left(N_b^2 - N_c^2\right)\mathbf{N}^2\right], \tag{4.29}$$

while $\mathscr{H}^{(6)}_\mathrm{cd}$ contains operator with 6$^\mathrm{th}$ power of $\mathbf{N}$, and so on.

The fine-structure Hamiltonian $\mathscr{H}_\mathrm{fs}$ contains the electron spin-rotation terms with constants ϵ_{ii} and their centrifugal dependences:

$$\begin{aligned}\mathscr{H}_\mathrm{fs} = {}& \epsilon_{aa}N_aS_a + \epsilon_{bb}N_bS_b + \epsilon_{cc}N_cS_c + (\epsilon_{ab}+\epsilon_{ba})(N_aS_b + N_bS_a)/2\\ &+ \Delta^S_N\mathbf{N}^2(\mathbf{N}\cdot\mathbf{S}) + (1/2)\,\Delta^S_{NK}\left[\mathbf{N}^2, N_aS_a\right]_+ + \Delta^S_{KN}N_a^2(\mathbf{N}\cdot\mathbf{S}) + \Delta^S_KN_a^3S_a\\ &+ \delta^S_N\left(N_b^2 - N_c^2\right)(\mathbf{N}\cdot\mathbf{S}) + \delta^S_K\left[N_aS_a, \left(N_b^2 - N_c^2\right)\right]_+ + \ldots\end{aligned} \tag{4.30}$$

The $\mathscr{H}_\mathrm{hfs}$ operator is the hyperfine-structure Hamiltonian and can be separated into several com-

ponents:

$$\mathscr{H}_{\rm hfs} = \mathscr{H}_{\rm d-d}(^{14/15}{\rm N}) + \mathscr{H}_{\rm d-d}({\rm H/D}) + \mathscr{H}_{\rm Q}(^{14}{\rm N}) + \mathscr{H}_{\rm Q}({\rm D}). \quad (4.31)$$

$\mathscr{H}_m rmd - d$(X) and $\mathscr{H}_m rmQ$(X) represent the Hamiltonian for dipole-dipole interactions and nuclear quadrupole interaction for the nucleus X, respectively. In the present analysis, the effect of isotropic (a_F) and anisotropic (T_{ii}) electronic spin-nuclear spin coupling constants were considered for all nuclei. The electric quadrupole (eQq) and spin-rotation (C_{ii}) coupling constants could be determined for the ^{14}N-nitrogen nucleus and, in some cases, for deuterium.

4.2.3 ^{14}NHD

High-resolution pure rotational spectral data of NHD have been collected in the submm-region at the Centre for Astrochemical Studies of the Max-Planck-Institut für extraterrestrische in Garching (see § 3.2) and in the FIR domain at the AILES beamline of the SOLEIL (§ 3.5).

The measurements in Garching have been carried out using the CASAC spectrometer. Below 1.1 THz, a WR9.0SGX module (80–125 GHz) associated to a series of active and passive harmonic doublers/triplers in cascade has been employed as radiation sources, thus achieving a frequency multiplication factors as high as 9. Measurements above this frequency have been performed with a stand-alone active multiplier system operating in the 1.1–1.2 THz (AMC-680) interval. The NHD radical was produced in a glow discharge (70 mA, ~ 1.1 kV) of a 1:2 mixture of NH_3 (4 μbar) and D_2 (8 μbar) diluted in Ar buffer (total pressure ~ 25 μbar), with the cell kept at ~ 180 K by cold vapour/liquid N_2 circulation. Besides preventing cell overheating, the cooling was found to be critical to improve the amidogen production in the plasma. However, below the indicated temperature NHD signals decreased due to massive ammonia condensation on the cold cell walls. The spectrum was recorded in selected frequency regions from 430 GHz to 1.2 THz. Slow (0.67–1.67 MHz s^{-1}) back-and-forth scans around target lines were perfomed employing a frequency step of 10–25 kHz and a time constant RC = 3 ms.

At SOLEIL, the FIR spectrum of NHD has been recorded using a Bruker IFS125HR FT-IR spectrometer exploiting the bright synchrotron radiation extracted by the AILES beamline. The spectrum results from the co-addition of 104 scans recorded at the ultimate resolution of the instrument, R = 0.001 cm^{-1}, in the 50–250 cm^{-1} range. A 6 μm Mylar beamsplitter and a 4.2 K liquid helium cooled bolometer were used. The NHD radical was produced using a post-discharge set-up successfully employed in the past to produce the NH_2 and NH radicals as well as their ^{15}N isotopic variants [53, 94, 43]. In this configuration, a radio-frequency discharge cell is connected perpendicularly to the center of a White-type multipass absorption cell. A 2.5 m baselength White-type cell allowing 150 m of absorption path length was used. The absorption cell was separated from the interferometer by two polypropylene films of 60 μm thickness.

The NHD radical was produced by a 1000 W radiofrequency discharge in a ND_3 + H_2 mixture at partial pressures of 30 and 15 μbar, respectively. Production of NHD, as well as ND_2, were found to be more efficient when the gas mixture was injected at one end of the absorption cell

while pumping connections were set at the other end of that cell, so that no gas was directly injected through the RF discharge cell. Such configuration enabled a propagation of the plasma into the absorption cell. A discharge-off spectrum was also recorded to quickly identify the lines arising from transient species. The recorded FIR spectrum was calibrated using residual water lines whose accurate frequencies have been reported in the literature [103]; the resulting accuracy on line frequency is estimated to be of $0.0002\,\mathrm{cm}^{-1}$.

Since there are no spin statistics in the case of NHD, all hyperfine sublevels (up to a maximum of 18) are allowed for each N_{K_a,K_c} rotational level. The electric dipole selection rules [1] on this sublevels manifold produce very complex hyperfine patterns for each rotational transition due to the additional fine/hyperfine selection rules $\Delta J = 0, \pm 1$, $\Delta F_1 = 0, \pm 1$, $\Delta F_2 = 0, \pm 1$, and $\Delta F = 0, \pm 1$. The most intense components have $\Delta J = \Delta F_1 = \Delta F_2 = \Delta F = \Delta N$. An example of the complexity is given in Figure 4.6, which illustrates the above described interactions for the fundamental *b*-type transition $N_{K_a,K_c} = 1_{11} \leftarrow 0_{00}$. Each line of the fine-structure doublet, separated by some GHz, is then split in a multitude of hyperfine components, roughly gathered in loose triplets, due to the dominant effect of electron spin–nuclear spin coupling due to the ^{14}N nucleus.

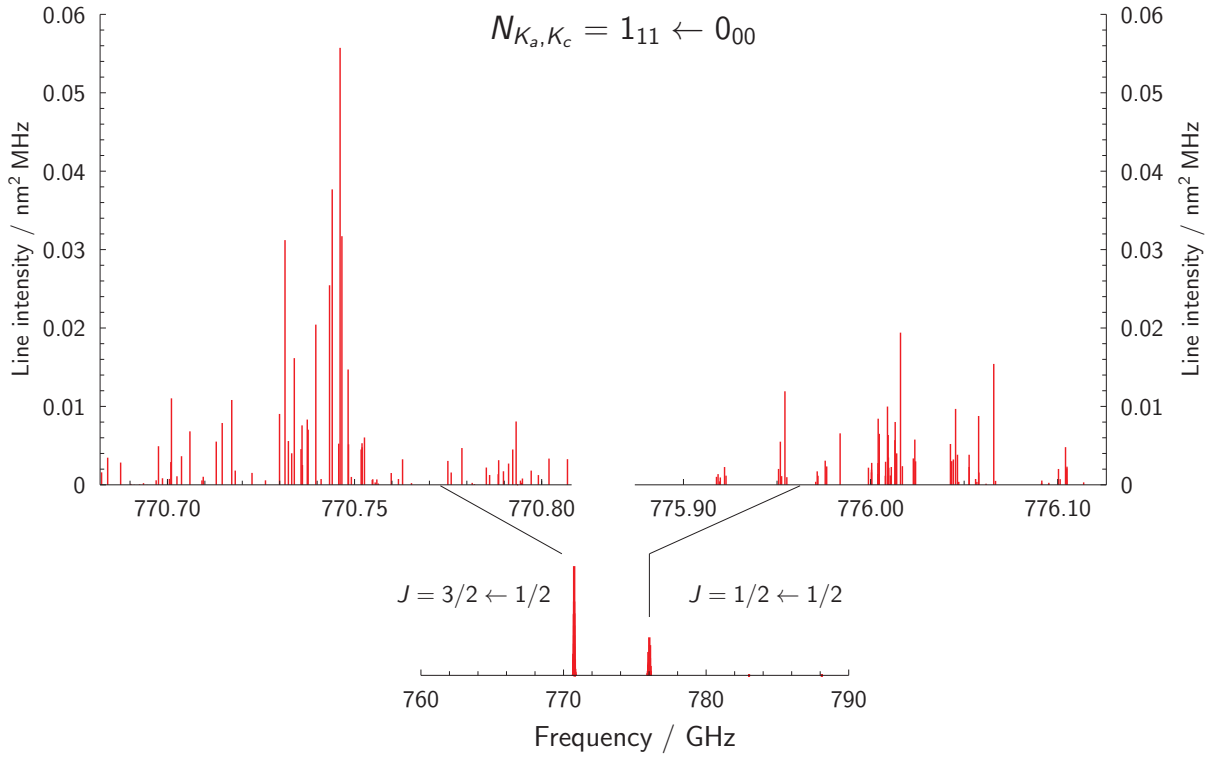

Figure 4.6: Synthetic spectrum of the $N_{Ka,Kc} = 1_{11} \leftarrow 0_{00}$ rotational transition of NHD simulated at 298 K.

The spectral recordings performed with the CASAC spectrometer covered the frequency interval from 430 GHz to 1200 GHz, exploring the region above 520 GHz for the first time. Since NHD is a very light molecule, the rotational transitions are quite isolated in the spectrum and

separated by several tens of GHz. The transitions recorded in this frequency domain are summarized in Table 4.16, which also reports the hypothetically unsplit frequency of the rotational lines and the number of assigned hyperfine components.

Table 4.16: List of NHD rotational transitions with HFS recorded in the submillimeter region.

Transition	Type[a]	Unsplit Freq. (MHz)	no. of FS lines	no. of HFS lines
$1_{1,0} - 1_{0,1}$	${}^{b}Q_{+1,-1}$	432580.3	4	44
$2_{0,2} - 1_{1,1}$	${}^{b}R_{-1,+1}$	456235.5	2	5
$2_{1,1} - 2_{0,2}$	${}^{b}Q_{+1,-1}$	515448.6	2	19
$3_{1,2} - 3_{0,3}$	${}^{b}Q_{+1,-1}$	656654.9	2	30
$1_{1,1} - 0_{0,0}$	${}^{b}R_{+1,+1}$	772506.7	2	15
$4_{1,3} - 4_{0,4}$	${}^{b}Q_{+1,-1}$	869336.3	2	7
$3_{0,3} - 2_{1,2}$	${}^{b}R_{-1,+1}$	902924.7	2	12
$3_{2,1} - 3_{1,2}$	${}^{b}Q_{+1,-1}$	1020828.9	2	5
$6_{2,4} - 6_{1,5}$	${}^{b}Q_{+1,-1}$	1062344.6	2	6
$2_{1,2} - 1_{0,1}$	${}^{b}R_{+1,+1}$	1112159.2	2	4
$3_{1,3} - 2_{1,2}$	${}^{a}R_{0,+1}$	1122794.6	1	1
$5_{1,4} - 5_{0,5}$	${}^{b}Q_{+1,-1}$	1157071.0	1	6
$3_{0,3} - 2_{0,2}$	${}^{a}R_{0,+1}$	1199330.9	2	6

[a] The symbol ${}^{x}M_{\delta K_a,\delta K_c}$ is used to label in a compact form the transition type for an asymmetric rotor: x indicates the dipole moment component involved, $M = P, Q, R$ is the symbol for the transitions with $\Delta N = -1, 0, +1$, respectively, and δK_a and δK_c refer to the (signed) change in the K_a and K_c pseudo-quantum numbers [1].

Under our experimental conditions, isolated NHD absorption lines have a FWHM of 1.5–3.0 MHz due to the sizable Doppler broadening characteristic of this spectral range (e.g., $\Delta\nu_{\mathrm{d}} \sim 1.5$ MHz at 700 GHz for NHD at 150 K). However, due to the density of the hyperfine structure, overlap of numerous components is common and blends of lines, resolved to different extents, are typically observed. To facilitate the retrieval of the corresponding central line frequencies, we have modeled the recorded absorption profiles using the `proFFiT` line analysis code [44] adopting a FM Voigt profile function and considering the full complex representation of the Fourier-transformed dipole correlation function. When necessary, the background contribution has also been accounted for using a third-order polynomial expansion. In most cases, this approach typically allowed for a satisfactory fit of the recorded spectral profiles, with some minor discrepancies due to the occasional presence of noise features or weak interfering lines. An example is presented in Figure 4.7, which shows the recordings of the $N_{K_a,K_c} = 4_{1,3} \leftarrow 4_{0,4}$, $J = {}^{9}/_{2} \leftarrow {}^{9}/_{2}$ fine-structure component of NHD: twelve hyperfine components are blended in six resolvable lines illustrating the predominance of the N coupling (three

main groups), followed by the H coupling (closely separated doublets).

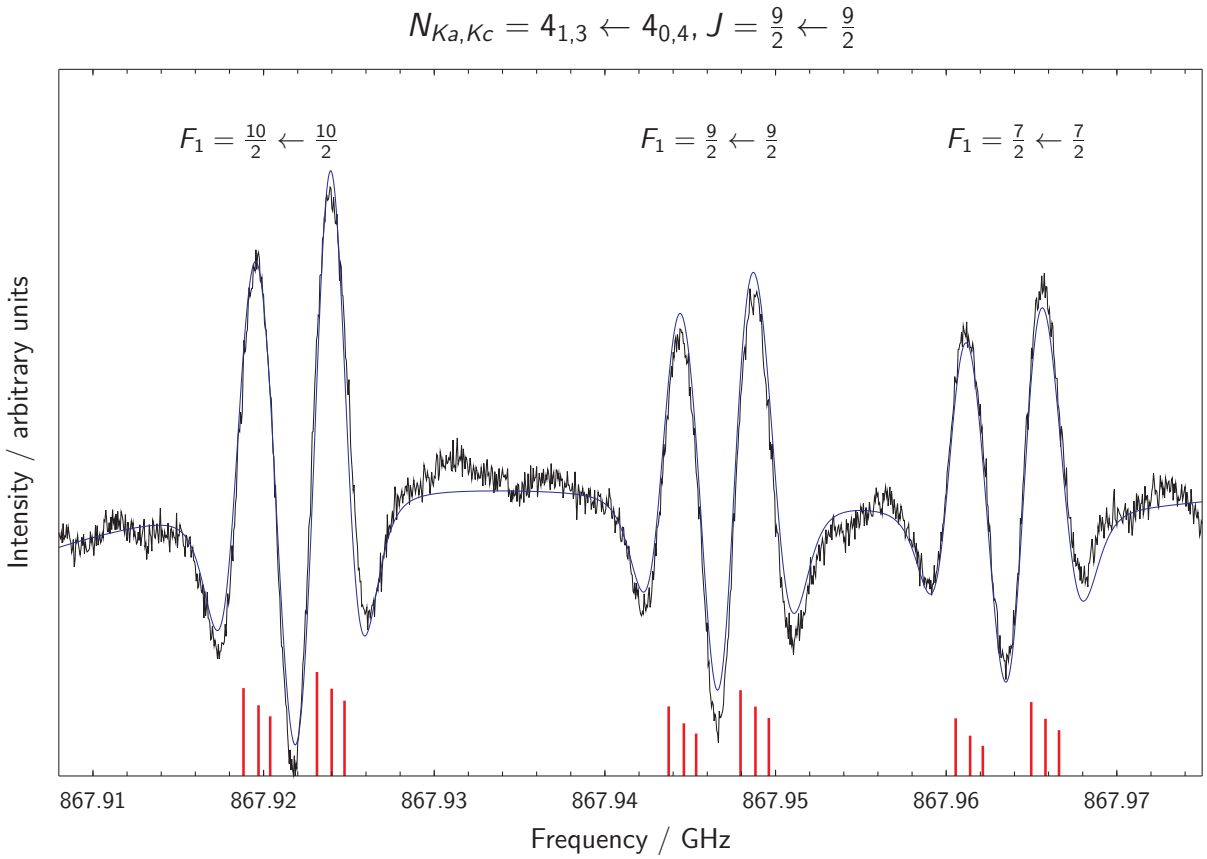

Figure 4.7: Recording (black trace) of the $N_{K_a,K_c} = 4_{1,3} \leftarrow 4_{0,4}$, $J = {}^9/_2 \leftarrow {}^9/_2$ fine-structure transitions showing six resolvable components. Integration time: 390 s; $RC = 3$ ms; scanning rate: 1.3 MHz/s; modulation depth: 850 kHz. The blue trace plots the modeled spectrum computed with `proFFiT` using a modulated Voigt profile (see text). The red sticks indicates the position and relative intensity of the twelve hyperfine components. Note that the F_2 and F quantum number are not shown in the plot.

The modeled profile has been obtained by fixing the Doppler FWHM at 1.834 MHz (computed at 150 K) and adjusting the line positions and the Lorentzian FWHM (collisional broadening), $\Delta\nu_d = 1.42(15)$ MHz, assumed equal for all the components. This procedure allowed us to obtain line positions with an associate error ranging in the 30–100 kHz interval, depending on the S/N of the spectrum and on the overall goodness of the line profile fit. Whenever possible, a single hyperfine transition has been assigned to a given resolved feature detected in the rotational spectrum. Measurements corresponding to tight line blends have been instead assigned to the subset of components which make up the dominant intensity contribution. In these cases the intensity-averaged frequency is compared with the experimental one in the least-squares fit. Loose blends of unresolved components, resulting in very broad or distorted line profiles, have not been used in the analysis.

In the FIR experiment, deuterium scrambling in the NH_3 + D_2 discharge mixture appears very

efficient as strong transitions of NHD are observed, about 10 of the strongest lines are even saturated (these transitions have been excluded from the analysis). As a point of comparison, using the same experimental condition in pure ND_3 or NH_3, similarly strong signals of ND_2 and NH_2, respectively are observed, while in the present spectrum only relatively weak signals of ND_2 (10 % absorption at best) and no NH_2 are observed. As previously observed in similar studies on the NH_2 radical and its isotopologues, the hyperfine splitting due to the nitrogen atom is partially or fully resolved for several *b*-type transitions on the spectrum, as illustrated in Fig. 4.8.

Table 4.17: Center frequencies used to calculate the offset values in Figure 4.8. These frequencies correspond to unresolved nitrogen hyperfine structure.

N'	K'_a	K'_c	J'	N''	K''_a	K''_c	J''	Obs. frequency /cm^{-1}
2	2	0	3	1	1	1	2	68.5090
2	2	0	2	1	1	1	1	68.7396
3	2	1	4	2	1	2	3	85.9796
3	2	1	3	2	1	2	2	86.1901
4	2	2	5	3	1	3	4	106.2754
4	2	2	4	3	1	3	3	106.4740
5	2	3	6	4	1	4	5	129.9514
5	2	3	5	4	1	4	4	130.1496
6	2	4	7	5	1	5	6	157.1743
6	2	4	6	5	1	5	5	157.3806
7	2	5	8	6	1	6	7	187.7432
7	2	5	7	6	1	6	6	187.9622

Because the natural width of the transitions is lower than the experimental resolution in this spectral region, many lines exhibit a cardinal sine profile at their base (arising from the boxcar apodization). While this effect can be canceled by applying an apodization to the interferogram before Fourier transform, the resulting width broadening prevented from the resolution of the nitrogen hyperfine structure on most transitions; consequently such apodization was not applied. In total, 512 transitions have been assigned to 447 experimental frequencies in the range 54–236 cm^{-1}, 141 *a*-type and 371 *b*-type transitions with $N'_{\max} = 15$ (for $K'_a = 0 - 2$) and $K'_{a_{\max}} = 7$ (for $N' = 7$). Among these transitions, 107 transitions (80 different frequencies, mostly *b*-type) with $K'_a = 0 - 3$ exhibit partially or fully resolved nitrogen hyperfine structure. The uncertainty on line frequency is doubled for lines that appear broadened by unresolved hyperfine structure or asymmetric splitting.

The analysis was carried out with the SPFIT/SPCAT suite of programs [46]. The experimental frequencies were fitted to the Hamiltonian of Eqs. (4.26)–(4.31) in a least-square procedure, in which the weight of each datum was proportional to the inverse square of its error. The data set includes previously measured [95, 96] and newly observed mm-, submm-wave, and FIR

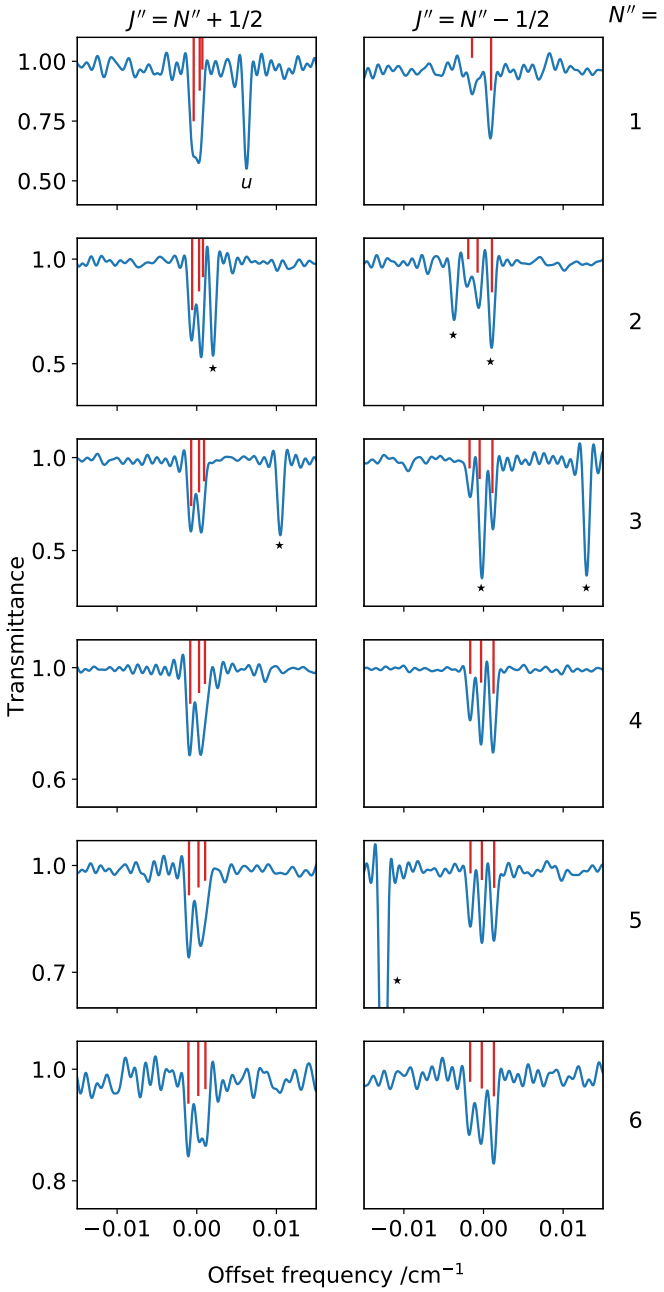

Figure 4.8: Observation on the FIR spectrum of the hyperfine structure due to the nuclear spin of the N atom in NHD for the *b*-type $^{r}R(1)$ branch with $K''_a + K''_c - N'' = 0$. Frequencies are reported as the offset frequencies from the predicted transition when no hyperfine structure is taken into account and span the 68–188 cm^{-1} range (see Table 4.17 for the numerical values). Predicted frequency of each component (neglecting the H and D hyperfine splittings) is indicated by red sticks (intensity in arbitrary units). Transitions labeled with "⋆" symbol are still present with the discharge off and most likely arise from ND_3; the line labeled with a "*u*" remains unassigned.

transitions. The data from Ref. [95] were given uncertainties of 7.5×10^{-4} cm^{-1}, i.e., an order

Table 4.18: Rotational spectroscopic parameters determined for NHD.

Constant	Unit	Present work	Ref. [96]	Ref. [95][a]
A	MHz	602874.1082(64)	602873.269(18)	602879.3(24)
B	MHz	243153.818(15)	243150.415(29)	243147.6(9)
C	MHz	169872.513(15)	169875.877(26)	169871.5(9)
Centrifugal distortion				
Δ_N	MHz	9.29361(23)	9.2833(9)	9.239(9)
Δ_{NK}	MHz	31.2187(11)	30.303(13)	31.226(45)
Δ_K	MHz	250.2294(21)	250.825(10)	250.90(21)
δ_N	MHz	3.07038(10)	3.04088(12)	3.0672(30)
δ_K	MHz	48.7864(81)	46.854(14)	47.502(66)
Φ_N	kHz	1.0098(24)		0.785(42)
Φ_{NK}	MHz	0.04883(14)	−0.0901(11)	0.04569(60)
Φ_{KN}	MHz	−0.17115(50)		−0.1638(21)
Φ_K	MHz	0.79326(48)	0.59213(25)	0.8223(87)
ϕ_N	kHz	0.4888(12)		0.475(18)
ϕ_{NK}	MHz	0.023248(49)		0.02099(42)
ϕ_K	MHz	0.2588(11)		0.1256(19)
L_{NNK}	kHz	−2.373(14)		
L_{KKN}	kHz	0.0437(32)		0.0615(84)
L_K	kHz	−3.91(29)		−3.20(17)
l_K	kHz	0.307(22)		0.0210(48)
P_K	Hz	8.43(29)		17.6(16)
p_K	Hz	−1.40(16)		
O_K	Hz	−0.0196(18)		−0.0591(57)
Number of FIR lines		649		
Number of MW lines		353		
rms FIR	cm^{-1}	4.2×10^{-4}		
rms submm	kHz	51.8		
σ		0.963		
N'_{max}, $K'_{a,max}$		15,9		

Number in parenthesis are one standard deviation in units of the last quoted digit. **[a]** The values, originally reported in cm^{-1}, are converted to MHz.

of magnitude smaller than their resolution of 0.0075 cm^{-1}, while the errors reported in Ref. [96] were retained. A total of 58 spectroscopic parameters could be determined from the analysis of more than 1000 distinct frequencies. Their values are reported in Table 4.18–4.20 and compared

Table 4.19: Fine-structure spectroscopic parameters determined for NHD.

Constant	Unit	Present work	Ref. [96]	Ref. [95][a]
ϵ_{aa}	MHz	−7043.123(16)	−7043.180(27)	−7041.0(12)
ϵ_{bb}	MHz	−1149.383(17)	−1149.38(9)	−1150.96(45)
ϵ_{cc}	MHz	7.809(17)	7.82(8)	8.7(11)
$(\epsilon_{ab} + \epsilon_{ba})/2$	MHz	1088.64(60)	1093.9(11)	1056(7)
Centrifugal distortion				
Δ_N^S	MHz	0.12026(78)	0.1187(20)	0.140(9)
Δ_{KN+NK}^S	MHz	0.2401(87)		
$\Delta_N^S K$	MHz	1.77(35)	0.234(13)	
Δ_K^S	MHz	16.2441(91)	16.245(12)	16.16(21)
δ_N^S	MHz	0.06300(30)	0.0640(7)	0.075(8)
δ_K^S	MHz	0.9553(83)	0.96(4)	1.20(11)
Φ_K^S	MHz	−0.06755(59)	−0.0634(7)	−0.0570(45)
L_K^S	kHz	0.2270(96)		0.135(30)

Number in parenthesis are one standard deviation in units of the last quoted digit. **[a]** The values, originally reported in cm^{-1}, are converted to MHz.

with the results of former studies.

All the observed transition frequencies could be fitted within their experimental uncertainty: the weighted deviation of the fit is close to one ($\sigma = 0.96$) and the *rms* error is 0.052 MHz for transitions in the mm-/submm-wave region and 4.1×10^{-4} cm^{-1} for those in the FIR (1.9×10^{-4} cm^{-1}). While the studies of Morino *et al.* [95] and Kobayashi *et al.* [96], published almost simultaneously, provided two different sets of constants relying on different data sets, our global analysis comprises all those transitions, in addition to a larger set of submm-wave and FIR data. To this respect, a more comprehensive set of spectroscopic constants is produced in this work. Overall, the rotational, centrifugal distortion, and fine-interaction constants of Table **??** are now refined, and their values agree well with those reported previously by the cited authors. Still, some sporadic discrepancies are present, e.g., the Φ_{NK} constant determined in Ref. [95] is two times larger than ours and has opposite sign. The hyperfine-interaction parameters are almost identical to those of Ref. [96], because the magnitude of the hyperfine coupling effect decreases with the increase of the rotational quantum numbers involved in the transitions. Nonetheless, 23 hyperfine constants (2 more than in [96]) were determined with high accuracy.

4.2.4 $^{14}ND_2$

The rotational spectrum of ND_2 radical in its ground vibrational state has been investigated in selected frequency regions between 588 GHz and 1.13 THz using the source-modulation millime-

Table 4.20: Hyperfine spectroscopic parameters (MHz) determined for NHD.

Constant	Atom	This work	Ref. [96]
a_F	(N)	28.1077(71)	28.124(10)
$\Delta^K a_F$	(N)		−0.0157(12)
T_{aa}	(N)	−43.3319(77)	−43.329(8)
T_{bb}	(N)	−44.2125(97)	−44.218(11)
T_{ab}	(N)	0.550[a]	0.550[a]
X_{aa}	(N)	−0.288(13)	−0.297(14)
$(X_{bb} - X_{cc})$	(N)	−6.738(28)	−6.725(32)
X_{ab}	(N)	1.370[a]	1.370[a]
C_{aa}	(N)	0.3486(33)	0.3505(37)
C_{bb}	(N)	0.0738(29)	0.0742(37)
X_{aa}	(D)	0.167(15)	0.143(40)
$(X_{bb} - X_{cc})$	(D)	0.100(44)	
a_F	(D)	−10.230(10)	−10.229(13)
T_{aa}	(D)	8.0530(91)	8.052(10)
T_{bb}	(D)	−7.251(13)	−7.251(14)
T_{ab}	(D)	6.1(14)	6.7(14)
C_{aa}	(D)	0.0482(34)	0.0491(36)
a_F	(H)	−67.128(11)	−67.116(13)
T_{aa}	(H)	−23.305(31)	−23.254(24)
T_{bb}	(H)	28.460(23)	28.434(22)
T_{ab}	(H)	−47.9(19)	−48.7(20)
$\Delta^K T_{aa}$	(H)	−0.122(16)	−0.0621(51)
$\Delta^J T_{aa}$	(H)	0.0192(69)	
C_{aa}	(H)	0.0844(75)	0.1152(64)
C_{bb}	(H)	0.0864(50)	0.1042(60)
C_{cc}	(H)	−0.0157(48)	

Number in parenthesis are one standard deviation in units of the last quoted digit. **[a]** Kept fixed.

ter/submillimeter wave spectrometer described in Section 3.1. The ND_2 radical was produced within the electrical glow-discharge system. A mixture of ND_3 (5-7 mTorr) and Ar (20 mTorr) was used, as in Ref. [100]. Typically, a discharge current of 70 mA and a voltage of about 1 kV were maintained between the electrodes while recording the spectrum. The absorption cell was cooled continuously just above the freezing point of ammonia with liquid nitrogen, in order to avoid an excessive overheating of the two electrodes. The estimated uncertainties of the mea-

surements are 50 kHz in most cases, 100 kHz in a few cases. The accuracy depends on the S/N of the observed spectrum and on line-blending due to unresolved hyperfine components.
Besides the study of the ground vibrational state, we decided to study the ND_2 radical in the first vibrational excited level, i.e., the v_2=1 state. With this respect, the ro-vibrational band (010) was recorded with the FT-IR spectrometer located at the AILES beamline (§3.5). The apparatus was used in the same configuration described in §4.1.5, the only exceptions being the radiation source used. At these frequencies, the performances of the synchrotron light and a standard Globar source are similar, so the latter was employed.
The initial predictions of the pure rotational spectrum were made using the Pickett's program SPCAT [46] with the constants derived by Kanada *et al.* [100]. The production of ND_2 was optimized by observing the $J = 0 \leftarrow 0$ component of the $N = 1_{10} \leftarrow 1_{01}$ transition. Then, the fine components of new eight rotational transitions were recorded and their hyperfine structure could be easily assigned thanks to the already known hyperfine-interaction parameters. Sixty-four distinct frequencies were measured and analyzed in a weighted least-squares procedure, in which previous data (millimeter/submillimeter, MODR and FIR studies) were included. In this procedure, performed with the Pickett's program SPFIT [46], the mm and submm lines previously measured in Ref. [100] were given uncertainties of 50 kHz, whereas the FIR data [95] were given uncertainties of 0.0007 cm^{-1} (as in the analysis of NH_2 [92]), in accordance with the residuals from the original papers. For the MODR data [99] the same uncertainties given in the original work were assumed (typically 0.5 MHz). Surprisingly, the older sets of frequency data were never analyzed simultaneously, so that different sets of spectroscopic constants, not fully consistent, have been reported in the literature for ND_2. The present global analysis allows to obtain spectroscopy constants which are compatible with the entire body of rotational data available for this radical. Moreover, we were able to complete and/or correct previous assignments. As far as MODR data are concerned, about 20% of the observed transitions were not considered in the fit of Ref. [99] because of the failure to unambiguously assign their hyperfine components. Our more extensive data analysis allowed us to overcome this difficulty, so that a large number of previously unused MODR frequencies could be included in our fit. Furthermore, during the merging process some FIR transitions appeared to be misassigned, so they have been reassigned correctly in this study. In particular, a few transitions with $N \geq 10$ had been wrongly assigned as $\Delta K_a = \pm 3$ instead of $\Delta K_a = \pm 1$. In the final fit, unresolved lines were treated using the intensity-weighted average of the individual components involved. A total number of 41 ground-state spectroscopic constants were included in the least squares analysis, giving a satisfactory dimensionless standard deviation of 0.87.
Tables 4.21–4.23 show the list of spectroscopic parameters determined in the present work, where they are compared to those obtained previously.
In general, all derived parameters are determined with higher precision than in the previous works: for instance, the standard errors of the rotational constants are one order of magnitude lower and the hyperfine constants are three times more precise. This is mainly due to the simul-

Table 4.21: Rotational spectroscopic parameters derived for $^{14}ND_2$ in the ground vibrational state.

Constant	Unit	This work	Previous mm-wave [a]	Previous FIR [b]
A	MHz	399989.5534(87)	399985.879(81)	399993.9(19)
B	MHz	194498.192(15)	194488.65(16)	194498.1(10)
C	MHz	128610.445(15)	128613.987(57)	128610.0(13)
Centrifugal distortion				
Δ_N	MHz	7.86074(33)	7.323(10)	7.839(11)
Δ_{NK}	MHz	−33.4838(26)	−33.812(25)	−33.388(42)
Δ_K	MHz	198.7064(57)	196.771(33)	198.783(84)
δ_N	MHz	3.08080(20)	3.03[c]	3.0858(36)
δ_k	MHz	8.5567(82)	6.300(39)	8.279(29)
Φ_N	kHz	1.4776(80)		1.376(35)
Φ_{NK}	kHz	−6.28(31)		−5.606(35)
Φ_{KN}	kHz	−43.70(98)		−43.45(96)
Φ_K	kHz	320.34(90)		321.0(23)
ϕ_N	kHz	0.7224(33)		0.740(14)
ϕ_{NK}	kHz	−0.834(99)		−1.01(21)
ϕ_K	kHz	65.9(13)		33.37(65)
L_{KKKN}	kHz	0.0834(14)		0.0707(38)
L_K	kHz	−0.7022(85)		−0.694(26)
l_K	kHz	−0.1230(33)		−0.0311(16)
M_K	Hz	1.069(38)		1.08(10)
No. of MW lines		182		
MW *rms* error	kHz	51.0		
No. of IR lines		181		
IR *rms* error	cm^{-1}	6.9×10^{-4}		
No. of MODR lines		198		
MODR *rms* error	MHz	0.376		
σ		0.87		

Number in parenthesis are one standard deviation in units of the last quoted digit. **[a]** Ref. [100]. **[b]** Ref. [95]. The values, originally reported in cm^{-1}, are converted to MHz. **[c]** Fixed in the analysis.

taneous analysis of MW spectroscopy measurements (high frequency precision and resolving power) with FT-FIR data (large range of N and K_a quantum numbers). The newly determined values of the spectroscopic constants agree well with those previously reported by [95, 100], the only exceptions being ϕ_K and l_K. This discrepancy should be ascribed to the reassignment

Table 4.22: Fine-structure spectroscopic constants derived for $^{14}ND_2$ in the ground vibrational state.

Constant	Unit	This work	Previous mm-wave [a]	Previous FIR [b]
ϵ_{aa}	MHz	−5128.126(22)	−5127.81(11)	−5127.71(41)
ϵ_{bb}	MHz	−668.697(18)	−668.507(78)	−668.76(16)
ϵ_{cc}	MHz	3.462(17)	3.413(63)	3.23(12)
Centrifugal distortion				
Δ_N^S	MHz	0.07613(57)	0.0469(66)	0.0779(29)
Δ_{KN+NK}^S	MHz	−0.9498(57)	−0.967(81)	−0.875(29)
Δ_{NK}^S	MHz	1.05(20)		
Δ_K^S	MHz	9.8548(76)	9.587(66)	9.476(99)
δ_N^S	MHz	0.03843(36)		0.0353(16)
δ_K^S	MHz	0.1005(59)	0.0356(45)	0.150(36)
Φ_{NKK}^S	kHz	3.76(51)		
Φ_K^S	kHz	−23.10(81)		−15.36(72)

Number in parenthesis are one standard deviation in units of the last quoted digit. **[a]** Ref. [100]. **[b]** Ref. [95]. The values, originally reported in cm^{-1}, are converted to MHz.

Table 4.23: Hyperfine-interaction parameters (MHz) derived for $^{14}ND_2$ in the ground vibrational state.

Constant	Atom	This work	Previous mm-wave [a]
a_F	(N)	28.0577(122)	28.055(33)
T_{aa}	(N)	−43.1451(183)	−43.136(48)
T_{bb}	(N)	−44.2715(213)	−44.277(63)
C_{aa}	(N)	0.2660(75)	0.269(27)
C_{bb}	(N)	0.0458(55)	0.045(21)
C_{cc}	(N)	0.0145(64)	0.019(22)
a_F	(D)	−10.2446(103)	−10.241(28)
T_{aa}	(D)	2.8536(168)	2.874(45)
T_{bb}	(D)	−2.0916(247)	−2.108(69)
X_{aa}	(N)	0.2191(297)	0.213(84)
X_{bb}	(N)	−3.744(34)	−3.75(11)

Number in parenthesis are one standard deviation in units of the last quoted digit. **[a]** Ref. [100].

process of some FIR transitions (see above).

As far as the v_2=1 state of ND_2 is concerned, a set of spectroscopic constants was available thanks to the LMR experiment of Hills & McKellar [98], but the rest frequency of the measured transitions were not given because of the nature of the LMR experiment. So, to predict the infrared band of the D−N−D bending mode, we used the parameters reported in Ref. [98] in combination with the newly determined ground state constants (Tables 4.21–4.23). The symmetry of this vibrational state is A'. Consequently, the vibronic wavefunction has the same symmetry of the ground vibrational state. The spin-statistics discussed in §4.2.2 is still valid.

The ro-vibrational spectrum of the (010) band is pretty much dominated by the strong absorptions of the precursor (ND_3), which hide nearly half of the transitions we expected to see for ND_2. Nonetheless, a large set of distinct frequencies (~ 200) could be observed and successfully analyzed. At the condition used to record the spectrum, they exhibit absorption around 5 % (the signals due to the precursor saturate most of the time). Considered the density of the lines within the spectrum, it is pointless to show an overview of the band. Instead, a simulation of the ND_2 spectrum where observed transitions are highlighted is given in Figure 4.9.

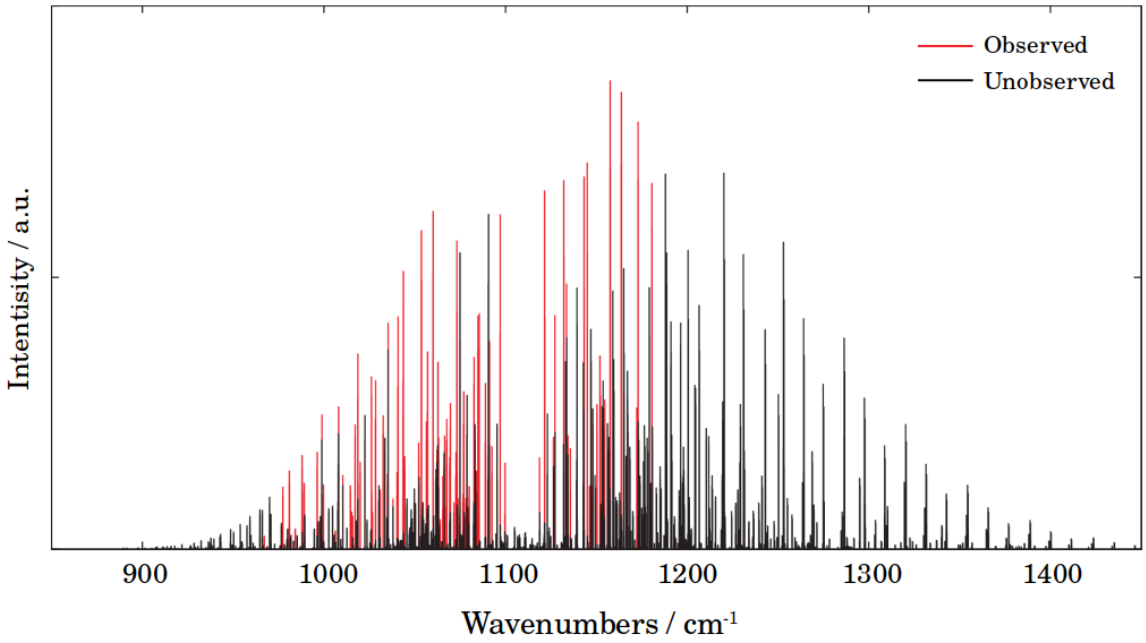

Figure 4.9: Simulation of the v_2 band of ND_2 at 298 K. Red and black sticks represent observed and unobserved transitions, respectively.

The ro-vibrational transition frequencies were added to the dataset described earlier and the analysis was performed fitting 16 additional parameters for the v_2=1 state. They include the vibrational energy E_2, the rotational constants and some centrifugal distortion terms up to the sixth-order, the electron spin-rotation constants and their main K^2 dependence (Δ_K^S). The results obtained for the excited state parameters are given in Table 4.24 and compared with the previous study [98].

Table 4.24: Spectroscopic parameters of ND_2 in the $v_2 = 1$ state.

Parameter	Unit	This Work	Previous LMR[a]
E_v	cm^{-1}	1108.74371(15)	1108.7493(7)
A	MHz	426754.4(24)	426755.2(63)
B	MHz	196398.07(62)	196430.9(33)
C	MHz	127046.26(33)	127035.0(42)
Δ_N	MHz	−8.4906(65)	−9.003(96)
Δ_{NK}	MHz	40.90(11)	−40.81(28)
Δ_K	MHz	−284.26(25)	−286.0(10)
δ_N	MHz	−3.4134(32)	−3.759(54)
δ_K	MHz	−16.182(85)	−16.998(57)
Φ_N	kHz	1.478[b]	
Φ_{NNK}	kHz	−11.1(17)	
Φ_{KKN}	kHz	−43.69[b]	
Φ_K	MHz	0.5546(67)	0.82(10)
ϕ_N	kHz	0.7223[b]	
ϕ_{NK}	kHz	−0.8382[b]	
ϕ_K	kHz	0.0584(96)	
ϵ_{aa}	MHz	−6187.4(55)	−6088(21)
ϵ_{bb}	MHz	−701.5(15)	−727.9(81)
ϵ_{cc}	MHz	5.01(90)	15[c]
Δ_N^S	MHz	0.0761[b]	
Δ_{KN+NK}^S	MHz	−0.9498[b]	
Δ_{NK}^S	MHz	1.046[b]	
Δ_K^S	MHz	15.01(32)	8.6(14)
δ_N^S	MHz	0.1006[b]	
δ_K^S	MHz	0.0384[b]	
No. of lines		191	
rms	cm^{-1}	5.0×10^{-4}	
σ		1.00	

Number in parenthesis are one standard deviation in units of the last quoted digit. **[a]** Ref. [98]. **[b]** Fixed to ground state value. **[c]** Fixed in their analysis.

The agreement between the two set of parameters is generally good but our precision is from 2 to 5 times higher. A further improvement can only be obtained by measuring pure rotational transitions within the $v_2 = 1$ state.

4.2.5 $^{15}ND_2$

The rotational spectrum of $^{15}ND_2$ radical has been investigated up to the THz region by means of the Bologna millimeter/submillimeter spectrometer (Section 3.1). The $^{15}ND_2$ radical was produced in the positive column of a DC glow discharge. Initially, a mixture of $^{15}N_2$ (5 mTorr), D_2 (1-2 mTorr) and Ar (15 mTorr) was used. These conditions are similar to those employed to produce the imidogen radical ^{15}ND (see Section 4.1.6). In fact, both molecules are produced but with different abundances, as shown in Fig. 4.10.

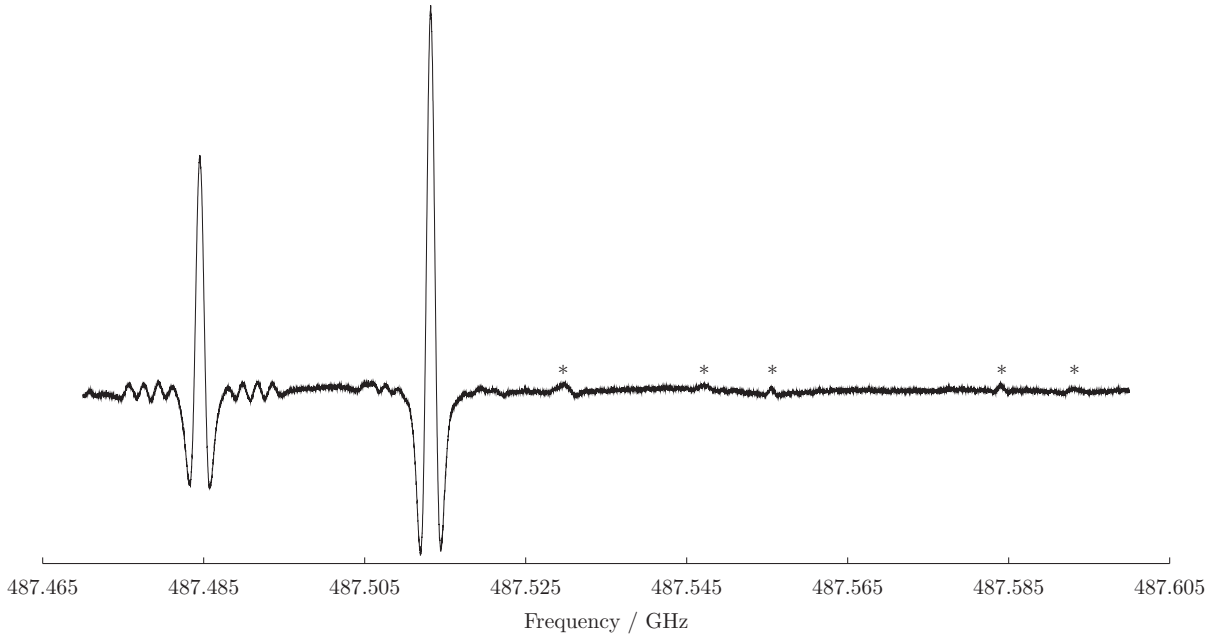

Figure 4.10: Observed spectrum of the $J = 7/2 \leftarrow 7/2$ component of the $3_{12} \leftarrow 3_{03}$ transition for $^{15}ND_2$. The asterisks mark the ^{15}ND lines.

Afterwards, $^{15}ND_3$ (5-7 mTorr) in argon (20 mTorr) as buffer gas was used as precursor, in agreement with Kanada *et al.* [100], which indeed proved to be the most efficient way to produce $^{15}ND_2$. The typical discharge conditions were given by a current of 70 mA and a voltage of about 1 kV. The absorption cell was cooled with liquid nitrogen at about 250 K, in order to avoid excessive overheating of the electrodes.

For the previously unstudied $^{15}ND_2$ species, we detected 354 transitions, corresponding to 180 different frequencies, in the range 264-1051 GHz with $0 \leq N \leq 5$, $0 \leq K_a \leq 3$ and $0 \leq K_c \leq 4$. The sample of observed transitions is graphically summarized in Figure 4.11, while the $1_{11} \leftarrow 0_{00}$ transition is shown as example in Figure 4.12.

Not all the components of a single $N'_{K'_a K'_c} \leftarrow N''_{K''_a K''_c}$ transition could be resolved. The unresolved lines were included in the fit with the same frequency and fitted as a single blended line with intensity-averaged components as performed by Pickett's program SPFIT [46]. The uncertainty associated to the experimental frequencies was chosen case-by-case and was either 50 or 100 kHz. Twenty nine parameters were determined from the fit and they include: the rotational

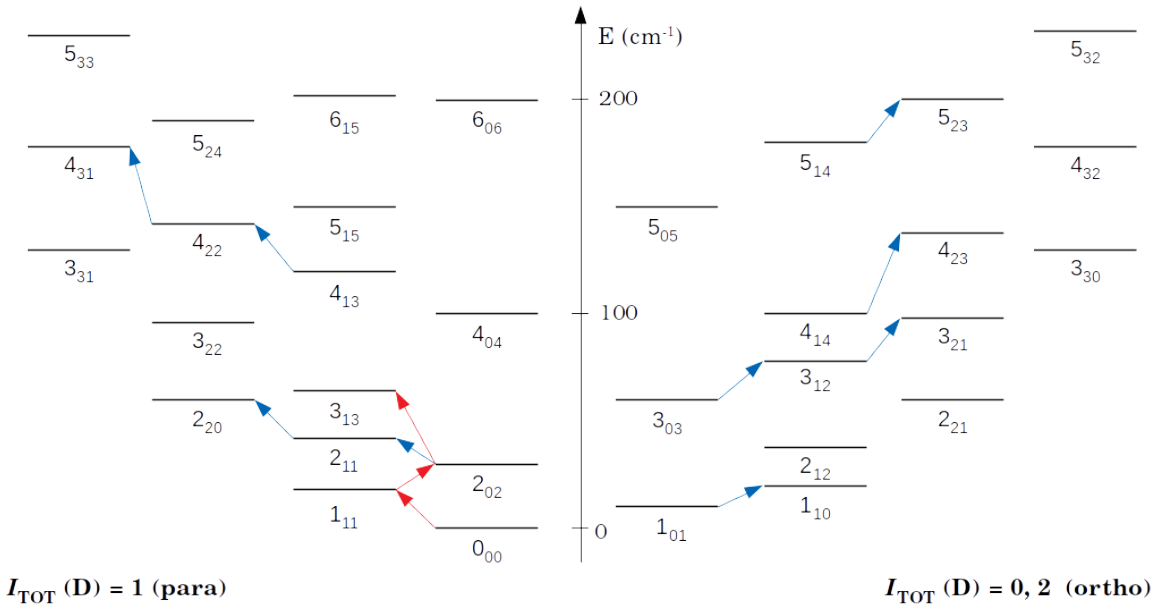

Figure 4.11: Schematic representation of rotational energy levels (without fine and hyperfine structures). Transitions recorded and analyzed in this work are marked by red (R type) and blue (Q type) arrows.

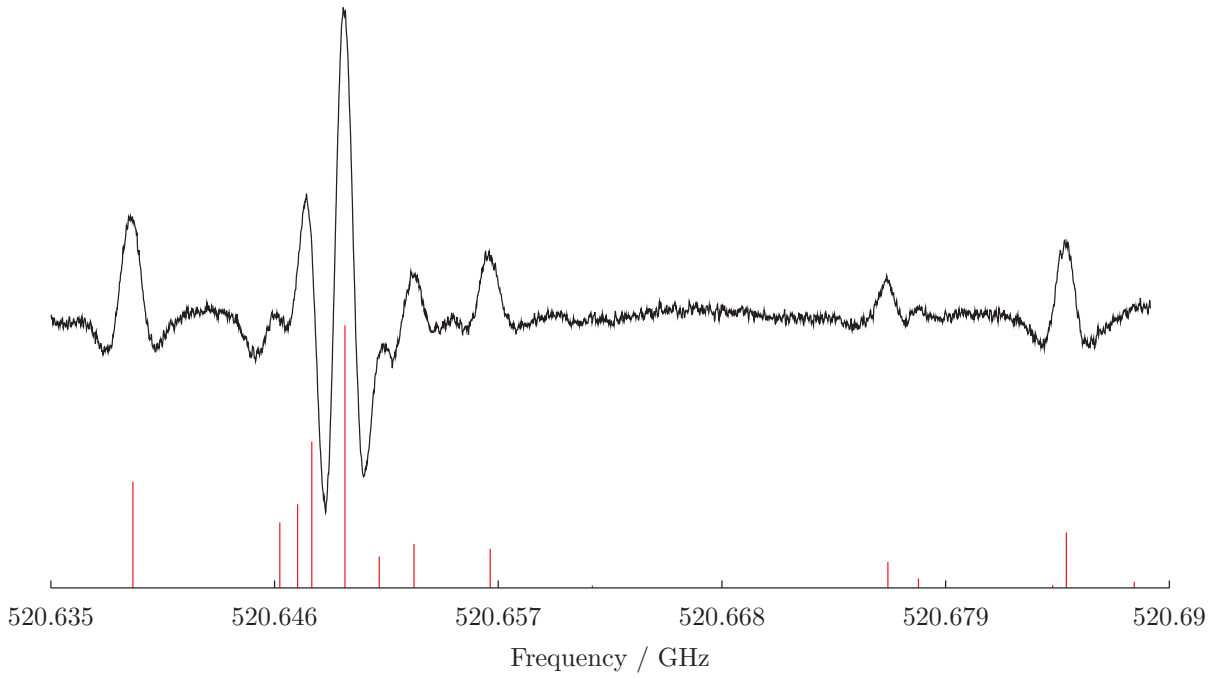

Figure 4.12: Observed spectrum of the J= 1.5←0.5 fine structure component of the 1_{11}←0_{00} transition for $^{15}ND_2$. The hyperfine components are indicated.

constants A, B, C; all the quartic centrifugal distortion constants; four sextic centrifugal distortion constants (Φ_{NK}, Φ_{KN}, Φ_K, ϕ_K); the electron spin-nuclear rotation constants (ϵ_{il}), their quar-

tic centrifugal distortion parameters and one sextic term (Φ_K^S); the electron spin-nuclear spin constants for nitrogen and deuterium [$a_F(^{15}\mathrm{N})$, $a_F(\mathrm{D})$, $T_{ii}(^{15}\mathrm{N})$, $T_{ii}(\mathrm{D})$]; the nuclear rotation-nuclear spin parameters for nitrogen [$C_{ii}(^{15}\mathrm{N})$]. The parameters from the final fit are collected in Tables 4.25–4.27.

Table 4.25: Rotational spectroscopic constants derived for $^{15}ND_2$.

Constant	Unit	Value
A	MHz	394064.890(10)
B	MHz	194501.561(84)
C	MHz	127983.466(94)
Δ_N	MHz	7.8519(14)
Δ_{NK}	MHz	−33.090(12)
Δ_K	MHz	193.165(20)
δ_N	MHz	3.08571(50)
δ_k	MHz	7.992(54)
Φ_N	kHz	1.471[a]
Φ_{NK}	kHz	−11.5(16)
Φ_{KN}	kHz	−28.2(48)
Φ_K	kHz	294.6(30)
ϕ_N	kHz	0.7199[a]
ϕ_{NK}	kHz	−0.8457[a]
ϕ_K	kHz	38.1(77)
No. of lines		180
σ		0.82
rms	kHz	56.1

Number in parenthesis are one standard deviation in units of the last quoted digit. **[a]** Kept fixed in the analysis. See text for details.

The centrifugal distortion and hyperfine constants reported in Tables 4.25–4.27 without error could not be refined and were held fixed in the fitting procedure. The fixed centrifugal distortion parameters were constrained to scaled values obtained from the corresponding literature parameters reported for $^{15}NH_2$ [94], $^{14}NH_2$ [53] and $^{14}ND_2$ (Section 4.2.4) according to the scaling scheme $p(^{15}ND_2) = p(^{14}ND_2)\times[p(^{15}NH_2)/p(^{14}NH_2)]$, where p is a general centrifugal distortion parameter. The same scaling procedure was accurate enough to be adopted to predict the initial constants to undertake the search, since no parameters were known.

The electron-spin centrifugal distortion term Δ_{NK}^S was fixed to the value obtained for ND_2 (Table 4.22), namely 1.05(20) MHz, and not scaled because the value reported in Ref. [94]

Table 4.26: Fine-structure spectroscopic constants derived for $^{15}ND_2$.

Constant	Unit	Value
ϵ_{aa}	MHz	−5051.019(24)
ϵ_{bb}	MHz	−668.643(21)
ϵ_{cc}	MHz	3.457(17)
Δ_N^S	MHz	0.0718(19)
Δ_{KN+NK}^S	MHz	−0.9187(65)
Δ_{NK}^S	MHz	1.05[a]
Δ_K^S	MHz	9.609(15)
δ_N^S	MHz	0.03942(59)
δ_K^S	MHz	0.0934(57)
Φ_K^S	kHz	−23.2(14)

Number in parenthesis are one standard deviation in units of the last quoted digit. **[a]** Kept fixed in the analysis. See text for details.

Table 4.27: Hyperfine-interaction spectroscopic constants derived for $^{15}ND_2$.

Constant	Atom	Unit	Value
a_F	(^{15}N)	MHz	−39.293(16)
T_{aa}	(^{15}N)	MHz	60.513(29)
T_{bb}	(^{15}N)	MHz	62.078(27)
C_{aa}	(^{15}N)	MHz	−0.375(14)
C_{bb}	(^{15}N)	MHz	−0.0659(80)
C_{cc}	(^{15}N)	MHz	−0.02034[a]
a_F	(D)	MHz	−10.2469(92)
T_{aa}	(D)	MHz	2.827(15)
T_{bb}	(D)	MHz	−2.065(19)

Number in parenthesis are one standard deviation in units of the last quoted digit. **[a]** Kept fixed in the analysis. See text for details.

for $^{15}NH_2$ [15.7(22) MHz] seems to be unreasonably different from both the values of $^{15}NH_2$ [0.950(85) MHz] [53] and ND_2. The $C_{cc}(^{15}N)$ constant could not be determined in the fit. Since the magnetic hyperfine parameters are directly proportional to the nuclear magnetic moment m and inversely proportional to the nuclear spin I, it was constrained to the value reported for ND_2 (Table 4.23) multiplied by $[m(^{15}N)/I(^{15}N)]/[m(^{14}N)/I(^{14}N)]$, namely -0.02034 MHz. The values

of the nuclear magnetic moments of ^{15}N and ^{14}N were taken from Ref. [104]. Also, the deuterium quadrupole constants could not be obtained from the fit. Indeed, the only literature value of χ_{bb} for ND_2 [100] was not determined [0.01(20) MHz]. The electron spin resonance (e.s.r.) spectrum of $^{15}ND_2$ in matrix has been recorded in 1970 by Smith & Seddon [105]. The authors reported the values of the isotropic hyperfine parameters A_D and $A_{^{15}N}$, 3.9 and 21.3 G respectively, as determined from their analysis. Such values, after conversion from Gauss to MHz, are calculated to be A_D= −11.0 MHz and $A_{^{15}N}$=−59.8 MHz. The first term is in excellent agreement with our value for a_F(D), −10.2469(92) MHz, while the second one is fairly different from our $a_F(^{15}N)$=−39.293(16) MHz. This partial agreement is due to the intrinsic differences between our gas−phase spectra and a condensed phase e.s.r. experiment, which strongly depends on the matrix, as pointed out by Smith & Seddon [105].
The overall quality of our fit is very satisfactory and the *rms* error is 57 kHz. Because of the fewer number of observed transitions, the set of determined parameters is less extended than that of $^{14}ND_2$, where 41 constants, including octic centrifugal distortion terms, were obtained from the analysis. It is however a fairly complete set of spectroscopic constants from which highly accurate predictions of unobserved rotational transitions can be calculated.

4.2.6 Outlook

Among the isotopologues of the amidogen radical, only the doubly substituted ^{15}NHD remains to be investigated.

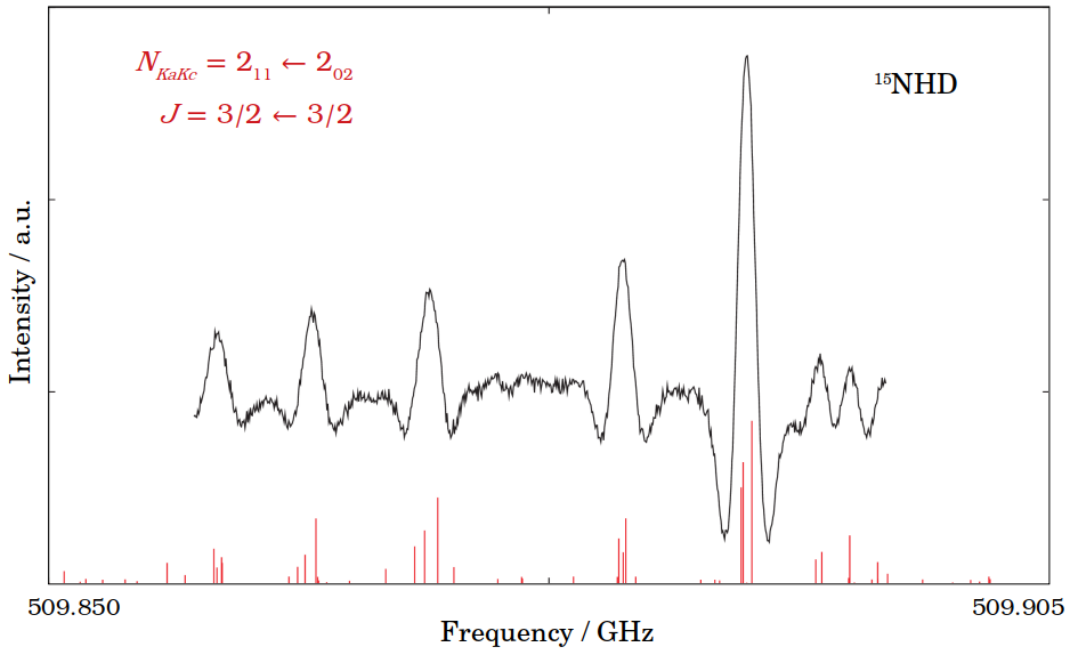

Figure 4.13: Experimental (black trace) and simulated (red sticks) spectrum of ^{15}NHD, as observed while DC discharging $^{15}ND_3$ with H_2 in Ar as buffer gas.

Few transitions of its rotational spectrum have been already detected (see Fig. 4.13) and are

currently being analysed. The remaining transitions in the operating frequency range of our spectrometer will be observed and the analysis finalized.

Meanwhile, a standard proposal at SOLEIL synchrotron whose aim is to record the FIR spectrum of ^{15}NHD has been accepted and scheduled for November 2019, 25th to 29th. In that experiment, the pure rotational spectrum of ^{15}NHD will be recorded for the first time between 50 and 300 cm^{-1} with an accuracy better than 1×10^{-4} cm^{-1}. As already demonstrated for $^{14}NH_2$, ^{14}NHD, and $^{15}NH_2$, the analysis of the observed transitions will enable an extended centrifugal study of this species. A further paper will be produced pertaining the pure rotational spectrum of ^{15}NHD and submitted to the *Physical Chemistry Chemical Physics* journal. Eventually, the semi-experimental equilibrium structure will be evaluated for the amidogen radical.

4.3 Deuterated cyanoacetylene

During the first months of PhD activity I was involved in the measurements of the rotational spectrum of HC_3N, a project which was close to its final stage and conducted by Dr. L. Bizzocchi and Dr. F. Tamassia. That work has been published within my first year of PhD school:

- L. Bizzocchi, F. Tamassia, J. Laas, B. M. Giuliano, C. Degli Esposti, L. Dore, M. Melosso, *et al.*, "Rotational and high-resolution infrared spectrum of HC_3N: Global ro-vibrational analysis and improved line catalog for astrophysical observations," *Astrophys. J. Suppl. S.*, vol. 233, issue 1, no. 11 (20pp), 2017 [125].

After the study of the main isotopologue of cyanoacetylene, we decided to study its deuterated version DC_3N, a species of astrophysical interest and for which the spectroscopic knowledge could be remarkably improved. This project started in my second year and is where I have put a lot of effort into. My contribution to this work can be summarized as follow:

- conceptualization and literature/data searches;
- measurements of all the infrared spectra and about half of the millimeter/submillimeter spectra;
- data assignment and analysis, with the generous help of Dr. Filippo Tamassia;
- manuscripts writing (ongoing);

4.3.1 Introduction

Cyanoacetylene (HC_3N, also known as propynenitrile) is the simplest member of the family of cyanopolyynes, i.e., linear molecules with general chemical formula $HC_{2n+1}N$. This compounds are chemically stable under certain conditions only, e.g., in the solid state at low temperature or in the gas-phase at low pressure. Since these conditions are both satisfied in Space, and because of their high degree of insaturation, cyanopolyynes are widespread in the interstellar medium. Indeed, the presence of several carbon-chain molecules is among the most characteristic features of the chemical composition of starless cores [3]; the Taurus Molecular Cloud (TMC-1), for instance, is one of the brightest source of carbon-chain species. Cyanoacetylene was found to be an abundant species in a variety of astronomical object: in starless cores [106], post-AGB objects [107], carbon-rich circumstellar envelopes [108], massive star-forming regions [109], protoplanetary disks [110], and solar-type protostars [111]. Moreover, its recent detection in comets has highlighted its astrobiological potential [112].
The deuterated form of cyanoacetylene DC_3N has been detected in the ISM as well. As pointed out in Section 4.1.1, deuterium fractionation (or D/H ratio) is very useful to understand the

scenario of the origin and evolution of planetary systems [74]. The first astronomical observation of DC_3N has been reported towards TMC-1 [113] by the detection of emission from its $J = 5 \rightarrow 4$ rotational transition around 42 GHz. Successively, DC_3N has tentatively been detected in the high-mass star-forming regions Orion KL [114] and Sagittarius B2 [115]. In these regions, deuterium fractionation is not as effective as in dark clouds, thus preventing a strong enhancement above the deuterium cosmic abundance. Very recently, DC_3N has been detected for the first time in the solar-type protostar IRAS 16293–2422 [111]. In the latter case, the cyanoacetylene deuteration reaches 50% in the outer and cold envelope, but is lower (5%) in the warm inner region. All these detections relied on laboratory spectroscopic studies reported earlier.

Microwave transitions of DC_3N were firstly reported for the ground and four lowest singly-excited states [116], during the course of an extensive study of cyanoacetylene isotopologues. A large number of vibrational excited states was re-examined in depth some years later [117] and a rigorous determination of the effective molecular parameters attained. Lately, the laboratory investigation of the rotational spectrum of DC_3N has been extended to the THz regime for the ground and the $v_7 = 1$ states [118]. In the same paper, the authors revised the ^{14}N and D hyperfine structure derived in Refs. [119, 120] using a supersonic-jet Fourier-Transform Microwave (FT-MW) spectrometer.

As far as its infrared spectrum is concerned, position and intensity of all fundamentals (besides the weak ν_4 mode) has been determined in low resolution (0.5 cm^{-1}) IR studies [121, 122]. Some combination and overtone bands were also observed in the same work. Two medium resolution (0.025-0.050 cm^{-1}) infrared studies were performed by Mallinson & Fayt [123] and Coveliers *et al.* [124]. In the former, the band center of the three stretching modes of DC_3N (namely ν_1,ν_2, and ν_3) has been determined; in the latter, the FIR spectrum was recorded between 200 and 365 cm^{-1} and the ν_7 fundamental analyzed together with three forbidden bands ($\nu_6 \leftarrow \nu_7$, $\nu_5 \leftarrow \nu_7$, and $\nu_4 \leftarrow \nu_6$) and their hot-bands.

It has to be pointed out that an accurate evaluation of molecular column densities from astrophysical observations depends, among other quantities, on the value of the partition function $U(T)$. Because in hot regions the value of $U(T)$ can be affected by low-lying vibrational excited states, it is fundamental to have an accurate knowledge of the energy of ro-vibrational levels. Such detailed analysis has been reported for HC_3N [125] and its ^{15}N-isotopologue [126] only.

In this thesis, a detailed investigation of the infrared and submillimeter-wave spectra of DC_3N is reported. Pure rotational transitions of all the vibrational states with energy lower than 1015 cm^{-1} have been detected and 14 fundamental, overtone, combination, and hot ro-vibrational bands have been analysed.

4.3.2 Experiment

The DC_3N sample was kindly synthesized by Dr. J.C. Guillemin following the procedure described in Ref. [122]. Briefly, propiolic acid ($HC{\equiv}CCOOH$) was added dropwise to a cold solution of sulfuric acid (H_2SO_4) and absolute methanol (CH_3OH) and the reaction mixture was stirred for four days. After that period, a saturated solution of $NaHCO_3$ was added to the reaction mixture. The obtained ester ($HC{\equiv}CCOOCH_3$) was extracted from the organic phase and vacuum distilled from the acid. In the second step, the ester was added dropwise to liquid ammonia and is 100% converted in $HC{\equiv}CCONH_2$. Successively, the propiolic amide was mixed along with phosphorous anhydride (P_2O_5) and calcinated white sand; the whole system was heated up to 225°C over 2 h and connected to a liquid nitrogen-cooled trap. Once cyanoacetylene had been synthesized and collected into the trap, it was added to a mixture of heavy water (D_2O) and potassium carbonate (K_2CO_3) in inert atmosphere. The biphasic mixture was then stirred for about 20 min.

Subsequently, *d*-cyanoacetylene was condensed in a 77 K cooled trap, while water was condensed in a 220 K trap. The operation was repeated 3 times by addition of D_2O and K_2CO_3 to the condensed *d*-cyanoacetylene. Residual D_2O was removed by addition of phosphorous pentoxide (P_4O_{10}) and DC_3N condensed in a trap cooled at 150 K. *d*-cyanoacetylene can be indefinitely stored at -25°C without decomposing. The synthesis process can be summarized as follow:

$$HCCCOOH + CH_3OH \longrightarrow HCCCOOCH_3 + H_2O \tag{4.32}$$

$$HCCCOOCH_3 + NH_3 \longrightarrow HCCCONH_2 + CH_3OH \tag{4.33}$$

$$HCCCONH_2 \xrightarrow{P_2O_5} HCCCN \tag{4.34}$$

$$HCCCN \xrightarrow{D_2O} DCCCN \tag{4.35}$$

Rotational spectra of DC_3N have been recorded with the Bologna submillimeter-wave spectrometer (Sec. 3.1) and with the CASAC spectrometer (Sec. 3.2). The former was used in the region 240–400 GHz with a single-pass configuration. Depending on the vibrational states to be observed, the DC_3N vapor was injected in the cell at a pressure between 0.5 and 15 bar. A 48 kHz modulation frequency f was used to record spectra in the $2f$ scheme. The CASAC spectrometer was used in the region around 90 GHz and at frequency above 400 GHz. Four broad scans ($\sim$ 2.5 GHz) of four consecutive transitions ($J = 9 - 12$) were initially performed to facilitate the assignment of each excited state. Afterwards, transitions were recorded at higher frequencies line-by-line.

The infrared spectra in the 450–1600 cm^{-1} range were recorded in Bologna using the Bomem DA3.002 Fourier-Transform spectrometer described in Section 3.4. It was equipped with a Globar source, a KBr beam splitter, and a liquid N_2-cooled HgCdTe detector. A multi-pass cell with different absorption base-lengths from 4 m to 8 m was employed for the measurements. Sample

pressures ranging between 0.25 and 6 mbar were used to record the spectra. The resolution was generally 0.004 cm^{-1}, except for the very weak ν_4 band, which was recorded at a lower resolution of 0.012 cm^{-1}. Several hundreds of scans, typically 800, were co-added in order to improve the S/N of the spectra. The absolute calibration of the wavenumber axis was attained by referencing ro-vibrational transitions of H_2O and CO_2.

4.3.3 Theory

From a spectroscopic point of view, DC_3N is a closed-shell ($^1\Sigma$) linear rotor. It has 7 vibrational modes, 3 of which are doubly-degenerated bending (E symmetry). The other 4 are stretching modes (A symmetry). They are summarized in Table 4.28.

Table 4.28: Vibrational modes of DC_3N.

Modes	Description	Energy (cm^{-1})	Abs. intensity ($amt^{-1}cm^{-2}$)
ν_1	C−D stretc.	2608.520(3)[a]	81.3 ± 5.7[b]
ν_2	C≡C stretc.	2252.155(3)[a]	50.5 ± 2.4[b]
ν_3	C≡N stretc.	1968.329(3)[a]	38.7 ± 4.0[b]
ν_4	C−C stretc.	**867.63(7)**[c]	< 0.1[d]
ν_5	CCD bend.	**522.26378(2)**[c]	83.8 ± 4.7[b]
ν_6	CCC bend.	**492.74876(2)**[c]	106. ± 8[b]
ν_7	CCN bend.	**211.54950(4)**[c]	0.89 ± 0.11[d]

[a] Ref. [123]. **[b]** From low-resolution integrated band-intensity measurements at 296 K (Ref. [122]). **[c]** PhD work. **[d]** From low-resolution integrated band-intensity measurements at 293 K (Ref. [121]).

For my PhD thesis, I have decided to focus on the low-lying vibrational states for two main reasons: (i) only the states with low energy are of astrophysical interest and (ii) the states above our threshold of 1015 cm^{-1} are involved in the several resonances, while the states below that threshold are either unperturbed or belong to a small polyad of resonant levels. Therefore, the stretching modes ν_1, ν_2, and ν_3, lying above this threshold, have not been investigated. A given vibrational state can be unequivocally labeled using the notation $(v_4, v_5^{l_5}, v_6^{l_6}, v_7^{l_7})_{e/f}$, where l_t quantum numbers label the vibrational angular momentum associated to each bending mode t and the e/f subscripts indicate the parity of the symmetrized wave functions [127]. The ro-vibrational wave-functions can be symbolized with the ket $\left|v_4, v_5^{l_5}, v_6^{l_6}, v_7^{l_7}; J, k\right\rangle_{e/f}$. The vibrational part of the wave-function is expressed as a one- or two-dimensional harmonic oscillator, whereas the rotational part is the symmetric-top wave-function whose quantum number k must follow $k = l_5 + l_6 + l_7$. The following Wang-type linear combinations [128] lead to symmetry-

adapted basis functions:

$$\left|v_4, v_5^{l_5}\ , v_6^{l_6}, v_7^{l_7}; J, k\right\rangle_{e/f} = \frac{1}{\sqrt{2}}\left\{\left|v_4, v_5^{l_5}, v_6^{l_6}, v_7^{l_7}; J, k\right\rangle \pm (-1)^k \left|v_4, v_5^{-l_5}, v_6^{-l_6}, v_7^{-l_7}; J, -k\right\rangle\right\}\ , \quad (4.36a)$$

$$\left|v_4, 0^0\ , 0^0, 0^0; J, 0\right\rangle_e = \left|v_4, 0^0, 0^0, 0^0; J, 0\right\rangle\ . \quad (4.36b)$$

The upper and lower signs ($\pm$) correspond to e and f wave-functions, respectively. For Σ states ($k = 0$), the first non-zero l_t is chosen positive. The omission of the e/f label indicates unsymmetrised wave-functions.

The Hamiltonian used to reproduce the ro-vibrational energy levels is:

$$\mathscr{H} = \mathscr{H}_{\mathrm{rv}} + \mathscr{H}_{l-\mathrm{type}} + \mathscr{H}_{\mathrm{res}}\ , \quad (4.37)$$

where $\mathscr{H}_{\mathrm{rv}}$ is the ro-vibrational energy including centrifugal distortion corrections, $\mathscr{H}_{l-\mathrm{type}}$ represents the l-type interaction between the l sub-levels of excited bending states, and $\mathscr{H}_{\mathrm{res}}$ accounts for resonances among accidentally quasi-degenerate ro-vibrational states.

The Hamiltonian matrix is built by using unsymmetrised ro-vibrational functions. It is subsequently factorized and symmetrized using Eqs. (4.36). The matrix elements of the effective Hamiltonian are expressed using the formalism already employed for the analysis of HC_3N [125]. Here, the following shorthand will be used:

$$f_0(J, k) = J(J+1) - k^2\ , \quad (4.38a)$$

$$f_{\pm n}(J, k) = \prod_{p=1}^{n} J(J+1) - [k \pm (p-1)](k \pm p)\ . \quad (4.38b)$$

The $\tilde{H}_{\mathrm{vibrot}}$ term of the Hamiltonian is purely diagonal in all the quantum numbers. It has the form:

$$\begin{aligned}\langle l_5, l_6, l_7; k|\, \mathscr{H}_{\mathrm{rv}}\, |l_5, l_6, l_7; k\rangle &= G_v + \sum_t x_{L(tt)} l_t^2 + \sum_{t\neq t'} x_{L(tt')} l_t l_{t'} \\ &+ \left\{B_v + \sum_t d_{JL(tt)} l_t^2 + \sum_{t\neq t'} d_{JL(tt')} l_t l_{t'}\right\} f_0(J,k) - D_v f_0(J,k)^2 + H_v f_0(J,k)^3 + L_v f_0(J,k)^4\ . \quad (4.39)\end{aligned}$$

The $\mathscr{H}_{l-\mathrm{type}}$ Hamiltonian is diagonal in v, but it has off-diagonal matrix elements in the quantum numbers l_t and with $\Delta k = 0, \pm 2, \pm 4$. The vibrational l-type doubling terms with $\Delta k = 0$ have the general formula

$$\begin{aligned}\langle l_t \pm 2, l_{t'} \mp 2; k|\, \mathscr{H}_{l-\mathrm{type}}\, |l_t, l_{t'}; k\rangle &= {}^1\!/_4 \left\{r_{tt'} + r_{tt'J} J(J+1)\right\} \\ &\times \sqrt{(v_t \mp l_t)(v_t \pm l_t + 2)(v_{t'} \mp l_{t'} + 2)(v_{t'} \pm l_{t'})}\ . \quad (4.40)\end{aligned}$$

The rotational l-type resonance terms with $\Delta k = \pm 2$ are given by

$$\langle l_t \pm 2; k \pm 2 | \mathscr{H}_{l-\text{type}} | l_t; k \rangle = {}^1\!/_4 \left\{ q_t + q_{tJ} J(J+1) + q_{tJJ} J^2 (J+1)^2 \right\} \times \sqrt{(v_t \mp l_t)(v_t \pm l_t + 2)}\, \sqrt{f_{\pm 2}(J,k)}\,, \quad (4.41)$$

The terms with $\Delta k = \pm 4$ are

$$\langle l_t \pm 4; k \pm 4 | \mathscr{H}_{l-\text{type}} | l_t; k \rangle = {}^1\!/_4 u_{tt} \{ (v_t \mp l_t)(v_t \pm l_t + 2)(v_t \mp l_t - 2)(v_t \pm l_t + 4) \}^{1/2} \sqrt{f_{\pm 4}(J,k)}\,, \quad (4.42)$$

$$\langle l_t \pm 2, l_{t'} \pm 2; k \pm 4 | \mathscr{H}_{l-\text{type}} | l_t, l_{t'}; k \rangle = {}^1\!/_4 u_{tt'} \{ (v_{t'} \mp l_{t'})(v_{t'} \pm l_{t'} + 2) (v_t \mp l_t)(v_t \pm l_t + 2) \}^{1/2} \sqrt{f_{\pm 4}(J,k)}\,. \quad (4.43)$$

The terms of the effective Hamiltonian for the ro-vibrational resonances can be written as

$$\mathscr{H}_{\text{res}} = \sum_{m,n} C_{mn} \hat{\mathscr{L}}^m \hat{J}^n\,, \quad (4.44)$$

where C_{mn} is the resonance coefficient, m the total degree in the vibrational ladder operators $\hat{\mathscr{L}}^{\pm}$, and n the total degree in the rotational angular momentum operators $\hat{J}$ [129, 130]. See Ref. [125] for the matrix elements of the resonance Hamiltonian $\mathscr{H}_{\text{res}}$.

4.3.4 Infrared spectrum

Although the infrared spectra were recorded in the 450–1600 cm^{-1} frequency range, our analysis was limited to the portion of the electromagnetic spectrum below $\sim$ 1040 cm^{-1}, because of the reasons explained in §4.3.6. The highest energy state within our threshold of 1015 cm^{-1} is the $|0110\rangle$ state, whose combination band falls in the region 999-1035 cm^{-1}. In total, 14 fundamental, overtone, combination, and hot-bands have been observed for the first time at high resolution and successfully analysed. They are listed in Table 4.29 along with the observed sub-bands, frequency, J ranges, number of data used in the analysis, and the *rms* error from the final fit.

A general overview of the spectrum between 450 and 800 cm^{-1} is shown in Figure 4.14.

The MIR region is dominated by the very strong fundamentals ν_6 and ν_5. This region is particularly crowded due to the proximity of the two fundamentals, the presence of their associated hot-bands, and of the ν_6 fundamental band of HC_3N (see Fig. 4.15).

Having a medium IR intensity, the combination bands $\nu_6 + \nu_7$ and $\nu_5 + \nu_7$ are well visible in the right-part of the spectrum as seen in Fig. 4.14. The overtone $2\nu_6$ and the combination $\nu_5 + \nu_6$ bands are centered around 975-1018 cm^{-1} and 999-1035 cm^{-1}, respectively, and are clearly detectable as well, despite the presence of strong absorption lines due to HDO. The very weak

Table 4.29: Ro-vibrational bands recorded and analysed in this work.

Band	Sub-bands	Freq. range (cm^{-1})	J range	No. of lines	$rms \times 10^4$ (cm^{-1})
ν_6	$\Pi - \Sigma^+$	466-522	2-109	267	3.3
$\nu_6 + \nu_7 \leftarrow \nu_7$	$(\Sigma^\pm, \Delta) - \Pi$	478-508	5-56	329	6.7
$\nu_6 + 2\nu_7 \leftarrow 2\nu_7$	$\Pi - (\Sigma^+, \Delta)$	476-512	12-65	93	3.5
$2\nu_6 \leftarrow \nu_6$	$\Sigma^\pm - \Pi$	500-519	10-68	43	7.1
ν_5	$\Pi - \Sigma^+$	500-557	0-117	255	3.3
$\nu_5 + \nu_7 \leftarrow \nu_7$	$(\Sigma^+, \Delta) - \Pi$	505-545	2-75	464	4.4
$\nu_5 + 2\nu_7 \leftarrow 2\nu_7$	$\Pi - (\Sigma^\pm, \Delta)$	505-542	2-82	106	5.3
$\nu_6 + \nu_7$	$\Sigma^+ - \Sigma^+$	686-736	1-89	166	2.5
$\nu_6 + 2\nu_7 \leftarrow \nu_7$	$\Pi - \Pi$	690-718	4-53	153	4.7
$\nu_5 + \nu_7$	$\Sigma^+ - \Sigma^+$	715-769	1-105	170	3.0
$\nu_5 + 2\nu_7 \leftarrow \nu_7$	$\Pi - \Pi$	721-748	2-45	296	4.1
ν_4	$\Sigma^+ - \Sigma^+$	830-865	0-61	109	9.6
$2\nu_6$	$\Sigma^+ - \Sigma^+$	975-1018	2-101	141	5.2
$\nu_5 + \nu_6$	$\Sigma^+ - \Sigma^+$	999-1035	3-63	102	3.8

(< 0.1 atm^{-1} cm^{-2}) ν_4 fundamental at 830-865 cm^{-1} had to be recorded at higher pressure (4 mbar) and lower resolution (0.012 cm^{-1}). In this case, up to 2600 scans were co-added to improve the S/N of the spectrum (Fig. 4.16).

4.3.5 Rotational spectrum

Rotational spectra were recorded for all the 14 states whose vibrational energy do not exceed our threshold of 1015 cm^{-1}. Literature data were available for some of these states, as already pointed out in Section 4.3.1. However, line positions of some millimeter-wave transitions from Ref. [116] are affected by large uncertainties (up to 300 kHz) and many data are limited to low frequencies. For these reasons, we decided to re-investigate and extend the spectrum all these vibrational states. The biggest improvements have been realized for the interacting states $|1000\rangle$, $|0110\rangle$, $|0020\rangle$, and $|0004\rangle$, for which extended data-sets were obtained. Remarkably, the $v_5 = v_6 = 1$ state has first been observed in this study and it was not included in the analysis of the resonant system of Ref. [117].

Table 4.30 summarizes the body of rotational data used in the analysis, specifying the observed sub-levels, J and frequency ranges, number of distinct fitted frequencies, the *rms* error from the final fit, and the corresponding references used.

Rotational lines of all states but the $v_4 = 1$ lie at frequencies higher than that of the corresponding ground state transition. This can be seen in Figure 4.17, where the long scan covers the

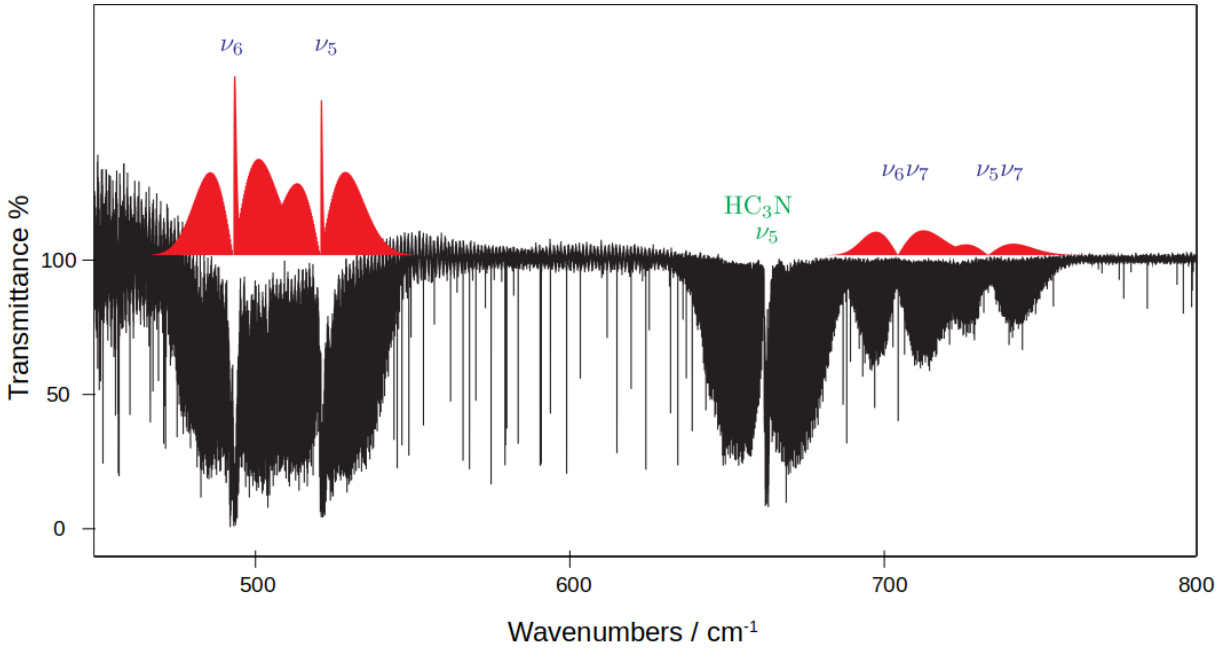

Figure 4.14: Survey of the infrared spectrum of *d*-cyanoacetylene recorded up to 800 cm^{-1}. The spectrum results from the co-addition of 800 scans and was recorded at 0.004 cm^{-1} resolution using an absorption path of 8 m, an iris diameter of 1 mm, with DC_3N at a pressure of 0.6 mbar. The strong ν_5 and ν_6 fundamental show a prominent Q branch (saturated in the spectrum) characteristic of $\Pi - \Sigma^+$ band, which is absent in the $\nu_6\nu_7$ and $\nu_5\nu_7$ bands ($\Sigma^+ - \Sigma^+$ symmetry). Strong absorption lines of water and fringes due to imperfect baseline-removal are clearly observable around 600 cm^{-1}. A simulated spectrum (red) of the most intense bands is also reported.

$J = 13 \leftarrow 12$ transitions for all the vibrational satellites. In this excerpt, the *l*-type resonance patterns of all the excited bending states analysed are visible. From a visual inspection, it is easy to associate some of these patterns to the pertaining state: the ground and $v_4 = 1$ exhibit a single line, while each bending state has $\sum_t = (l_t + 1)$ lines (even though not always resolved).

4.3.6 Analysis

The sample of pure rotational and ro-vibrational data contains more than 3600 distinct frequencies for 14 vibrational states. In particular, all the ro-vibrational MIR frequencies have been observed for the first time. On the other hand, rotational transitions had previously been observed but they have been extended well into the submillimeter-wave region in this work. Moreover, transitions with J up to 126 were recorded at THz frequencies (1.069 THz) for the ground state. The composition and general features of the data-sets are summarized in Tables 4.29 and 4.30. In the global fit, a different weight was given to each datum in order to take into account the different measurement precision. Uncertainties spanning from 0.0004 to 0.00075 cm^{-1} were used for the infrared measurements (4×10^{-4} cm^{-1} for most transitions, around 7×10^{-4} cm^{-1} for the weaker ones); the weak ν_4 band being the only exception with $\sigma = 0.001$ cm^{-1}. As

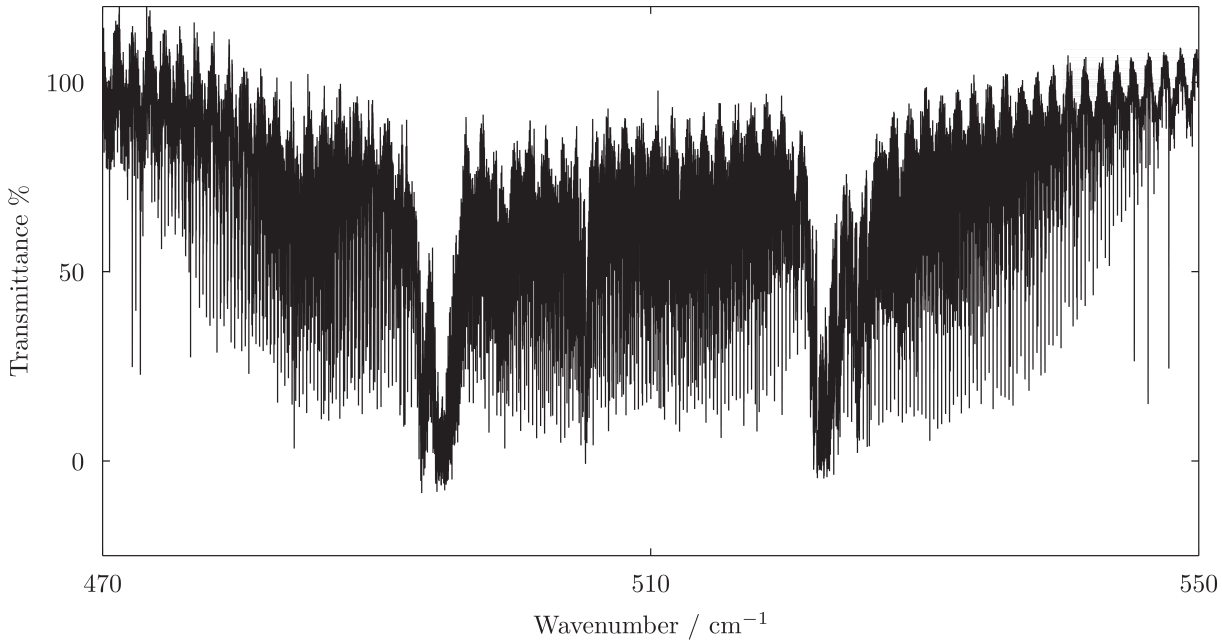

Figure 4.15: Portion of the infrared spectrum of DC_3N around 500 cm^{-1}, where the strong fundamentals ν_5 and ν_6 are located. The experimental conditions are the same of Fig. 4.14 except for the lower pressure of DC_3N (0.25 mbar) employed to reduce line saturation.

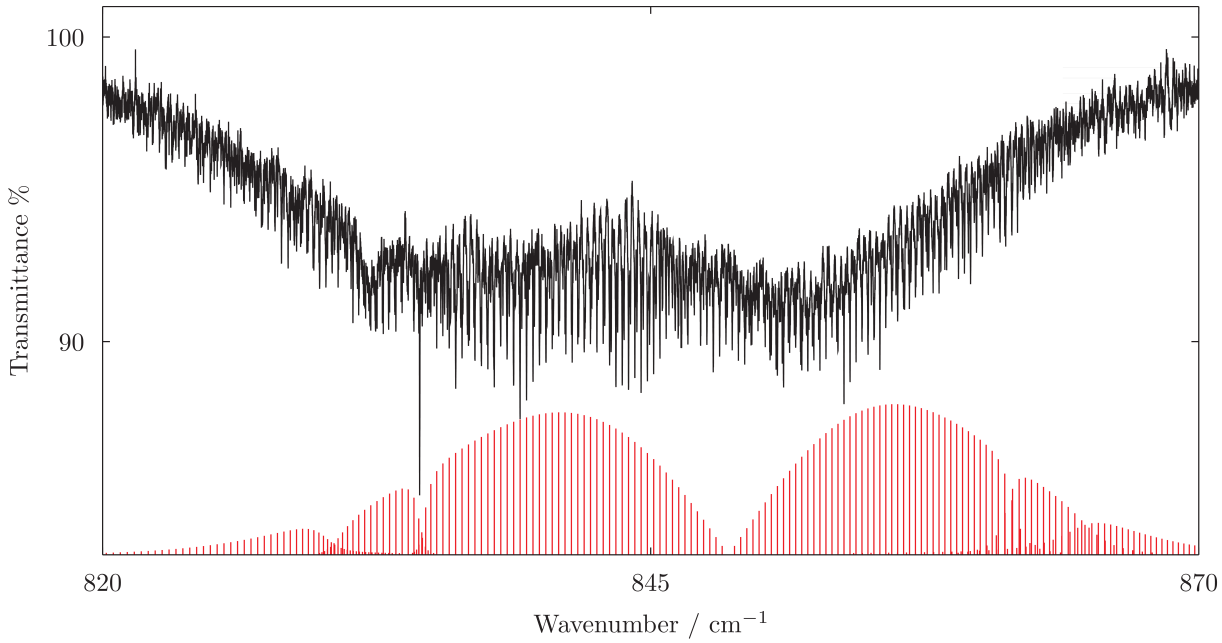

Figure 4.16: Zoom (50 cm^{-1} window) on the ν_4 stretching mode. The weakness of this band required a compromise in term of spectral resolution (nominally 0.012 cm^{-1}). A simulation of the band obtained with the final spectroscopic parameters is given in red. Being a $\Sigma^+ - \Sigma^+$ band, only the P and R branches are present.

far as pure rotational lines are concerned, we assumed a typical experimental error of 10 – 20 kHz for our new millimeter/submillimeter measurements: generally 10 kHz for transitions

Table 4.30: Summary of the rotational data used in the global analysis.

State	$\|k\|$	J range	Freq. range (GHz)	No. of lines	*rms* (kHz)	Reference
Ground state	0	3-126	33-1069	52	13.2	TW, Ma78, Pl88, Sp08
$v_7 = 1$	$1_{e,f}$	5-105	50-896	67	10.9	TW, Ma78, Pl88, Sp08
$v_6 = 1$	$1_{e,f}$	7-44	67-381	42	15.5	TW, Pl88
$v_5 = 1$	$1_{e,f}$	7-44	67-381	42	14.7	TW, Pl88
$v_4 = 1$	0	7-51	67-439	32	19.3	TW, Pl88
$v_7 = 2$	$0, 2_{e,f}$	7-44	67-383	61	21.1	TW, Ma78, Pl88
$v_7 = 3$	$(1, 3)_{e,f}$	7-44	68-384	77	18.8	TW, Ma78, Pl88
$v_7 = 4$	$0,(2, 4)_{e,f}$	7-48	68-419	85	25.5	TW, Pl88
$v_6 = 2$	$0, 2_{e,f}$	7-44	67-382	54	44.7	TW, Pl88
$v_6 = v_7 = 1$	$(0, 2)_{e,f}$	7-44	67-382	93	30.8	TW, Ma78, Pl88
$v_5 = v_7 = 1$	$(0, 2)_{e,f}$	7-44	67-382	78	20.8	TW, Pl88
$v_5 = v_6 = 1$	$(0, 2)_{e,f}$	9-44	84-381	63	15.7	TW
$v_6 = 1, v_7 = 2$	$(\pm1, 3)_{e,f}$	7-46	68-400	95	21.9	TW, Pl88
$v_5 = 1, v_7 = 2$	$(\pm1, 3)_{e,f}$	9-44	85-383	97	17.1	TW
interstate		44-49	364-429	10	16.3	TW

Abbreviations are used as follow: **TW** This work, **Ma78** Mallinson & De Zafra (1978) [116], **Pl88** Plummer *et al.* (1988) [117], **Sp08** Spahn *et al.* (2008) [118].

around 100 GHz, 20 kHz for those recorded at higher frequencies (above 240 GHz). Data from literature were used with the uncertainty stated in the original papers [116, 117, 118]. Only few lines from Ref. [116], whose residuals were far off their errors, were not used in our fit. The list of discarded transitions include most of the lines measured around 127 GHz ($J = 15 \leftarrow 14$) and few others above 200 GHz ($J = 25 \leftarrow 24$).

The spectral analysis was performed using a custom PYTHON code that employs the SPFIT program [46] as computational core (see Ref. [125] for details). The data were fitted to the Hamiltonian presented in Section 4.3.3 and its coefficients optimized in an iterative least-squares procedure. Some spectroscopic parameters could not be determined from the available experimental data. In these cases, the constant of a given vibrational level were derived from the corresponding optimized values obtained for other levels belonging to the same vibrational manifold considering, whenever feasible, a linear v dependence. In other cases, they were simply fixed to zero. The spectroscopic parameters obtained from the global fit procedure are collected in Tables 4.31-4.34.

As pointed out before, most of the states could be analysed as isolated states. Four of the fourteen investigated states, instead, showed anomalous effects due to the existence of accidental

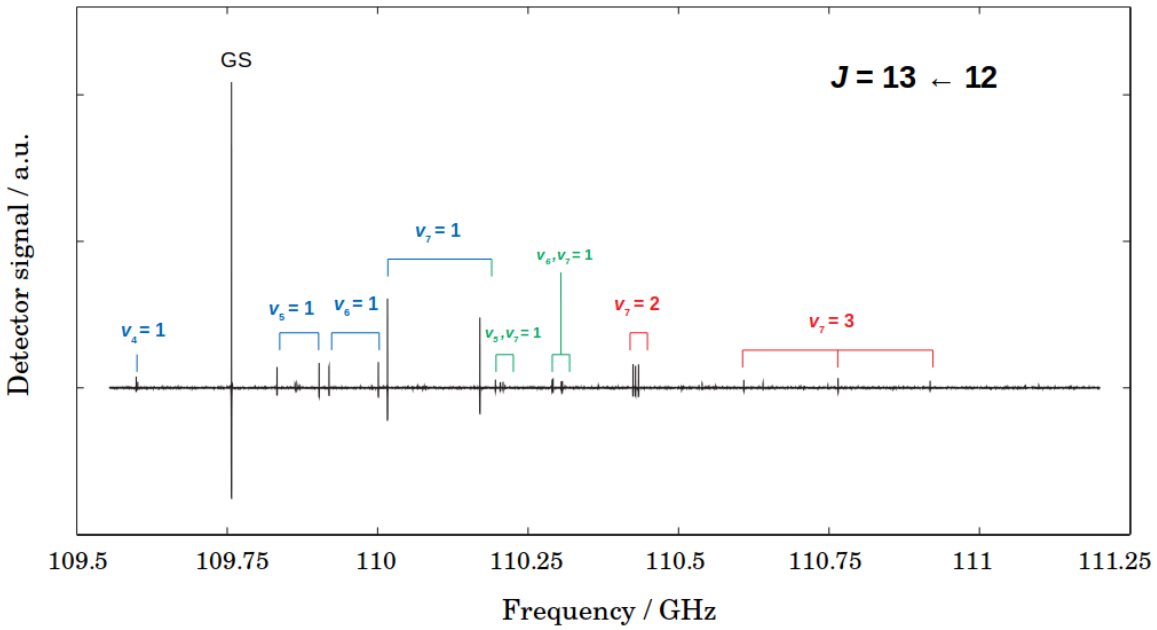

Figure 4.17: 2 GHz long scan of the $J = 13 \leftarrow 12$ rotational transition of DC_3N around 110 GHz. The spectrum was recorded at room temperature, with DC_3N at a pressure of 0.5 bar, RC= 3 ms, frequency step 50 kHz, FM = 120 kHz, one sweep back and forth.

Table 4.31: Spectroscopic constants derived for DC_3N in the ground and $v_4 = 1$ states.

Constant	Unit	Ground state	$v_4 = 1$
G_v	cm^{-1}	0.0	867.634(67)
B_v	MHz	4221.580842(34)	4212.262(14)
D_v	kHz	0.4517842(81)	0.45364(11)
H_v	mHz	0.03944(71)	0.03944[a]
L_v	nHz	−0.154(20)	−0.154[a]

Number in parenthesis are one standard deviation in units of the last quoted digit. [a] Kept fixed to ground state value.

resonances. They are the $v_4 = 1$, $v_5 = v_6 = 1$, $v_6 = 2$, and $v_7 = 4$ states. The vibrational energies in this polyad lie in the window 867–1014 cm^{-1} and have a molecular symmetry which allow anharmonic interactions. The resonance system is similar to that observed for HC_3N [125], the only difference is that the $v_5 = v_7 = 1$ in HC_3N is replaced in the polyad by $v_5 = v_6 = 1$ in DC_3N. Indeed, the most prominent difference between the HC_3N energy levels and DC_3N one's is seen for the v_5 mode, which correspond to the H−C≡C/D−C≡C bendings. As expected, replacing the hydrogen atom with the heavier deuterium drastically decreases the frequency of the v_5 fundamental, from 663.368484(31) [125] to 522.263782(24) cm^{-1}.

For the states involved in this resonance system, we have a lot of experimental information. In

Table 4.32: Spectroscopic constants derived for DC_3N in singly-excited bending states.

Constant	Unit	$v_7 = 1$	$v_6 = 1$	$v_5 = 1$
G_v	cm^{-1}	211.549497(41)	492.748755(23)	522.263782(24)
$\chi_{L_{(tt)}}$	GHz	19.5438[a]	56.74[a]	...
B_v	MHz	4234.519473(30)	4229.25389(12)	4225.835798(93)
D_v	kHz	0.4718873(56)	0.462040(54)	0.452452(29)
H_v	mHz	0.08244(28)	0.0764(62)	0.03944[b]
L_v	nHz	−0.154[b]	−0.154[b]	−0.154[b]
$d_{JL_{(tt)}}$	kHz	−9.975[a]	139.4[a]	...
q_t	MHz	5.907887(59)	3.15097(21)	2.68907(19)
q_{tJ}	Hz	−13.653(11)	−1.585(65)	−1.714(58)
q_{tJJ}	uHz	43.63(56)	...	...

Number in parenthesis are one standard deviation in units of the last quoted digit. [a] Constrained value, see text in Sec. 4.3.6. [b] Kept fixed to ground state value.

Table 4.33: Spectroscopic constants derived for DC_3N in overtone states.

Constant	Unit	$v_7 = 2$	$v_7 = 3$	$v_7 = 4$	$v_6 = 2$
G_v	cm^{-1}	422.375591(58)	632.03369[a]	841.98380(23)	982.979(70)
$\chi_{L_{(tt)}}$	GHz	19.390(27)	19.1978(18)	19.0635(16)	56.73(52)
B_v	MHz	4247.45269(16)	4260.38130(15)	4273.30515(11)	4236.566(14)
D_v	kHz	0.491989(38)	0.512506(34)	0.533370(30)	0.471989(55)
H_v	mHz	0.03944[b]	0.03944[b]	0.03944[b]	0.03944[b]
L_v	nHz	−0.154[b]	−0.154[b]	−0.154[b]	−0.154[b]
$d_{JL_{(tt)}}$	kHz	−10.427(42)	−10.953(22)	−11.3672(49)	139.5(35)
q_t	MHz	5.9391(50)	5.95864(14)	5.98665(34)	3.15097[a]
q_{tJ}	Hz	−13.856[a]	−14.061(46)	−14.674(54)	−1.584[a]
q_{tJJ}	uHz	43.63[a]	43.63[a]	43.63[a]	...

Number in parenthesis are one standard deviation in units of the last quoted digit. [a] Constrained value, see text in Sec. 4.3.6. [b] Kept fixed to ground state value.

the MIR, we recorded the ν_4, $\nu_5 + \nu_6$, and $2\nu_6$ bands that provide the energy position of the interacting levels. The energy of the $v_7 = 4$ was indirectly determined through the resonance effects.

A large pure rotational data-set is also available for all four states. Besides rotational transitions observed within the vibrational states, a small set of interstate transitions between the $v_4 = 1$ and $v_7 = 4$ states were observed, which helped in constraining the energy of the latter state. The spectroscopic constants determined for the four interacting states are reported in Tables 4.31-

Table 4.34: Spectroscopic constants derived for DC_3N in combination states.

Constant	Unit	$v_6 = v_7 = 1$	$v_5 = v_7 = 1$	$v_5 = v_6 = 1$	$v_6 = 1, v_7 = 2$	$v_5 = 1, v_7 = 2$
G_v	cm^{-1}	703.842905(48)	734.057843(39)	1014.2834(10)	914.19996(21)	945.143878(53)
$\chi_{L_{(aa)}}$	GHz	56.74[a]	...	...	56.74[a]	...
$\chi_{L_{(bb)}}$	GHz	19.3346[a]	19.5438[a]	56.74[a]	19.1254(78)	19.3144(14)
$\chi_{L_{(ab)}}$	GHz	16.16642(54)	23.13192(59)	40.232(30)	16.2848(51)	23.0219(27)
$r_{(ab)}$	GHz	−17.04693(96)	0.31890(81)	−63.474(60)	−16.6532(73)	0.87061(30)
$r_{(abJ)}$	kHz	−5.791(70)	−65.955(69)	...	−11.9(11)	−64.11(10)
B_v	MHz	4242.276259(91)	4238.741858(100)	4233.55786(15)	4255.3007(18)	4251.64459(16)
D_v	kHz	0.481883(30)	0.472613(32)	0.463445(36)	0.502238(33)	0.492994(29)
H_v	mHz	0.03944[b]	0.03944[b]	0.03944[b]	0.03944[b]	0.03944[b]
L_v	nHz	−0.154[b]	−0.154[b]	−0.154[b]	−0.154[b]	−0.154[b]
$d_{JL_{(aa)}}$	kHz	−11.229[a]	...	...	139.4[a]	...
$d_{JL_{(bb)}}$	kHz	139.4[a]	−9.975[a]	139.4[a]	−12.48(68)	−10.480(49)
$d_{JL_{(ab)}}$	kHz	43.51(13)	−5.09(12)	80.31(26)	43.71(42)	−6.810(41)
q_a	MHz	3.17876(20)	2.70698(31)	2.69110(28)	3.19096(18)	2.72679(14)
q_{aJ}	Hz	−1.584[a]	−1.714[a]	−1.714[a]	−1.584[a]	−1.714[a]
q_b	MHz	5.94488(22)	5.90991(74)	3.15097[a]	5.9489(15)	5.93174(21)
q_{bJ}	Hz	−13.653[a]	−13.88(12)	−1.584[a]	−14.14(30)	−13.653[a]
q_{bJJ}	uHz	43.63[a]	43.63[a]	...	43.63[a]	43.63[a]
u_{ab}	Hz	...	...	−1.629(66)	...	...

Number in parenthesis are one standard deviation in units of the last quoted digit. [a] Constrained value, see text in Sec. 4.3.6. [b] Kept fixed to ground state value.

4.34, while the coefficients C_{mn} of the resonance Hamiltonian are given in Table 4.35.

Table 4.35: Resonance parameters.

Interacting states	Parameter	Unit	Value
$(v_4 = 1) - (v_6 = 2)$	C_{30}	cm^{-1}	17.438(29)
$(v_4 = 1) - (v_5 = v_6 = 1)$	C_{30}	cm^{-1}	−6.521(12)
$(v_4 = 1) - (v_7 = 4)$	C_{50}	GHz	2.69759(70)
	C^J_{50}	kHz	11.86(13)

Number in parenthesis are one standard deviation in units of the last quoted digit.

Regrettably, vibrational energies could be determined for all states but the $v_7 = 3$, for which no ro-vibrational bands have been observed in this work. Indeed, its energy could only be determined from the observation of a hot-band starting from this state. However the $v_7 = 3$ level, *ca.* 632 cm^{-1} above the ground state, is not populated enough and the line density in the spectrum is too high to confidently assign such hot-bands. The highest chance to clearly observe an infrared feature involving this state is to record the ν_7 band system at FIR frequencies (~ 210 cm^{-1}) exploiting the bright synchrotron radiation. Recently, we have recorded the ν_7 band of the parent isotopologue HC_3N and, although the analysis is still ongoing, we detected transitions arising from the $2\nu_7 \leftarrow \nu_7$, $3\nu_7 \leftarrow 2\nu_7$, $4\nu_7 \leftarrow 3\nu_7$, and $5\nu_7 \leftarrow 4\nu_7$ hot-bands. Presumably, we expect the same for DC_3N.

4.3.7 Outlook

In this thesis, a large set of high-resolution rotational and ro-vibrational data of DC_3N has been analysed. The aim of this work was to have a detailed knowledge of all the vibrational states whose energy does not exceed a fixed threshold of 1015 cm^{-1}.

To achieve the goal, infrared spectra of DC_3N have been recorded in the range 450–1600 cm^{-1} at high resolution (0.004 cm^{-1}). In this frequency region, 14 of fundamental, overtone, combination, and hot-bands have been observed and analysed. Notably, the weak ν_4 fundamental has also been detected, even if at lower resolution (0.012 cm^{-1}). Rotational transitions of fourteen states have also been recorded to extend the spectrum well into the submillimeter-wave region (up to *ca.* 500 GHz).

More than 3600 experimental transitions were included in a least-squares fit procedure from which a large number of spectroscopic parameters have been determined for 14 different vibrational states. The whole set of data has been fitted with an overall weighted standard deviation σ_w of 0.85, meaning that all data are reproduced well within their given uncertainties. Vibrational energies have been derived for all states with the exception of the $v_7 = 3$, for which the energy G_v has been extrapolated from those of the $|0001\rangle$, $|0002\rangle$, and $|0004\rangle$. Combining both

high-resolution IR data and pure rotational measurements, we obtained a complete and accurate modeling of the spectrum of DC_3N, including perturbations produced by the anharmonic resonances in the energy manifold. Remarkably, the interaction between $v_4 = 1$ and $v_5 = v_6 = 1$ states has been recognized for the first time, solving the residual disagreements encountered in Refs. [117, 124].
The results from this work have two major outcomes:

- the determination of a large number of spectroscopic parameters for DC_3N, together with the literature data available for all the other isotopologues, poses a strong bases for deriving an experimental anharmonic force fields of HC_3N;

- the improved set of molecular data presented provides a guidance for the searches of DC_3N in extraterrestrial environments and may help to retrieve accurate quantitative information from the astrophysical observations.

As far as the latter point is concerned, Belloche *et al.* recently reported the first results from a new spectral survey (ReMoCA) towards Sagittarius B2 [131], with higher angular resolution and sensitivity than those previously achieved [115]. As stated in the introduction (Section 4.3.1), DC_3N was only tentatively detected in the EMoCA survey, because of some overlaps with other molecular lines. However, with ReMoCA it should be possible to clearly identify emissions arising from DC_3N in the ground state and possibly from low-lying excited states. Finally, the values of the partition function $U(T)$ have been revised, as shown in Table 4.36

Table 4.36: Value of the ro-vibrational partition function $U(T)$ of DC_3N calculated at different temperatures.

Temperature (K)	G.S. only[a]	All states[b]
300	1481.5213	4733.4792
225	1111.1362	2314.4780
150	740.8099	1009.6729
75	370.5424	383.5728
37.5	185.4308	185.5385
18.75	92.8808	92.8808
9.375	46.6077	46.6077

[a] From the Cologne Database for Molecular Spectroscopy. **[b]** This work

As obvious, the discrepancy is emphasized at high temperature, while the match is perfect at temperatures below 50 K (i.e. no vibrational excited state is populated). However, since HC_3N has been detected in Sagittarius B2 with a T_{rot} of *ca.* 200 K, the variation of the partition function

at this temperature is important. Indeed, the newly determined value of $U(225\,\mathrm{K})$ is more than two times larger than that obtained considering the ground vibrational state only.
I am currently writing a paper reporting all the contents of this chapter, that will be submitted to the *Journal of Quantitative Spectroscopy and Radiative Transfer*.

4.4 Titanium nitride

During the 6 months I have been in Kassel in 2018, I used most of the time the SuJeSTA experiment. The sample of species studied with the SuJeSTA spectrometer includes the ^{18}O-isotopologue of iron monoxide (FeO), disilicon carbide (Si_2C), silicon dicarbide (SiC_2), and titanium nitride (TiN). Among them, only the latter falls in the "family" of nitrogen containing species and this is why I have chosen to report its case study. However, the project is still ongoing. Here, some preliminary results are reported along with a perspective on future plans.
In this study, I have worked on (i) the optimization of the yield of TiN produced in the laser ablation system and (ii) spectral prediction, recording and analyses of different isotopologues of titanium nitride.

4.4.1 Introduction

Titanium (Ti) is the ninth-most abundant element in Earth's crust and the lightest transition metal [1]. On Earth, Ti is composed of five stable isotopes, namely ^{46}Ti (8.25%), ^{47}Ti (7.44%), ^{48}Ti (73.72%), ^{49}Ti (5.41%), and ^{50}Ti (5.18%). However, much more radioisotopes have been discovered and characterized; the most stable of them is ^{44}Ti with an half-life of 60 years.
In astronomy, titanium oxides (TiO and TiO_2) are found to be very important constituents of different objects. Titatium(II) oxide (TiO), which gives strong electronic bands in oxygen-rich late-type stars, has recently been detected in the atmosphere of the hot-Jupiter planet WASP-19b [132], and, lately, it has been observed towards the cooler region of the red supergiant VY Canis Majoris [133]. In the latter work, titanium(IV) dioxide (TiO_2) has been detected for the first time.
The radioisotope ^{44}Ti is of astronomical interest, particularly to understand processes that take place in core-collapse supernovae, where it is thought to be produced in high quantity. In principle, the age of supernovae may be determined through measurements of γ-ray emissions from ^{44}Ti and its abundance.
Titanium nitride (TiN) may be present in metal-rich circumstellar envelopes as well. Consequently, an extensive laboratory work would be helpful to aid its astronomical identification.
The first laboratory observation of TiN was accomplished in the visible region thanks to a shock tube experiment [134]; the vibrational and rotational structure were recognized but not resolved, due to the limited spectral resolution. Successively, the electronic band $\Pi \rightarrow X^2\Sigma$ was recorded in the red and the rotational pattern of TiN analysed for the first time [135]. This work was followed by similar studies [136, 137] in the same spectral region. The first pure rotational transition of titanium nitride was observed in a microwave-optical double resonance spectroscopic study during the 1990 [138]. They recorded the $N = 2 \leftarrow 1$ transition of TiN, which was produced in a microwave discharge of a mixture composed by titanocene dichloride ($Ti(C_5H_5)_2Cl_2$) and nitrogen (N_2). An improved set of spectroscopic parameters for the ground

[1] IUPAC definition does not include scandium among the transition metals, although Sc is in the 3*d* group.

state of titanium nitride was determined from the MODR experiment, but the hyperfine structure due to the nitrogen was not resolved. Later on, the hyperfine interactions in the spectrum of TiN has been investigated for the main and for the ^{47}Ti-isotopologue [139]. Lastly, the pure rotational spectrum of ^{48}TiN has been investigated in a wide frequency range by Namiki *et al.* [140]. They used a submillimeter-wave spectrometer equipped with a DC discharge system: TiN was produced in the same way of Ref. [138] and its spectrum recorded up to 450 GHz.
Here we report the first observation in a supersonic jet of the submillimeter spectrum of titanium nitride. An alternative production method to those used in the literature, based on a laser ablation system, is presented together with the first study of the rotational spectra of ^{46}TiN and ^{50}TiN.

4.4.2 Experimental details

High-resolution millimeter and submillimeter-wave absorption spectra of TiN radical in its ground electronic state ($X^2\Sigma^+$) have been recorded using the Supersonic Jet Spectrometer for Terahertz Applications (SuJeSTA) described in Section 3.3.
Titanium nitride was produced by a laser ablation system. The 1064 nm Q-switched Nd:YAG laser beam at 30 Hz repetition rate was focused onto a rotating titanium rod (99.6% purity, Goodfellow). The ablated material was seeded in a pulsed gas flow of a 5–20% NH_3 in helium as buffer gas mixture. The production of TiN was found to be little sensitive to the concentration of ammonia, so that a mixture containing 10% of NH_3 was typically used. Also, the room temperature stagnation pressure of the gases could be adjusted between 2 and 5 bar without affecting the yield of TiN. After the injecting valve, before reaching the titanium rod, the gas mixture undergoes an adiabatic pre-cooling to below 100 K. During a few sec, the ablated titanium can react with the gas mixture in a 0.1 cm^3 reaction channel at a few hundred mbar pressure before adiabatically expanding into a vacuum chamber where a supersonic jet is observed (see Refs. [141, 142] for more details). The TiN radical formed in the adiabatically cooled jet interacts with a millimeter-wavelength radiation beam 20 mm down-stream from the nozzle exit, where it has a rotational temperature of a few tens K. A multi-pass optics (12 paths Herriott type) perpendicular to the jet propagation is used to enhance the absorption. Radiations between 250 and 340 GHz were used to record the spectra. The signals detected by the liquid-He cooled InSb hot-electron bolometer were recorded during 100 sec. A 0.1 MHz step was typically used to scan over spectral ranges of some MHz, to record individual rotational lines of TiN. To increase the signal-to-noise ratio, the signal at each frequency position was averaged over 8 laser-shots. The accuracy of measured line center positions is 10 kHz with typical line widths of 0.6 MHz.

4.4.3 Theory

Titanium nitride is a diatomic free radical with a $X^2\Sigma^+$ ground electronic state. Its rotational spectrum shows a fine structure due to the magnetic coupling of the molecular rotation with the

unpaired electron.
The coupling scheme of angular momenta in TiN is appropriately described by a Hund's case (*b*) [37]:

$$\mathbf{J} = \mathbf{N} + \mathbf{S}\,, \tag{4.45}$$

as seen in the case of NH.
Here, the electronic spin angular momentum **S** assumes the value of one half. The two fine-structure levels J generated from each rotational level N are those with $J = N + \frac{1}{2}, N - \frac{1}{2}$. For $N = 0$, only the $J = \frac{1}{2}$ component exists.
Inclusion of nitrogen and titanium (only for isotopes with odd mass number) hyperfine interactions leads to the couplings:

$$\mathbf{F}_1 = \mathbf{J} + \mathbf{I}_\mathrm{N}\,, \qquad \mathbf{F} = \mathbf{F}_1 + \mathbf{I}_\mathrm{Ti}\,. \tag{4.46}$$

where $I_\mathrm{N} = 1$ and $I_\mathrm{Ti} = 5/2$ or $7/2$ for ^{47}Ti and ^{49}Ti, respectively.
For a particular isotopologue in the ground vibronic state, the effective Hamiltonian can be written as:

$$\mathscr{H} = \mathscr{H}_\mathrm{rv} + \mathscr{H}_\mathrm{fs} + \mathscr{H}_\mathrm{hfs} \tag{4.47}$$

with

$$\mathscr{H}_\mathrm{rv} = B\mathbf{N}^2 - D\mathbf{N}^4 + H\mathbf{N}^6 + \ldots\,, \tag{4.48}$$

$$\mathscr{H}_\mathrm{fs} = \left(\lambda + \lambda_N\mathbf{N}^2 + \ldots\right)(\mathbf{N}\cdot\mathbf{S})\,, \tag{4.49}$$

$$\begin{aligned}\mathscr{H}_\mathrm{hfs} = &\sum_i b_F(i)\,\mathbf{I}_i\cdot\mathbf{S} + \sum_i c(i)\left(I_{iz}S_z - \frac{1}{3}\mathbf{I}_i\cdot\mathbf{S}\right)\\ &+ \sum_i eQq(i)\,\frac{(3I_{iz}^2 - \mathbf{I}_i^2)}{4I_i(2I_i-1)} + \sum_i C_I(i)\,\mathbf{I}_i\cdot\mathbf{N}\,.\end{aligned} \tag{4.50}$$

The Dunham-type expansion introduced in Section 4.1.2 can be analogously applied to TiN.

4.4.4 Analysis and results

Rotational spectra of three isotopologues of TiN – namely ^{46}TiN, ^{48}TiN, and ^{50}TiN – were recorded in the frequency region 250–340 GHz. Three different rotational transitions $N' \leftarrow N$ (for each isotopologue) are lying in this frequency range. In the supersonic expansion, the rotational temperature is estimated to be around 20 K, meaning that intensity of the transitions observed at these frequencies is decreasing sharply. However, due to the shape and size of optical elements, the SuJeSTA experiment gives its best performance around 300 GHz and it hardly goes to lower frequencies. Nonetheless, this compromise allowed the observation of three different isotopologues (see Figs. 4.18–4.20) but not that of ^{47}TiN and ^{49}TiN; an explanation for this failure will be given later.
The rotational spectrum of the parent species ^{48}TiN was already known with good accuracy, so

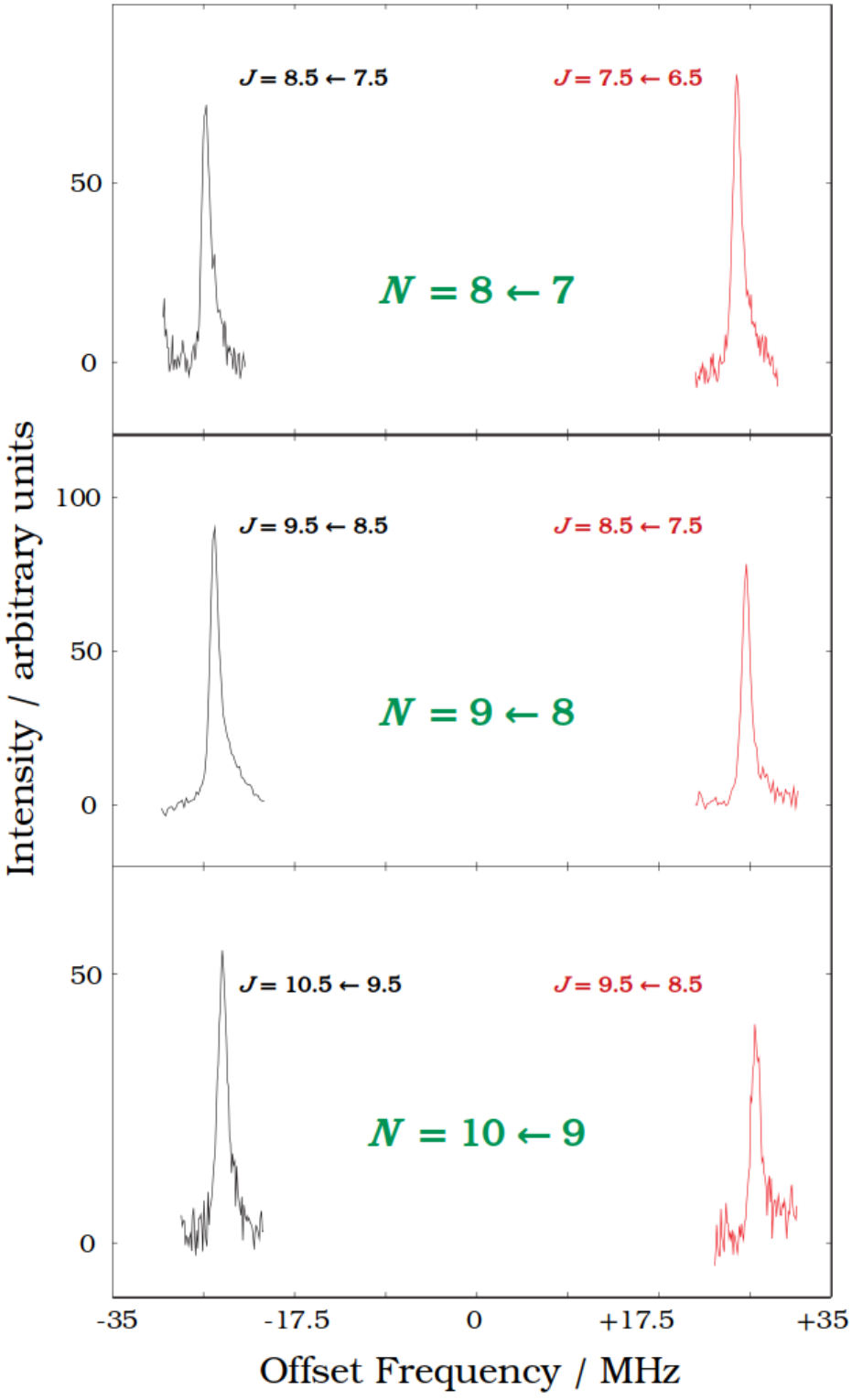

Figure 4.18: Observed transitions for ^{48}TiN. Line positions are given as offset frequency from 260215 (*top*), 297375 (*middle*), and 334530 (*bottom*) MHz.

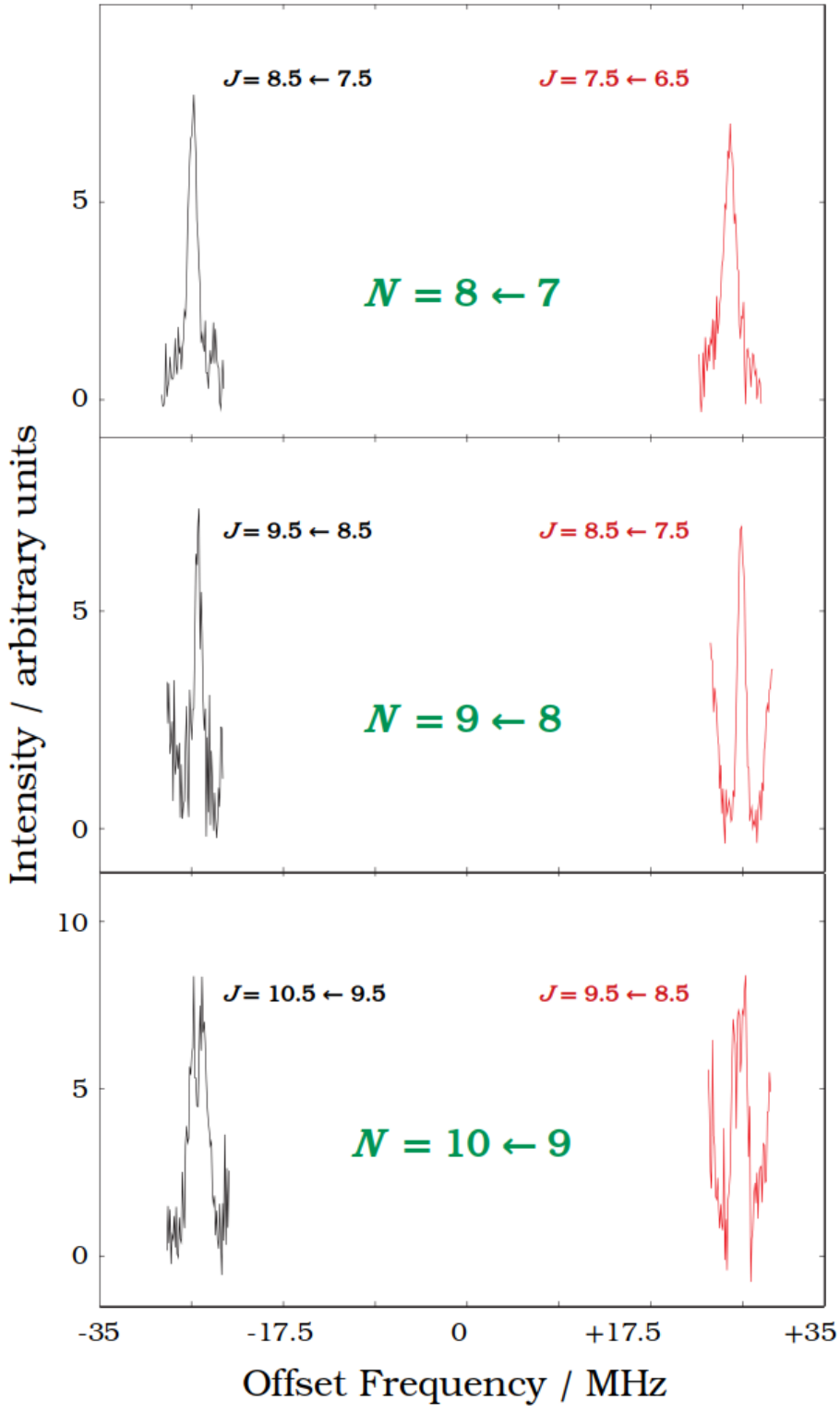

Figure 4.19: Observed transitions for ^{46}TiN. Line positions are given as offset frequency from 262758 (*top*), 300287 (*middle*), and 337807 (*bottom*) MHz.

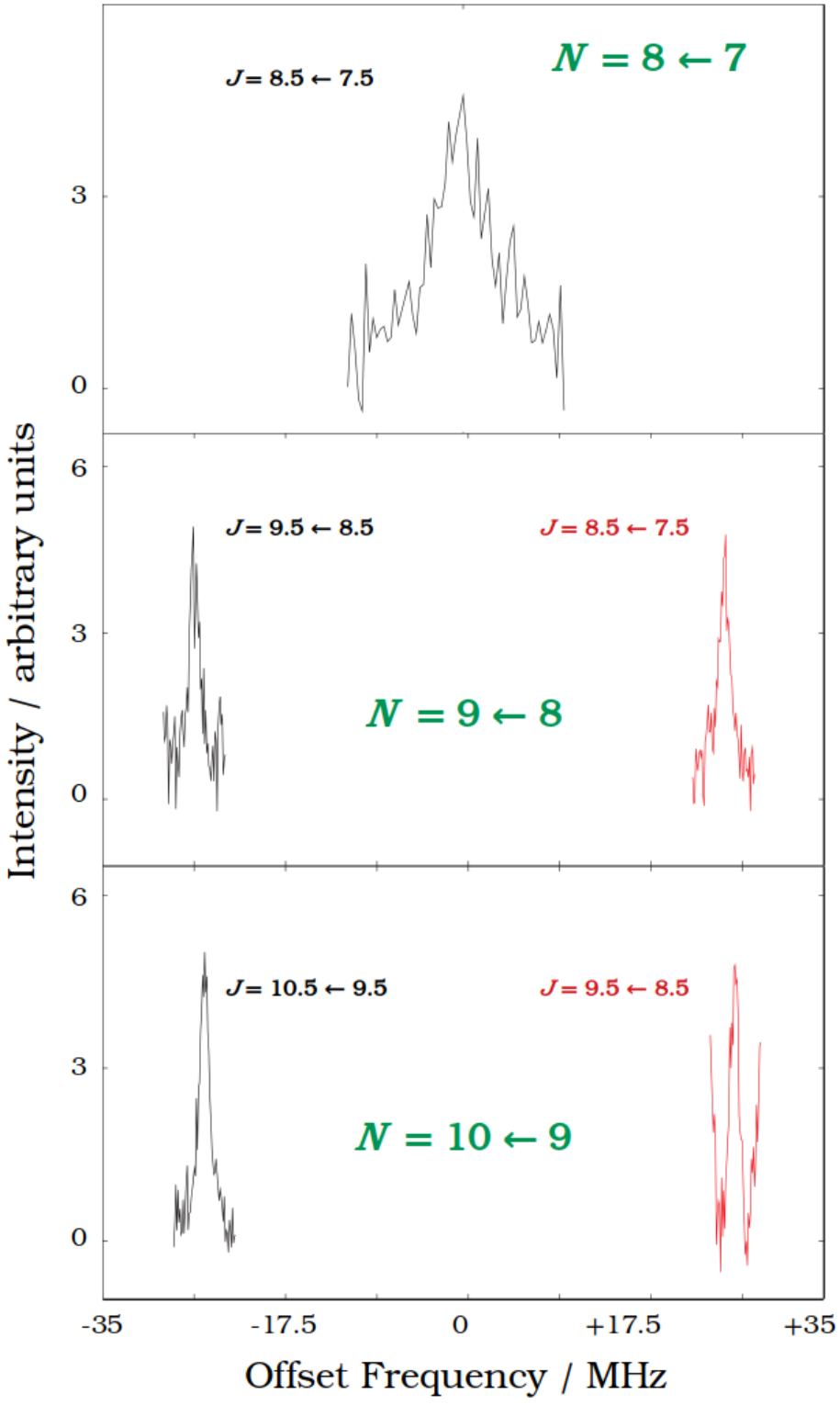

Figure 4.20: Observed transitions for ^{50}TiN. Line positions are given as offset frequency from 257892 (*top*), 294695 (*middle*), and 331515 (*bottom*) MHz. The x axis on the top panel is just 16 MHz instead of 70 MHz.

the spectroscopic parameters from Ref. [140] were used to predict the transitions between 250 and 340 GHz. The $J = 8.5 \leftarrow 7.5$ component of the $N = 8 \leftarrow 7$ transition was first used to optimize the formation of TiN in the laser ablation system and, then, to monitor its production while recording the spectra of less abundant isotopologues. As for the parent species, five of the six newly recorded transitions were not observed previously and they add information to the data set available from literature [138, 140]. They are listed in Table 4.37 together with the transitions observed for ^{46}TiN and ^{50}TiN.

Table 4.37: Measured transition frequencies and least-squares residuals for newly observed transitions of titanium nitride. Units are MHz

Species	$N' \leftarrow N$	$J' \leftarrow J$	Frequency[a]	Obs.−Calc.
^{46}TiN	$7 \leftarrow 6$	$7.5 \leftarrow 6.5$	262736.840	−0.010
		$6.5 \leftarrow 5.5$	262789.152	0.001
	$8 \leftarrow 7$	$8.5 \leftarrow 7.5$	300261.470	0.040
		$7.5 \leftarrow 6.5$	300313.775	−0.024
	$9 \leftarrow 8$	$9.5 \leftarrow 8.5$	337780.803	−0.031
		$8.5 \leftarrow 7.5$	337833.260	0.024
^{48}TiN	$7 \leftarrow 6$	$7.5 \leftarrow 6.5$	260189.007	0.046
		$6.5 \leftarrow 5.5$	260240.844	0.057
	$8 \leftarrow 7$	$8.5 \leftarrow 7.5$	297349.913	0.040
		$7.5 \leftarrow 6.5$	297401.740	−0.024
	$9 \leftarrow 8$	$9.5 \leftarrow 8.5$	334505.724	−0.018
		$8.5 \leftarrow 7.5$	334557.677	0.003
^{50}TiN	$7 \leftarrow 6$	$7.5 \leftarrow 6.5$	257894.399	0.011
	$8 \leftarrow 7$	$8.5 \leftarrow 7.5$	294668.907	−0.006
		$7.5 \leftarrow 6.5$	294720.355	−0.012
	$9 \leftarrow 8$	$9.5 \leftarrow 8.5$	331489.862	0.006
		$8.5 \leftarrow 7.5$	331541.342	0.001

[a] The experimental accuracy is estimated to be 30 kHz.

The rotational spectra of ^{46}TiN and ^{50}TiN had never been studied, so no predictions were available. The Dunham's relationships presented earlier for NH (§ 4.1.2) were exploited to predict their rotational frequencies from the spectroscopic parameters available for the parent species ^{48}TiN. They were easily found within 2–3 MHz from the predicted frequencies; the error is due to the negligence of any Born–Oppenheimer term which, however, should be determinable but relatively small. Based on the isotopic ratios, the spectra of ^{46}Ti and ^{50}Ti were expected 9 and 14 times weaker, respectively. These factors are experimentally confirmed (see Figs. 4.18–4.20) and, thus, each line needed to be recorded for a longer integration time in order to achieve a

decent S/N. We were able to record and analyze 6 transitions for ^{46}Ti and 5 for ^{50}Ti in the investigated frequency range. From their least-square analysis it was possible to determine B, D, and λ for both isotopologues. The remaining centrifugal parameters (H and λ_D) were fixed to the corresponding value fitted for the the main isotopologue ^{48}Ti, while no hyperfine constants were included for nitrogen because the hyperfine structure is collapsed in a unique line. The parameters derived for each isotopologue are reported in Table 4.38.

Table 4.38: Spectroscopic parameters derived for titanium nitride

Constant	Atom	Units	^{48}TiN	^{46}TiN	^{50}TiN
B		MHz	18589.35095(98)	18771.4317(84)	18421.7329(37)
D		MHz	0.026242(22)	0.026978(61)	0.025901(26)
H		Hz	−0.23(11)[a]	−0.23[b]	−0.23[b]
λ		MHz	−52.2084(29)	−52.620(51)	−51.704(20)
λ_D		kHz	0.29(12)[a]	0.29[b]	0.29[b]
b_F	(N)	MHz	18.4930(45)		
c	(N)	MHz	0.166(14)		
C	(N)	MHz	0.0137(25)		
eQq	(N)	MHz	−2.271(26)		
no. of lines			35	6	5
MW *rms*		kHz	24	25	8
σ_w			0.92	0.85	0.27

Number in parenthesis are one standard deviation in units of the last quoted digit.
[a] These parameters are badly determined in the fit ($< 3\sigma$) but their inclusion was necessary to reproduce the data within their stated uncertainties. **[b]** Constrained.

We also attempted to observe the rotational spectrum of ^{47}TiN. The isotopic abundance of ^{47}Ti is 10 times less than that of ^{48}Ti; although more abundant than ^{50}Ti which was observed in this work, the presence of an isotope with non-vanishing nuclear spin ($I_{^{47}Ti} = 5/2$) prevented any observation of ^{47}TiN. Indeed, the hyperfine interaction between the nuclear spin of ^{47}Ti and the electronic spin of the molecule would lead to a further splitting of a given level into six subcomponents. These sub-levels are predicted to be separated enough to resolve the hyperfine pattern, meaning that each line is 6 times weaker than a "theoretically unsplit" line. In total, the rotational transitions of ^{47}TiN are expected to be a factor of *ca.* 60 less intense than those of ^{48}TiN. In practice, this would require an integration time 3600 times longer (i.e., $\sim$ 200 h per line) to attain a similar S/N ratio in the spectrum. Experimentally, this is complicated by the facts that (i) the production of titanium nitride worsen after 1 or 2 hours, because some ablated material starts to accumulate on the rod surface and the chemistry inside the plasma changes, and (ii) there is still some uncertainty on the line positions, meaning that a broader spectral scan

is required. So, despite we were scanning the spectrum for weeks, we were not able to observe any feature of ^{47}TiN. The case of ^{49}TiN is even more critical because the spectrum is predicted to be two order of magnitude weaker than ^{48}TiN.

4.4.5 Outlook

The vibrational mode of TiN is predicted to be centered around 1039 cm^{-1} [136, 137], a spectral region covered by the Quantum Cascade Laser spectrometer located in Kassel. Since the laser ablation system is identical to that described in § 4.4.2, the production of titanium nitride should be as efficient as in SuJeSTA. To complete the Dunham analysis of titanium nitride and to determine accurate spectroscopic constants for ^{47}TiN and ^{49}TiN, we are planning to record the vibrational spectrum of TiN.

The spectrometer is described in details in Ref. [143]. Briefly, the spectral range between 900 and 1300 cm^{-1} is covered by several narrow line width (100 kHz) continuous-wave QCLs. The QCL beam intersects a supersonic jet (analogous to that used in SuJeSTA) perpendicularly in a Herriott-type multi-path cell, few millimeters downstream of the exit of the ablation source. A fast liquid nitrogen cooled mercury cadmium telluride (MCT) detector will be used to record the signal. Given the maximum resolution achievable with the QCL spectrometer (4×10^{-3} cm^{-1}), ro-vibrational transitions belonging to the isotopologues ^{47}TiN and ^{49}TiN would exhibit an unresolved hyperfine structure, making the intensity of these transitions as strong as those of ^{46}TiN and ^{50}TiN. These conditions will allow us to derive reliable spectroscopic constants of all isotopologues with good accuracy and to carry out a Dunham-type analysis of titanium nitride. Simultaneously, the *in situ* formation of TiN will be tested in the glow discharge of our frequency-modulation spectrometer to possibly extend the measurements into the submillimeter region. Finally, when the MIR data will be collected and analysed, the Dunham analysis of titanium nitride will be presented in a paper to be submitted to the *Journal of Molecular Spectroscopy*.

4.5 Aminoacetonitrile

In the last three years, I have been studying ro-vibrational spectra of many Complex Organic Molecules, such as aminoacetonitrile (NH_2CH_2CN), cyanomethanimine (NCCHNH), ethanimine (CH_3CHNH), vinyl alcohol (CH_2CHOH), ethylene glycol (CH_2OHCH_2OH), and so on. Among them, I have chosen to report in this thesis the case of aminoacetonitrile because of its high prebiotic importance and because the study reported here, in collaboration with the Toho University, led to my first scientific publication:

- C. Degli Esposti, L. Dore, M. Melosso, K. Kobayashi, C. Fujita, and H. Ozeki, "Millimeter-wave and Submillimeter-wave Spectra of Aminoacetonitrile in the Three Lowest Vibrational Excited States," *Astrophys. J. Suppl. S.*, vol. 230, no. 26, 2017 [144].

Also, the spectroscopic investigation of aminoacetonitrile is still an open project and future plans are presented in the Outlook Section (§4.5.6).
My contribution to this work can be summarized as follow:

- conceptualization
- measurements of the rotational spectra in Bologna;
- joint analysis, including the data recorded in Toho;
- treatment of resonance effects;
- manuscripts co-writing;
- co-writing of the SOLEIL proposal, for which I am the principal investigator.

Sections §4.5.1–§4.5.5 are reproduced from the aforementioned paper.

4.5.1 Introduction

Attempts to detect amino acids in Space have so far been unsuccessful even for its simplest form, glycine (NH_2CH_2COOH), despite decades of efforts devoted by many observational studies [145, 146, 147]. There can be several explanations for this failure. One is that rotational constants are relatively large and the line strength of each line is not very strong. Another is the expected spatial distribution of the molecule. Garrod developed a sophisticated chemical models for hot cores and indicated that glycine is formed almost exclusively within or upon dust-grain ice-mantles [148]. Since the high evaporation temperature of the molecule (200 K) makes the emission region extremely compact, it can be hardly expected to detect glycine with a single dish telescope. The feasibility of detecting glycine highly depends on the selection of sources to be observed with ALMA at sub-arcsecond resolutions. Garrod proposed as a candidate source the hot core NGC 6334 IRS1, where relatively narrow emission lines are expected

[148]. In addition, Jiménez-Serra *et al.* claimed that glycine may be detectable in low-mass prestellar cores such as L1544 because congestion of spectral lines can be avoided [149].
From a chemical point of view, it is also important to consider sources where possible glycine precursors are abundant. Aminoacetonitrile NH_2CH_2CN is one of the possible precursors of glycine via Strecker synthesis [150, 151] (see Figure 4.21).

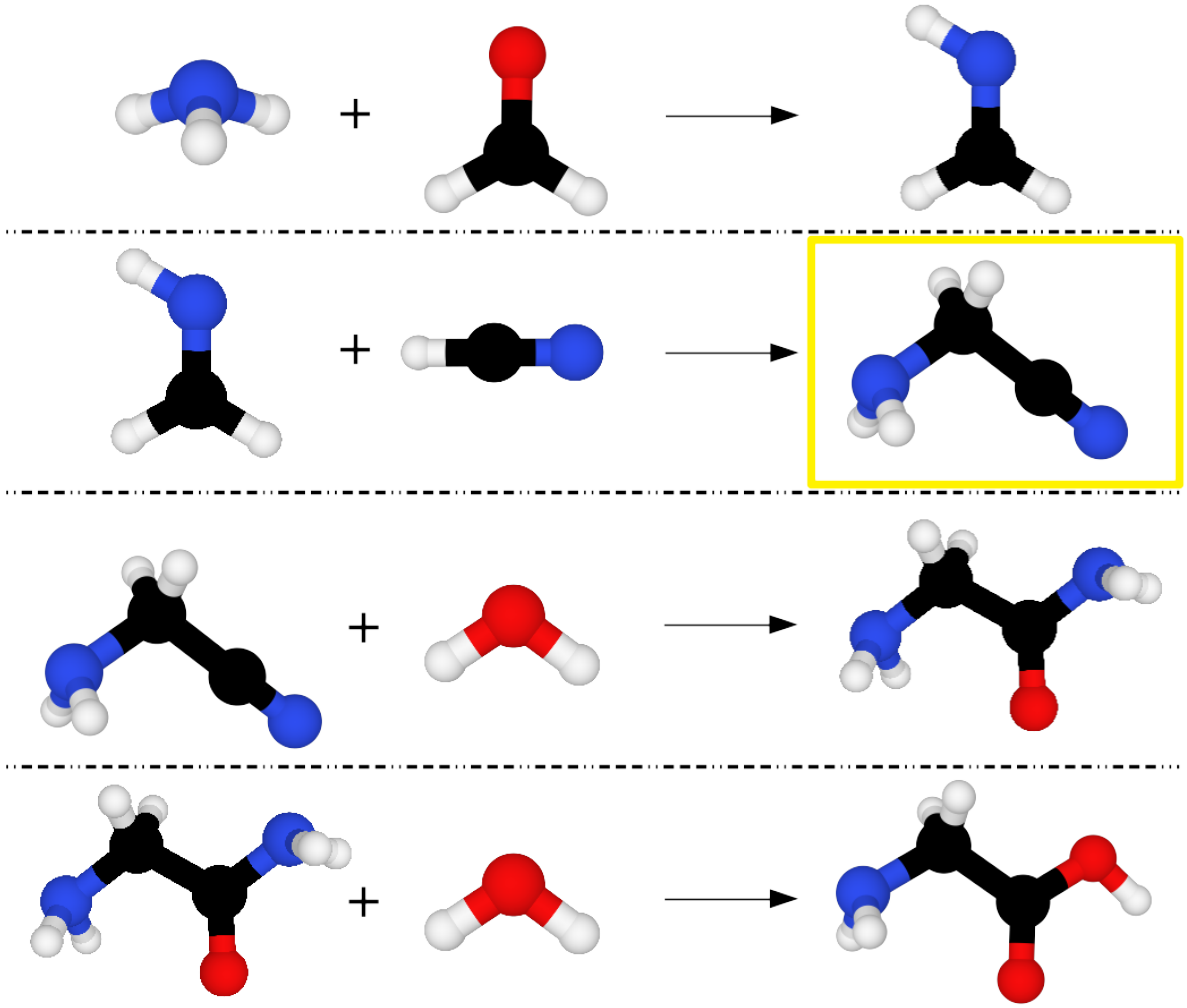

Figure 4.21: Four-steps Strecker synthesis of glycine. The process starts with the reaction between ammonia (NH_3) and formaldehyde (H_2CO) to produce methanimine (H_2CNH). In the second step, methanimine reacts with a molecule of hydrogen cyanide (HCN) to form aminoacetonitrile (NH_2CH_2CN, yellow box). In the third and fourth steps, NH_2CH_2CN is hydrolyzed to give aminoacetamide ($NH_2CH_2CONH_2$), and finally glycine (NH_2CH_2COOH).

Belloche *et al.* reanalyzed previous microwave spectroscopic studies of aminoacetonitrile in the millimeter-wave region [152, 153, 154] and succeeded in the detection of this molecule toward Sgr B2(N) [155]. They derived a column density of 2.8×10^{16} cm^{-2}, or fractional abundance of 2.2×10^{-9} (see explanations in §2.2) at a temperature of 100 K. Garrod showed that a peak gas-phase fractional abundance of a few 10^{-9} to 10^{-8} is expected at around 120 K in each time-

scale model [148]. At such a high kinetic temperature, it looks plausible that the molecule can be populated in the high J rotational levels in the vibrational ground state, or in the low-lying excited states.

The measurements of the rotational spectrum of aminoacetonitrile have been performed up to 1.3 THz [154], and several misassignments of b-type transitions were found. Therefore, firm spectroscopic data of aminoacetonitrile in the ground vibrational state were provided by correcting those errors [156]. During the course of that measurements, several satellite bands near the ground state line were found, due to spectral lines of vibrational excited states. Preliminary analyses of the satellite transitions belonging to six different vibrational states revealed the presence of perturbations in several spectra, including also those of the two states of lower energy [157].

The assignment of vibrational states of aminoacetonitrile (*trans* form, C_s symmetry group) has been established by experimental and theoretical studies. Bak *et al.* [158] observed and assigned the three lowest fundamental bands at 216 (ν_{11}, A' symmetry), 247 (ν_{18}, A'' symmetry), and 370 cm^{-1} (ν_{17}, A'' symmetry), respectively, by gas-phase, low-resolution IR spectroscopy. Bernstein *et al.* [159] performed density-functional theory calculations on aminoacetonitrile at the B3LYP/6-31+G(d) level. The harmonic frequencies computed for the three lowest modes were 204.9, 259.6, and 377.2 cm^{-1}, which were described as $C-C\equiv N$ bend, $-NH_2$ torsion, and NH_2-CH_2 torsion, respectively.

Simultaneously to my PhD work, Kolesniková *et al.* [160] reported rotational spectra for 29 vibrational excited states. Although perturbation effects were recognized, effective rotational and centrifugal distortion constants for each state were obtained by fitting their rotational spectra using the standard semi-rigid rotor model [102]. No vibration-rotation couplings between the excited states of the exhaustive list were considered, despite the remarkable effects they can produce in the higher rotational states. In this thesis, the study was focused on the three lowest vibrational excited states. We have extended the measurements in vibrational excited states to much higher frequencies (450 GHz) than the previous study [160], and have taken into account the Coriolis resonance existing between the two lowest states. This made it possible to include higher rotational states in the fitting, so that our obtained molecular constants have better predictive capabilities. The spectral data of these astronomically important states are essential for future observation of the molecule in relatively high kinetic temperature conditions.

4.5.2 Experimental details

The present experiments were carried out in two laboratories, at Bologna and Toho Universities, respectively. The experiment at Bologna was conducted in the frequency ranges 80–115 and 240–290 GHz using a source-modulation millimeter/submillimeter-wave spectrometer (§3.1).

The experiment at Toho University was conducted in frequency regions complementary to those investigated in Bologna, reaching a frequency as high as 450 GHz, with essentially the same apparatus and experimental conditions of their previous work [156].

The aminoacetonitrile sample (> 98% purity, Sigma Aldrich) was purchased and used without further purification. All the spectra were taken at room temperature. The accuracy of each line frequency varies from 20 to 200 kHz, depending on the S/N of the observed spectrum and line-blending due to unresolved hyperfine components enveloped in a single line profile.

4.5.3 Theory

Aminoacetonitrile is a nearly-prolate asymmetric-top rotor with a Ray's asymmetry parameter $\kappa = -0.97$. It exists only in the *trans* form (C_s symmetry group), with the $-NH_2$ group pointing toward the $-CN$ moiety (see Fig. 4.21). The electric dipole moment of aminoacetonitrile lies on the *a/b* plan; its components were determined through Stark-effect measurements and are $\mu_a = 2.577(7)$ and $\mu_b = 0.5754(10)$ D [153], respectively. The μ_c component is null for symmetry reasons.

Being a rotor close to the prolate limit, the ro-vibrational energy levels can be represented adopting a Watson's S-reduced Hamiltonian in its I^r representation [102]:

$$\mathscr{H}_{\text{rot}} = \mathscr{H}^{(S)} + \mathscr{H}_{\text{cd}} + \mathscr{H}_{\text{Q}}\,, \tag{4.51}$$

where $\mathscr{H}^{(S)}$ contains the rotational constants in the S-Watson reduced form and the vibrational energy:

$$\mathscr{H}^{(S)} = G_v + \tfrac{1}{2}(B+C)\,\mathbf{P}^2 + \left[A - \tfrac{1}{2}(B+C)\right] P_a^2 + \tfrac{1}{4}(B-C)\left(P_+^2 - P_-^2\right), \tag{4.52}$$

$\mathscr{H}_{\text{cd}}$ can be decomposed in a sum of terms, each containing different powers of the angular momentum. For instance, the $\mathscr{H}_{\text{cd}}^{(4)}$ part accounts for the centrifugal distortion terms up to 4^{th} power of the angular momentum

$$\mathscr{H}_{\text{cd}}^{(4)} = -D_J\mathbf{P}^4 - D_{JK}\mathbf{P}^2P_a^2 - D_KP_a^2 + d_1\mathbf{P}^2\left(P_+^2 + P_-^2\right) + d_2\left(P_+^4 + P_-^4\right), \tag{4.53}$$

while $\mathscr{H}_{\text{cd}}^{(6)}$ contains operator with 6^{th} power of $\mathbf{P}$:

$$\begin{aligned}\mathscr{H}_{\text{cd}}^{(6)} = {} & H_J\mathbf{P}^6 + H_{JK}\mathbf{P}^4P_a^2 + H_{KJ}\mathbf{P}^2P_a^4 + H_KP_a^6 \\ & + h_1\mathbf{P}^4\left(P_+^2 + P_-^2\right) + h_2\mathbf{P}^2\left(P_+^4 + P_-^4\right) + h_3\left(P_+^6 + P_-^6\right).\end{aligned} \tag{4.54}$$

In the present work, centrifugal distortion terms up to sextic order have been used.

The nuclear quadrupole interaction due to the presence of two nitrogen nuclei ($I_{\text{N}} = 1$) is expressed by:

$$\mathscr{H}_{\text{Q}} = eQq_0\frac{2J+3}{J}Y(J,I,F)\,, \tag{4.55}$$

with

$$Y(J,I,F) = \frac{\frac{3}{4}\mathscr{C}(\mathscr{C}+1) - I(I+1)J(J+1)}{2(2J-1)(2J+3)I(2I-1)} \tag{4.56}$$

and

$$\mathscr{C} = F\,(F+1) - J\,(J+1) - I\,(I+1)\ . \tag{4.57}$$

In order to analyze the observed hyperfine-structure components, the following angular momenta coupling scheme between the ^{14}N-nuclear spins $\mathbf{I}_1$(nitrogen of the $-NH_2$ group) and $\mathbf{I}_2$(nitrogen of the $-CN$ group) and the rotational angular momentum $\mathbf{J}$ was adopted: $\mathbf{I} = \mathbf{I}_1 + \mathbf{I}_2$, $\mathbf{F} = \mathbf{J} + \mathbf{I}$.

4.5.4 Analysis and results

At room temperature, all the three lowest vibrationally excited states of aminoacetonitrile were sufficiently populated to assure the identification of the respective rotational spectra.
Close to each $a-$type R branch of the ground state, we were able to identify three different sequences of lines having the same K_a structure, but with reduced intensities, as expected for vibrational satellites produced by low-lying states, as shown in Figure 4.22.

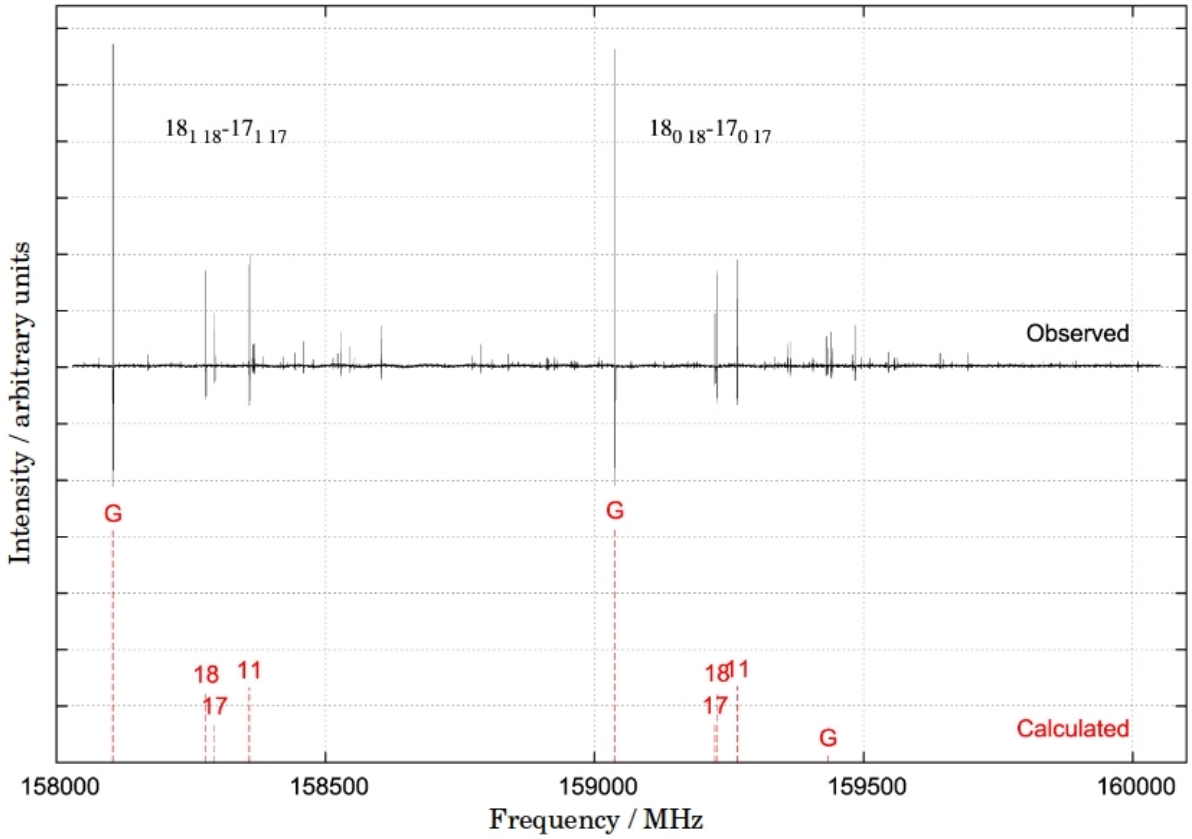

Figure 4.22: Observed and calculated spectrum of aminoacetonitrile in the ground ("G") and excited vibrational states (denoted by "11", "17", and "18" for $v_{11} = 1$, $v_{17} = 1$, and $v_{18} = 1$ states, respectively) around 160 GHz.

Preliminary fits to these sets of lines always provided B and C rotational constants a few MHz greater than those of the ground state. From intensity-ratio measurements, it was possible to

make an approximate evaluation of the excited-state energies, which were found in the range from 200 to 400 cm^{-1}, in qualitative agreement with the IR data [158, 159]. The measurements for the three excited states were then extended up to 450 GHz, so that a fairly large set of *a*- and *b*-type transition frequencies could be obtained for each vibrational state. The measurements probed rotational energy levels in the J interval from 6 to 56 and K_a interval from 0 to 15. Small splittings due to the ^{14}N nuclear spin of the two nitrogen atoms were observed for a few $a-$type R branch transitions with high K_a values measured in the 100 GHz region. An example is provided in Figure 4.23, which shows a K_a sequence for the $J = 10 \leftarrow 9$ a-type band in the ν_{18} state, in which splittings due to the electric quadrupole coupling are detectable for K_a = 7, 8, and 9.

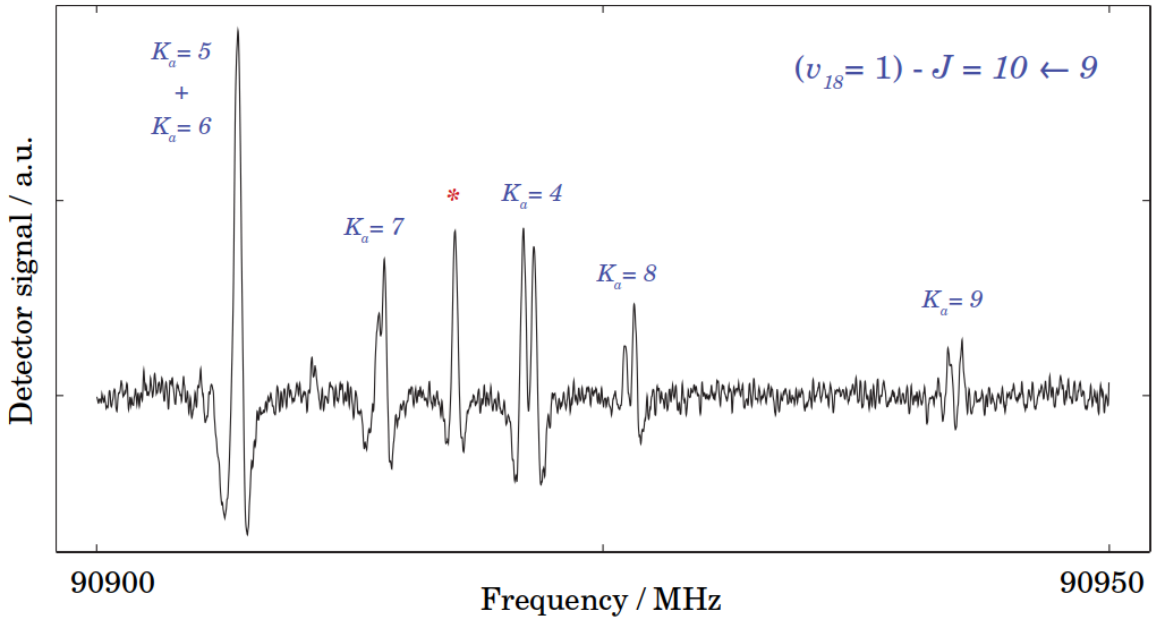

Figure 4.23: Portion of the $J = 10 \leftarrow 9$ a-type band of aminoacetonitrile in the ν_{18} state (integration time 100 s, RC= 10 ms, FM = 180 kHz). Splittings caused by electric quadrupole coupling are detectable for K_a= 7, 8, and 9. The K_a=4 transition shows the asymmetry splitting. An asterisk indicates a line of the ν_{17} state.

The complete data sets for the three excited states were then assembled by combining the mm- and submm-wave transition frequencies measured at Bologna and Toho. They were analyzed using Pickett's SPFIT program [46]. In the fitting procedure, the experimental data were weighted according to the inverse square of their uncertainty. The required ^{14}N electric quadrupole coupling constants were held fixed to the values determined for the vibrational ground state [161], that are χ_{aa} = -2.77 MHz and $\chi_{bb} - \chi_{cc}$ = -0.37 MHz for nitrogen of the NH_2 group, χ_{aa} = -3.48 MHz and $\chi_{bb} - \chi_{cc}$ = -0.48 MHz for nitrogen of the CN group.
The rotational lines of the weakest spectrum, corresponding to ν_{17} =1, could be fitted very well using the standard semi-rigid Hamiltonian. Centrifugal-distortion constants values close

to those of the ground-state were determined. The same procedure gave, however, unsatisfactory results when used to analyze the transition frequencies measured for the two states of lower energy. Large deviations, opposite in signs, were produced for $a-$type R branch lines with $K_a \geq J/2$, and strongly diverging values of the quartic centrifugal distortion constants D_K and d_2 resulted. This was a clear indication of the existence of some ro-vibrational interaction between these states. Since aminoacetonitrile has C_s symmetry, its vibrations must belong to the A' or A'' irreducible representations. On the one hand, two fundamental levels of the same symmetry, either A' or A'', are connected by the c-axis term included in the H_{21} Coriolis operator [162]. On the other hand, two states of different symmetry are connected by a- and b-axis Coriolis operators. We observed that the quality of the fits could be greatly improved by assuming the existence of an a-type Coriolis interaction. The two states were coupled through the off-diagonal $G_a\mathbf{P}_z$ Coriolis operator, and the transition frequencies of the two states were simultaneously analyzed fitting also the Coriolis coupling constant G_a and the vibrational energy difference between the two states. The standard deviation of the fit decreased by more than a factor of ten, even if small systematic obs.$-$calc. deviations still remained, indicating the need of improving the coupling model. No significant effect was obtained either considering also a b-axis Coriolis interaction, or higher order terms deriving from H_{22} [162], while a further lowering of the standard deviation of the fit was achieved by taking into account small dependences of G_a from the rotational quantum numbers J and K. The best results were obtained using two more adjustable parameters, adopting an off-diagonal Coriolis operator of the form $(G_a + G_a^J\mathbf{P}^2 + G_a^{JK}\mathbf{P}^2\mathbf{P}_z^2)\mathbf{P}_z$. The effectiveness of an a-type Coriolis coupling demonstrates that the two lowest vibrational states of aminoacetonitrile must be of different symmetry, as stated in Ref. [158] and confirmed by the *ab initio* calculations of Ref. [159].

As far as the $v_{17} = 1$ state is concerned, 352 different line frequencies measured in the frequency interval from 80 to 450 GHz were analyzed. They correspond to transitions between rotational levels for which J ranges from 6 to 50, and K_a from 0 to 15. The three rotational constants, the full set of quartic centrifugal distortion constants, and the sextic centrifugal distortion parameters H_J, H_{KJ} and h_1 were fitted to the measured frequencies, obtaining a standard deviation value of 25.4 kHz. The remaining sextic centrifugal distortion constants, not useful for a further improvement of the fit, were held fixed to the respective ground-state values [156], and the ^{14}N electric quadrupole coupling constants [161] as well.

As to the $v_{11} = 1$ / $v_{18} = 1$ resonance system, a total number of 866 distinct line frequencies were measured, corresponding to rotational transitions spanning nearly the same J and K_a ranges previously mentioned for the the $v_{17} = 1$ state. The measured frequencies were analyzed by fitting all rotational and quartic centrifugal distortion constants, and three sextic distortion constants H_J, H_{JK} and h_1 of each interacting state. In addition, the vibrational energy difference ΔE_{vib} and the Coriolis coupling coefficients G_a, G_a^J, and G_a^{JK} were optimized to achieve a satisfactorily low standard deviation of 29.8 kHz. The vibrational energy difference between the two interacting states is accurately determined to be 34.31731(26) cm^{-1}. The derived molecular

constants, including interaction parameters and the energy difference $\nu_{18} - \nu_{11}$, are summarized in Table 4.39.

Table 4.39: Molecular constants of aminoacetonitrile in the lowest three excited states.

Constant	Unit	$\nu_{11} = 1$	$\nu_{18} = 1$	$\nu_{17} = 1$
A	MHz	30279.63(15)	30366.32(15)	30143.7042(28)
B	MHz	4776.48577(13)	4769.41405(15)	4764.23731(13)
C	MHz	4316.65567(13)	4314.50868(14)	4316.433637(93)
D_J	kHz	3.048626(79)	3.07047(14)	3.07242(11)
D_{JK}	kHz	−52.555(85)	−55.690(85)	−55.0291(22)
D_K	kHz	649.87(15)	779.287(23)	695.85(19)
d_1	kHz	−0.674571(61)	−0.675957(75)	−0.672041(62)
d_2	kHz	−0.0336185(89)	−0.029711(16)	−0.026762(13)
H_J	Hz	0.009114(22)	0.009503(42)	0.009616(33)
H_{JK}	Hz	−0.13109(89)	−0.1120(15)	−0.12406[a]
H_{KJ}	Hz	−2.7126[a]	−2.7126[a]	−2.606(16)
H_K	Hz	53.2285[a]	53.2285[a]	53.2285[a]
h_1	mHz	3.6369(14)	3.6833(27)	3.766(22)
h_2	mHz	0.4749[a]	0.4749[a]	0.4749[a]
h_3	mHz	0.05229[a]	0.05229[a]	0.05229[a]
$\Delta E(\nu_{18} - \nu_{11})$	cm^{-1}	34.31731(26)		
G_a	MHz	16401.4(46)		
G_a^J	MHz	0.0330(27)		
G_a^{JK}	kHz	-0.03308(54)		
rms error	kHz	29.8		25.4
σ		0.729		0.648

Number in parenthesis are one standard deviation in units of the last quoted digit. ^{14}N electric quadrupole coupling constants were held fixed to the value determined by Brown *et al.* [161]. **[a]** Kept fixed to ground state value.

4.5.5 Discussion

The rotational spectra of aminoacetonitrile in the three lowest vibrational states ($\nu_{11} = 1$, $\nu_{18} = 1$, and $\nu_{17} = 1$) were clearly identified. The $\nu_{17} = 1$ state was almost isolated and inclusion of any perturbation was not necessary, while the $\nu_{11} = 1$ and $\nu_{18} = 1$ states proved to be interacting through an a-type-Coriolis coupling. The determined vibrational energy difference between the two interacting states compares fairly well with the value from the previous infrared study [158] and from computational results [159]. In addition, the values of the centrifugal distortion constants determined for the two interacting states are very close to those of the ground state, thus confirming the effectiveness of our analysis.

The fitted value of the main Coriolis coupling coefficient is 16 401 ± 5 MHz. It was compared with the corresponding *ab initio* computed value which was obtained using the Gaussian 09 program [163] at the MP2/6-311++G(d,p) level. The G_a Coriolis coefficient which couples the ν_{11} and ν_{18} vibrational states has the following theoretical expression [162]:

$$G_a = A_e \frac{\omega_{11} + \omega_{18}}{\sqrt{\omega_{11}\omega_{18}}} {}^a\zeta_{11,18}. \tag{4.58}$$

A_e is the equilibrium value of the rotational constant A, ω_{11} and ω_{18} are the harmonic frequencies of the interacting states, and ${}^a\zeta_{11,18}$ is the corresponding Coriolis coupling constant. Using the *ab initio* computed values for all the parameters (A_e = 30 155.6 MHz , ω_{11} = 209.16 cm^{-1}, ω_{18} = 264.77 cm^{-1}, ${}^a\zeta_{11,18}$ = 0.20622), it results in G_a = 12 524 MHz. A very negligible change is obtained using experimental vibrational frequencies and the ground state value of the rotational constant A. It seems, therefore, that the 30% disagreement between fitted and *ab initio* computed G_a values is mainly due to inaccuracy in the computed ${}^a\zeta_{11,18}$ constant.

Comparing the values of the spectroscopic constants determined in the present work with those recently published [160], large discrepancies do obviously appear for the $\nu_{11} = 1$ and $\nu_{18} = 1$ states, because of the substantial difference of the fitting procedures. We have measured and analyzed transition frequencies corresponding to higher J and K_a values, so that the a-type Coriolis coupling existing between these two states had to be necessarily taken into account to obtain a reasonably good fit. In this way the contribution of the corresponding resonant term which is inversely proportional to $\pm(\omega_{11} - \omega_{18})$ is removed from the ${}^A\alpha_{11}$ and ${}^A\alpha_{18}$ vibration-rotation interaction constants, and this explains the differences of *ca.* ±261 MHz between the effective A constants determined in the present work and those published by Kolesniková *et al.* [160] for the same states. Significant changes are also produced for some centrifugal distortion constants which converge to rather unreliable values (i.e., too far from those of the ground state) if the resonance is neglected. Anomalous values of the quartic centrifugal distortion constants D_K and d_2, and of the sextic H_{JK} and h_1 are apparent in the results of Ref. [160], although they analyzed transition frequencies corresponding to lower J and K_a values. On the contrary, normal values are obtained by our analysis for these constants. It is to be noticed that if the spectroscopic constants determined by Kolesniková *et al.* [160] are used to predict the whole set of transition frequencies that we have measured for the $\nu_{11} = 1$ and $\nu_{18} = 1$ states, then obs.−calc. values greater than 1 MHz are produced for nearly all transitions recorded above 273 GHz, and for 33 transitions the frequency discrepancies are larger than 10 MHz. As to the unperturbed $\nu_{17} = 1$ state, the molecular constants determined in the present work are essentially the same as those reported in Ref. [160]. Small discrepancies beyond the quoted uncertainties are anyway observable, probably due to (i) the extension of our measurements into a higher frequency region, (ii) a different choice of the sextic centrifugal distortion constants released in the effective fits, and (iii) a better accuracy of our frequency measurements when hyperfine splittings due to the electric quadrupole coupling were resolved.

The vibration-rotation partition function of aminoacetonitrile was calculated for several temperatures by taking the three lowest vibrational excited states into account. The observed vibrational frequencies in the gas phase (216, 247 and 370 cm^{-1} for $\nu_{11} = 1$, $\nu_{18} = 1$, and $\nu_{17} = 1$ states, respectively) were used as term values for these states. The results are listed in Table 4.40.

Table 4.40: Value of the ro-vibrational partition function of aminoacetonitrile.

Temperature (K)	G.S. only[a]	All states[b]
300	34824	64711
225	22817	35635
150	12456	15599
75	4403	4520
37.5	1557	1558
18.75	552	552
9.375	196	196

[a] From the Cologne Database for Molecular Spectroscopy. **[b]** This work

According to Bak *et al.* [158], the vibrational frequency next to the lowest three modes is 558 cm^{-1}, whose effect on the vibrational partition function can contribute to the uncertainties of the present data by 6% at 300 K, and less than 1% at 100 K. In order to calculate the spectral intensity of the molecule for conducting a search in the ISM, we needed to assume the components of the dipole moment in the vibrational excited states to be the same as those in the ground state [153]. The spectral line catalog was then constructed with Pickett's SPCAT program [46]. By using these data, an initial attempt to detect these transitions in the ALMA survey toward Sgr B2 showed that there are some weak hints of their presence [2]. All the lines were blended and we need more sensitive data to confirm the first detection. The previous study [155] indicates that the emission of aminoacetonitrile came from a compact source and ALMA's high spatial resolution nature provides an ideal tool to observe this kind of species.

4.5.6 Outlook

No high-resolution infrared spectra of aminoacetonitrile have been recorded to date. Therefore, an important piece of information about the spectroscopic knowledge of NH_2CH_2CN is still missing. The most intense vibrational transitions of this molecule lie in the far-infrared domain, between 200 and 1000 cm^{-1}, where seven bands (out of 18) are located. It is highly desirable to record at high-resolution (0.001 cm^{-1}) this part of the infrared spectrum. We proposed [3]

[2] Private communication, Belloche (2016)

[3] Proposal no. 20191573 submitted to the SUNSET portal of SOLEIL Synchrotron.

therefore to record the far-infrared spectrum of aminoacetonitrile where the three lowest fundamental bands ν_{11} (A', C−C≡N bending at 216 cm^{-1}), ν_{17} (A'', NH_2-CH_2 torsion at 370 cm^{-1}), and ν_{18} (A'', NH_2 torsion at 247 cm^{-1}) are lying [158]. At these energies, conventional infrared spectrometers show in fact much poorer performances than the synchrotron light. In preparation of this study we have performed high level quantum chemical calculations at the MP2/cc-pVTZ level of theory. The calculated band centers of 210, 265, and 382 cm^{-1} for ν_{11}, ν_{18}, and ν_{17}, respectively, are in excellent agreement with the literature values. These high-resolution infrared measurements will be helpful to guide astronomical identification of aminoacetonitrile by means of its vibrational signatures. Furthermore, an accurate knowledge of the low-lying vibrational excited states is necessary to successfully analyze the hot-bands associated to any other vibrational mode of NH_2CH_2CN. Moreover, significant correlation exists between the spectroscopic parameters of the resonant states that will be lifted by the ro-vibrational analysis.

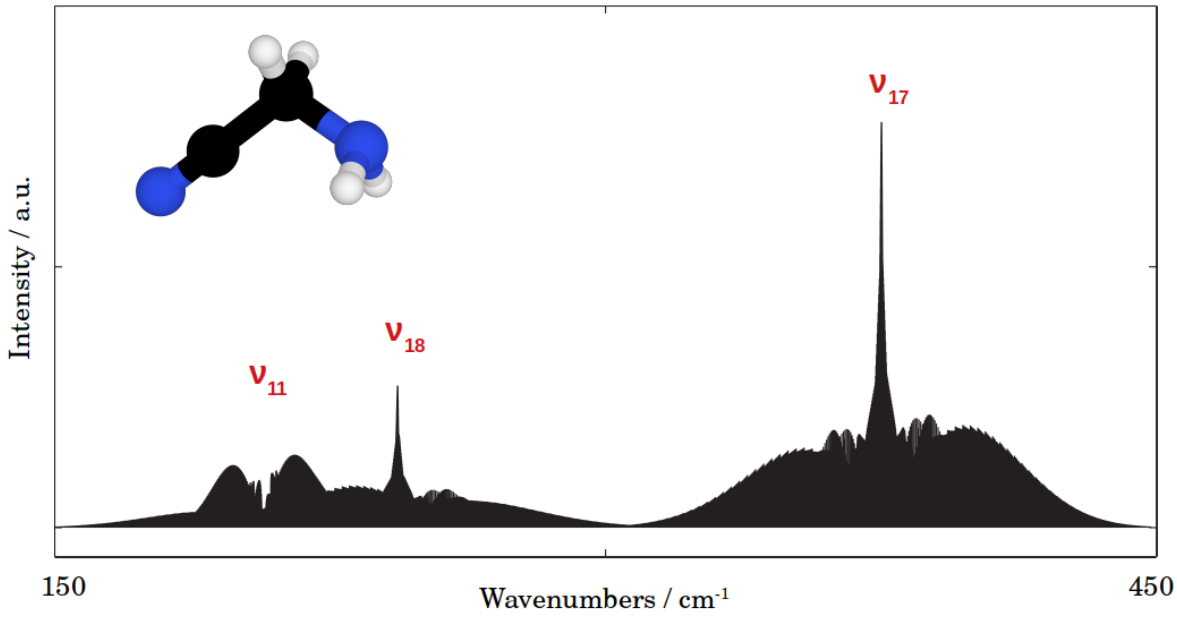

Figure 4.24: Simulation of the ro-vibrational spectrum of aminoacetonitrile in the FIR region. The Q-branches of the c-type bands ν_{17} and ν_{18} are predicted to be the dominant features of the spectrum.

The far-infrared spectrum of aminoacetonitrile will be recorded using the long absorption path length of the AILES beamline aligned in its optimum configuration for 150 m of absorption. A 6 µm Mylar beamsplitter, polypropylene windows, and a liquid-He cooled bolometer will be used. Vapor pressure of aminoacetonitrile sample (> 98 % purity) will be injected in the cell. Considering the different symmetries and calculated intensities of the bands (ν_{18}, c-type, 45 km/mol; ν_{17}, c-type, 13 km/mol; ν_{11}, a/b-type, I = 11 km/mol), we plan to record 3 high resolution spectra at estimated pressure ranging from few to few hundreds of bar to observe all bands with a good signal-to-noise ratio. The first spectrum, at the lowest pressure, will be

recorded at conditions maximizing the signal-to-noise ratio of ν_{18}, the second spectrum will target ν_{17}, and the final spectrum (at the highest pressure) will allow the observation of the weak ν_{11} band. We prospect that several hot bands and vibrational satellites will be observable as well.
We expect to:

- Record the first high resolution spectrum of aminoacetonitrile in the far infrared and detect three fundamentals and many hot bands and vibrational satellites;
- Perform a global fit of the pure rotation and ro-vibration transition, and reduce the correlation among resonance parameters thanks to the newly determined accurate energy difference between the states;
- Assign some of the states from Ref. [160] which remain unassigned (from hot bands and combination bands observation)

These results will provide a strong base to continue the investigation of the IR spectrum at even higher frequency.

5 Astrophysical detections

5.1 NHD and ND_2 in IRAS 16293-2422

The astronomical sample

IRAS 16293-2422 is a Class 0 protostar, located in the nearby (∼120 pc) ρ-Ophiuchi star-forming region [164]. It mainly consists of two low-mass protostars A and B, separated by a distance of 600 AU (Astronomical Units, 1 AU = 1.5×10^8 km).

The chemistry in IRAS 16293-2422 is exceptionally rich [165]. Observations suggested that the emission from complex organic molecules (COMs) arises from small regions toward the continuum sources, where temperatures around 100 K would allow evaporation from grain-mantles. For example, glycolaldehyde ($HCOCH_2OH$), the simplest sugar, and chloromethane (CH_3Cl) have first been detected around this solar-type young star thanks to ALMA observations [166, 167].

Moreover, this source is very famous because deuterated molecules are present in enormous amount. As a matter of fact, deuterated species are observed in IRAS 16293-2422 with ratios relative to the normal ones (D/H) orders of magnitude higher than the cosmic ratio of about 1×10^{-5} [168]. Deuterium fractionation processes have been shown to increase such values by up to a factor of 10^{13}. Among the multiply-deuterated molecules detected in IRAS 16293-2422, it is possible to find water D_2O [169], formaldehyde D_2CO [67], hydrogen sulfide D_2S [69], methanol CD_3OH [70], and ammonia ND_3 [85].

Spectral survey

During the lifetime of the Herschel Space Observatory, a Key Project named Chemical Herschel Surveys of Star forming regions (CHESS) was carried out. The CHESS targets included the source and the surrounding of low- and high-mass protostars, from pre- to post-collapse. IRAS 16293-2422 was one of the targets and it has been observed in all seven bands of Herschel, from 487.5 to 1902 GHz. The observations were obtained in double-sideband (DSB) using the wide band spectrometer (WBS), with resolution of *ca.* 1.1 MHz, during March 2010 for 50 h in total [170].

Chemical models

IRAS 16293-2422 has also been targeted to study deuteration processes of ammonia. Roueff *et al.* [85] used the CSO, IRAM 30 m, and Arecibo telescopes to map the emission of NH_3, NH_2D, NHD_2, and ND_3 in this source. Additionally, three possible models have been developed to reproduce the actual abundances in dark clouds. The temperature is assumed equal to 10 K for all models, while the density of H_2 is 10^4, 10^4, and 10^6 cm^{-3} in Model 1, 2, and 3, respectively; moreover, carbon and oxygen depletion factors for Models 2 and 3 are 5 and 15 times larger than in Model 1. In these models, the column densities of imidogen (NH and ND) and amidogen

(NH_2, NHD, and ND_2) were estimated as well, although their observations were hindered by the spectral coverage of the telescopes used.
The models have showed that deuterium fractionation of nitrogen hydrides (NH, NH_2, and NH_3) can be very effective in high-density, highly-depleted clouds.

Table 5.1: Estimated fractional abundances from Ref. [85], where a hydrogen column density of $1 \times 10^{24} cm^{-2}$ is assumed.

Species	Model 1	Model 2	Model 3
NH	4.89×10^{-9}	6.80×10^{-9}	1.66×10^{-9}
ND	1.18×10^{-9}	4.67×10^{-9}	1.70×10^{-9}
NH_2	6.01×10^{-8}	8.48×10^{-8}	1.25×10^{-8}
NHD	2.99×10^{-9}	7.64×10^{-9}	1.51×10^{-9}
ND_2	3.05×10^{-11}	2.05×10^{-10}	5.09×10^{-11}
NH_3	5.49×10^{-8}	8.82×10^{-8}	2.00×10^{-8}
NH_2D	2.71×10^{-9}	8.80×10^{-9}	2.94×10^{-9}
NHD_2	8.82×10^{-11}	6.10×10^{-10}	2.37×10^{-10}
ND_3	3.44×10^{-12}	5.14×10^{-11}	2.14×10^{-11}

As for the detected species, the predicted abundance ratios of the deuterated ammonia isotopologues and their progenitors agree reasonably well with existing observations. Concerning the previously undetected deuterated forms of amidogen, the fractional abundance of NHD is predicted to be as high as that of NH_2D, while for ND_2 is estimated to be from 2 to 9 times larger than the ND_3 abundance.

Detection of NHD and ND_2

Using the observations of IRAS16293 retrieved from the Herschel Spectral Archive, we have searched for NHD and ND_2 on the base of our newly determined spectroscopic constants (§ 4.2). We detected the $N_{Ka,Kc} = 1_{1,1} - 0_{0,0}$ transition of NHD around 770 GHz and two transitions of ND_2, namely the $1_{1,1} - 0_{0,0}$ and $2_{0,2} - 1_{1,1}$ at 527 and 785 GHz, respectively. Both species are observed in absorption, because of their low excitation temperature (less than 8 K) and the strong continuum of the source. The detected transitions fall into two different sub-bands of Herschel, the 1a (487.5–553.5 GHz) and the 2b (722–794 GHz).
The hyperfine structure of these transitions were fitted to the spectral survey using a custom PYTHON code, which use the CLASS software as main core. Our code allows to fit or fix several parameters, such as the excitation temperature $T_{\rm exc}$, the column density N, the linewidth Δ_v, the local standard of rest (LSR) velocity $v_{\rm LSR}$, and the optical depth τ.
For comparison, we have also re-analyzed the HFS components of NH_2 which is seen in absorption against the continuum of the protostar [82]. In all spectra, the contribution from the

continuum (C) was subtracted using the equation experimentally derived in Ref. [82]:

$$T_{\rm C} = 1.10 \times \nu - 0.42\,, \tag{5.1}$$

with ν express in THz and $T_{\rm C}$ in Kelvin. The two J components of the fundamental transition $N_{Ka,Kc} = 1_{1,1} - 0_{0,0}$ of NH_2 in its *ortho* form are detected around 952 and 959 GHz (Fig. 5.1). From these observations, all the physical parameters could be derived for NH_2 without any assumption. Their values are listed in Table 5.2, together with those determined for NHD and ND_2.

Table 5.2: Parameters derived for NH_2, NHD, and ND_2.

Species	N (cm^{-2})	$T_{\rm exc}$ (K)	Vel. (km/s)	FWHM (km/s)	$X_{\rm H_2}$	[X]/[NH_2]
o-NH_2	5.84(24) $\times 10^{13}$	8.6(1)	4.25(1)	0.72(2)	1.1 $\times 10^{-9}$	
NHD	4.24(63) $\times 10^{13}$	7.3(2)	4.19(3)	0.78(5)	7.7 $\times 10^{-10}$	0.73
p-ND_2	5.48(77) $\times 10^{12}$	4.5[a]	4.66(6)	0.70[a]	1.0 $\times 10^{-10}$	0.09
o-ND_2	3.46(10) $\times 10^{11}$	4.5[a]	4.32(2)	0.70[a]	6.3 $\times 10^{-12}$	0.006

Numbers in parenthesis denote the standard error and apply to the last significant digits. **[a]** Assumed

The same transition is observed for both NHD and *o*-ND_2 at 770 and 527 GHz, respectively (Figs. 5.2–5.3).

Also, we detected the $2_{0,2} - 1_{1,1}$ transition of *p*-ND_2.

In the case of ND_2 the line fit required some constraints: the excitation temperature could not be determined simultaneously to the column density, so it was constrained to a value of 4.5 K. As initial guess, we assumed its $T_{\rm exc}$ equal to that of NHD, but this is in contrast with the fact that the $N_{Ka,Kc} = 1_{1,1} - 0_{0,0}$ transition is observed in absorption. Moreover, a temperature of 4.5 K would justify the *ortho*-to-*para* ratio observed for ND_2. The linewidth was also kept fixed to the NH_2 value, i.e., 0.7 km/s. The results from the hyperfine-structure analyses of NHD and ND_2 are given in Table 5.2.

Results and Discussion

We used the spectral surveys of the CHESS project obtained with Herschel Space Observatory to detect deuterated forms of amidogen radical towards the pre-stellar core IRAS16293-2422. This is very first detection of NHD and ND_2 in the ISM. Assuming a hydrogen column density $N_{\rm H_2} = 5.5 \times 10^{22}$ [82], we have derived fractional abundances for NHD and ND_2 of 7.7 $\times 10^{-10}$ and 1.0 $\times 10^{-10}$, respectively. Also, the deuterium fractionation is calculated to be around 73% for NHD and 9% for ND_2. These values are much higher than those predicted by the mod-

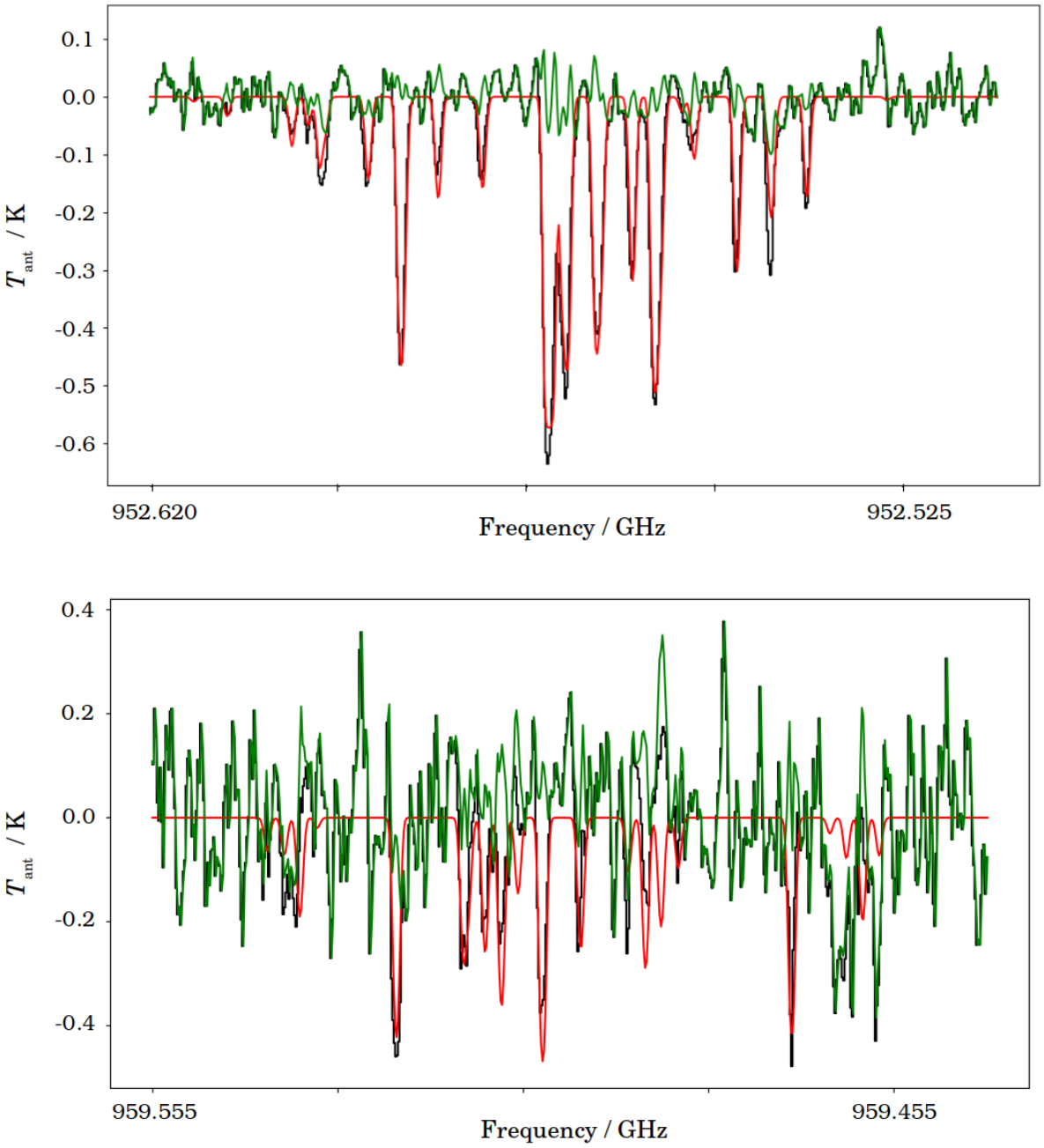

Figure 5.1: The $J = {}^3/_2 - {}^1/_2$ (*top panel*) and $J = {}^1/_2 - {}^1/_2$ (*bottom panel*) components of the $N_{Ka,Kc} = 1_{1,1} - 0_{0,0}$ transition of o-NH_2 as observed in absorption towards IRAS16293-2422. The synthetic spectrum (red trace) is plotted against the actual spectrum (black trace); residuals from the fit are shown in green. Intensities on the y-axis are given as function of the antenna temperature T_{ant}.

els [85]. Therefore our results indicate that an improvement of the models is required because some important formation channels are probably missing. Additionally, future observations (although complicated by the atmospheric opacity) would be desirable. The most intense tran-

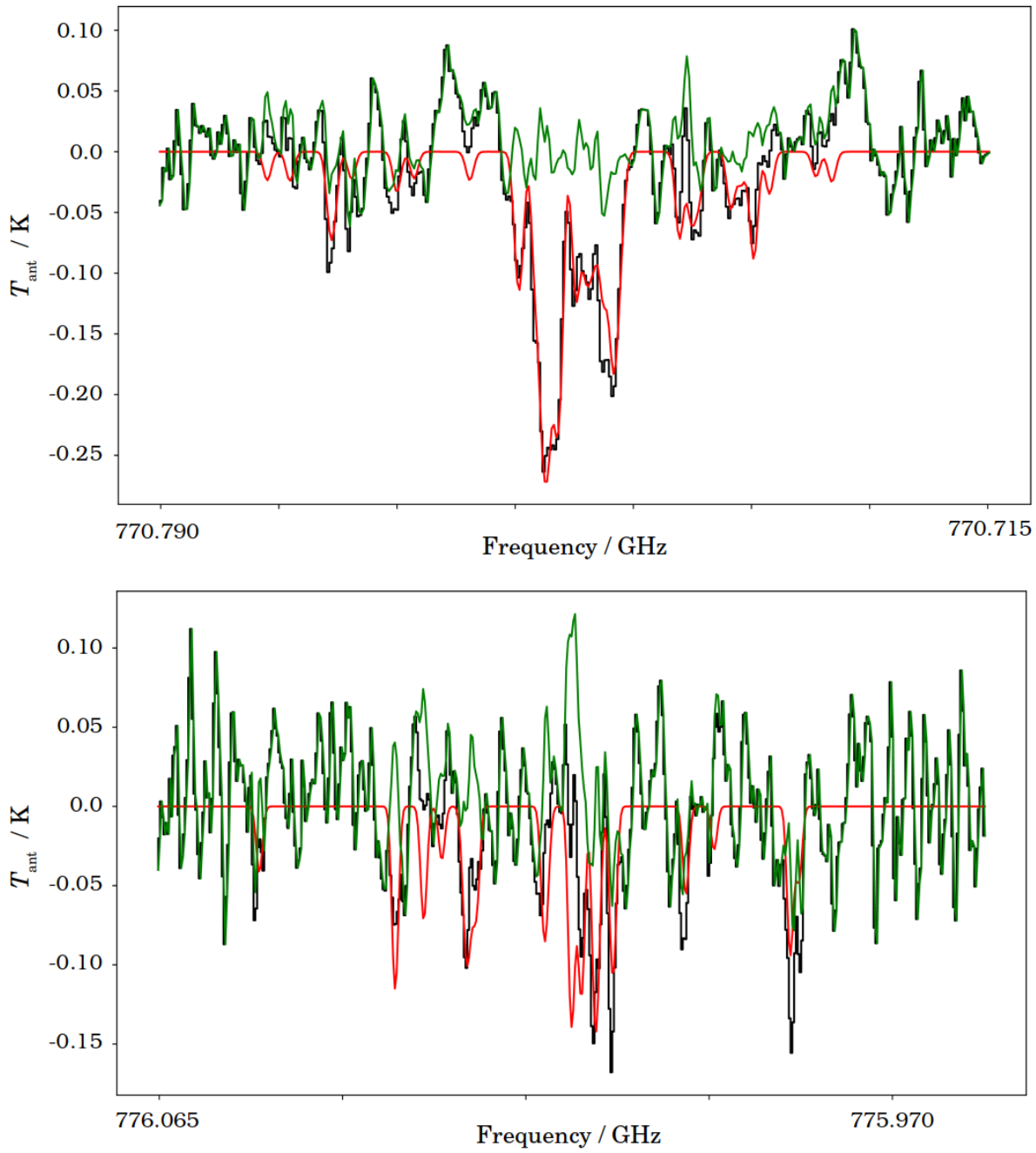

Figure 5.2: The $J = {}^3/_2 - {}^1/_2$ (*top panel*) and $J = {}^1/_2 - {}^1/_2$ (*bottom panel*) components of the $N_{Ka,Kc} = 1_{1,1} - 0_{0,0}$ transition of NHD as observed in absorption towards IRAS16293-2422. The synthetic spectrum (red trace) is plotted against the actual spectrum (black trace); residuals from the fit are shown in green.

sition of NHD located at 770 GHz is not accessible with the ground-based facilities working at present, because of a strong water absorption at this frequency. Thus, its observation can rely mainly on the *a*-type $N_{Ka,Kc} = 1_{0,1} - 0_{0,0}$ transition around 413 GHz (a frequency range covered by the ALMA 8 Band and the FLASH+ receiver of APEX). As for ND_2, the transitions

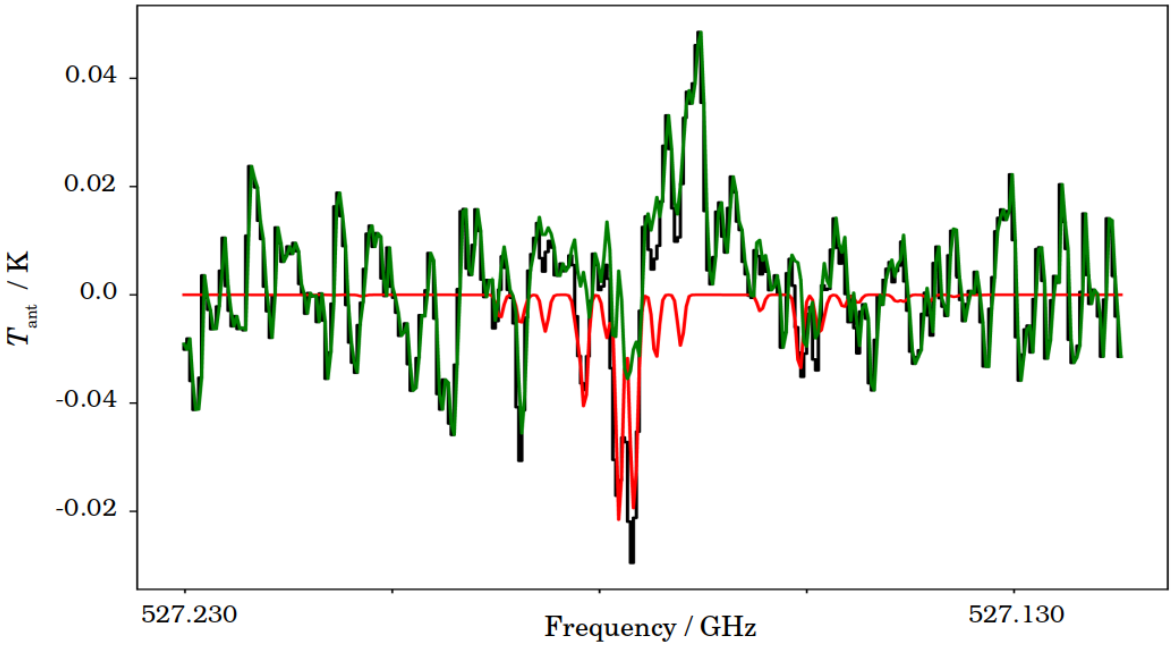

Figure 5.3: Same as Figure 5.2 but for *o*-ND_2.

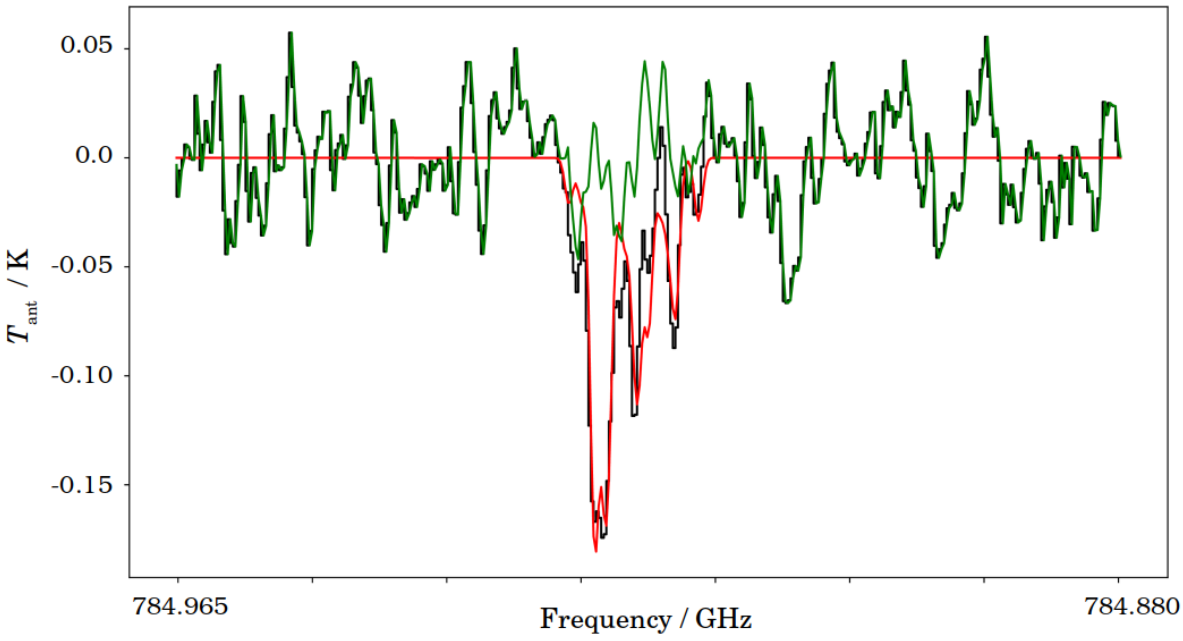

Figure 5.4: Same as Figure 5.3 but for the $J = {}^5/_2 - {}^3/_2$ component of the $N_{Ka,Kc} = 2_{0,2} - 1_{1,1}$ transition of *p*-ND_2.

detected in this work fall in spectral windows accessible either with the 4GREAT facility on board SOFIA (490–635 GHz) or ALMA 10 Band (787–950 GHz). This comprehensive study opens new perspectives for further observations of NHD and ND_2 in space, which would enable to make a step towards a more complete understanding of ammonia formation in the ISM.

5.2 Vibrationally excited aminoacetonitrile in Sagittarius B2

All the data contained in this Section are kindly shared by Dr. Arnaud Belloche, as part of a collaboration that join laboratory data with astronomical observation. These results will lead to a scientific publication (to be submitted to the *Astronomy & Astrophysics* journal), as soon as the ro-vibrational spectrum of aminoacetonitrile will be recorded and analysed (see §4.5.6).

The astronomical sample

Sagittarius B2 is a giant, chemically-rich molecular cloud located at 120 pc toward the center of our galaxy, the Milky Way. Sgr B2 is probably the largest molecular cloud in the vicinity of the core and one of the largest in the galaxy, spanning a region about 45 parsecs across. The internal structure of this cloud is very complex: it is divided into three main cores, north (N), main (M) and south (S), where Sgr B2(M) and Sgr B2(N) are sites of prolific star formation.
The cloud hosts various kinds of complex molecules. The surfaces of dust grains are thought to play a significant role in the network of chemical reactions in Sgr B2, especially in the production of COMs. Temperatures from 40 K to 300 K allow these molecules to evaporate from the grain-surface and join the gas-phase of Sagittarius B2. Almost half of all the known interstellar molecules were first found within Sgr B2, and nearly every other currently known molecule has since been observed in this source.

Spectral survey

We have used a complete spectral line survey toward Sgr B2(N1S), recorded with ALMA in the frequency range 84.1 GHz and 114.4 GHz (Band 3). More details about the observational setup are given in Table 1 of Ref. [131]. The observations were performed with a channel spacing of 244 kHz and each spectrum was smoothed to a resolution of 488 kHz (1.7 to 1.3 km/s at these frequencies). The beam sizes in the ReMoCa survey are 2.5 to 4 times smaller than those obtained with the EMoCA survey[115]. The sensitivity, in terms of flux density, is a factor of three times better.

Detection of aminoacetonitrile

We used the spectroscopic results described in § 4.5 to search for aminoacetonitrile toward Sgr B2(N1S), together with the spectral prediction available for the ground state [156]. The portions of the spectrum covered by the ReMoCa survey where we expect to detect rotational transitions above the noise level are shown in Figs. 5.5–5.7. Figure 5.5 shows the synthetic spectrum of NH_2CH_2CN in the ground vibrational state, computed assuming a temperature of 200 K, a line-width of 5.0 km/s, and systemic velocity of 62 km/s.
The matches between the synthetic and ReMoCA spectra are quite good, with coincident matches in those region where aminoacetonitrile signal is uncontaminated by other emissions. Many

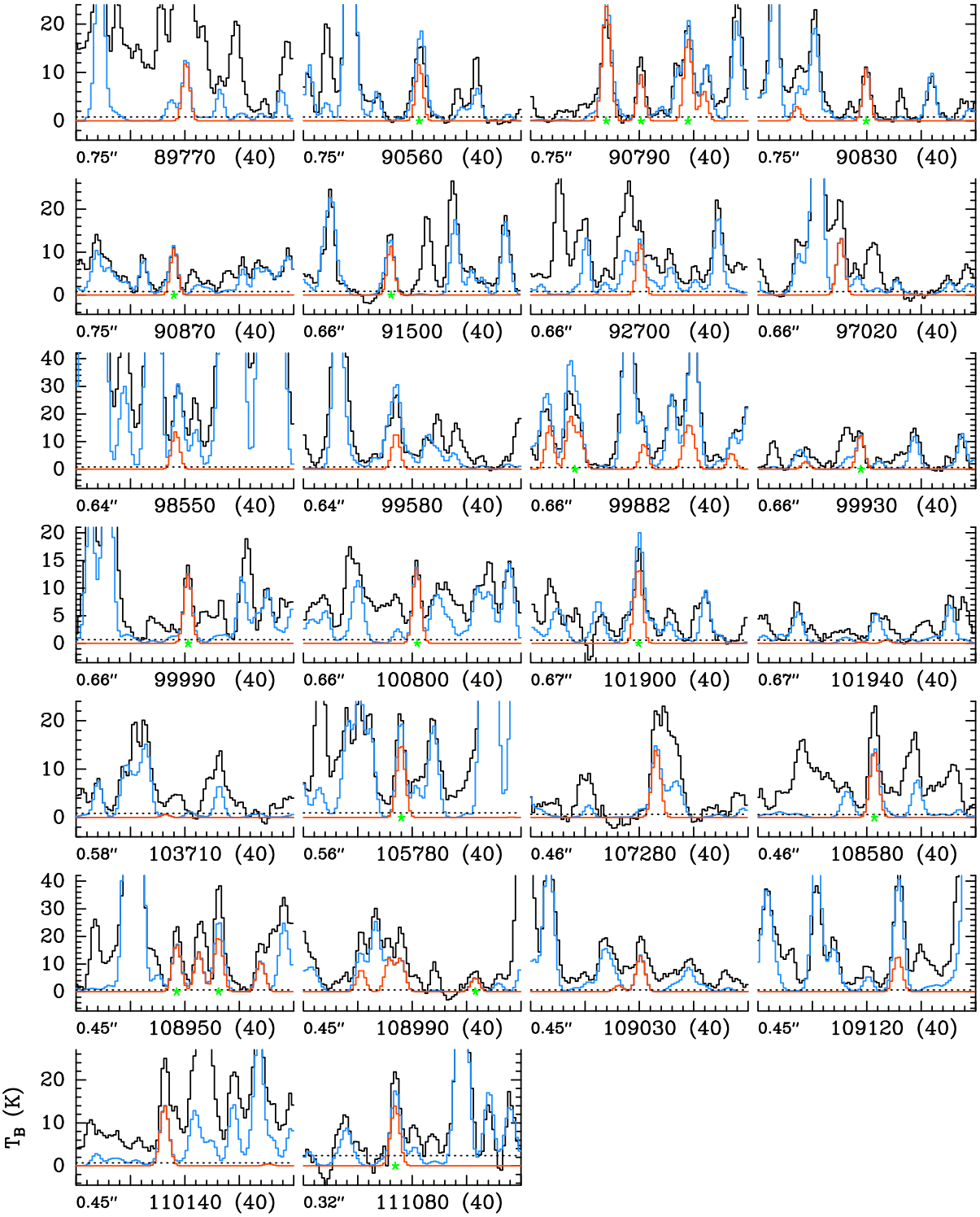

Figure 5.5: LTE spectrum of aminoacetonitrile in its ground vibrational state. The black trace is the actual spectrum, the red one is the spectrum simulated for NH_2CH_2CN only, and the blue synthetic spectrum contains the contributions of all molecules identified in the survey so far, including aminoacetonitrile.

transitions are blended or completely overlapped by stronger lines and cannot be unambigu-

ously identified, but eighteen transitions are clearly detected and they are marked with green stars in Fig. 5.5. These transitions are reported in Table 5.3 along with some spectroscopic information.

Moreover, five transitions arising from the resonant states $v_{11} = 1$ ($E_v \sim 216$ cm^{-1}) and $v_{18} = 1$ ($E_v \sim 249$ cm^{-1}) are detected without contamination from other signals. They are marked with green stars in Figure 5.6, which shows the synthetic spectrum expected for these two vibrationally excited states.

In addition to the ground and two lowest-lying excited states, we also searched for transitions from within the third vibrationally excited state ($v_{17} = 1, E_v \sim 370$ cm^{-1}). Unfortunately, only few transitions are predicted to be above the detection limit (3σ) but they are blended with stronger emissions of other species, thus preventing their identification (see Fig. 5.7).

The physical parameters used to fit the spectrum of aminoacetonitrile are reported in Table 5.4, together with those reported earlier [155] in Sgr B2(N).

A rotational diagram has also been built to assess the quality of the simulation.

One of the difficulties is that most transitions of aminoacetonitrile are contaminated to some extent by emission from other species. The fit of the ground state only (Fig. 5.8) is unconstrained, while the one including the $v_{11} = 1$ and $v_{18} = 1$ states (Fig. 5.9) yields a temperature of 250±50 K. This result is consistent with the excitation temperature assumed for the modeling (200 K). For each population diagram, the optical depth correction has been applied to both the observed and synthetic populations and the contamination by all other species has been removed from the observed data-points (right panels of Figs. 5.8–5.9).

Comparison between Sgr B2(N1S) and Sgr B2(N)

The previous line survey where aminoacetonitrile has been detected [155] was taken with the IRAM 30 m single-dish telescope, whose angular resolution is 25–30" at 100 GHz. This means that the IRAM 30 m spectrum of Sgr B2(N) contains the contributions of several hot cores (N1, N2, N3, and N4 [171]). The 30 m spectrum is dominated by N1, but it includes all scales probed in the 25–30" beam. Conversely, the ReMoCA spectral survey has a beam of 0.5", which is sufficient to spatially resolve the source N1. The continuum emission toward the source center is nearly optically thick, meaning that the molecular emission cannot be probed at very small scales toward the center. This is the reason why the source position analyzed is slightly offset to the south (see details in Ref. [131]), i.e. the N1S core.

It turns out that the modeling of the IRAM 30 m [155] and ReMoCA spectra of Sgr B2(N1) [131] can give different parameters because of all these effects. Thus, the ReMoCA data give more reliable results because the complex structure of the Sgr B2(N) region is better accounted. Table 5.4 reports the column density obtained for NH_2CH_2CN in Sgr B2(N1S) on the basis of the new ReMoCA survey. For comparison, the value obtained in Sgr B2(N) [155]. It can be readily seen that the newly determined column density is 3 times larger in Sgr B2(N1S) and also the temperature is constrained to a value 2 times higher than before (200 K *vs.* 100 K).

Table 5.3: Spectroscopic parameters and integrated intensities of aminoacetonitrile transitions detected toward Sgr B2(N1S) in the ReMoCA survey.

State	Transition	Frequency (Δf)[a] (MHz)	A_{ul}[b] (10^{-5} s^{-1})	E_u[c] (K)	g_u[d]	I_{obs}[e] (K km s^{-1})	I_{mod}[f] (K km s^{-1})	I_{all}[g] (K km s^{-1})
$v = 0$	$10_{2,9} - 9_{2,8}$	90561.324(2)	2.62	28.9	21	125.1(12)	64.1	135.0
$v = 0$	$10_6 - 9_6$	90783.530(3)	1.76	68.3	21	166.1(13)	154.3	179.6
$v = 0$	$10_5 - 9_5$	90784.276(3)	2.07	54.8	21	–	–	–
$v = 0$	$10_7 - 9_7$	90790.250(3)	1.41	84.3	21	78.5(12)	52.1	53.6
$v = 0$	$10_{4,7} - 9_{4,6}$	90798.679(2)	2.31	43.7	21	156.2(12)	101.0	159.1
$v = 0$	$10_{4,6} - 9_{4,5}$	90799.243(2)	2.31	43.7	21	–	–	–
$v = 0$	$10_{3,8} - 9_{3,7}$	90829.939(2)	2.51	35.1	21	73.3(12)	59.3	60.8
$v = 0$	$10_{3,7} - 9_{3,6}$	90868.033(2)	2.51	35.1	21	70.8(12)	59.3	72.6
$v = 0$	$10_{2,8} - 9_{2,7}$	91496.110(2)	2.71	29.0	21	84.6(12)	62.8	84.7
$v = 0$	$11_5 - 10_5$	99869.305(3)	2.92	59.6	23	251.1(11)	169.4	342.9
$v = 0$	$11_7 - 10_7$	99871.143(3)	2.19	89.1	23	–	–	–
$v = 0$	$11_{3,9} - 10_{3,8}$	99928.881(3)	3.41	39.9	23	86.5(9)	67.3	73.4
$v = 0$	$11_{3,8} - 10_{3,7}$	99990.562(3)	3.42	39.9	23	80.5(9)	67.6	71.2
$v = 0$	$11_{2,9} - 10_{2,8}$	100800.879(3)	3.66	33.8	23	90.0(9)	73.1	76.7
$v = 0$	$11_{1,10} - 10_{1,9}$	101899.797(3)	3.88	30.6	23	113.4(8)	75.4	135.7
$v = 0$	$12_{1,12} - 11_{1,11}$	105777.966(3)	4.36	34.3	25	133.3(12)	83.6	113.6
$v = 0$	$12_{2,11} - 11_{2,10}$	108581.402(3)	4.62	38.9	25	144.0(8)	74.5	83.1
$v = 0$	$12_6 - 11_6$	108948.516(3)	3.60	78.4	25	137.4(9)	96.1	101.6
$v = 0$	$12_5 - 11_5$	108956.211(3)	3.97	64.8	25	205.7(8)	107.4	144.5
$v = 0$	$12_{10} - 11_{10}$	109001.592(4)	1.47	157.1	25	51.2(9)	27.0	28.1
$v = 0$	$12_{1,11} - 11_{1,10}$	111076.901(3)	5.05	36.0	25	127.1(29)	76.0	106.4
$v_{18} = 1$	$10_5 - 9_5$	90906.892(20)	2.07	410.6	21	46.0(11)	26.8	31.4
$v_{18} = 1$	$10_6 - 9_6$	90906.892(20)	1.77	424.4	21	–	–	–
$v_{11} = 1$	$10_7 - 9_7$	91000.408(20)	1.41	389.9	21	11.8(9)	10.1	12.8
$v_{11} = 1$	$11_7 - 10_7$	100102.569(20)	2.21	394.7	23	58.4(11)	38.2	46.8
$v_{11} = 1$	$11_5 - 10_5$	100104.598(20)	2.94	365.4	23	–	–	–
$v_{11} = 1$	$11_{1,10} - 10_{1,9}$	102166.400(20)	3.91	336.7	23	33.3(7)	16.6	25.5
$v_{11} = 1$	$12_5 - 11_5$	109213.482(20)	3.99	370.6	25	45.0(9)	37.3	50.0
$v_{11} = 1$	$12_8 - 11_8$	109214.610(20)	2.69	418.2	25	–	–	–

[a] Frequency uncertainty. **[b]** Einstein coefficient for spontaneous emission. **[c]** Upper-level energy. **[d]** Upper-level degeneracy. **[e]** Integrated intensity of the observed spectrum in brightness temperature scale. The statistical standard deviation is given in parentheses in unit of the last digit. **[f]** Integrated intensity of the synthetic spectrum of NH_2CH_2CN. **[g]** Integrated intensity of the model that contains the contribution of all identified molecules, including NH_2CH_2CN.

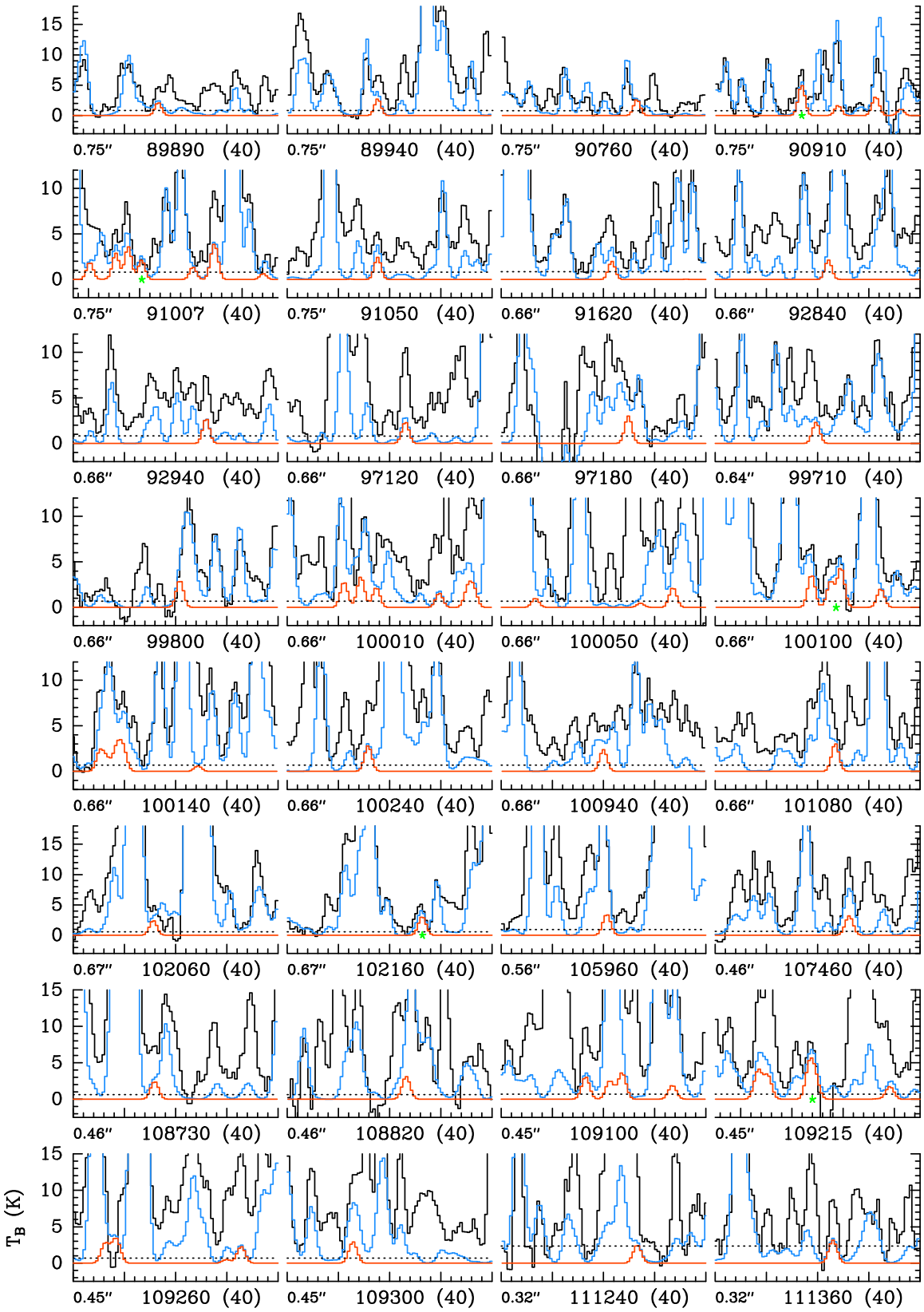

Figure 5.6: LTE spectrum of aminoacetonitrile in the resonant vibrational states $v_{11} = 1$ and $v_{18} = 1$.

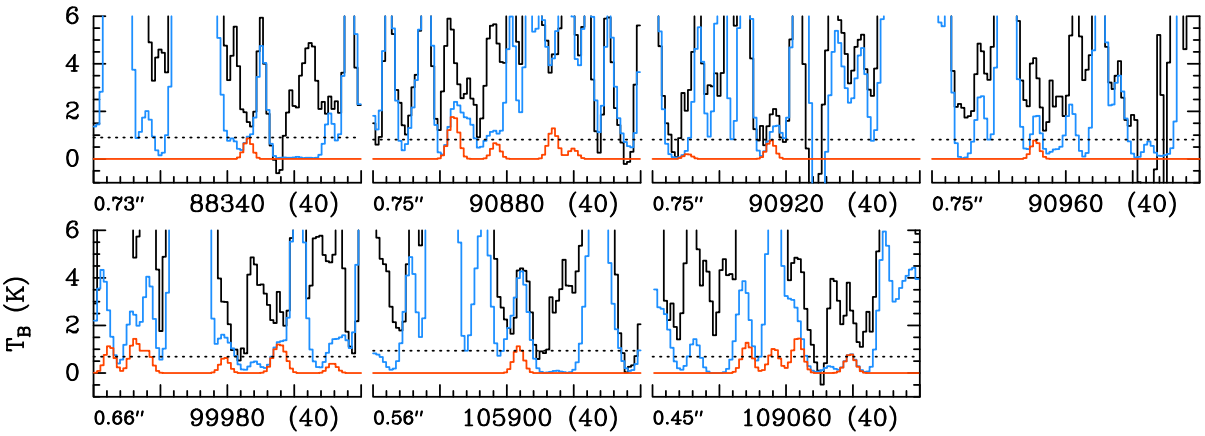

Figure 5.7: LTE spectrum of aminoacetonitrile in the vibrational state $v_{17} = 1$.

Table 5.4: Parameters used to compute the synthetic spectrum.

Source	N (cm^{-2})	T (K)	Size[a] (")	Vel. (km/s)	FWHM (km/s)	Reference
Sgr B2(N1S)	8.7×10^{16}	200	2.0	62	5.0	This work
Sgr B2(N2)	2.8×10^{16}	100	2.0	64	7.0	Ref. [155]

[a] Source diameter.

Results

We used the complete 3 mm line survey (84.1–114.4 GHz) obtained with ALMA toward the hot-core Sgr B2(N1S) to search for aminoacetonitrile signatures. Specifically, we have searched for emission arising from aminoacetonitrile in its ground and the three low-lying ($v_{11} = 1$, $v_{17} = 1$, and $v_{18} = 1$) vibrational states.

We report the detection of the pre-biotic molecule aminoacetonitrile toward this source, which is the second detection of this molecule in the ISM and the first astronomical observation of vibrationally excited lines.

These observations are based on the spectroscopy described in § 4.5 and on previous works [154, 156]. Eighteen ground state and five excited states transitions (from $v_{11} = 1$ and $v_{18} = 1$) are free of any contamination and clearly detected. We failed to detect any emission from aminoacetonitrile in the $v_{17} = 1$ state, which is the highest in energy ($E_v \sim 370$ cm^{-1}), because the few lines expected to be above the detection level are contaminated by stronger transitions of other species.

An aminoacetonitrile column density of 8.7×10^{16} cm^{-2} has been derived for a temperature of 200 K and a linewidth of 5 km/s. Such temperature is much more constrained with respect to previous observations and justifies the detection of vibrationally hot lines. Also, the column density results to be 3 times larger in Sgr B2(N1S). The high abundance and temperature seem

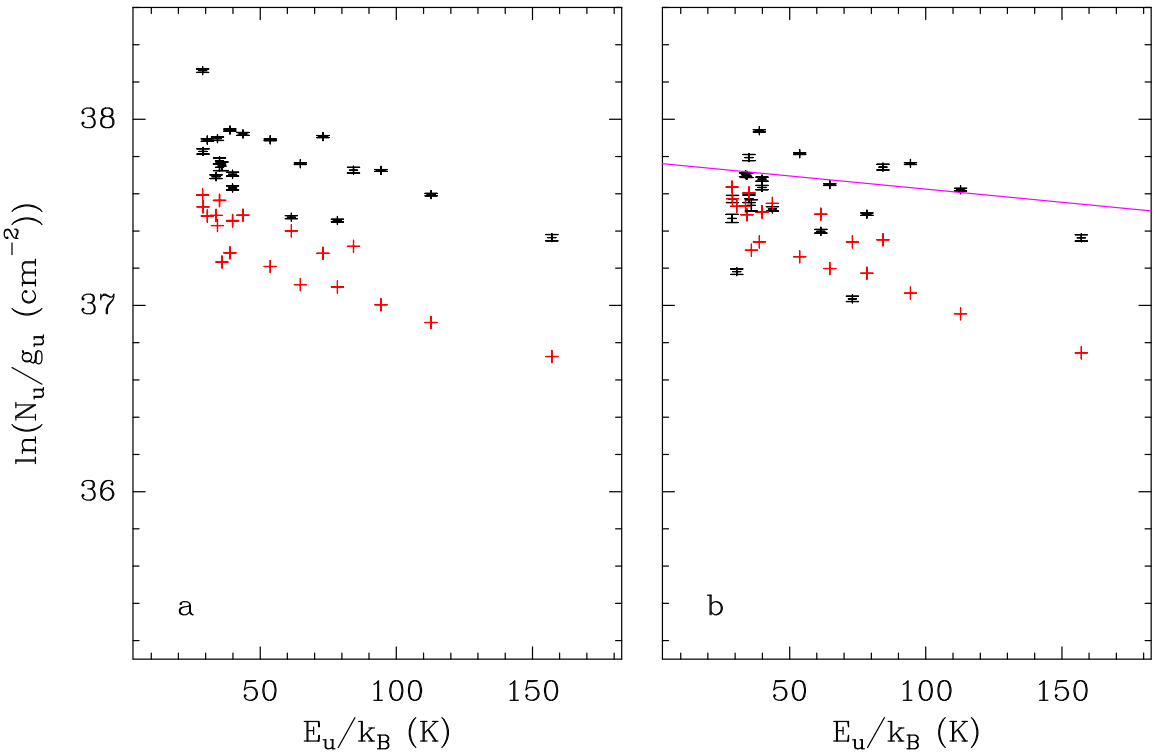

Figure 5.8: Rotational diagram of NH_2CH_2CN in its ground state. Experimental points are indicated in black, while the synthetic population is depicted in red. The purple line is a linear fit to the observed populations.

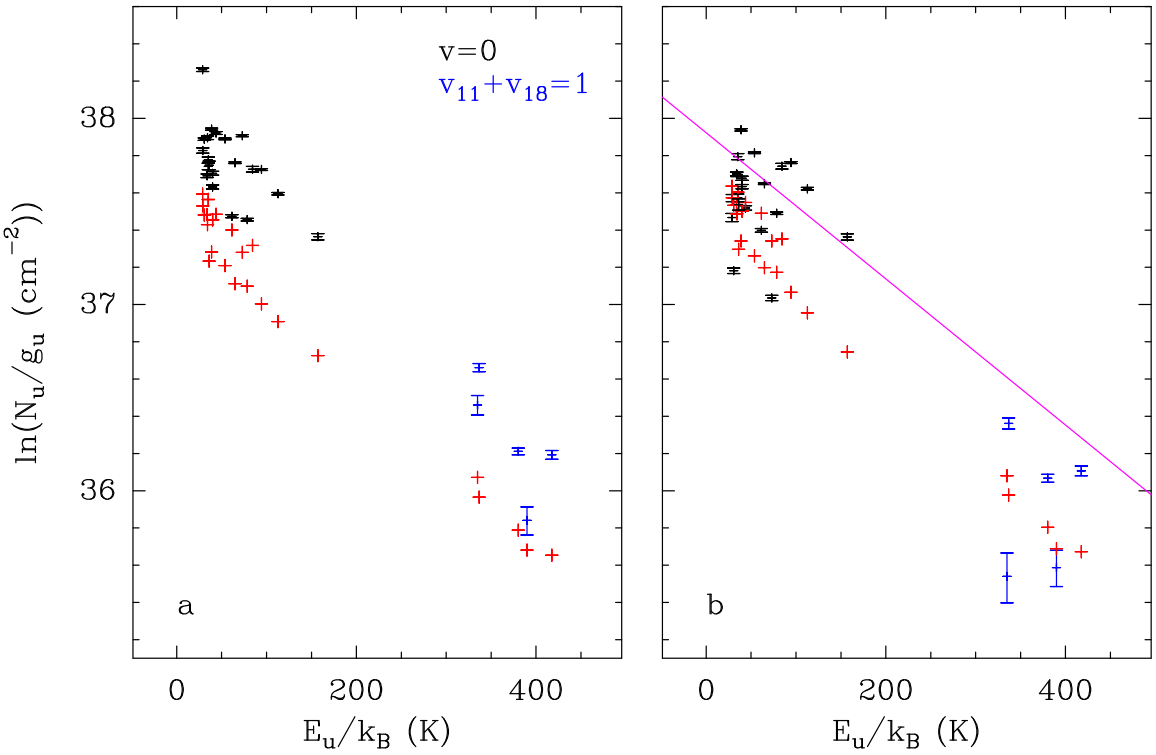

Figure 5.9: Same as Fig. 5.8 with the inclusion of excited state emissions (in blue).

to confirm that aminoacetonitrile is formed by grain-surface chemistry and the released into the gas-phase.

Lastly, our future objective is to experimentally determine the energy of the $v_{11} = 1$ and $v_{18} = 1$ states from the FIR spectrum of NH_2CH_2CN, in order to better evaluate the partition function $U(T)$ and column density values for aminoacetonitrile.

6 Conclusions

Of the more than 200 molecules detected in the interstellar medium to date, more than 80% were discovered through observations of their pure rotational transitions. With few exceptions, the detection and characterization of molecules in the ISM is preceded by high-resolution spectroscopic investigations in the laboratory. It is evident that spectroscopy and astrochemistry are interdisciplinary subjects which allow astronomers to study celestial objects in many ways.
Each chemical species is an helpful tracer of evolutionary stages of stars and some of them represent a good proxy for inferring physical properties of a cloud, such as temperature, density, or shape. Besides the fascination of a new detection of interstellar molecules, astrochemical observations are crucial to constraint chemical models in astronomy.
In this thesis, I have presented the spectroscopic characterization of small nitrogen-containing species of astrochemical relevance, from diatomic radicals to complex organic molecules. Any of these studies aimed at reproducing the ro-vibrational energy levels of these species, in order to assist their astronomical observations with radio-telescopes. Generally speaking, the interpretation of rotational spectra may be complicated by the existence of resonances, spin-rotation couplings, and other factors. The use of suitable Hamiltonians and a bit of experience are good ingredients to disentangle such complexity. Moreover, the accuracy reached by high-resolution molecular spectroscopy cannot be replaced by quantum-chemical calculations or other *ab initio* predictions. This is why I would like to stress out the need for dedicated laboratory spectroscopy to support and exploit future molecular line observations with new upcoming facilities, especially those working at high-frequencies, i.e., up to the THz domain.
Among the results obtained in the last three years, I have reported the first astronomical detection of two deuterated radicals, NHD and ND_2. These substituted forms of amidogen radical were expected to be present in the interstellar medium but they were unobserved, mainly because an important piece of laboratory data was missing. Thanks to our studies, it was possible to clearly identify molecular absorptions of these species towards the pre-stellar core IRAS16293-2422, as recorded by the Herschel Space Observatory mission. These observations confirm the strong deuterium enhancement generally observed in this cloud but they reveal that models underestimate the abundances of NHD and ND_2. It would be desirable to have further astrochemical observation of deuterated amidogen radical in different clouds in order to better understand the chemical processes which lead to the formation of ammonia and its progenitor.
Another important outcome was the interstellar detection of vibrationally hot aminoacetonitrile. As explained before (§ 4.2), NH_2CH_2CN is considered the closest precursor of glycine, the simplest amino acid. One of the main aim of astrochemistry, indeed, is the search of prebiotic molecules, i.e., those molecules which are building blocks for the development of life as we know it. Aminoacetonitrile has already been detected in Sagittarius B2(N2) more than 10 years ago. To date, it was the unique detection of this molecule. Our recent spectroscopic study allowed the search and the discovery of molecular lines belonging to aminoacetonitrile in its

low-lying vibrational excited states towards Sgr B2(N1S). The high abundance and temperature observed in this thesis seem to confirm that aminoacetonitrile is formed by grain-surface chemistry and the released into the gas-phase; this represents a small step toward the comprehension on how complex organic molecules are formed and which processes can lead to the formation of glycine.

These new discoveries should encourage new laboratory studies, in several directions. The isotopic fractionation processes are one of the most interesting, because it is known the isotopic ratios in Space change from region to region. Deuterium, ^{13}C, and ^{15}N-substituted species are often targeted in astronomical observations, so they are good candidate to be studied by spectroscopists.

Another interesting class is constituted by pre-biotic molecules. With the aim of understanding the origin of life, any species related to amino acids, nucleic acid, or other biological molecules offer a starting point from which the chemical complexity increases. In general, this family is composed by molecules containing carbon, nitrogen, and oxygen, three elements considered essential for life. Also, phosphorous-containing species have recently been included because of its biological role.

The last kind of species I would like to mention is unstable molecules. Interstellar environments are quite different from the terrestrial ones and this results, of course, in different chemical compositions. Radical and ions can survive only for very short periods on Earth, while they can be abundant in the ISM. For sure, there would be constituents of molecular clouds which are hard to be studied, and produced, in laboratory. To this regard, it is important to equip our spectrometers with systems which efficiently produce unstable species.

In my thesis, I have mainly mentioned electric discharge and a laser ablation systems for the production of radicals. Other feasible techniques, for example, are thermolysis, photolysis, and pyrolysis. Our submillimeter spectrometer in Bologna is connected to a quartz reactor surrounded by a 1200°C oven for Flash Vacuum Pyrolysis experiments. This system has been used successfully for the production and the study of a number of semi-stable molecules (some of them are reported in the **Appendixes**). However, not all the species formed in the pyrolysis mixture survive before entering the absorption cell: radicals and ions are quickly destroyed by collisions.

Future plans for our laboratory consist in the building of a new absorption cell that will allow us to (i) study the whole pyrolysis mixture at temperatures up to 1300°C and (ii) perform high-temperature spectroscopic studies. The cell (6 cm in diameter) will be made out of quartz and surrounded by a 1 meter-long oven. In this way, the electromagnetic radiation passing through the cell will probe every species formed during the pyrolysis.

Hopefully, the new set-up will open new perspectives on the spectroscopic characterization of astrophysical important species. Our efforts will focus on the study of new radicals and vibrational excited states of molecules present in warm region of the interstellar medium.

7 Appendixes

7.1 Infrared and Millimeter Spectra of Trifluoroethene in some Vibrational Excited States

In the last decades, great attention has been devoted to the search for suitable replacements of those gases used for domestic and industrial purposes which strongly contribute to atmospheric pollution, in particular to the ozone hole and to the greenhouse effect. Unsaturated hydrofluoroolefins (HFO's) are interesting alternatives to chlorofluorocarbons.
The atmospheric importance of trifluoroethene (CF_2=CHF) has stimulated a number of spectroscopic papers. We report a combined microwave and infrared investigation carried out on trifluoroethene, an asymmetric top molecule. The rotational spectra were recorded using a frequency-modulation millimeter spectrometer. Extensive measurements and assignments were made for the ground and the low-lying vibrational states. Accurate spectroscopic constants were obtained from the analysis of thousand lines recorded in the frequency ranges 80–96 and 245–260 GHz. The high-resolution (0.004 cm^{-1}) FT-IR spectra were studied in the region and 450–1600 cm^{-1}; besides the assignments of the fundamentals, absorptions coming from the hot bands were identified.

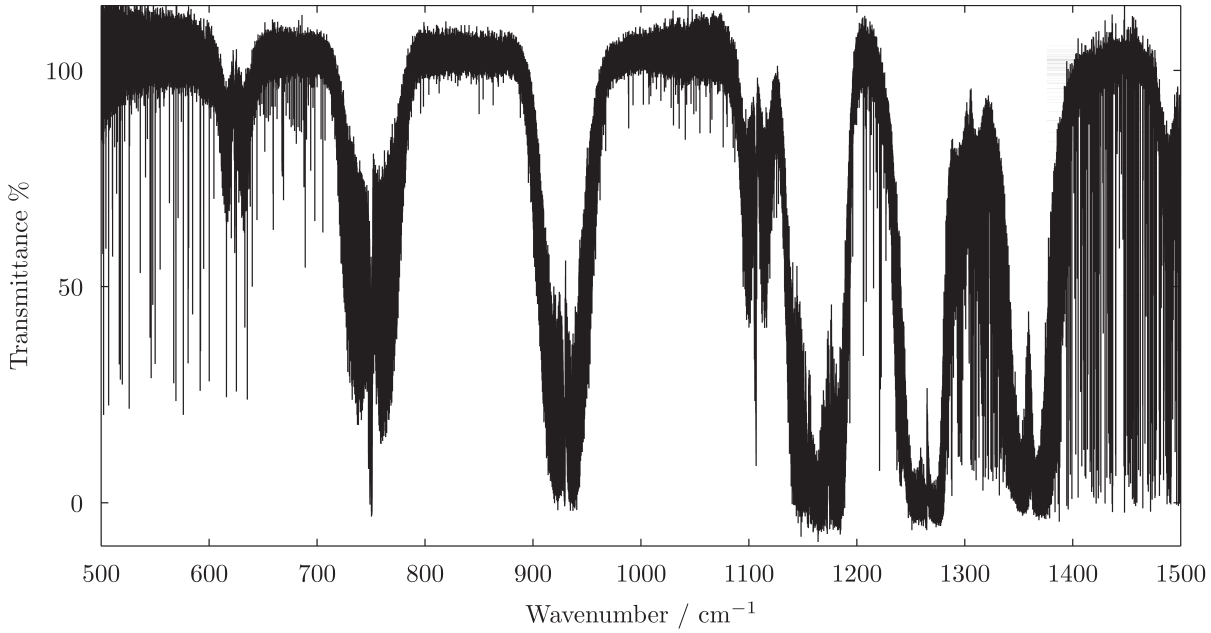

Figure 7.1: Portion of the infrared spectrum of trifluoroethene recorded at P = 0.8,Torr, L = 3 m, 800 scans).

Also, a lower resolution spectrum (0.01 cm^{-1}) was recorded and assigned in the region (200–400 cm^{-1}) of the two lowest fundamentals ν_9 and ν_{12}. The manuscript is currently on the writing stage and will be submitted to the *Journal of Quantitative Spectroscopy and Radiative Transfer*.

7.2 The THz Spectrum of Ethylene Glycol and Application to ALMA Band 10 Spectral Line Data of NGC 6334I

The rotational spectrum of the most stable conformer of ethylene glycol (*aGg'* $HO(CH_2)_2OH$) has been recorded between 360–890 GHz using a frequency-modulation submillimeter spectrometer. The refinement and extension of the spectroscopic parameters over previous efforts provides predicted catalog frequencies for ethylene glycol with sufficient accuracy for comparison to high-frequency astronomical data. The improvement in the cataloged line positions, and the need for improved accuracy enabled by high-frequency laboratory work, is demonstrated by an analysis of ethylene glycol emission at 890 GHz in the high-mass star-forming region NGC 6334I using in ALMA Band 10.

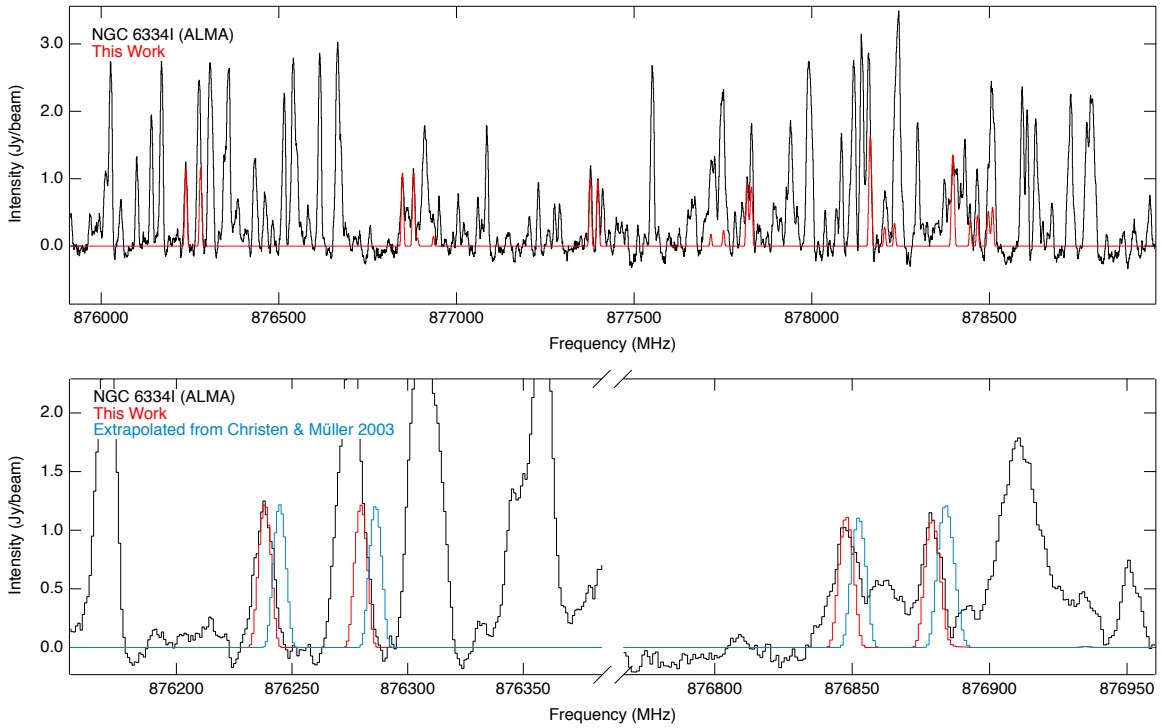

Figure 7.2: **(Top)** ALMA spectra of NGC 6334I in Band 10, with simulated lines of EG from the analysis carried out in this work overlaid in red. The simulation was performed at T_{exc} = 135 K, ΔV = 3.2 km s^{-1}, and v_{LSR} = -7 km s^{-1}. **(Bottom)** ALMA spectra of NGC 6334I in Band 10, again with simulations from this work in red and using the constants derived by Christen & Müller [172] inverted and in blue, zoomed in to show the frequency disagreement.

The manuscript has just been accepted for publication in *The Journal of Physical Chemistry A* (DOI: 10.1021/acs.jpca.9b10803).

7.3 Lamb-dip Spectroscopy of $CH_2D^{35}Cl$ and $CH_2D^{37}Cl$

When a monochromatic radiation crosses two times the absorption cell in the so-called "double-pass configuration" and the sample pressure is kept low (saturation regime), the resulting line profile is distorted because of optical saturation. More precisely, a depletion centered at the rest frequencies of each absorption transition is observed [173]. This effect is known as Lamb-dip and its advantage consists in the fact that the dip does not show a Doppler broadening. As result, line positions are measured with enormous accuracy even at high frequencies. In this work we exploited the Lamb-dip technique to study the millimeter spectra of $CH_2D^{35}Cl$ and $CH_2D^{37}Cl$, which were unknown. Hundreds transitions, both *a*- and *b*-type, were recorded for each isotopologues. The hyperfine structure, caused by the presence of the non-vanishing nuclear spin of Cl, has been resolved in most cases, as shown in Figure 7.3.

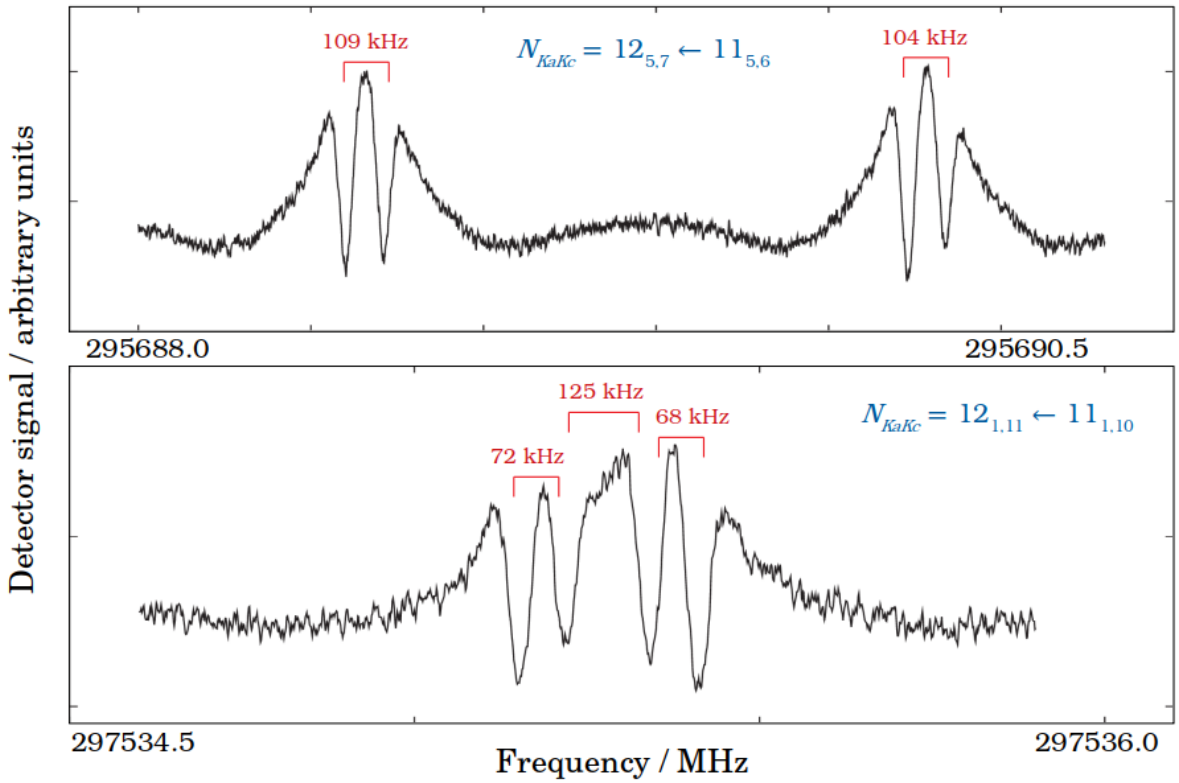

Figure 7.3: Two transitions of $CH_2D^{35}Cl$ recorded in the Lamb-dip regime. The size of each hyperfine splitting is indicated for clarity.

Chloromethane (CH_3Cl) is the simplest CFC and has known to be present in our atmosphere since a long time. More recently, it has also been observed in the ISM for the first time. Together with CH_3F, it has been detected in the gas surrounding the low-mass protostar IRAS16293-2422 using ALMA. Since this object is one of the richest source of deuterated species in the ISM, a dedicated search of CH_2DCl in some IRAM 30 m spectral surveys will be performed in the early 2020.

7.4 Rotational and Infrared Spectroscopy of Ethanimine: a Route toward its Astrophysical and Planetary Detection

Ethanimine (CH_3CHNH), a possible precursor of amino acids, is considered an important prebiotic molecule and thus may play important roles in the formation of biological building-blocks in the interstellar medium. In addition, its identification in Titan's atmosphere would be important for understanding the abiotic synthesis of organic species. An accurate computational characterization of the molecular structure, energetics and spectroscopic properties of the *E* and *Z* isomers of ethanimine has been carried out by means of a composite scheme based on coupled-cluster techniques, which also accounts for extrapolation to the complete basis-set limit and core-valence correlation correction, combined with density functional theory for the treatment of vibrational anharmonic effects.

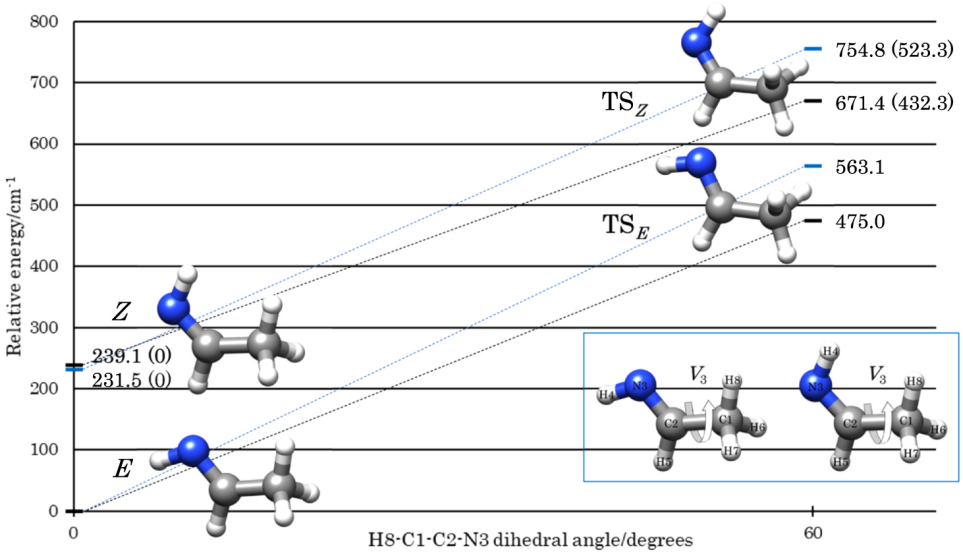

Figure 7.4: Equilibrium (CCSD(T)/CBS+CV, in black) and ZPE-corrected (B2PLYP-D3BJ/maug-cc-pVTZ-*d*H, in blue) energies for the *Z* isomer minimum and methyl internal rotation transition states (TS_E, TS_Z) with respect to *E*-CH_3CHNH. Values in parentheses are referred to the *Z* isomer.

By combining the computational results with new millimeter-wave measurements up to 300 GHz, the rotational spectrum of both isomers can be accurately predicted in the millimeter-wave region. Furthermore, our computations allowed us to revise the infrared spectrum of both *E*- and *Z*-CH_3CHNH, thus predicting all fundamental bands with high accuracy. This work has been published in *The Astrophysical Journal* (Melli *et al.*, **855**:123, 10pp, 2018).

7.5 Semi-Experimental Equilibrium Structure of Phosphapropyne from Spectroscopy of CH_3CP and CD_3CP

Trideuterated 1-phosphapropyne (CD_3CP) has been produced by co-pyrolysis of phosphorus trichloride and esadeuterated ethane. The rotational spectra of CD_3CP in the ground and the low-lying vibrational states v_8 (CCP bending mode) and $2v_8$ have been investigated in the millimeter-wave region. Very accurate values of the quartic centrifugal distortion constants D_J and D_{JK} and of the sextic distortion constants H_{JK} and H_{KJ} have been obtained for the ground state. l-type resonance effects have been taken into account in the analysis of the spectra of the degenerate bending states, so that the energy difference between the $v_8^{|l|} = 2^0$, and $v_8^{|l|} = 2^2$ states could be determined, together with a number of spectroscopic constants involved in the l-type resonance. Moreover, for the parent isotopologue CH_3CP a new set of excited-state lines ($v_8 = 1$, 2 and $v_4 = 1$) were recorded up to 330 GHz, and a global analysis including all available rotational and ro-vibrational transitions related to the ground and $v_8 = 1$, 2 states has been performed. A satisfactory fit could only be obtained by making a reassignment of the few transition wavenumbers previously measured for the $2v_8^0 \leftarrow v_8^{\pm 1}$ hot band [174].
The experimental work has been combined with quantum-chemical computations. Quadratic and cubic force constants of 1-phosphapropyne have been calculated at MP2 level of theory with a basis set of triple-ζ quality. A semi-experimental equilibrium structure has been derived by correcting experimental ground-state rotational constants by means of theoretical vibration-rotation interaction constants.

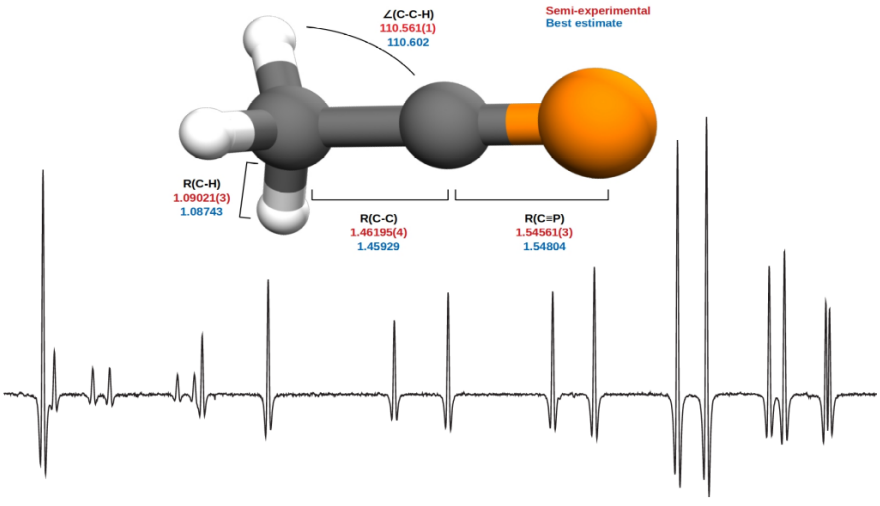

Figure 7.5: Portion of the millimeter-wave spectrum of CH_3CP overlaid to the best equilibrium structures of 1-phosphapropyne.

The manuscript has just been accepted for publication in the *Journal of Molecular Structure* (DOI: 10.1016/j.molstruc.2019.127429).

7.6 Rotational and High-resolution Infrared Spectrum of HC_3N: a Global Ro-vibrational Analysis

Cyanoacetylene (HC_3N) is an ubiquitous molecule in interstellar environments, from external galaxies, to Galactic interstellar clouds, star forming regions, and planetary atmospheres. Observations of its rotational and vibrational transitions provide important information on the physical and chemical structure of the above environments. We have recorded the high-resolution infrared spectrum from 450 to 1350 cm^{-1}, a region dominated by the intense ν_5 and ν_6 fundamental bands, located at 660 and 500 cm^{-1}, respectively, and their associated hot bands. Pure rotational transitions in the ground and vibrationally excited states have been recorded in the millimeter and submillimeter regions in order to extend the frequency range so far considered in previous investigations. This work represents the most complete global analysis of the spectroscopic data of HC_3N. All the transitions from the literature and from this work involving energy levels lower than 1000 cm^{-1} have been fitted together to an effective Hamiltonian. Because of the presence of various anharmonic resonances, the Hamiltonian includes a number of interaction constants, in addition to the conventional rotational and vibrational *l*-type resonance terms. The data set contains about 3400 ro-vibrational lines of 13 bands and some 1500 pure rotational lines belonging to 12 vibrational states. An extensive list of highly accurate rest frequencies has been produced to assist astronomical searches and data interpretation. These improved data, have enabled a refined analysis of the ALMA observations towards Sgr B2(N2).

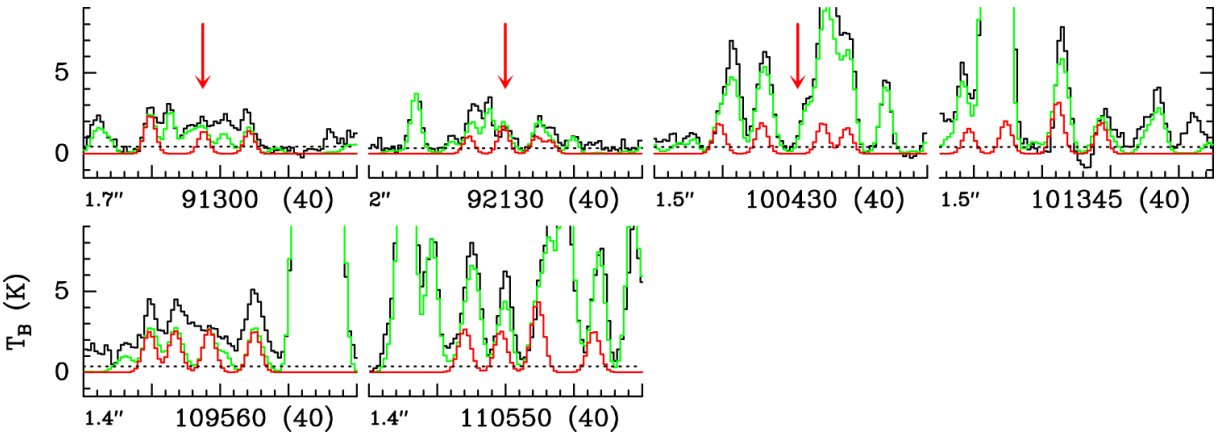

Figure 7.6: Transitions of HC_3N, $v_4 = 1$ covered by the EMoCA survey. The best-fit LTE synthetic spectrum of HC_3N is displayed in red and overlaid on the observed spectrum of Sgr B2(N2), shown in black. The green synthetic spectrum contains the contributions of all molecules identified in the survey. The arrows mark lines where the new spectroscopic predictions improve the agreement between the synthetic and observed spectra.

This work has been published in *The Astrophysical Journal Supplement Series* (Bizzocchi *et al.*, **233**:11, 20pp, 2017).

7.7 Laboratory Measurements and Astronomical Search of C-cyanomethanimine

C-cyanomethanimine (HNCHCN), existing in the two *Z* and *E* isomeric forms, is a key prebiotic molecule. Prior to our work, only the *E* isomer had been detected toward the massive star-forming region Sgr B2(N). With the aim of detecting HNCHCN in Sun-like-star forming regions, the laboratory investigation of its rotational spectrum has been extended to the millimeter-/submillimeter-wave spectral window in which several unbiased spectral surveys have been already carried out. We then searched for the C-cyanomethanimine spectral features in the mm-wave range using the high-sensitivity and unbiased spectral surveys obtained with the IRAM 30-m antenna in the ASAI context, the earliest stages of star formation from starless to evolved Class I objects being sampled. Unfortunately, no C-cyanomethanimine emission has been detected toward the ASAI targets, and upper limits of the column density of $\sim 10^{11}$–10^{12} cm^{-2} could only be derived.

After our work, the first detection in the ISM of the *Z*-isomer of C-cyanomethanimine has been reported towards the Galactic Centre quiescent molecular cloud G+0.693 with the IRAM 30m telescope, thanks to the identification of six transitions around 100 GHz.

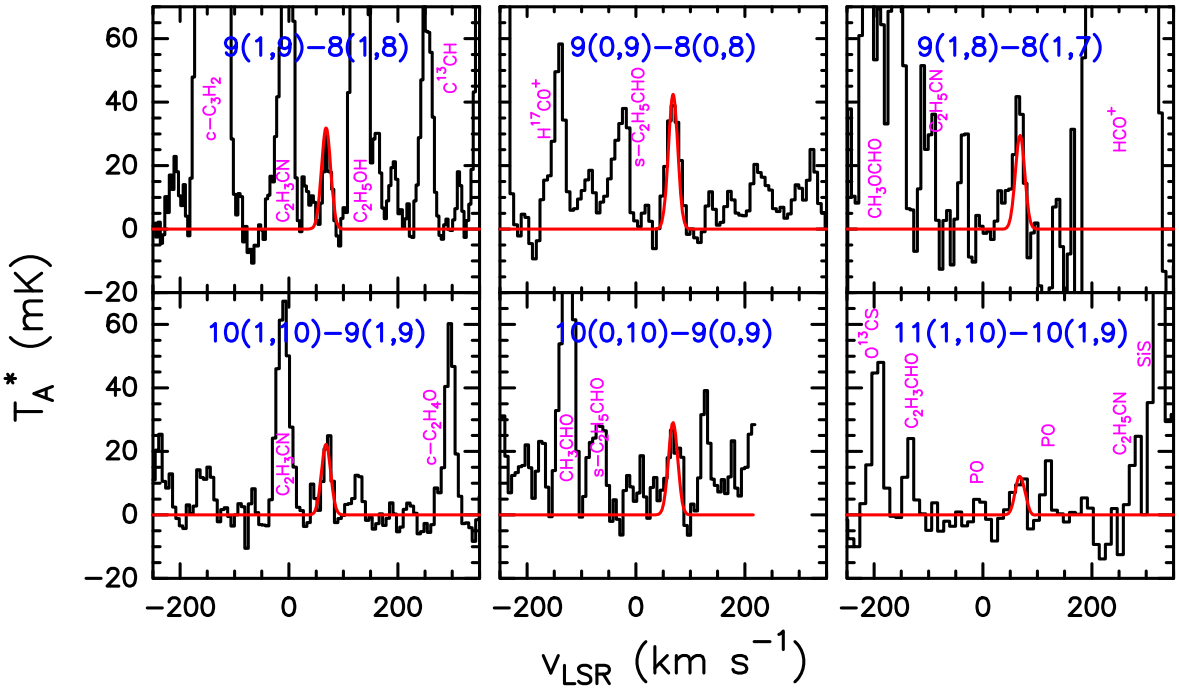

Figure 7.7: IRAM 30m spectra of *Z*-cyanomethanimine towards G+0.693. The red curves correspond to the LTE best fit obtained with T_{ex} = 8 K, ΔV = 20 km s^{-1}, v_{lsr} = 68.3 km s^{-1}, and N = 2×10^{14} cm^{-2}. The quantum numbers of each transition are shown in blue in each panel. Other molecular species identified in the spectra are also indicated.

7.8 Unveiling Deuterium Splittings in the Hyperfine Structure of NH_2D with Lamb-dip Spectroscopy

Recently, the analysis of rotational lines of interstellar NH_2D has been revised to take into account the hyperfine splitting caused by the deuterium nucleus [175]. The study was motivated by the inconsistencies found between the line widths of the transitions around 3 mm and those at 1 mm, probably originating from the negligence of D splittings.

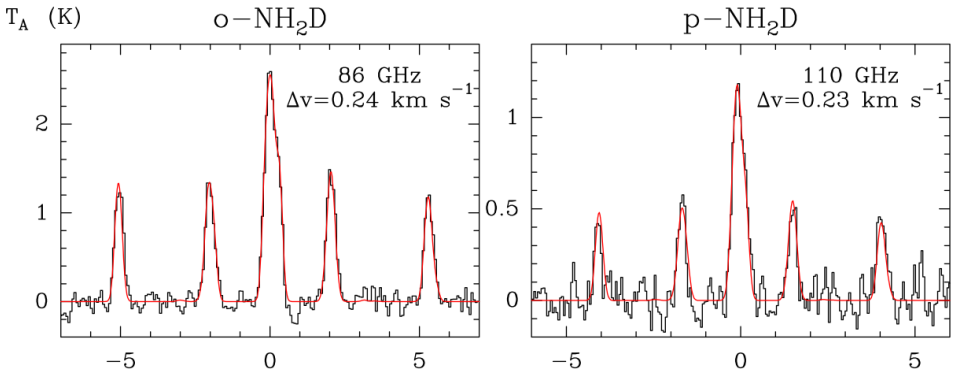

Figure 7.8: Fits of o-NH_2D and p-NH_2D lines at 86 and 110 GHz, respectively.

The authors pointed out that such negligence leads to an overestimation of the linewidth of about 50%, which reflects directly on the derived column densities. We decided to re-investigate the millimeter spectrum of deuterated ammonia NH_2D with the Lamb-dip technique, in order to resolve the D-hyperfine structure and confirm the results of Daniel *et al.* [175].

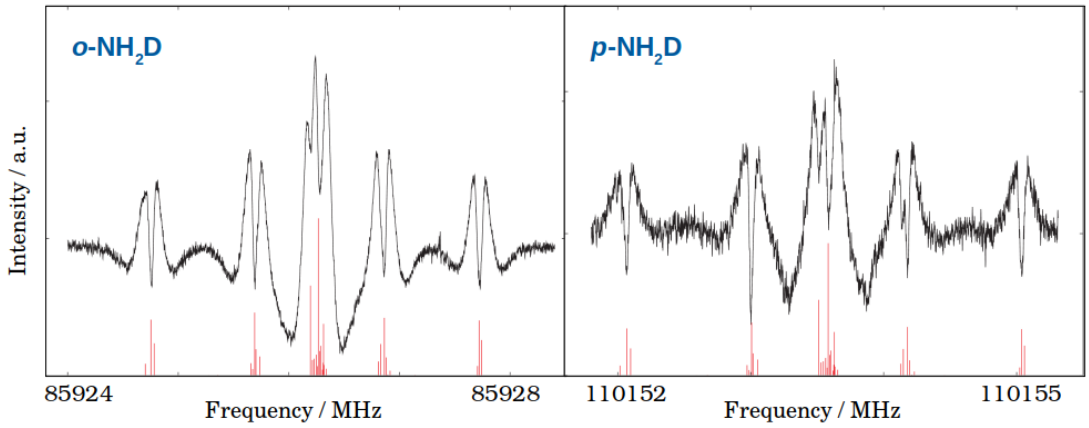

Figure 7.9: Lamb-dip spectra of the $1_{1,1} - 1_{0,1}$ transition for o-NH_2D and p-NH_2D, where some splittings due to D hyperfine interactions are resolved. Computed spectra are shown in red.

The measurements have been carried out with a tiny flow of ammonia (less than 1 bar) in a glass absorption cell where D_2 had previously been discharged. These conditions allowed us to resolve some D-hyperfine components for both the *ortho* and *para* species.

Bibliography

[1] W. Gordy and R. L. Cook, *Microwave molecular spectra*. Wiley,, 1984.

[2] P. F. Bernath, *Spectra of atoms and molecules*. Oxford university press, 2015.

[3] S. Yamamoto, *Introduction to Astrochemistry: Chemical Evolution from Interstellar Clouds to Star and Planet Formation*. Springer, 2017.

[4] E. Herbst and W. Klemperer, "The formation and depletion of molecules in dense interstellar clouds," *Astrophys. J.*, vol. 185, pp. 505–534, 1973.

[5] E. Galloway, ET & Herbst, "A refined study of the rate of $N^+ + H_2 \rightarrow NH^+ + H$ reaction under interstellar conditions: implications for NH_3 production," *Astron. Astrophys.*, vol. 211, pp. 413–418, 1989.

[6] E. Herbst, D. DeFrees, and A. McLean, "A detailed investigation of proposed gas-phase syntheses of ammonia in dense interstellar clouds," *Astrophys. J.*, vol. 321, pp. 898–906, 1987.

[7] G. B. Scott, C. G. Freeman, and M. J. McEwan, "The interstellar synthesis of ammonia," *Mon. Not. R. Astron. Soc.*, vol. 290, no. 4, pp. 636–638, 1997.

[8] M. Gerin, D. A. Neufeld, and J. R. Goicoechea, "Interstellar hydrides," *Ann. Rev. Astron. Astrophys.*, vol. 54, pp. 181–225, 2016.

[9] C. G. FREEMAN, P. W. HARLAND, and M. J. McEWAN, "The interstellar synthesis of HC_3N and HC_5N," *Astrophys. Lett.*, vol. 19, no. 4, pp. 133–135, 1978.

[10] L. Huang, O. Asvany, A. Chang, N. Balucani, S. Lin, Y. Lee, Kaiser, RI, and Y. Osamura, "Crossed beam reaction of cyano radicals with hydrocarbon molecules. IV. Chemical dynamics of cyanoacetylene (HCCCN; $X^1\Sigma^+$) formation from reaction of CN ($X^2\Sigma^+$) with acetylene, C_2H_2 ($X^1\Sigma_g^+$)," *J. Chem. Phys.*, vol. 113, no. 19, pp. 8656–8666, 2000.

[11] M. Melosso, B. A. McGuire, F. Tamassia, C. Degli Esposti, and L. Dore, "Astronomical search of vinyl alcohol assisted by submillimeter spectroscopy," *ACS Earth and Space Chemistry*, vol. 3, no. 7, pp. 1189–1195, 2019.

[12] M. Caris, *A Supersonic Jet Spectrometer for Terahertz Applications (SuJeSTA)*. Cuvillier Verlag, 2006.

[13] L. Bizzocchi, M. Melosso, L. Dore, *et al.*, "Accurate laboratory measurement of the complete fine structure of the $N = 1 - 0$ transition of ^{15}NH," *Astrophys. J.*, vol. 863, no. 1, p. 3, 2018.

[14] M. Melosso, L. Bizzocchi, F. Tamassia, C. Degli Esposti, E. Canè, and L. Dore, "The rotational spectrum of ^{15}ND. Isotopic-independent Dunham-type analysis of the imidogen radical," *Phys. Chem. Chem. Phys.*, vol. 21, no. 7, pp. 3564–3573, 2019.

[15] M. Alexander, P. Dagdigian, M. E. Jacox, *et al.*, "Nitramine propellant ignition and combustion research," *Prog. Energy Combust. Sci.*, vol. 17, no. 4, pp. 263–296, 1991.

[16] J. A. Miller and C. T. Bowman, "Mechanism and modeling of nitrogen chemistry in combustion," *Prog. Energy Combust. Sci.*, vol. 15, no. 4, pp. 287–338, 1989.

[17] R. Wagenblast, D. A. Williams, T. J. Millar, and L. A. M. Nejad, "On the origin of NH in diffuse interstellar clouds," *Mon. Not. R. Astron. Soc.*, vol. 260, no. 2, p. 420, 1993.

[18] P. Feldman, K. Fournier, V. Grinin, and A. Zvereva, "The abundance of ammonia in Comet P/Halley derived from ultraviolet spectrophotometry of NH by ASTRON and IUE," *Astrophys. J.*, vol. 404, pp. 348–355, 1993.

[19] J. L. Schmitt, "An investigation of the NH bands in stellar spectra," *Publ. Astron. Soc. Pac.*, vol. 81, no. 482, p. 657, 1969.

[20] S. Ridgway, D. Carbon, D. Hall, and J. Jewell, "An atlas of late-type stellar spectra, 2400-2778 inverse centimeters," *Astrophys. J. Supp.*, vol. 54, pp. 177–209, 1984.

[21] N. Grevesse, D. Lambert, A. Sauval, E. Van Dishoeck, C. Farmer, and R. Norton, "Identification of solar vibration-rotation lines of NH and the solar nitrogen abundance," *Astron. Astrophys.*, vol. 232, pp. 225–230, 1990.

[22] M. Geller, C. Farmer, R. Norton, A. Sauval, and N. Grevesse, "First identification of pure rotation lines of NH in the infrared solar spectrum," *Astron. Astrophys.*, vol. 249, pp. 550–552, 1991.

[23] K. Meyer, DM & Roth, "Discovery of interstellar NH," *Astrophys. J.*, vol. 376, pp. L49–L52, 1991.

[24] C. M. Persson, J. H. Black, J. Cernicharo, *et al.*, "Nitrogen hydrides in interstellar gas-Herschel/HIFI observations towards G10. 6-0.4 (W31C)," *Astron. Astrophys.*, vol. 521, p. L45, 2010.

[25] Bacmann, A., Daniel, F., Caselli, P., *et al.*, "Stratified NH and ND emission in the prestellar core 16293E in L1689N," *Astron. Astrophys.*, vol. 587, p. A26, 2016.

[26] A. Bacmann, E. Caux, P. Hily-Blant, *et al.*, "First detection of ND in the solar-mass protostar IRAS16293-2422," *Astron. Astrophys.*, vol. 521, p. L42, 2010.

[27] P. T. O'Neill, S. Viti, and D. A. Williams, "Surface hydrogenation in diffuse and translucent interstellar clouds," *Astron. Astrophys.*, vol. 388, pp. 346–354, June 2002.

[28] R. Le Gal, P. Hily-Blant, A. Faure, G. Pineau des Forêts, C. Rist, and S. Maret, "Interstellar chemistry of nitrogen hydrides in dark clouds," *Astron. Astrophys.*, vol. 562, p. A83, 2014.

[29] J. Aléon, "Multiple Origins of Nitrogen Isotopic Anomalies in Meteorites and Comets," *Astrophys. J.*, vol. 722, pp. 1342–1351, 2010.

[30] B. Marty, M. Chaussidon, R. C. Wiens, A. J. G. Jurewicz, and D. S. Burnett, "A ^{15}N-Poor Isotopic Composition for the Solar System As Shown by Genesis Solar Wind Samples," *Science*, vol. 332, p. 1533, 2011.

[31] E. Füri and B. Marty, "Nitrogen isotope variations in the Solar System," *Nature Geoscience*, vol. 8, pp. 515–522, 2015.

[32] M. Gerin, N. Marcelino, N. Biver, *et al.*, "Detection of ^{15}NH{2}D in dense cores: a new tool for measuring the ^{14}N/^{15}N ratio in the cold ISM," *Astron. Astrophys.*, vol. 498, pp. L9–L12, 2009.

[33] R. Ram and P. Bernath, "Revised molecular constants and term values for the $x^3\sigma$ and $a^3\pi$ states of NH," *J. Mol. Spectrosc.*, vol. 260, no. 2, pp. 115–119, 2010.

[34] L. Dore, L. Bizzocchi, C. Degli Esposti, and F. Tamassia, "Fine and hyperfine structure of the $n = 1 \leftarrow 0$ transition of ND ($x^3\sigma$) in vibrational excited states," *Mol. Phys.*, vol. 109, no. 17-18, pp. 2191–2198, 2011.

[35] J. L. Dunham, "The Energy Levels of a Rotating Vibrator," *Phys. Rev.*, vol. 41, pp. 721–731, 1932.

[36] R. J. Le Roy, "Improved parameterization for combined isotopomer analysis of diatomic spectra and its application to HF and DF," *J. Mol. Spectrosc.*, vol. 194, no. 2, pp. 189–196, 1999.

[37] J. M. Brown, J. M. Brown, and A. Carrington, *Rotational spectroscopy of diatomic molecules*. Cambridge university press, 2003.

[38] A. H. M. Ross, R. S. Eng, and H. Kildal, "Heterodyne measurements of ^{12}C ^{18}O, ^{13}C ^{16}O, and ^{13}C ^{18} O laser frequencies; mass dependence of Dunham coefficients," *Opt. Comm.*, vol. 12, pp. 433–438, 1974.

[39] J. K. G. Watson, "The isotope dependence of diatomic Dunham coefficients," *J. Mol. Spectrosc.*, vol. 80, pp. 411–421, 1980.

[40] J. K. G. Watson, "The isotope dependence of the equilibrium rotational constants in $^1\Sigma$ states of diatomic molecules," *J. Mol. Spectrosc.*, vol. 45, pp. 99–113, 1973.

[41] J. M. Brown and J. K. G. Watson, "Spin-orbit and spin-rotation coupling in doublet states of diatomic molecules," *J. Mol. Spectrosc.*, vol. 65, pp. 65–74, 1977.

[42] E. Tiemann, H. Arnst, W. Stieda, T. Törring, and J. Hoeft, "Observed adiabatic corrections to the Born-Oppenheimer approximation for diatomic molecules with ten valence electrons," *Chem. Phys.*, vol. 67, no. 2, pp. 133–138, 1982.

[43] S. Bailleux, M. Martin-Drumel, L. Margulès, *et al.*, "High-resolution terahertz spectroscopy of the ^{15}NH radical ($x^3\sigma$-)," *Astron. Astrophys.*, vol. 538, p. A135, 2012.

[44] L. Dore, "Using Fast Fourier Transform to compute the line shape of frequency-modulated spectral profiles," *J. Mol. Spectrosc.*, vol. 221, no. 1, pp. 93–98, 2003.

[45] R. Ram, P. Bernath, and K. Hinkle, "Infrared emission spectroscopy of NH: Comparison of a cryogenic echelle spectrograph with a Fourier transform spectrometer," *J. Chem. Phys.*, vol. 110, no. 12, pp. 5557–5563, 1999.

[46] H. M. Pickett, "The fitting and prediction of vibration-rotation spectra with spin interactions," *J. Mol. Spectrosc.*, vol. 148, no. 2, pp. 371–377, 1991.

[47] F. Lewen, S. Brünken, G. Winnewisser, M. Šimečková, and Š. Urban, "Doppler-limited rotational spectrum of the NH radical in the 2 THz region," *J. Mol. Spectrosc.*, vol. 226, no. 2, pp. 113–122, 2004.

[48] T. Bernath, Peter F & Amano, "Difference frequency laser spectroscopy of the $v = 1 \leftarrow 0$ transition of NH," *J. Mol. Spectrosc.*, vol. 95, no. 2, pp. 359–364, 1982.

[49] J. Flores-Mijangos, J. M. Brown, F. Matsushima, *et al.*, "The far-infrared spectrum of the ^{14}NH radical in its $x^3\sigma$- state," *J. Mol. Spectrosc.*, vol. 225, no. 2, pp. 189–195, 2004.

[50] S. Saito and M. Goto, "Laboratory submillimeter-wave observation of the N = 1-0 transition of the ND ($^3\sigma^-$) radical," *Astrophys. J.*, vol. 410, pp. L53–L55, 1993.

[51] S. Takano, T. Klaus, and G. Winnewisser, "The ND radical: Laboratory measurement of the N = 2–1 rotational transition at 1 THz," *J. Mol. Spectrosc.*, vol. 192, no. 2, pp. 309–319, 1998.

[52] P. Ram, RS & Bernath, "Fourier transform infrared emission spectroscopy of ND and PH," *J. Mol. Spectrosc.*, vol. 176, no. 2, pp. 329–336, 1996.

[53] M. Martin-Drumel, O. Pirali, and M. Vervloet, "Synchrotron based FT-FIR pure rotational spectroscopy of the NH_2 radical in its two lowest vibrational states," *J. Phys. Chem. A*, vol. 118, no. 8, pp. 1331–1338, 2014.

[54] M. Wang, G. Audi, F. G. Kondev, W. J. Huang, S. Naimi, and X. Xu, "The AME2016 atomic mass evaluation (II). Tables, graphs and references," *Chinese Physics C*, vol. 41, p. 030003, 2017.

[55] A. Kratzer, "Die ultraroten Rotationsspektren der Halogenwasserstoffe," *Z. Physics*, vol. 3, p. 289, 1920.

[56] C. L. Pekeris, "The Rotation-Vibration Coupling in Diatomic Molecules," *Phys. Rev.*, vol. 45, p. 98, 1934.

[57] C. Puzzarini, "Ab initio characterization of XH_3 (X = N, P). I. Ammonia, phosphine and their related ions and radicals: structure and thermochemistry," *Theor. Chem. Acc.*, vol. 120, no. 4-6, pp. 325–336, 2008.

[58] CFOUR, a quantum-chemical program package by J.F. Stanton, J. Gauß, M.E. Harding, M.E.P.G. Szalay with contributions from A.A. Auer, R.J. Bartlett, U. Benedikt, C. Berger, D.E. Bernholdt, Y.J. Bomble, L. Cheng, O. Christiansen, M. Heckert, O. Heun, C. Huber, T.-C. Jagau, D. Jonsson, J. Jusélius, K. Klein, W.J. Lauderdale, D.A. Matthews, T. Metzroth, L.A. Mück, D.P. O'Neill, D.R. Price, E. Prochnow, C. Puzzarini, K. Ruud, F. Schiffmann, W. Schwalbach, S. Stopkowicz, A. Tajti, J. Vázquez, F. Wang, J.D. Watts and the integral packages MOLECULE (J. Almlöf and P.R. Taylor), PROPS (P.R. Taylor), ABACUS (T. Helgaker, H.J. Aa. Jensen, P. Jørgensen, and J. Olsen), and ECP routines by A. V. Mitin and C. van Wüllen. For the current version, see http://www.cfour.de.

[59] L. Bizzocchi, C. Degli Esposti, L. Dore, J. Gauss, and C. Puzzarini, "The Born–Oppenheimer equilibrium bond distance of GeO from millimetre-and submillimetre-wave spectra and quantum-chemical calculations," *Mol. Phys.*, vol. 113, no. 8, pp. 801–807, 2015.

[60] E. A. Scarl and F. W. Dalby, "High field Stark effects in CH and NH," *Can. J. Phys.*, vol. 52, p. 1429, 1974.

[61] A. Robinson, J. Brown, J. Flores-Mijangos, L. Zink, and M. Jackson, "Spectroscopic study of the ^{14}NH radical in vibrationally excited levels of the $X^3\Sigma$ state by far infrared laser magnetic resonance," *Mol. Phys.*, vol. 105, pp. 639–662, 2007.

[62] J. Gauss and C. Puzzarini, "Quantum-chemical calculation of Born-Oppenheimer breakdown parameters to rotational constants," *Mol. Phys.*, vol. 108, pp. 269–277, 2010.

[63] K. K. Irikura, "Experimental vibrational zero-point energies: Diatomic molecules," *J. Phys. Chem. Ref. Data*, vol. 36, no. 2, pp. 389–397, 2007.

[64] E. Roueff, J. Loison, and K. Hickson, "Isotopic fractionation of carbon, deuterium, and nitrogen: a full chemical study," *Astron. Astrophys.*, vol. 576, p. A99, 2015.

[65] M. Melosso, C. Degli Esposti, and L. Dore, "Terahertz spectroscopy and global analysis of the rotational spectrum of doubly deuterated amidogen radical ND_2," *Astrophys. J. Suppl. Ser.*, vol. 233, no. 15, 2017.

[66] M. Melosso, B. Conversazioni, C. Degli Esposti, L. Dore, E. Cané, F. Tamassia, and L. Bizzocchi, "The pure rotational spectrum of $^{15}ND_2$ observed by millimetre and submillimetre-wave spectroscopy.," *J. Quant. Spectrosc. Ra.*, vol. 222, pp. 186–189, 2019.

[67] C. Ceccarelli, A. Castets, L. Loinard, E. Caux, and A. Tielens, "Detection of doubly deuterated formaldehyde towards the low-luminosity protostar IRAS 16293-2422," *Astron. Astrophys.*, vol. 338, pp. L43–L46, 1998.

[68] D. Lis, E. Roueff, M. Gerin, *et al.*, "Detection of triply deuterated ammonia in the Barnard 1 cloud," *Astrophys. J. Lett.*, vol. 571, no. 1, p. L55, 2002.

[69] C. Vastel, T. Phillips, C. Ceccarelli, and J. Pearson, "First detection of doubly deuterated hydrogen sulfide," *Astrophys. J. Lett.*, vol. 593, no. 2, p. L97, 2003.

[70] B. Parise, A. Castets, E. Herbst, *et al.*, "First detection of triply-deuterated methanol," *Astron. Astrophys.*, vol. 416, no. 1, pp. 159–163, 2004.

[71] T. Millar, "Modelling deuterium fractionation in interstellar clouds," *Planet. Space Sci.*, vol. 50, no. 12-13, pp. 1189–1195, 2002.

[72] S. A. Sandford, "Interstellar processes leading to molecular deuterium enrichment and their detection," *Planet. Space Sci.*, vol. 50, no. 12-13, pp. 1145–1154, 2002.

[73] E. Roueff and M. Gerin, "Deuterium in molecules of the interstellar medium," *Space Sci. Rev.*, vol. 106, no. 1-4, pp. 61–72, 2003.

[74] C. Ceccarelli, P. Caselli, D. Bockelée-Morvan, *et al.*, "Deuterium fractionation: The Ariadne's thread from the precollapse phase to meteorites and comets today," *Protostars and Planets VI*, pp. 859–882, 2014.

[75] H. Roberts and T. Millar, "Gas-phase formation of doubly-deuterated species," *Astron. Astrophys.*, vol. 364, pp. 780–784, 2000.

[76] H. Roberts, E. Herbst, and T. Millar, "Enhanced deuterium fractionation in dense interstellar cores resulting from multiply deuterated H_3^+," *Astrophys. J. Lett.*, vol. 591, no. 1, p. L41, 2003.

[77] P. Caselli, T. Stantcheva, O. Shalabiea, V. I. Shematovich, and E. Herbst, "Deuterium fractionation on interstellar grains studied with modified rate equations and a Monte Carlo approach," *Planet. Space Sci.*, vol. 50, no. 12-13, pp. 1257–1266, 2002.

[78] B. Turner, B. Zuckerman, M. Morris, and P. Palmer, "Microwave detection of interstellar deuterated ammonia," *Astrophys. J.*, vol. 219, pp. L43–L47, 1978.

[79] E. Roueff, S. Tiné, L. Coudert, G. Pineau des Forêts, E. Falgarone, and M. Gerin, "Detection of doubly deuterated ammonia in L134N," *Astron. Astrophys.*, vol. 354, pp. L63–L66, 2000.

[80] P. Swings, A. McKellar, and R. Minkowski, "Cometary emission spectra in the Visual Region," *Astrophys. J.*, vol. 98, pp. 142–152, 1943.

[81] E. F. van Dishoeck, D. J. Jansen, P. Schilke, and T. Phillips, "Detection of the interstellar NH_2 radical," *Astrophys. J.*, vol. 416, p. L83, 1993.

[82] P. Hily-Blant, S. Maret, A. Bacmann, *et al.*, "Nitrogen hydrides in the cold envelope of IRAS 16293-2422," *Astron. Astrophys.*, vol. 521, p. L52, 2010.

[83] P. Rousselot, O. Pirali, E. Jehin, *et al.*, "Toward a unique nitrogen isotopic ratio in cometary ices," *Astrophys. J. Lett.*, vol. 780, no. 2, p. L17, 2013.

[84] Y. Shinnaka, H. Kawakita, H. Kobayashi, M. Nagashima, and D. C. Boice, "$^{14}NH_2/^{14}NH_2$ ratio in comet C/2012 S1 (ISON) observed during its outburst in 2013 November," *Astrophys. J. Lett.*, vol. 782, no. 2, p. L16, 2014.

[85] E. Roueff, D. C. Lis, F. Van der Tak, M. Gerin, and P. Goldsmith, "Interstellar deuterated ammonia: from NH_3 to ND_3," *Astron. Astrophys.*, vol. 438, no. 2, pp. 585–598, 2005.

[86] D. Flower, G. P. Des Forêts, and C. Walmsley, "The importance of the ortho: para H_2 ratio for the deuteration of molecules during pre-protostellar collapse," *Astron. Astrophys.*, vol. 449, no. 2, pp. 621–629, 2006.

[87] E. A. Bergin and W. D. Langer, "Chemical evolution in preprotostellar and protostellar cores," *Astrophys. J.*, vol. 486, no. 1, p. 316, 1997.

[88] A. Belloche and P. Andre, "Disappearance of N_2H^+ from the gas phase in the class 0 protostar IRAM 04191," *Astron. Astrophys.*, vol. 419, no. 3, pp. L35–L38, 2004.

[89] P. Davies, D. Russell, B. Thrush, and H. Radford, "Rotational and hyperfine parameters of NH_2 (X^2B_1) from LMR spectra," *Chem. Phys. Lett.*, vol. 42, no. 1, pp. 35–38, 1976.

[90] G. Hills and J. Cook, "Fine and hyperfine parameters for NH_2 in X^2B_1 (000)," *J. Mol. Spectrosc.*, vol. 94, no. 2, pp. 456–460, 1982.

[91] A. Charo, E. Herbst, F. De Lucia, and K. Sastry, "Laboratory measurements of millimeter and submillimeter rotational transitions of NH_2," *Astrophys. J.*, vol. 244, p. L111, 1981.

[92] H. S. Müller, H. Klein, S. P. Belov, G. Winnewisser, I. Morino, K. M. Yamada, and S. Saito, "Terahertz spectroscopy of the amidogen radical, NH_2," *J. Mol. Spectrosc.*, vol. 195, no. 1, pp. 177–184, 1999.

[93] R. Gendriesch, F. Lewen, G. Winnewisser, and H. S. Müller, "Far-infrared laser-sideband measurements of the amidogen radical, NH_2, near 2 thz with microwave accuracy," *J. Mol. Struct.*, vol. 599, no. 1-3, pp. 293–304, 2001.

[94] L. Margulès, M. Martin-Drumel, O. Pirali, *et al.*, "Terahertz spectroscopy of the $^{15}NH_2$ amidogen radical," *Astron. Astrophys.*, vol. 591, p. A110, 2016.

[95] I. Morino and K. Kawaguchi, "Fourier Transform Far-Infrared spectroscopy of the NH_2, NHD, and ND_2 radicals," *J. Mol. Spectrosc.*, vol. 182, no. 2, pp. 428–438, 1997.

[96] K. Kobayashi, H. Ozeki, S. Saito, M. Tonooka, and S. Yamamoto, "The microwave spectrum of the NHD radical in the ground electronic state, $^2A''$," *J. Chem. Phys.*, vol. 107, no. 22, pp. 9289–9296, 1997.

[97] K. Dressler and D. A. Ramsay, "The electronic absorption spectra of NH_2 and ND_2," *Philos. Trans. R. Soc. London A*, vol. 251, no. 1002, pp. 553–602, 1959.

[98] G. Hills and A. McKellar, "Laser magnetic resonance spectrum of the $\nu 2$ band of ND_2," *J. Chem. Phys.*, vol. 71, no. 8, pp. 3330–3337, 1979.

[99] J. Cook and G. Hills, "Microwave optical double resonance spectroscopy of ND_2 in (000) of x^2b_1," *J. Chem. Phys.*, vol. 78, no. 5, pp. 2144–2153, 1983.

[100] M. Kanada, S. Yamamoto, and S. Saito, "The microwave spectrum of the ND_2 radical," *J. Chem. Phys.*, vol. 94, no. 5, pp. 3423–3428, 1991.

[101] J. Brown, S. Chalkley, and F. Wayne, "Determination of the dipole moment of the amino radical by optical stark spectroscopy with a tunable dye laser," *Mol. Phys.*, vol. 38, no. 5, pp. 1521–1537, 1979.

[102] J. K. Watson, "Aspects of quartic and sextic centrifugal effects on rotational energy levels," *Vibrational spectra and structure*, vol. 6, pp. 1–89, 1977.

[103] F. Matsushima, H. Odashima, T. Iwasaki, S. Tsunekawa, and K. Takagi, "Frequency-measurement of pure rotational transitions of H_2O from 0.5 to 5 THz," *J. Mol. Struct.*, vol. 352, pp. 371–378, 1995.

[104] I. Mills *et al.*, *Quantities, units and symbols in physical chemistry*. Oxford; Boston: Blackwell Science; Boca Raton, Fla.: CRC Press [distributor],, 1993.

[105] D. Smith and W. Seddon, "Electron spin resonance spectra of ^{15}n labelled amino radicals," *Can. J. Chem.*, vol. 48, no. 12, pp. 1938–1942, 1970.

[106] H. Suzuki, S. Yamamoto, M. Ohishi, *et al.*, "A survey of CCS, HC_3N, HC_5N, and NH_3 toward dark cloud cores and their production chemistry," *Astrophys. J.*, vol. 392, pp. 551–570, 1992.

[107] F. Wyrowski, P. Schilke, S. Thorwirth, K. Menten, and G. Winnewisser, "Physical conditions in the proto-planetary nebula CRL 618 derived from observations of vibrationally excited HC_3N," *Astrophys. J.*, vol. 586, no. 1, p. 344, 2003.

[108] L. Decin, M. Agúndez, M. J. Barlow, *et al.*, "Warm water vapour in the sooty outflow from a luminous carbon star," *Nature*, vol. 467, no. 7311, p. 64, 2010.

[109] J. Li, J. Wang, Q. Gu, Z.-y. Zhang, and X. Zheng, "Large-scale kinematics, astrochemistry, and magnetic field studies of massive star-forming regions through HC_3N, HNC, and C_2H mappings," *Astrophys. J.*, vol. 745, no. 1, p. 47, 2011.

[110] E. Chapillon, A. Dutrey, S. Guilloteau, *et al.*, "Chemistry in disks. VII. first detection of HC_3N in protoplanetary disks," *Astrophys. J.*, vol. 756, no. 1, p. 58, 2012.

[111] A. J. Al-Edhari, C. Ceccarelli, C. Kahane, *et al.*, "History of the solar-type protostar IRAS 16293–2422 as told by the cyanopolyynes," *Astron. & Astrophys.*, vol. 597, p. A40, 2017.

[112] K. I. Öberg, V. V. Guzmán, K. Furuya, *et al.*, "The comet-like composition of a protoplanetary disk as revealed by complex cyanides," *Nature*, vol. 520, no. 7546, p. 198, 2015.

[113] W. Langer, F. Schloerb, R. Snell, and J. Young, "Detection of deuterated cyanoacetylene in the interstellar cloud TMC-1," *Astrophys. J.*, vol. 239, pp. L125–L128, 1980.

[114] G. B. Esplugues, J. Cernicharo, S. Viti, *et al.*, "Combined IRAM and Herschel/HIFI study of cyano(di)acetylene in Orion KL: tentative detection of DC_3N," *Astron. & Astrophys.*, vol. 559, p. A51, 2013.

[115] A. Belloche, H. Müller, R. Garrod, and K. Menten, "Exploring molecular complexity with ALMA (EMoCA): Deuterated complex organic molecules in Sagittarius B2 (N2)," *Astron. & Astrophys.*, vol. 587, p. A91, 2016.

[116] P. Mallinson and R. L. de Zafra, "The microwave spectrum of cyanoacetylene in ground and excited vibrational states," *Mol. Phys.*, vol. 36, no. 3, pp. 827–843, 1978.

[117] G. Plummer, D. Mauer, K. Yamada, and K. Möller, "Rotational spectra of DC_3N in some excited vibrational states," *J. Mol. Spectrosc.*, vol. 130, no. 2, pp. 407–418, 1988.

[118] H. Spahn, H. S. Müller, T. F. Giesen, *et al.*, "Rotational spectra and hyperfine structure of isotopic species of deuterated cyanoacetylene, DC_3N," *Chem. Phys.*, vol. 346, no. 1-3, pp. 132–138, 2008.

[119] E. Fliege, H. Dreizler, and B. Kleibömer, "Deuterium and nitrogen quadrupole coupling in cyanodeuteroacetylene," *J. Mol. Struct.*, vol. 97, pp. 225–228, 1983.

[120] L. Tack and S. G. Kukolich, "Beam-maser spectroscopy on cyanoacetylene-D," *J. Chem. Phys.*, vol. 78, no. 11, pp. 6512–6514, 1983.

[121] M. Uyemura, S. Deguchi, Y. Nakada, and T. Onaka, "Infrared intensities of bending fundamentals in gaseous HCCCN and DCCCN," *B. Chem. Sso. Jpn.*, vol. 55, no. 2, pp. 384–388, 1982.

[122] Y. Bénilan, A. Jolly, F. Raulin, and J.-C. Guillemin, "IR band intensities of DC_3N and $HC_3^{15}N$: Implication for observations of Titan's atmosphere," *Planetary and Space Science*, vol. 54, no. 6, pp. 635–640, 2006.

[123] P. Mallinson and A. Fayt, "High resolution infra-red studies of HCCCN and DCCCN," *Mol. Phys.*, vol. 32, no. 2, pp. 473–485, 1976.

[124] B. Coveliers, W. Ahmed, A. Fayt, and H. Bürger, "Far-infrared spectra of DCCCN," *J. Mol. Spectrosc.*, vol. 156, no. 1, pp. 77–88, 1992.

[125] L. Bizzocchi, F. Tamassia, J. Laas, B. M. Giuliano, C. Degli Esposti, L. Dore, M. Melosso, *et al.*, "Rotational and high-resolution infrared spectrum of HC_3N: Global ro-vibrational analysis and improved line catalog for astrophysical observations," *Astrophys. J. Suppl. Ser.*, vol. 233, 2017.

[126] A. Fayt, C. Vigouroux, F. Willaert, *et al.*, "Global analysis of high resolution infrared and rotational spectra of $HC_3^{15}N$ up to 1335 cm^{-1}," *J. Mol. Struct.*, vol. 695, pp. 295–311, 2004.

[127] J. Brown, J. Hougen, K.-P. Huber, *et al.*, "The labeling of parity doublet levels in linear molecules," *J. Mol. Spectrosc.*, vol. 55, no. 1-3, pp. 500–503, 1975.

[128] K. M. Yamada, F. Birss, and M. Aliev, "Effective Hamiltonian for polyatomic linear molecules," *J. Mol. Spectrosc.*, vol. 112, no. 2, pp. 347–356, 1985.

[129] G. Wagner, B. Winnewisser, M. Winnewisser, and K. Sarka, "The infrared-spectrum of $HC^{15}NO$ in the range 170-1300 cm^{-1}," *J. Mol. Spectrosc.*, vol. 162, no. 1, pp. 82–119, 1993.

[130] T. Okabayashi, K. Tanaka, and T. Tanaka, "Analysis of rovibrational resonances observed in the microwave spectrum of FCCCN," *J. Mol. Spectrosc.*, vol. 195, no. 1, pp. 22–42, 1999.

[131] A. Belloche, R. Garrod, H. Müller, K. Menten, I. Medvedev, J. Thomas, and Z. Kisiel, "Re-exploring molecular complexity with ALMA (ReMoCA): Interstellar detection of urea," *arXiv preprint arXiv:1906.04614*, 2019.

[132] E. Sedaghati, H. M. Boffin, R. J. MacDonald, *et al.*, "Detection of titanium oxide in the atmosphere of a hot Jupiter," *Nature*, vol. 549, no. 7671, p. 238, 2017.

[133] T. Kamiński, C. Gottlieb, K. Menten, *et al.*, "Pure rotational spectra of TiO and TiO_2 in VY Canis Majoris," *Astron. Astrophys.*, vol. 551, p. A113, 2013.

[134] W. Parkinson and E. Reeves, "The spectrum of titanium nitride," *Can. J. Phys.*, vol. 41, no. 4, pp. 702–704, 1963.

[135] T. Dunn, L. K. Hanson, and K. A. Rubinson, "Rotational analysis of the red electronic emission system of titanium nitride," *Can. J. Phys.*, vol. 48, no. 14, pp. 1657–1663, 1970.

[136] A. Douglas and P. Veillette, "The electronic spectrum of TiN," *J. Chem. Phys.*, vol. 72, no. 10, pp. 5378–5380, 1980.

[137] T. Wong, D.-W. Mok, N.-K. Sze, and A.-C. Cheung, "Laser spectroscopy of the $a^2\pi$-$x^2\sigma$ system of TiN," *J. Quant. Spectrosc. Ra.*, vol. 50, no. 5, pp. 455–461, 1993.

[138] T. Steimle, J. Shirley, K. Jung, L. Russon, and C. Scurlock, "A microwave-optical double resonance spectroscopic study of TiO and TiN," *J. Mol. Spectrosc.*, vol. 144, no. 1, pp. 27–31, 1990.

[139] D. Fletcher, C. Scurlock, K. Jung, and T. Steimle, "Hyperfine interactions in the ground states of titanium monoxide and mononitride," *J. Chem. Phys.*, vol. 99, no. 6, pp. 4288–4299, 1993.

[140] K.-i. Namiki, S. Saito, J. S. Robinson, and T. C. Steimle, "The pure rotational spectra of TiO ($x^3\delta$) and TiN ($x^2\sigma^+$)," *J. Mol. Spectrosc.*, vol. 191, no. 1, pp. 176–182, 1998.

[141] A. A. Breier, B. Waßmuth, G. W. Fuchs, J. Gauss, and T. F. Giesen, "Mass-independent analysis of the stable isotopologues of gas-phase titanium monoxide – TiO," *J. Mol. Spectrosc.*, vol. 355, pp. 46–58, 2019.

[142] P. Neubauer-Guenther, T. Giesen, U. Berndt, G. Fuchs, and G. Winnewisser, "The cologne carbon cluster experiment: ro-vibrational spectroscopy on C_8 and other small carbon clusters," *Spectr. Acta A*, vol. 59, no. 3, pp. 431–441, 2003.

[143] D. Witsch, V. Lutter, A. Breier, *et al.*, "Infrared spectroscopy of disilicon-carbide, Si_2C: The ν_3 fundamental band," *J. Phys. Chem. A*, 2019.

[144] C. Degli Esposti, L. Dore, M. Melosso, K. Kobayashi, C. Fujita, and H. Ozeki, "Millimeter-wave and submillimeter-wave spectra of aminoacetonitrile in the three lowest vibrational excited states," *Astrophys. J. Suppl. S.*, vol. 230, no. 2, p. 26, 2017.

[145] R. D. Brown, P. D. Godfrey, J. W. Storey, *et al.*, "A search for interstellar glycine," *Mon. Not. R. Astron. Soc.*, vol. 186, pp. 5P–8P, 1979.

[146] C. Ceccarelli, L. Loinard, A. Castets, A. Faure, and B. Lefloch, "Search for glycine in the solar type protostar IRAS 16293-2422," *Astron. Astrophys.*, vol. 362, pp. 1122–1126, 2000.

[147] L. E. Snyder, F. J. Lovas, J. Hollis, *et al.*, "A rigorous attempt to verify interstellar glycine," *Astrophys. J.*, vol. 619, no. 2, p. 914, 2005.

[148] R. T. Garrod, "A three-phase chemical model of hot cores: The formation of glycine," *Astrophys. J.*, vol. 765, no. 1, p. 60, 2013.

[149] I. Jiménez-Serra, P. Caselli, S. Viti, *et al.*, "Detectability of glycine in solar-type system precursors," *Astrophys. J. Lett.*, vol. 787, no. 2, p. L33, 2014.

[150] A. Strecker, "Ueberdie künstlichebildung der milchsäure und einenneuen, demglycocollhomologen," *Ann. Chem. Pharm.*, vol. 75, pp. 27–45, 1850.

[151] J. E. Elsila, J. P. Dworkin, M. P. Bernstein, M. P. Martin, and S. A. Sandford, "Mechanisms of amino acid formation in interstellar ice analogs," *Astrophys. J.*, vol. 660, no. 1, p. 911, 2007.

[152] J. Macdonald and J. Tyler, "The microwave spectrum of aminoacetonitrile," *J. Chem. Soc., Chem. Comm.*, no. 17, pp. 995–995, 1972.

[153] H. M. Pickett, "The microwave spectrum, structure, and dipole moment of amino acetonitrile," *J. Mol. Spectrosc.*, vol. 46, no. 3, pp. 335–340, 1973.

[154] M. Bogey, H. Dubus, and J. Guillemin, "The millimeter-wave spectrum of aminoacetonitrile," *J. Mol. Spectrosc.*, vol. 143, no. 1, pp. 180–182, 1990.

[155] A. Belloche, K. Menten, C. Comito, *et al.*, "Detection of amino acetonitrile in Sgr B2 (N)," *Astron. Astrophys.*, vol. 492, no. 3, pp. 769–773, 2008.

[156] Y. Motoki, Y. Tsunoda, H. Ozeki, and K. Kobayashi, "Submillimeter-wave spectrum of aminoacetonitrile and its deuterated isotopologues, possible precursors of the simplest amino acid glycine," *Astrophys. J. Suppl. S.*, vol. 209, no. 2, p. 23, 2013.

[157] C. Fujita, H. Ozeki, and K. Kobayashi, "The microwave spectroscopy of aminoacetonitrile in the vibrational excited state," in *70th Internat. Symp. Mol. Spectrosc.*, 2015.

[158] B. Bak, E. Hansen, F. Nicolaisen, and O. Nielsen, "Vibrational spectra of aminoacetonitrile," *Can. J. Phys.*, vol. 53, no. 19, pp. 2183–2188, 1975.

[159] M. P. Bernstein, C. W. Bauschlicher Jr, and S. A. Sandford, "The infrared spectrum of matrix isolated aminoacetonitrile, a precursor to the amino acid glycine," *Adv. Space Res.*, vol. 33, no. 1, pp. 40–43, 2004.

[160] L. Kolesniková, E. Alonso, S. Mata, and J. Alonso, "Rotational spectra in 29 vibrationally excited states of interstellar aminoacetonitrile," *Astrophys. J. Suppl. S.*, vol. 229, no. 2, p. 26, 2017.

[161] R. Brown, P. Godfrey, A. Ottrey, and J. Storey, "Quadrupole hyperfine structure of the rotational spectrum of aminoacetonitrile," *J. Mol. Spectrosc.*, vol. 68, no. 3, pp. 359–366, 1977.

[162] D. Papousek and M. R. Aliev, "Molecular vibrational-rotational spectra," 1982.

[163] M. J. Frisch, H. P. Hratchian, and A. B. Nielsen, *Gaussian 09: Programmer's Reference*. gaussian, 2009.

[164] J. E. Pineda, A. J. Maury, G. A. Fuller, *et al.*, "The first ALMA view of IRAS 16293-2422-Direct detection of infall onto source B and high-resolution kinematics of source A," *Astron. Astrophys.*, vol. 544, p. L7, 2012.

[165] E. F. van Dishoeck, G. A. Blake, D. J. Jansen, and nd others, "Molecular abundances and low mass star formation II. Organic and deuterated species towards IRAS 16293-2422," *Astrophys. J.*, vol. 447, pp. 760–782, 1995.

[166] J. K. Jørgensen, C. Favre, S. E. Bisschop, T. L. Bourke, E. F. Van Dishoeck, and M. Schmalzl, "Detection of the simplest sugar, glycolaldehyde, in a solar-type protostar with ALMA," *Astrophys. J. Lett.*, vol. 757, no. 1, p. L4, 2012.

[167] E. C. Fayolle, K. I. Öberg, J. K. Jørgensen, *et al.*, "Protostellar and cometary detections of organohalogens," *Nat. Astron.*, vol. 1, no. 10, p. 703, 2017.

[168] E. Herbst and E. F. Van Dishoeck, "Complex organic interstellar molecules," *Ann. Rev. Astron. Astrophys.*, vol. 47, pp. 427–480, 2009.

[169] H. Butner, S. Charnley, C. Ceccarelli, S. Rodgers, J. Pardo, B. Parise, J. Cernicharo, and G. Davis, "Discovery of interstellar heavy water," *Astrophys. J. Lett.*, vol. 659, no. 2, p. L137, 2007.

[170] C. Ceccarelli, A. Bacmann, A. Boogert, *et al.*, "Herschel spectral surveys of star-forming regions-overview of the 555–636 GHz range," *Astron. Astrophys.*, vol. 521, p. L22, 2010.

[171] M. Bonfand, A. Belloche, K. Menten, R. Garrod, and H. Müller, "Exploring molecular complexity with ALMA (EMoCA): Detection of three new hot cores in Sagittarius B2 (N)," *Astron. Astrophys.*, vol. 604, p. A60, 2017.

[172] D. Christen and H. S. Müller, "The millimeter wave spectrum of *aGg'* ethylene glycol: The quest for higher precision," *Phys. Chem. Chem. Phys.*, vol. 5, no. 17, pp. 3600–3605, 2003.

[173] W. E. Lamb Jr, "Theory of an optical maser," *Phys. Rev.*, vol. 134, no. 6A, p. A1429, 1964.

[174] M. K. Bane, C. Jones, S. L. Choong, *et al.*, "High-resolution FTIR spectroscopy of the ν_7 and ν_8 bands of 1-phosphapropyne," *J. Mol. Spectrosc.*, vol. 275, pp. 9–14, 2012.

[175] F. Daniel, L. Coudert, A. Punanova, *et al.*, "The NH_2D hyperfine structure revealed by astrophysical observations," *Astron. Astrophys.*, vol. 586, p. L4, 2016.